SYNTHESIS, CHARACTERIZATION AND CHEMISTRY OF PLATINUM AND IRIDIUM NANOPARTICLES IN SOLUTION AND NANOPOROUS SILICAS

by

PARBATEE JAGASSAR

A dissertation submitted to the Graduate Faculty in Chemistry in partial fulfillment of the requirements for the degree of Doctor of Philosophy, The City University of New York

2012

This manuscript has been read and accepted for the
Graduate Faculty in Chemistry in satisfaction of the
dissertation requirement for the degree of Doctor of Philosophy.

09/11/2012	Dr. Harry D. Gafney
Date	Chair of Examining Committee
09/11/2012	Dr. Maria Tamargo
Date	Executive Officer

Dr. Harry D. Gafney

Dr. Hiroshi Matsui

Dr. Uri Samuni
Supervisory Committee

THE CITY UNIVERSITY OF NEW YORK

Abstract

SYNTHESIS, CHARACTERIZATION AND CHEMISTRY OF PLATINUM AND IRIDIUM NANOPARTICLES IN SOLUTION AND NANOPOROUS SILICAS

by

Parbatee Jagassar

Adviser: Dr. Harry D. Gafney

This project focuses on the synthesis of catalytically-active, transition-metal nanoparticles, their adsorption into porous Vycor glass (PVG), the removal of the poly(vinylpyrrolidone) (PVP) surfactant employed in their synthesis and their chemistry with Ru(II) diimine complexes. Platinum and iridium nanoparticles with a narrow size distribution were prepared by the alcohol reduction method with poly(vinylpyrrolidone) (PVP) as the size limiting surfactant. PVP/Pt nanoparticles adsorb into PVG and as much as 46 ± 4% of the PVP can be removed without further nanoparticle aggregation. XANES spectra show that removal of the PVP surfactant occurs without oxidation of the Pt nanoparticle. EXAFS of the adsorbed Pt nanoparticles after removal of the PVP yield a Pt-Pt bond length of 2.74 ± 0.01 Å which is slightly shorter than the Pt-Pt bond length measured in Pt foil, 2.78 Å. We have shown that the Pt nanoparticles, both the stripped and the unstripped of PVP in porous Vycor glass, does not influence their reactivity with either the $[Ru(bpy)_2dpp]^{2+}$ or the $[Ru(bpy)_2ppz]^{2+}$ complexes.

The addition of PVP/Pt or PVP/Ir nanoparticles to aqueous-ethanol solutions of $[Ru(bpy)_2ppz]^{2+}$ (ppz denotes 4,7-phenanthro-lino-5:6,5'6'pyrazine) leads to the spontaneous aggregation of the nanoparticles about the complex. A comparison of the aggregation about different Ru(II) diimines indicates aggregation initiates at the heteroleptic ligand. Although initiating at the ppz ligand, continued aggregation of the nanoparticles about the complex dilutes the specificity of the initial interaction leading to larger aggregates of differing shape. TEM analyses of the aggregates indicate the volume occupied by the individual nanoparticles is a small fraction of the total volume of the aggregate suggesting a somewhat open structure interlaced with the solvent. Correlating TEM analyses of the aggregation with the electronic spectra of the solutions reveals a new absorption assigned to the formation of the $[Ru(bpy)_2(ppz)^{2+}$-PVP/Pt] and $[Ru(bpy)_2(ppz)^{2+}$-PVP/Ir] aggregates. Analysis of the latter absorption as a function of the concentration of PVP/Pt nanoparticles indicates step-wise formation of the $[Ru(bpy)_2(ppz)^{2+}$-PVP/Pt] aggregates. Consistent with the self-assembly of the aggregates, intensity and lifetime quenching of the complex by the PVP/Pt nanoparticles shows that $\geq$ 80% of the quenching occurs by a static mechanism, *i.e.,* the self-assembly of the $[Ru(bpy)_2(ppz)^{2+}$-PVP/Pt] aggregates.

This dissertation is dedicated to
my husband Raj Jagassar

Acknowledgements

I would like to express my sincere gratitude to my mentor Dr. Harry D. Gafney, for whom I have the utmost respect and admiration. It is his constructive criticism, feedback, guidance and extensive knowledge of materials science chemistry that made my thesis possible.

Special thanks to my committee members, Dr. Hiroshi Matsui and Dr. Uri Samuni for their helpful suggestions and valuable comments on my research presentations. I am thankful to Dr. Sunil Dehipawala for his time and expertise in EXAFS measurements. I thank Dr. Jorge Morales, Dr. Jacopo Samson and Dr. Wei Su for their help with the TEM analyses. I am grateful to my colleagues, past and present; among them are Dr. Subhasish Chatterjee for his encouragement and advice, Anthony Perri for his collaborative efforts with Ru(II) diimines in fluid solution, Dr. Edward Look for his helpful discussions, Dr. Julie Colis Leventhal for her support with my research project, Jim Dimitrakopoulos for his aid in lifetime measurements and Marta Kowalczyk for her encouragement and friendship. I am also thankful to Professor Gerald Koeppl for his kindness and advice.

I am grateful to my family in Trinidad, especially my mother and father (Rajwanti Ramadhin and Samaroo Roopan), who have believed in my abilities and trusted me to choose my own path, my sisters (Surugdaye, Sindy, Indra and Annmarie) for their encouragement and support, and to my Aunt Madhurie and dearly departed Uncle Sonnylal: words are not enough to describe how their love has guided me.

Most of all, I would like to thank my husband and best friend Raj Jagassar, for his unconditional love and support.

Table of Contents

List of Tables

List of Figures

Chapter 1

1. INTRODUCTION

1.1. General Introduction

The huge demand for energy and the depletion of known energy reserves such as natural gas and petroleum focuses attention on solar energy conversion. One approach is to convert combustion products into combustible fuels. The combustion of methane, a major component of natural gas, for example, leads to carbon dioxide. Cycling carbon dioxide back into methane utilizing solar energy increases energy production and decreases greenhouse gas emissions. Small metal oxide nanoparticles, such as WO_3, adsorbed into Corning's code 7930 porous Vycor glass (PVG) photocatalytically convert CO_2 to CH_4 with water acting as the reducing agent and the source of hydrogen.[1,2] The quantum efficiency of conversion is surprisingly high, 0.14, but requires UV light, $\lambda_{ex} \leq$ 350 nm. This project focuses on one approach: photochemically driving multi-electron and proton reactions with visible light. To drive the conversion of CO_2 to CH_4 using longer wavelengths, for example, requires metals that are capable of: (1) multiple electron transfer; (2) exhibit absorption bands in the visible region themselves, or (3) can be attached to a compound that absorbs visible light and, when excited, is capable of promoting electron transfer in the metal. This research centers on: (1) the synthesis and characterization of Pt, Ir and Pt-Ir nanoparticles; (2) examining their adsorption into Corning's 7930 porous Vycor glass; (3) developing methodologies to remove the surfactant, poly(vinylpyrrolidone) (PVP), used to limit aggregation during synthesis; (4) examining the effect of removing the PVP on the nanoparticle, specifically its aggregation and spectroscopy and; (5) examining the coordination chemistry of the

stripped nanoparticle specifically their coordination chemistry with Ru(II) complexes possessing bridging diimine ligands.

1.2. Transition-Metal Nanoparticles

Metal nanoparticles of specific size have many properties different from those of the bulk material, such as changes in electronic structure,[3] increased magnetic susceptibility[4] and enhanced catalytic activity.[5] These properties make them suitable for applications in magnetic resonance imaging,[6-8] in drug delivery[9-11] and in DNA sensing.[12] Platinum is well known as a catalytic metal for the oxidation of CO and the reduction of NO_x in catalytic converters.[13-15] Platinum nanoparticles are generally prepared in the presence of a surfactant that limits aggregation. When used in the bulk form, however, the cost of the Pt dramatically increase the materials cost. However, when platinum is used in the form of nanoparticles, their surface area increases and their density is reduced thereby lowering their material cost.[16,17] In this study, the particles were prepared by an alcohol reduction method with poly(vinylpyrrolidone) (PVP) as the surfactant.[18] Some of the questions that need to be addressed and answered in this thesis are: (1) if the Pt nanoparticle assumes the face-centered cubic (FCC) structure of bulk Pt, which has atoms at the corners of the cube, can these atoms coordinate to a ligand and; (2) if the surfactant is removed, will the nanoparticle or some fraction of it undergo oxidation particular in aqueous media. Developing a reproducible method for the synthesis of PVP/Pt nanoparticles with a narrow size distribution, allowed the synthesis of other metals such as PVP/Ir and PVP/Pt-Ir by modifying the experimental procedure slightly.

1.3. Effect of Surfactant on Nanoparticle Reactivity

Poly(vinylpyrrolidone), PVP, is an off-white water-soluble polymer that has attracted much attention due to its unique properties which include a high density of 1.2 g/cm^3 and a molecular weight ranging from 10,000 to 1,200,000 g/mol.[19] Furthermore, it is environmentally friendly due to its low toxicity and biodegradable character.[20,21] PVP polymers have numerous applications, such as a binder for drugs in pharmaceuticals,[22] a disinfectant known as Betadine when PVP is bonded to iodine,[23] and a stabilizer for transition-metals nanoparticles by preventing them from aggregating in the growth

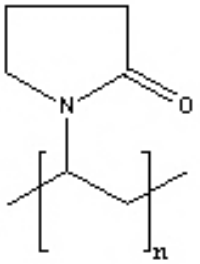

Figure 1. Molecular Structure of Poly(vinylpyrrolidone), PVP.

solution.[24] PVP polymer is a universal stabilizer for various transition-metal nanoparticles because of their hydrophilic groups, the amide functional group, which are capable of hydrogen bonding with other species (Figure 1).[25,26]

PVP is a polar, hygroscopic polymer which reduces the surface tension of the solvent for easier spreading. The concentration of a surfactant changes the size and shape of nanostructures. At lower surfactant concentrations, all the particles in solution are partially coated resulting in some aggregation. At higher concentrations, the surfactant molecule starts to aggregate forming micelles.[27] When nanoparticles aggregate, their sizes increases leading to polydispersity and instability followed by reduced catalytic

activity making it difficult for use in the chemical and pharmaceutical industry.[28,29] For example, a study conducted by Shiraishi and co-workers[30] provides evidence on the catalytic activity of PVP/Pt nanoparticles for the hydrogenation of methyl acrylate to methyl propionate. The catalytic activity of the samples was measured in units of mol-H_2 mol-Pt^{-1} s^{-1} versus the particles size obtained by TEM. The rate of the hydrogen uptake was measured under hydrogen at atmospheric pressure with 2.0 x 10^{-4} mmol of platinum nanoparticles dispersed in 0.3 cm^3 of ethanol. It was found that a decrease in the particles size of the PVP/Pt nanoparticles of 9.7 nm, increases the catalytic activity (0.308 mol-H_2 mol-Pt^{-1} s^{-1}) for the hydrogenation of methyl acrylate when compared to catalytic property of the Pt black (0.0042 mol-H_2 mol-Pt^{-1} s^{-1}). The latter was found to be much less active than the PVP/Pt nanoparticles because of the larger size associated with bulk metal. Interesting evidence in this study also shows that particle size can affect catalytic activity by the formation of aggregates of the PVP/Pt nanoparticles.[30]

1.3.1 Examples of PVP on Nanoparticle Reactivity

PVP has been extensively used as a capping agent with various metal nanoparticles such as Ag, Pd, Au, Pt and Rh to investigate their optical, structural and catalytic properties. For example, PVP/Ag nanoparticles were prepared by an ethanol reduction method with silver nitrate as the precursor and PVP as the surfactant. The solution was stirred and spin coated onto a silicon and glass substrates, heated at 70 ^oC and 180 ^oC and then irradiated under a mercury lamp after each heat treatment to investigate their optical properties.[31] Absorption spectra of the PVP/Ag films heated at 70 ^oC shows a low intensity, broad shoulder at *ca.* 400 nm before it was exposed to UV-

radiation. After the PVP/Ag films heated at 70 ^{o}C was exposed to UV-radiation, the peak intensity increases and shifted to longer wavelength of *ca.* 425 nm. Absorption spectra of the PVP/Ag films heated at 180 ^{o}C after UV-exposure, showed a slightly higher intensity peak than with the 70 ^{o}C heat treatment with a maximum absorbance at 450 nm. The authors suggest that the increase in intensity and shift to longer wavelength is due to an increase in the particle sizes of the PVP/Ag nanoparticles.[31] PVP/Pd nanoparticles were synthesized using ethylene glycol as the reductant and the solvent to study their size and morphology.[32] PVP-protected Au nanoparticles of spherical and wormlike shape were produced by preheating the samples at 50 ^{o}C for various times before refluxing, and then heating at 95 ^{o}C for different refluxing time.[33] So, by changing the experimental parameters such as temperature and time, different shape of the PVP/Au nanoparticles were produced. The synthesis of cubic PVP/Pt nanoparticles and cuboctahedra PVP/Rh nanoparticles were prepared with ethylene glycol as the reducing agent. This study shows that a charge transfer interaction occurred between the PVP donor groups, the amide functional group, as a function of the oxidized and reduced state of the surface atoms of Pt and Rh recorded by UV-Raman Spectroscopy.[34] In another experiment, PVP/Pt nanoparticles were prepared electrochemically by a rotating cathode method.[35]

1.3.2 The Effect of Other Surfactants on Nanoparticle Reactivity

Organic surfactants such as tetraoctylammonium bromide (TOAB),[36] oleic acid and oleylamine,[37] glucose[38] and poly(N-isopropylacrylamide)[39] can also be used to stabilize Pt nanoparticles. Wang et al[40] studied the effect of heating Pt nanoparticles stabilized with polyacrylate polymer at different temperatures. They found that the shape

of the cubic and tetrahedral Pt nanoparticles did not change after removal of the polymer between 180-250 ^{o}C, but when the temperature exceeds 500 ^{o}C, the cubic Pt nanoparticles changed to spherical and started to coalesce. The tetrahedral Pt nanoparticles did not change at 500 ^{o}C but started to reshape at the edges at 525 ^{o}C, which was suggested by the authors to be the more stable particle. Diffraction patterns obtained showed that the crystallinity of the "naked" nanoparticles was not affected at 500 ^{o}C, but as the temperature increases to 650 ^{o}C, surface melting of the nanoparticles occur producing larger particles with decreased crystallinity.[40]

1.3.3 Removal of Surfactant on Nanoparticle Reactivity

Du et al.[41] studied the thermal decomposition of PVP coated on the Pt nanoparticles from room temperature to > 500 ^{o}C. As the temperature increases to 500 ^{o}C, the PVP partially decomposed and TEM showed minimal Pt nanoparticles aggregation. Before heat treatment, FTIR spectra of PVP/Pt nanoparticles possess strong absorption bands at 2954 cm^{-1} (CH_2) and at 1655 cm^{-1} (CO). After heat treatment of the PVP/Pt nanoparticles, FTIR spectra of the CH_2 band decreased in intensity and a weak intensity band at 1624 cm^{-1} (CO) was observed. The changes in the CH_2 and CO bands suggest that the structure of the PVP after decomposition has changed into a new compound. The decomposition of the PVP did not change the catalytic properties of the Pt nanoparticles, and there was no evidence that the Pt-Pt bond length changed during the decomposition process. Because the Pt nanoparticles did not melt during the heating process and showed some degree of aggregation, the authors suggest that this kind of

behavior with a high melting point nanoparticle, the catalytic properties of the Pt nanoparticles were unaffected during the heating process.

The traditional Soxhlet extraction technique was used in this lab even though the extraction time is long and a large amount of solvent of 100 ml is used as compared to other techniques such as microwave-assisted extraction (MAE) heating, which removes additives such as poly(propylene) from polymers.[42] MAE is a fast, but expensive extraction system and a maximum solvent of 30 ml is utilized with a short extraction time. The solvent for MAE extraction must be able to absorb in the microwave region.[42] The Soxhlet extraction technique was chosen because it is inexpensive, it allows the use of any solvent, very little work space is needed for set up and a capping agent like PVP can be extracted without changing the structure or carbon backbone of the molecule.

To the best of our knowledge, the removal of the PVP-protected metal nanoparticles using a Soxhlet extraction apparatus was not reported. However, studies of thermal decomposition of the PVP/Pt nanoparticles conducted by Du and co-workers,[41] reported a changed to the structure of the PVP and minimal aggregation of the Pt nanoparticles. Can the structure of the PVP and the particle size of the Pt nanoparticles remained unaffected by adsorbing the nanoparticles into a nanoporous matrix and then remove the PVP surfactant by Soxhlet extraction techniques? We examined the adsorption of PVP-protected Pt nanoparticles into nanoporous silica matrices, the structure of the adsorbed Pt nanoparticles and explored the procedure to remove the protective PVP surfactant from the adsorbed particles. X-ray absorption spectroscopy (XAFS) was used to determine the oxidation state and bond length of the PVP/Pt

nanoparticles before and after adsorption into porous Vycor glass because silica can behave as an oxidizing matrix due to the presence of water.[43] The bond length and oxidation state of the Pt nanoparticles after extraction remains unaffected with minimal particle aggregation.

1.4. Porous Vycor Glass

Experiments examining the optical and catalytic properties of metal carbonyls and ruthenium complexes adsorbed into porous Vycor glasses (PVG) have been examined in this lab.[44-51] For example, Simon and co-workers[44] impregnated hexacarbonyl compounds, $M(CO)_6$ (M = Cr, Mo, W), into porous Vycor glass and absorption spectra recorded exhibit peaks at 280 nm (Cr), at 286 nm (Mo) and at 287 (W). The PVG containing the impregnated hexacarbonyl were excited at 312-nm. Upon excitation, pentacarbonyl, $M(CO)_5$ were generated. Adsorption of 2,2'-bipyridine ligand into the PVG containing $W(CO)_5$ formed a coordination compound with the $W(CO)_5$ to produce $W(CO)_4$(bpy). The formation of the $W(CO)_4$(bpy) complex was analyzed using resonance Raman spectroscopy. The pyridine vibrations at 992 cm^{-1} and 1035 cm^{-1} shifted to 1012 cm^{-1} and 1042 cm^{-1} respectively when reacted with the $W(CO)_5$ in PVG.

The PVG provided by Corning Incorporated was initially made from an alkali-borosilicate melt. Upon cooling, the melt phase separates into a boric oxide (B_2O_3) phase and a silica (SiO_2) phase. The melt is then quenched and the boron rich phase was acid leached leaving a final product of porous Vycor glass composed of 96% SiO_2, 3% B_2O_3, 1% Na_2O & Al_2O_3.[52,53] Porous Vycor glasses are ideal as a medium for the adsorption of PVP/Pt, PVP/Ir and PVP/Pt-Ir nanoparticles because of their narrow pore size

distribution of 10 ± 1 nm and high surface area of 184 ± 10 m^2/gram. Most importantly, their transparency allows the spectral properties of the adsorbed nanoparticles to be examined.[53] Two types of PVG were used in this experiment; one type is referred to as "rolled" or unpolished PVG because they possess a wavy-like pattern on the glass surface and were cut into pieces with an approximate dimension of 19 mm x 19 mm x 5 mm. The second type of PVG with dimensions of 25 mm x 25 mm x 2 mm is referred to as polished PVG because the surface of the glass is smooth and does not contain any wavy-like characteristics.

1.4.1 Reactivity of Supported Pt Nanoparticles

Many studies have been conducted of the optical and the catalytic properties of Pt nanoparticles dispersed in mesoporous substrates such as: (1) MCM-41 (Mobil Composition of Matter) for the hydrogenation of cinnamic acid.[54] MCM-41 is a porous silica matrix with a high surface of up to 1400 m^2/gram with a pore size of *ca.* 2-6 nm; (2) SBA-15 for hydrocarbon conversion.[55] SBA-15 is a hexagonal mesoporous silica but with larger pore size of 5-30 nm than that of MCM-41 and; (3) Ordered mesoporous carbon (OMC) supports also have high surface areas ranging from 400 to 1300 m^2/gram with pore size of *ca.* 3-7 nm. The latter have been used for oxygen reduction in fuel cells.[56] The pore size varies depending on the synthesis and properties of the silica framework. Mesoporous materials are advantageous because of their narrow pore size distributions, ordered structure and high surface area which would allow for higher adsorption rates and faster interactions.[57] PVP-protected Pt nanoparticles of *ca.* 5 nm in diameter supported on activated silica, which is silica gel heated at 12 hours at 150 ^oC,

show enhanced catalytic activity for the hydrogenation of cyclohexanone in comparison to the PVP/Pt nanoparticles in solution.[58]

1.4.2 Reactivity of Supported Ir Nanoparticles

Catalytically-active iridium oxide nanoparticles and iridium complexes containing bidentate ligand such as 2,2'-bipyridine are well known materials for the oxidation of water to dioxygen (O_2).[59-63] Iridium containing complexes have applications in organic light emitting diodes and oxygen sensors.[64] Dupont and co-workers[65] have prepared iridium nanoparticles on a medium of 1-*n*-butyl-3-methylimidazolium hexafluorophosphate by reduction of bis(1,5-cyclooctadiene)diiridium(I) dichloride and found an increase in the recyclability of the iridium catalyst for the hydrogenation of 1-decene at a temperature of 75 ^{o}C. This process is an ideal green chemistry approach because it reduces chemical waste and improves efficiency. Ir oxide nanoparticles were electrodeposited onto an etched titanium substrate by reduction of an iridium (IV) chloride solution at 90 ^{o}C and the resulting structure used as reproducible and cost effective pH sensor.[66] Increased catalytic activity was observed for the hydrogenation of quinaldine to 2-methyl-1,2,3,4-tetrahydroquinoline with surfactant-free Ir nanoparticles supported on carbon nanotubes. The Ir nanoparticles were prepared by adsorbing acetylacetonato-(1,5-cyclooctadiene)iridium(I) onto carbon nanotubes and heated at 60 ^{o}C. Iridium produced by this adsorption hydrogenolysis approach[67] has proven to be an effective catalyst. This project will allow us to study, for the first time, the properties of the nanoparticles before and after adsorption into porous Vycor glass which will open new ideas and methods in the field of surface catalysis.

1.4.3 Reactivity of Supported Bimetallic Pt-Ir Nanoparticles

Bimetallic nanoparticles are advantageous over monometallic nanoparticles because their selectivity and catalytic activities becomes more enhanced and their surface area to volume ratio is much larger.[68,69] Pt-Ir nanoparticles were chosen because of their catalytic role in the oxidation of methanol for fuel cells.[70,71] Using a bimetallic material is better than using just Pt alone. Because the CO intermediate poisons Pt, the efficiency of CO_2 evolution by the oxidation of methanol is reduced to *ca.* 27%.[71] The addition of another catalyst to Pt, reduces CO poisoning and increases efficiency. Pt-based bimetallic such as Pt-Ru and Pt-Au nanoparticles supported on multiwalled carbon nanotubes were prepared by a chemical fluid deposition in supercritical fluid carbon dioxide. Their electrochemical activities and efficiency were examined using cyclic voltammetry for the oxidation of methanol.[72] The addition of Ru and Au nanoparticles to platinum showed increase catalytic activity with a higher current ratio of *ca.* 60% in comparison to the monometallic platinum for the conversion of MeOH to CO_2.[72]

The catalytic properties of Pt and Ir nanoparticles on silica support have been discussed in great detail. Since our main focus is trying to find the best route to increase efficiency of CH_4 evolution, and these nanoparticles have been shown to be very effective catalysts, we will examine the coordination chemistry of the stripped nanoparticles from the adsorbed PVG and also examine the chemistry of the nanoparticles in solution with Ru(II) diimines.

1.5. Chemistry of Ru(II) Diimines with Platinum

$[Ru(bpy)_2L]^{2+}$ complexes, where bpy denotes 2,2'-bipyridine and L denotes the

bidentate bridging ligands dpp = (2,3-bis(pyridyl)pyrazine) or ppz = (4',7'-phenanthrolino-5',6':5,6-pyrazine) (Figure 2) are luminescent complexes with high extinction coefficients, $\geq 10^4$ $M^{-1}s^{-1}$ capable of excited state acid-base and redox chemistries. Absorption spectra of the $[Ru(bpy)_2dpp]^{2+}$ and $[Ru(bpy)_2ppz]^{2+}$ complexes are similar. They exhibit an MLCT band (d-π*) at 420 nm for bpy, 470 nm for dpp and at 480 nm for ppz.[73]

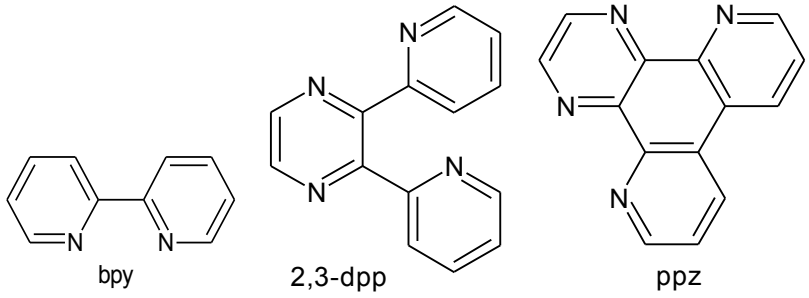

Figure 2. Molecular Structure of the Bridging Ligands.

The MLCT state of $[Ru(bpy)_2dpp]^{2+}$ is localized on the dpp ligand (π*- d), and emits at 700 nm with a lifetime of 135 ± 14 ns. The MLCT state of $[Ru(bpy)_2ppz]^{2+}$ is localized on the ppz ligand (π*- d), and emits at 690 nm with an emission lifetime of 180 ± 2 ns in water. The energy level diagram of $[Ru(bpy)_2dpp]^{2+}$ shows the excited state is situated 0.53 eV (voltage per electron) above the oxidized form (Figure 3).[73] Consequently, upon excitation, a strong base and strong reducing agent ($*[Ru(bpy)_2dpp]^{2+}$) are created. The light harvesting properties of these ruthenium(II) complexes when coordinated to a catalytically-active transition metal makes them an excellent candidate for CO_2 reduction and CH_4 evolution.[74-77]

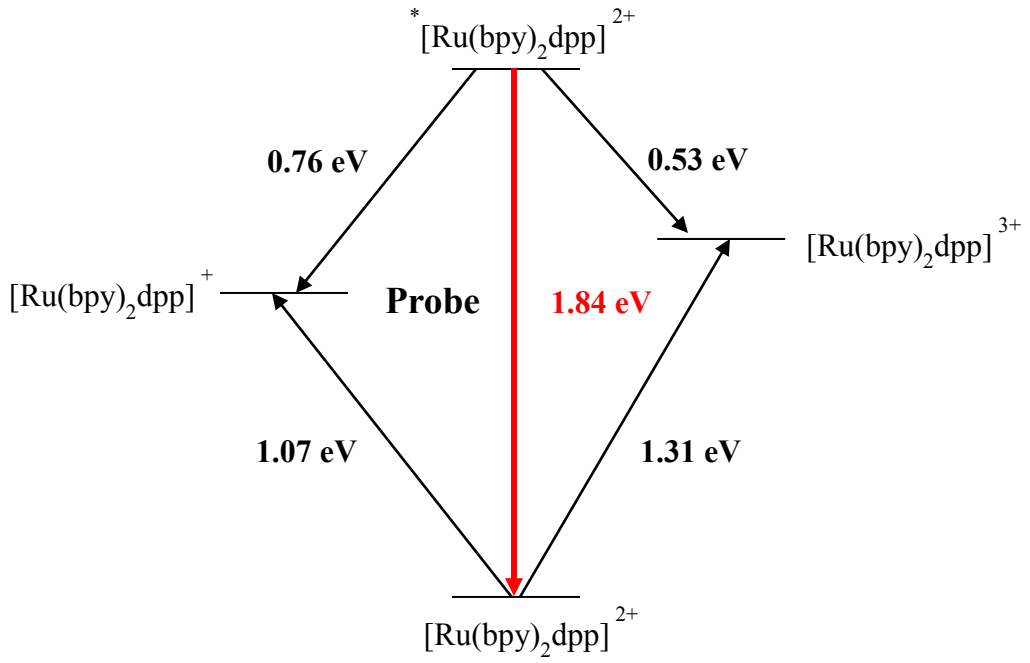

Figure 3. Excited-state potential diagram of $[Ru(bpy)_2\ dpp]^{2+}$.

Experiments involving the reactions between $[Ru(bpy)_2dpp]^{2+}$ (bis(2,2'-bipyridine)(2,3-bis(2-pyridyl)pyrazine) ruthenium(II)) and $PtCl_6^{2-}$ show that the Ru(II) diimine acts like a ligand and coordinates to the Pt(IV) to form the bimetallic $[Ru(bpy)_2(dpp)PtCl_4]^{2\pm}$ complex.[78] Granger and co-workers[79] reported Pt(IV) complexes coordinated to 1,10-phenanthroline. The Pt-N (1,10 phen) bond length is reported to be *ca.* 2.037 Å and the N-Pt-N (1,10 phen) bond angle is 80.6°. Pt(II) complexes coordinated to bipyridine has also been examined.[80] The Pt-N (bipy) is 2.010 Å and the N-Pt-N (bipy) bond angle is 80.1°. Will this $[Ru(bpy)_2(dpp)]^{2+}$ complex act as a ligand and coordinate to Pt^0 atom through the bridging ligand dpp? Figure 4 shows the face-centered cubic (FCC) structure[81] of Pt^0 with lattice constant of 3.9110 Å as determined from x-ray diffraction

method. Since the bond angle of the Pt^{4+} and Pt^{2+} coordinated to a diimine ligand is about 80^{o}, it is possible that Pt^{0} at the edges or corners has sufficient space to coordinate to the peripheral nitrogen of the dpp ligand.

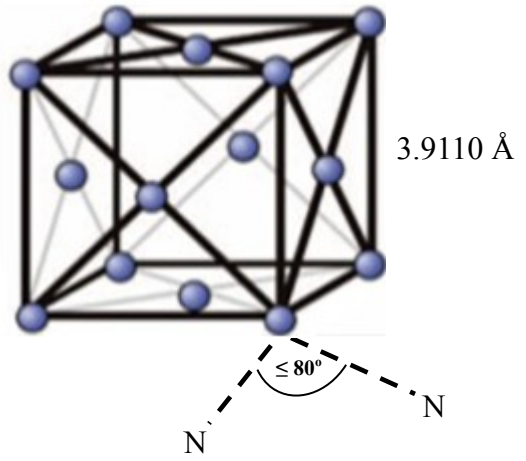

Figure 4. FCC structure of Pt coordinated to a diimine ligand.

In fact, previous studies provide evidence of coordination of Pt nanoparticles and 1,10-phenanthroline.[82,83] Will this complex bis(2,2'-bipyridine)(4,7-phenanthro-lino-5:6,5'6'pyrazine) ruthenium(II), $[Ru(bpy)_2(ppz)]^{2+}$ also act as a ligand and coordinate to Pt^{0} atom through the bridging ligand ppz and form a new complex? Based on the previous literature, metal complexes consisting of $[Ru(bpy)_2(dpp)]^{2+}$ and $[Ru(bpy)_2(ppz)]^{2+}$ will be used for coordination chemistry with the "naked" Pt nanoparticles in porous Vycor glass and with the PVP-protected Pt nanoparticles in fluid solution.

The synthesis, characterization and chemistry of Pt and Ir nanoparticles in porous Vycor glass and in room temperature fluid solution will be described in the following chapters comprising of experimental, results and discussion.

Chapter 2

2. EXPERIMENTAL

2.1. Materials

The chemicals used in these experiments; dihydrogen hexachloroplatinate (IV) hexahydrate, $H_2PtCl_6.6H_2O$, (99.9%, metal basis, Alfa Aesar), dihydrogen hexachloroiridate (IV) hydrate, $H_2IrCl_6.xH_2O$, (99.98%, metal basis, Sigma Aldrich), poly(vinylpyrrolidone), PVP, (MW = 55 000, Sigma Aldrich), potassium tetrachloroplatinate (II), K_2PtCl_4, (99.99%, Premion, Alfa Aesar), methanol (Pharmco-Aaper), ethanol (95%, Pharmco-Aaper), sulfuric acid (ACS Reagent Grade, Pharmco Products Incorporated), 2,2'-bipyridine(4',7'-phenanthroline-5,6:5',6'-pyrazine) ruthenium(II), $[Ru(bpy)_2(ppz)]^{2+}$, and 2,2'-bipyridine(2,3-bis(2-pyridyl)pyrazine) ruthenium(II), $[Ru(bpy)_2(dpp)]^{2+}$, were used without further purification. Pt foil (99.99%, Premion, Alfa Aesar), Ir foil (99.9%, e-Filaments) and Pt-Ir foil (80:20 wt%, 99.9%, Alfa Aesar) were used as reference materials. Polished and unpolished Corning's code 7930 porous Vycor glasses (PVG) with thickness of approximately 2 mm and 5 mm, respectively, were supplied by Corning Incorporated.

2.2. PVG

The PVG's provided by Corning Incorporated has a yellow appearance and absorption spectrum reveal a band at *ca.* 300 nm (Figure 5). This yellow appearance is due to the 300-nm band, which in turn, is due to the adsorption of organic compounds present in the environment.[84] To remove the contamination, the porous Vycor glasses were cleaned by continuous extraction with distilled water in a Soxhlet extractor. The

PVG is placed in the thimble of the extractor and extracted until absorption spectra of the glass gave no indication of the 300 nm absorption (Figure 6). The cleaned PVG was removed using forceps and placed inside a crucible (Coors, USA). The wet PVG had an opaque appearance, and was not initially dried at room temperature, but dried in a Thermolyne 1500 bench top furnace heated at 500 ^{o}C for 2 days. After the initial heating, the PVG was transparent with no visible cracks and finally placed in a desiccator and cooled to room temperature. The room temperature samples were then impregnated by previously described solution adsorption techniques.

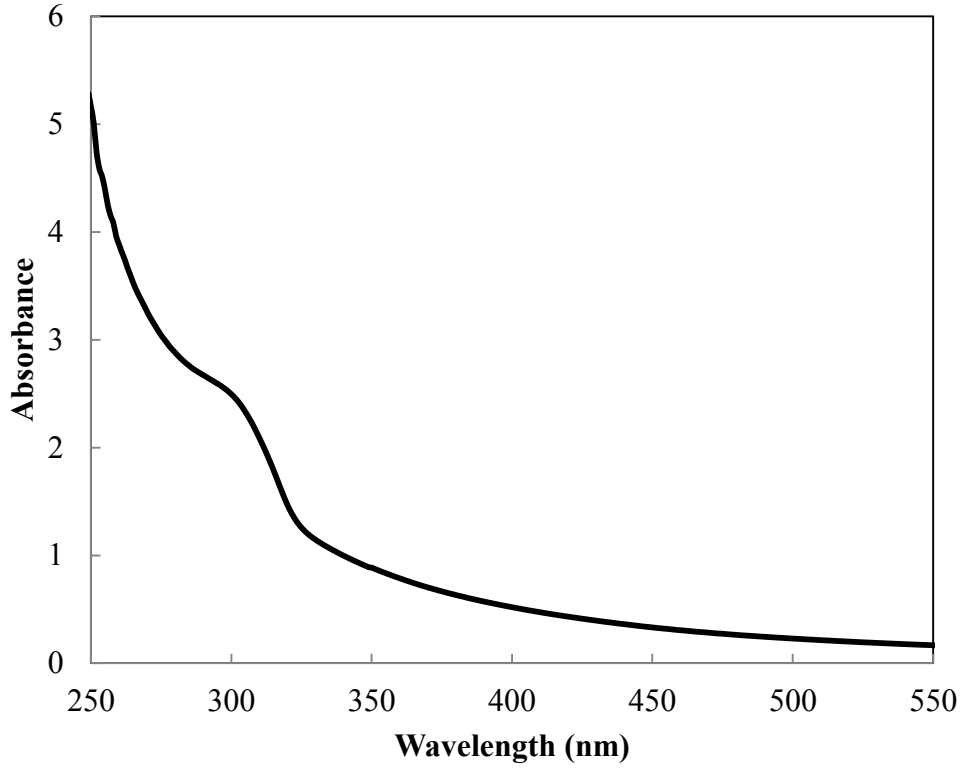

Figure 5. Absorption spectrum of unpolished porous Vycor glass with shoulder at *ca.* 300 nm before cleaning.

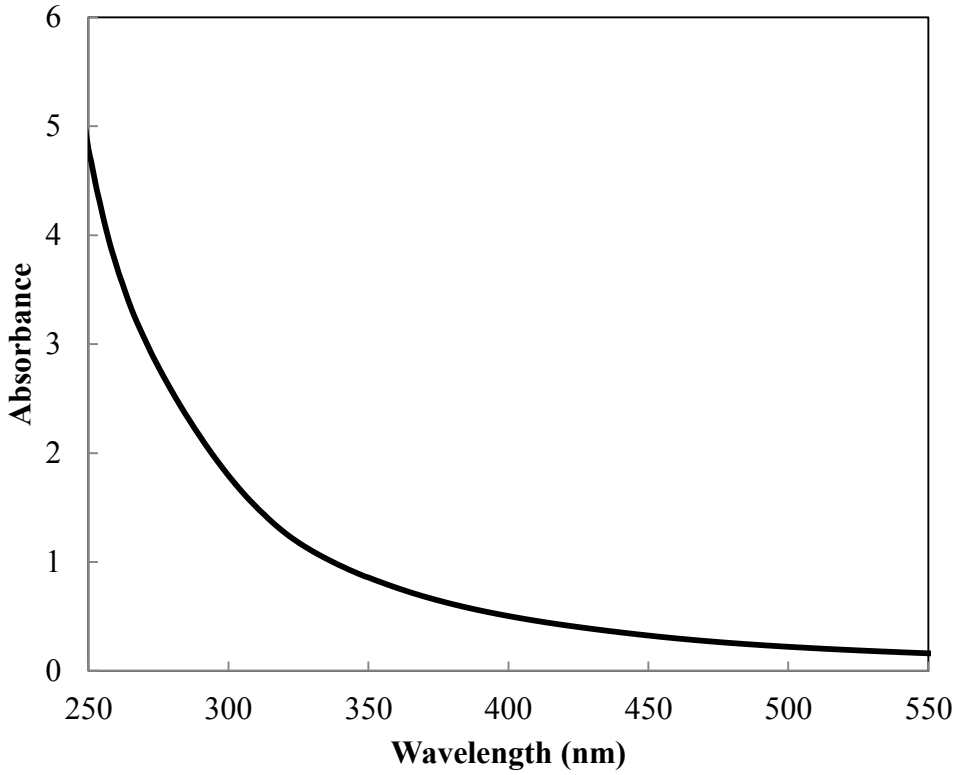

Figure 6. Absorption spectrum of unpolished porous Vycor glass with no shoulder at *ca.* 300 nm after cleaning and drying.

2.3. Synthesis

2.3.1 PVP/Pt Nanoparticles

Platinum nanoparticles with a narrow size distribution were synthesized according to the procedure by Rioux et al.[18] A 0.006 M dihydrogen hexachloroplatinate (IV) hexahydrate was placed in a 250 ml round bottom flask and dissolved in 20 ml distilled water, to which 0.133 g PVP is added. The solution was slightly swirled to dissolve the PVP, 180 ml methanol was added, and the mixture refluxed for 3 hours. Another batch of the Pt nanoparticles was prepared by the same procedure except that 95% ethanol was substituted for methanol. After the reaction was cooled to room temperature, the PVP/Pt

nanoparticles solution was isolated by evaporating the solution to dryness using a Rotavapor R110, washing several times in methanol or 95% ethanol and then dispersing the remaining Pt nanoparticles in either methanol or 95% ethanol. The samples for TEM analysis were prepared by placing a 5 μL of the Pt nanoparticles solution on a carbon coated copper grid (300 mesh) and dried in air.

2.3.2 PVP/Ir Nanoparticles

Rioux and co-workers[18] method of the PVP/Pt nanoparticles was used to prepare the PVP/Ir nanoparticles except that a 0.006 M dihydrogen hexachloroiridate (IV) hydrate was used. In this method, ethanol was used as the solvent and reductant with all other parameters kept the same. The PVP/Ir nanoparticles were separated from the reduced H_2IrCl_6 solutions by similar evaporation and washing method previously described with Pt nanoparticles. The resulting PVP/Ir nanoparticles were dispersed in 95% ethanol.

2.3.3 PVP/Pt-Ir Nanoparticles

Rioux et al.[18] method was also used to synthesize the PVP/Pt-Ir nanoparticles. A 0.003 M dihydrogen hexachloroplatinate (IV) hexahydrate was placed in beaker and dissolved in 10 ml distilled water (Solution 1). Then a 0.003 M dihydrogen hexachloroiridate (IV) hydrate was placed in another beaker and dissolved in 10 ml distilled water (Solution 2). The solutions were then mixed together in a 250 ml beaker, 0.133 g PVP was added followed by 180 ml ethanol. The PVP, H_2PtCl_6 and H_2IrCl_6 mixture was refluxed for 3 hours, and then evaporated to dryness. The PVP/Pt-Ir

nanoparticles were washed with 95% ethanol repeatedly, dried and then taking up in 95% ethanol.

2.3.4 $[Ru(bpy)_2(ppz)]^{2+}$

$[Ru(bpy)_2(ppz)]$ $(NO_3)_2$ was prepared according to a previously published method with minor modifications.[73] 4',7'-phenanthrolino-5,6:5',6'-pyrazine designated ppz, and *cis*-$Ru(bpy)_2Cl_2.2H_2O$ in a 2:1 molar ratio, respectively, were dissolved in 50 ml anhydrous ethanol and refluxed for 40 hours. After cooling to room temperature, aliquots of a saturated, 95% alcoholic solution of potassium hexafluorophosphate, KPF_6 was added. The solution was evaporated to dryness, extracted into methylene chloride, $MeCl_2$, and then filtered and evaporated again. The residue was eluted through a nitrate, NO_3^-, loaded ion exchange column using Dowex 1x8 chloride resin and then evaporated to dryness. The residue was dissolved in acetonitrile and then passes through an alumina column (neutral) and eluted with acetonitrile. Absorption spectroscopy identified the fractions containing the eluted product. The desired fractions of $[Ru(bpy)_2(ppz)]^{2+}$ were mixed together and the solvent was removed by evaporating to dryness in a Rotavapor R110 at 60^o C. The absorption spectra of $[Ru(bpy)_2(ppz)]$ $(NO_3)_2$ in 95% ethanol consists of two MLCT bands with maxima at 420 nm (ε = 1.4 x 10^4 $M^{-1}cm^{-1}$) and 476 nm (ε = 1.3 x 10^4 $M^{-1}cm^{-1}$) corresponding to the transfer of charge to the bpy and ppz ligands, respectively. The extinction coefficient of $[Ru(bpy)_2(ppz)]$ $(NO_3)_2$ in 80% water-ethanol is slightly different in comparison to 95% ethanol, the molar extinction coefficient at 420 nm is 1.1 x 10^4 $M^{-1}cm^{-1}$ and at 476 nm is 1.0 x 10^4 $M^{-1}cm^{-1}$. The emission spectra of the $[Ru(bpy)_2(ppz)]$ $(NO_3)_2$ complex exhibit a single band with maxima at 673 nm in 95%

ethanol and at 690 nm in 80% water-ethanol solution. Both absorption and emission spectra of the $[Ru(bpy)_2(ppz)]$ $(NO_3)_2$ complex were similar to the spectra of the previously published data.[73]

2.3.5 $[Ru(bpy)_2(dpp)]^{2+}$

$[Ru(bpy)_2(dpp)]$ $(PF_6)_2$ was prepared as previously described.[85] 2,3-bis(2-pyridyl)pyrazine (2 mmol) and *cis*-$Ru(bpy)_2Cl_2.2H_2O$ (1 mmol) were dissolved in 50 ml of a 200 proof ethanol and refluxed at 70 ^oC for 24 hours. After cooling to room temperature, a solution of ammonium hexafluorophosphate, NH_4PF_6, was added dropwise to the reaction mixture. The resulting precipitate was collected by filtering and then dissolved in a minimum amount of acetonitrile. The solution was charged onto an alumina column (neutral) and eluted with acetonitrile. The eluted fractions were collected and examined by absorption spectroscopy. The fractions containing $[Ru(bpy)_2(dpp)]^{2+}$ were combined and evaporated to dryness. Absorption and emission spectra of the isolated fractions agreed with published spectra of the complex.[85]

2.4. Instrumental

2.4.1 UV-Vis Absorption Spectroscopy (AS)

Electronic spectra were recorded on a Cary 5000 UV-Vis-NIR spectrophotometer. The nanoparticle solutions were measured using a 1 cm path length (ℓ) quartz cuvette, customized with a 14/20 ground glass joint (H.S. Martin, Incorporated), and the PVG samples with 0.2 and 0.5 cm path lengths were measured in the wavelength range of 200 nm–800 nm with a metal sample holder (Figure 7).

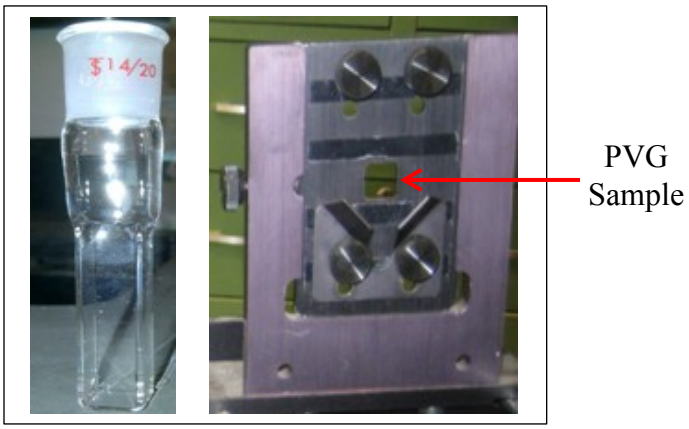

Figure 7. Quartz cell (left image) and sample holder for PVG (right image).

2.4.2 Photoluminescence Spectroscopy (PL)

Emission spectra were recorded on a Jobin Yvon FluoroMax-3 spectrophotometer. The samples are excited by radiation from a Xenon source passed through an excitation monochromator before passing through the sample. The emitted light from the sample is collected at 90^{o} to the excitation, passed through a monochromator and then detected by a photomultiplier tube (PMT). The relative intensity as a function of wavelength is then stored in the computer.

2.4.3 Transmission Electron Microscopy (TEM)

TEM images of the PVP/Pt, PVP/Ir and PVP/Pt-Ir nanoparticles in solution were recorded on a Zeiss EM 902A electron microscope with an accelerating voltage of 80 kV and a magnification of 250 000x. Higher resolution images were recorded on a JEOL JEM-2100 electron microscope with a beam current of 104 μA and an accelerating voltage of 200 kV. Figure 8 shows a schematic diagram of a transmission electron microscope. A beam of electrons produced from a thermionic electron gun impinges onto the sample and that which is transmitted through the sample is focused onto a location sensitive detector. In conjunction with supplied computer software the distribution of the transmitted electron is converted to an image of the object.

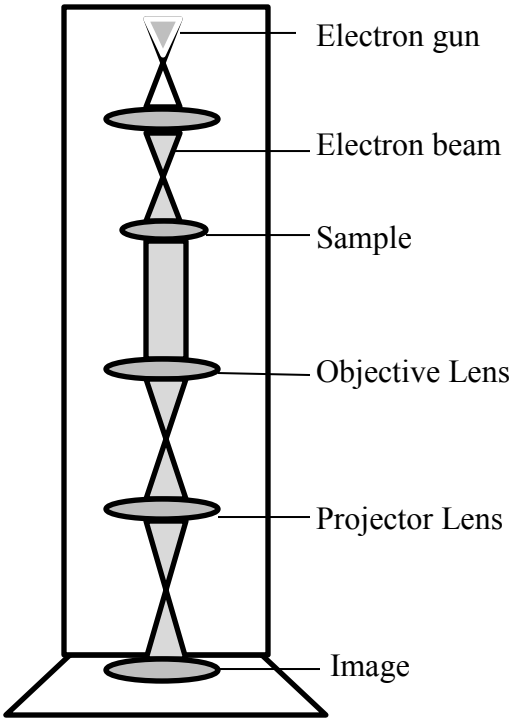

Figure 8. Schematic diagram of a transmission electron microscope (Adapted from Ref[86]).

2.4.4 X-Ray Diffraction (XRD)

Powdered X-ray diffraction (XRD) spectra were recorded using a Philips PW 3040 X'Pert PRO system with Cu Kα radiation (λ = 1.54 Å) operated at a voltage of 40 kV and a current of 30 mA. The nanoparticles were spread evenly on double sided tape with a spatula, and the reflections recorded over the angular range of $30^o \leq 2\theta \leq 90^o$. For Bragg's law (Figure 9) to be satisfied, the sample used for XRD must be a crystalline material. A crystalline material possesses a crystal lattice which is composed of a periodic arrangement of atoms. When a beam of x-rays strikes a crystalline sample at an angle (θ), the x-rays are diffracted according to Bragg's law,

$$n\lambda = 2d \sin \theta \quad (1)$$

where n is an integer, λ is the wavelength of the x-rays, d is the lattice spacing and θ is the angle between the incident ray and the scattering planes. The X-ray diffraction technique (XRD) was employed to determine the crystal structure of the nanoparticles, and the average particle size was calculated by means of Scherrer's equation.

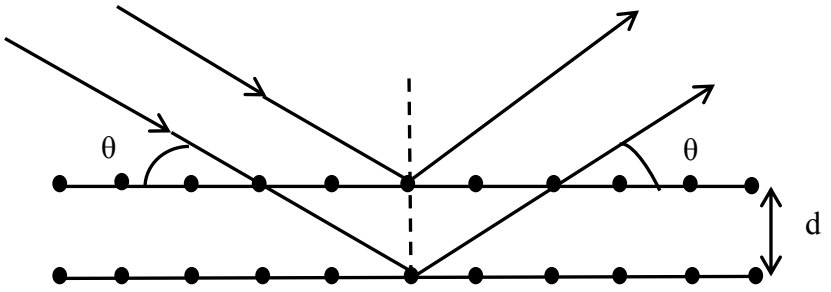

Figure 9. Bragg's Law (Adapted from Ref[87]).

2.4.5 Fourier Transform Infrared Spectroscopy (FTIR)

Infrared spectroscopy measures the molecular vibration of samples and provides structural and chemical identification of the nanoparticles and the surfactant molecule to be measured. Figure 10 shows a schematic diagram a Michelson interferometer. The IR source strikes the beam splitter which splits the beam into two halves. Reflections from both the fixed mirror and the movable mirror are recombined which passes through the sample, then through the detector which produces an interferogram. The raw data collected is then Fourier transformed in the computer to an IR spectrum. FTIR spectra of the PVP/Pt, PVP/Ir and PVP/Pt-Ir nanoparticles, along with the extracted PVP and pure PVP were collected using a Thermo Nicolet Nexus 870 Fourier Transform Infrared Spectrometer. The solid samples were dispersed in a drop of mineral oil (Rite Aid Cooperation) with an agar mortar and pestle, and the resulting paste dispersed over a calcium fluoride (CaF_2) IR window. The spectrum of the CaF_2 window and the mineral oil was subtracted from the nanoparticles and the PVP paste.

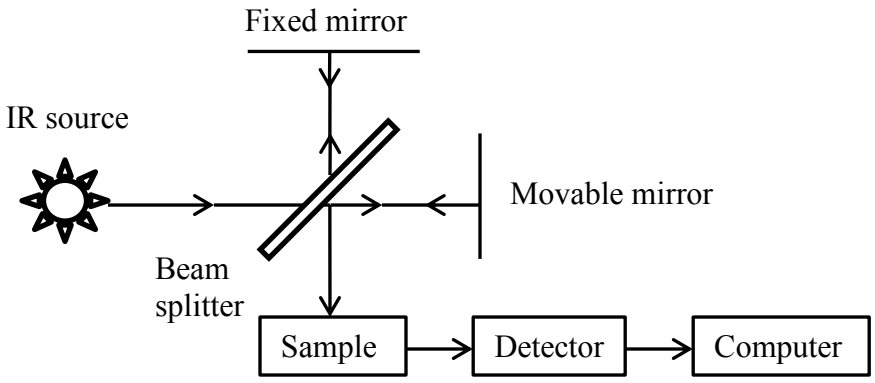

Figure 10. Michelson Interferometer (Adapted from Ref[88]).

2.4.6 Extended X-Ray Absorption Fine Structure Spectroscopy (EXAFS)

X-ray absorption spectroscopy (XAS) is divided into two parts, x-ray absorption near edge structure (XANES) and extended x-ray absorption fine structure (EXAFS). XANES is sensitive to the oxidation state of an atom and is the region of 50 eV before and after the absorption edge.[89,90] The L_{III}-edge energy of platinum (11564 eV) and iridium (11215 eV) are described as the transition of a 2p electron to 5d state of an absorbing atom.[91-93] EXAFS region, about 50 - 1000 eV above the absorption edge is also called a post-edge region and provides information on the metal-metal bond distance, identification of the near neighbor atom and the coordination number of the element.[94,95]

Extended x-ray absorption fine structure (EXAFS) and x-ray absorption near edge structure (XANES) data were collected at the Brookhaven National Laboratory at beamline X10C of National Synchrotron Light Source (NSLS) in fluorescence mode. Figure 11 shows the experimental x-ray absorption spectroscopy (XAS) setup for measuring the nanoparticles impregnated PVG samples. The bending mirror that focuses the beamline is coated with Rhodium and is situated at a distance of 12 meters from the x-ray source.[96] The beam intensity of polychromatic x-rays source is adjusted by passing the beam through vertical slits located before the monochromator. The monochromator is a double flat crystal monochromator (Si 220). Intensity of the incident beam, $I_{0,}$ before and after the hutch (experimental station) and transmission intensity, $I_{t,}$ (Figure 12) were measured using ion chambers filled with Nitrogen. Fluorescence X-ray intensity was measured using solid state detectors.

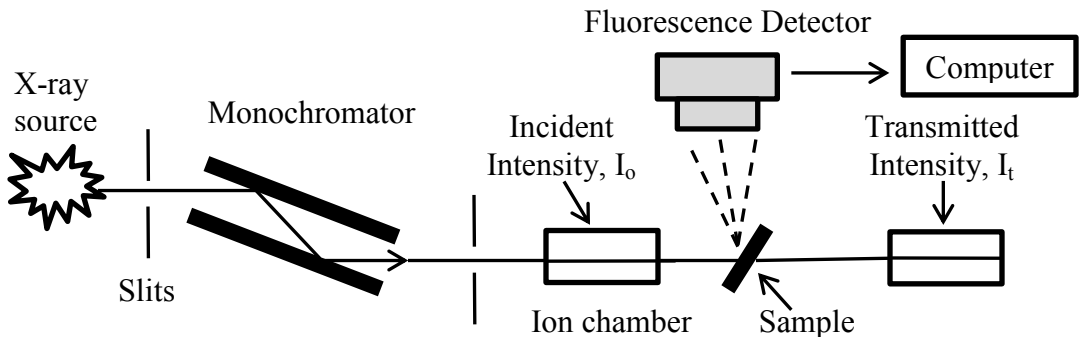

Figure 11. Schematic diagram of XAS setup (Adapted from Ref[97]).

XAS studies have been conducted on supported Pt,[98-101] Ir[102] and Pt-Ir[103] nanoparticles but have not been reported to date on their adsorption into porous Vycor glass. This project will allow us to investigate the chemical structure and local environments of Pt, Ir and Pt-Ir nanoparticles adsorbed into Corning's code 7930 porous Vycor glass on an L_3 absorption edge energy of 11564 eV (Pt) and 11215 eV (Ir). All EXAFS data were collected in the fluorescence mode because of the relatively small amount of Pt, Ir and Pt-Ir adsorbed into PVG. EXAFS and XANES spectra were referenced to Pt foil (Alfa Aesar), Ir foil (e-Filaments) and Pt-Ir foil (80:20 wt%, Alfa Aesar). X-ray absorption spectroscopy (XAS) such as x-ray absorption near edge structure (XANES) and extended x-ray absorption fine structure (EXAFS) were employed to determine the oxidation state and bond length of the PVP/Pt, PVP/Ir and PVP/Pt-Ir nanoparticles. All three nanoparticles samples were measured by dispersing the crushed particles onto Kapton adhesive tape and by adsorbing the PVP/Pt, PVP/Ir and PVP/Pt-Ir nanoparticles solutions into the porous Vycor glasses. The nanoparticles impregnated PVG samples were then dried in a vacuum oven without heating until the

opaqueness due to adsorbed water disappears. XAS of the PVP/Pt, PVP/Ir and PVP/Pt-Ir nanoparticles before and after adsorption into the silica were run on the Pt L_3-edge energy (11564 eV) and Ir L_3-edge energy (11215 eV).

The collected data were analyzed by importing the raw data file into PSI-Plot (Poly Software International) software, and then exporting the data into an arbitrarily named non-commercial program created in DOS for data reduction. The XANES, which is the region in XAS about 50 eV below and above the absorption edge of the spectra, was used to determine the oxidation states of the Pt and Ir nanoparticles. To determine the EXAFS function, $\chi(E)$, which is related to the Pt-Pt and Ir-Ir bond length within the nanoparticle, the background is subtracted from the EXAFS spectrum. The pre-edge region, which is the region before the absorption edge is fitted with a polynomial and is then extrapolated beyond the absorption edge, and subtracted from the measured absorption coefficient, $\mu(E)$, to remove the absorption from other edges. The photon energy (E) of the spectral data after background subtraction is then transformed into a photon electron wave vector (k) and is multiplied by k^3 for weighting the higher k portion. After Fourier transforming the data from k to R-space, the data were analyzed by importing into the PSI-Plot software, and plotted in terms of Fourier transform magnitude as a function of the radial distance (Å) to determine the bond length of the Pt, Ir and Pt-Ir nanoparticles present in the sample.

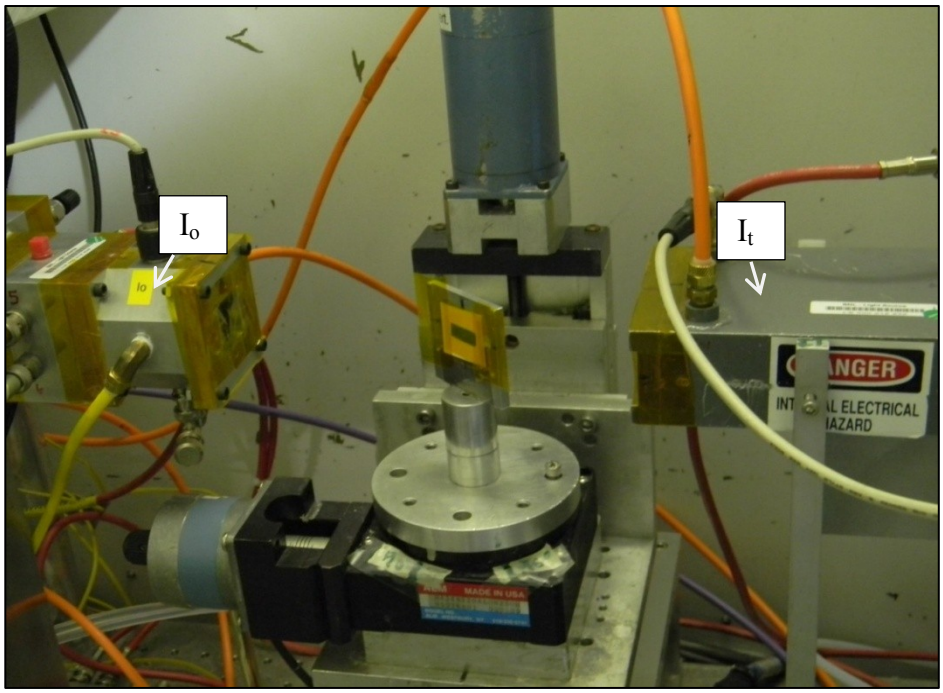

Figure 12. XAFS experimental setup at NSLS (Photograph courtesy of Dr. Sunil Dehipawala).

2.4.7 Time-Resolved Emission Spectroscopy

Time-resolved measurements were conducted using a Quanta-Ray Pulsed Nd:YAG (neodymium doped yttrium aluminum garnet) laser. A Stanford DG535 was used as a time delay device. The excitation wavelength was set at 532-nm. The resulting emission was recorded using a Princeton Instrument ICCD (intensified charge-coupled device) camera attached to a SpectraPro-300i Spectrograph. The data were viewed using WinSpec32 software on a Dell Intel Pentium 4 Windows XP system. The data were exported into IGOR Pro 6.12A and analyzed to determine the lifetime of the species. All samples were degassed in Argon for 5 minutes prior to all emission lifetime measurements.

Chapter 3

3. RESULTS

3.1. Characterization of PVP/Pt Nanoparticles

The synthesis of PVP-protected platinum nanoparticles prepared by an alcohol reduction method has been established.[18] Figures 13 and 14 shows the UV-visible absorption spectra of a methanol and ethanol solution of 1.2 x 10^{-5} M in PVP and (6.07 ± 0.08) x 10^{-4} M in H_2PtCl_6 before reflux (solid line) with an intense peak at 268 nm. The absorption spectrum of 1.0 x 10^{-4} M PVP used in the synthesis was also recorded before it was added to the H_2PtCl_6 solution. The absorption spectrum of PVP (Figure 15) shows a high intensity peak at *ca.* 240 nm, ε = 7185 $M^{-1}cm^{-1}$ with a nondescript tail extending into the visible.

PVP/Pt nanoparticles were generated previously with methanol and then in 95% ethanol because Rioux and co-workers[18] found that reducing the PVP/H_2PtCl_6 salt in 95% ethanol created slightly smaller Pt nanoparticles than reduction by methanol. Since we were interested in the smaller particle size for the adsorption of the PVP/Pt nanoparticles into porous Vycor glass (PVG), which has pores of ≤ 10 ± 1 nm, the PVP and H_2PtCl_6 was dissolved in methanol or 95% ethanol. Initially the solution was pale yellow. As the reflux proceeds, H_2PtCl_6 peak at 268 nm gradually decreases and the sample solution turned dark brown. Upon cooling to room temperature, the absorption spectra of the Pt sample solution exhibit a broad shoulder at *ca.* 280 nm.

Transmission electron microscopy (TEM) measurements were carried out on the PVP/Pt sample after reduction of the Pt(IV) salt to determine the size, morphology and

degree of aggregation (Figures 16a and 17a). If the particles are small, ≤ 10 nm, then it will adsorb into the PVG. With particles > 10 nm in diameter, then it will be difficult to adsorb the nanoparticles into the glass. The TEM images were recorded with a charge couple device (CCD) camera, and a MegaView III- iTEM digital acquisition system. One hundred Pt particles were examined and sized and then plotted as a function of nanoparticles diameter (nm). The highest peak in the histogram corresponding to 51 nanoparticles in the size range of 2.7-3.5 nm for the methanol synthesis (Figure 16b) and 52 nanoparticles in the size range of 2.4-3.0 nm for the ethanol synthesis (Figure 17b) were selected and the average sizes of the nanoparticles were obtained using Microsoft Excel. High resolution TEM of an individual PVP/Pt nanoparticle (Figure 16a inset) shows diffraction from the Pt core. Using the distance standard within the TEM yields a Pt lattice distance of 2.24 Å (111), this is within experimental error of the Pt lattice spacing in bulk platinum of 2.26 Å (111), obtained from the reference pattern parameters in the XRD database.

X-ray diffraction (XRD) methods were used to determine the crystal structure and size of the particles. The peak positions of the Pt nanoparticles are extracted by the line observed in the center of each peak in the XRD spectrum (Figures 18 and 19). These lines or stick patterns are not pasted or drawn onto the spectra, but appear when the samples being measured matches the reference pattern of Pt from the XRD database. XRD analyses show broad peaks of only Pt nanoparticles which indicates that Pt particles are small.[104] The crystal structure of the particles were determined using the X'Pert HighScore v2.1 Database, which is a program installed in the computer of the XRD. The

data obtained from the XRD indicates that Pt nanoparticles have a face-centered cubic (FCC) structure.

Fourier transform infrared spectroscopy (FTIR) was used for qualitative analysis of the pure PVP and of the PVP/Pt nanoparticles synthesized in methanol and ethanol. The PVP exhibits an intense peak at 1668 cm^{-1} assigned to the C=O vibration, a shoulder at 1490 cm^{-1} corresponding to the C-N region, an intense peak at 1460 cm^{-1} assigned to the CH_2 vibration and the 1376 cm^{-1} peak assigned to the C-H region[105] (Figure 20). Capping the Pt nanoparticles with the PVP, reduces the intensities of the C=O absorption at 1668 cm^{-1} in the PVP and shifts the C=O vibration to 1658 cm^{-1} in both the Pt nanoparticles prepared by methanol or ethanol reduction. The reduction in the C=O intensity and the 10 cm^{-1} shift to lower frequency, in the spectrum of the Pt nanoparticles capped with PVP, suggest that the Pt nanoparticles is attached to the carbonyl group of the PVP.

Energy-dispersive X-ray spectrometer (EDS) attached to the transmission electron microscope was used for elemental analysis of the PVP/Pt nanoparticles and to confirm the presence of Pt using DET 1 v6.04 software. The electron beam is focused onto the sample being analyzed. Ejection of a core electron upon excitation produces an electron hole. An electron from the outer-most shell with higher energy fills the hole with the emission of an x-ray. X-rays characteristic of the samples being analyzed are produced from the difference in the energy released.[106] EDS spectra of the Pt sample (Figures 21 and 22) detected carbon (C), copper (Cu) and platinum (Pt) bands. The carbon and copper

bands are attributed to the grid while the band position at *ca.* 2.05, 9.41 and 11.01 keV are attributed to Pt.

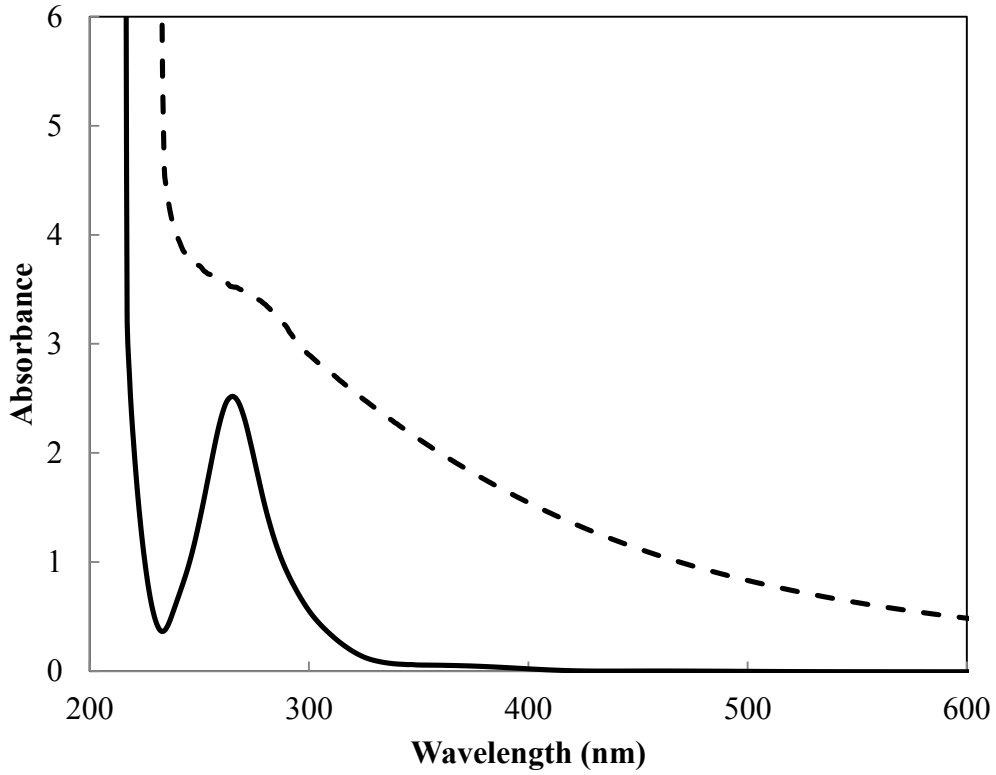

Figure 13. Absorption spectra of PVP/H_2PtCl_6 solution before reflux (——) and PVP/Pt nanoparticles after reflux (– – –·) synthesized in methanol.

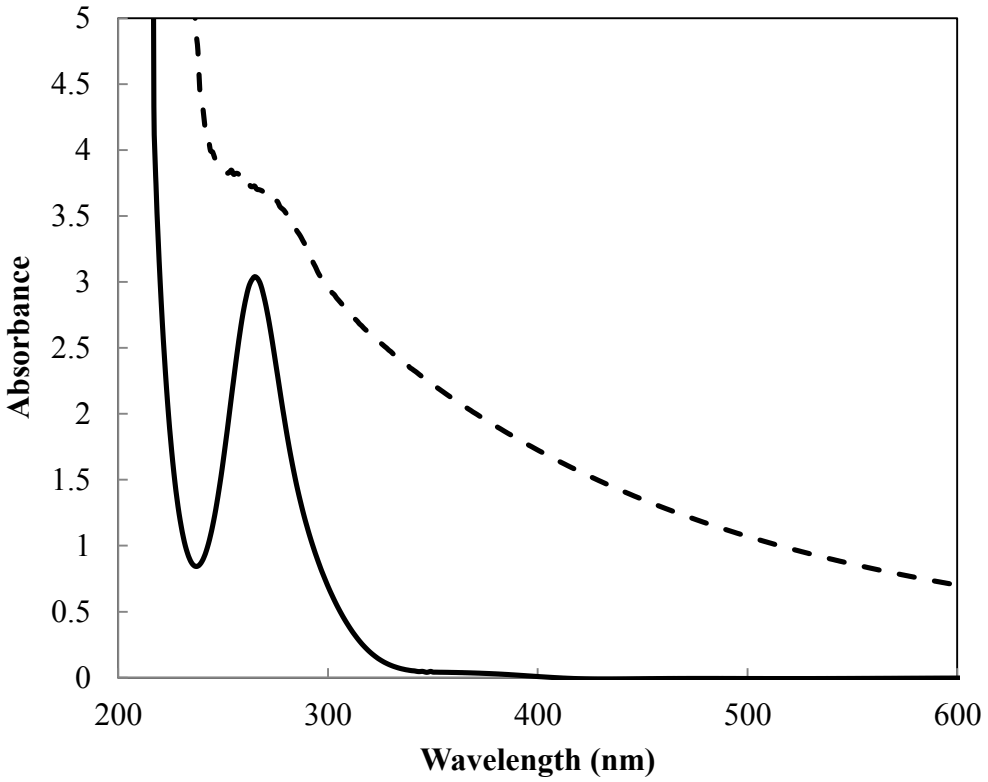

Figure 14. Absorption spectra of PVP/H_2PtCl_6 solution before reflux (——) and PVP/Pt nanoparticles after reflux (– – –) synthesized in ethanol.

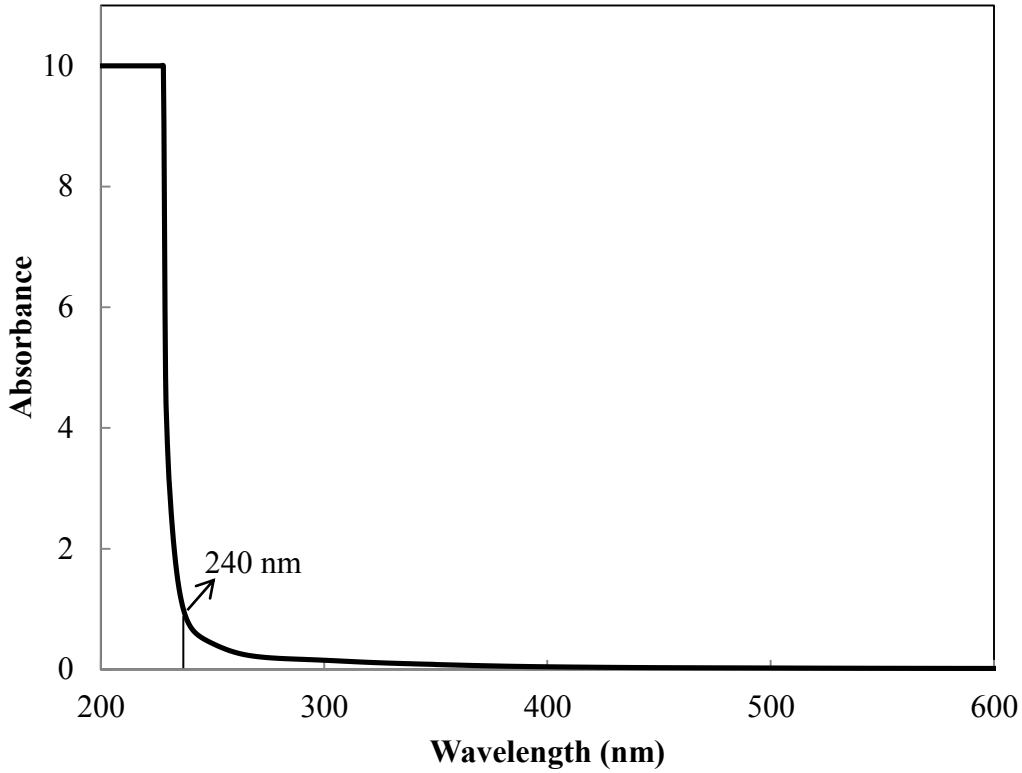

Figure 15. Absorption spectrum of pure PVP.

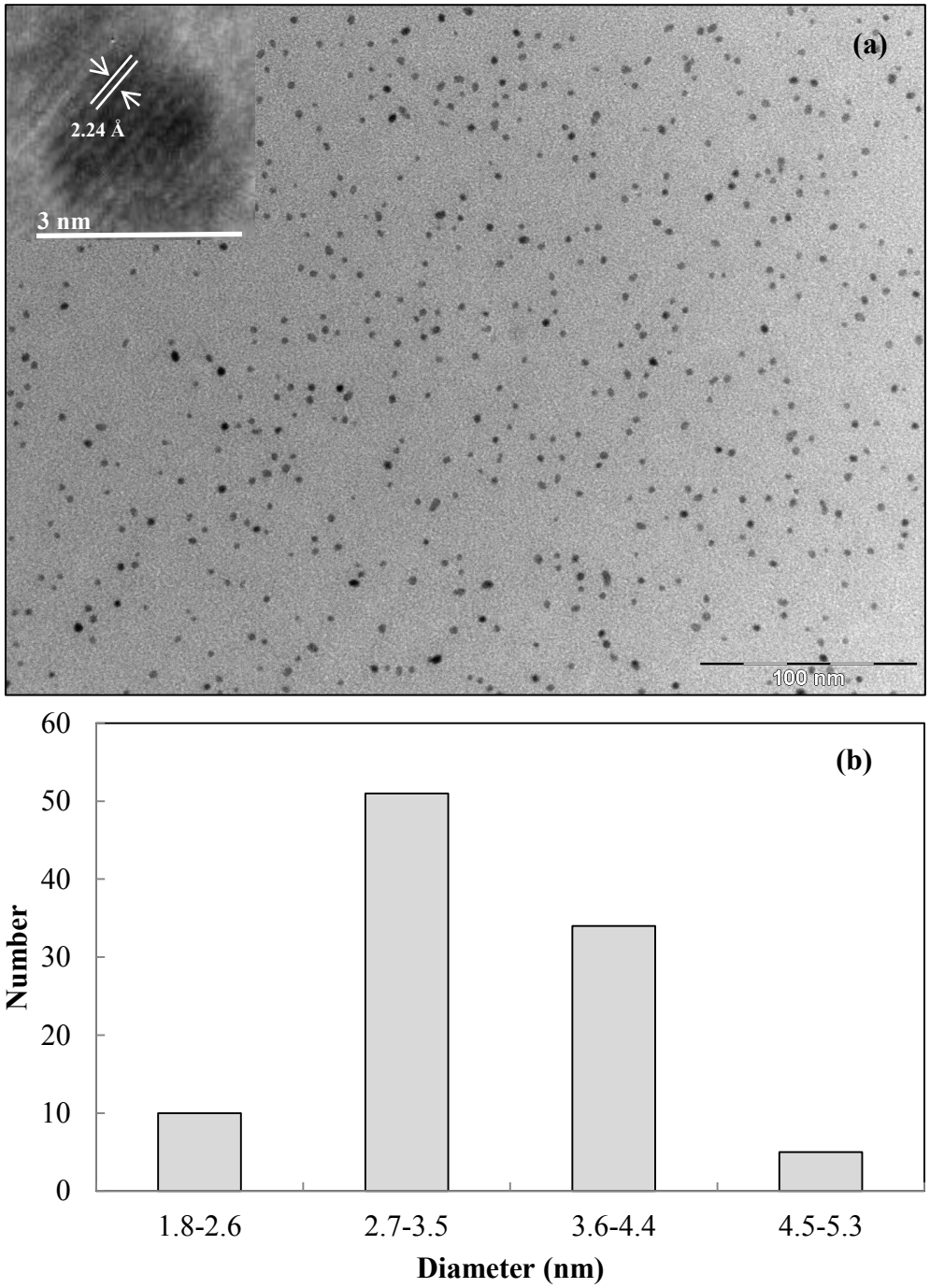

Figure 16. TEM image of (a) PVP/Pt nanoparticles synthesized in methanol and diffraction pattern (inset) from an individual PVP/Pt nanoparticle (b) histogram of the PVP/Pt nanoparticles with an average size of 3.1 ± 0.4 nm in diameter.

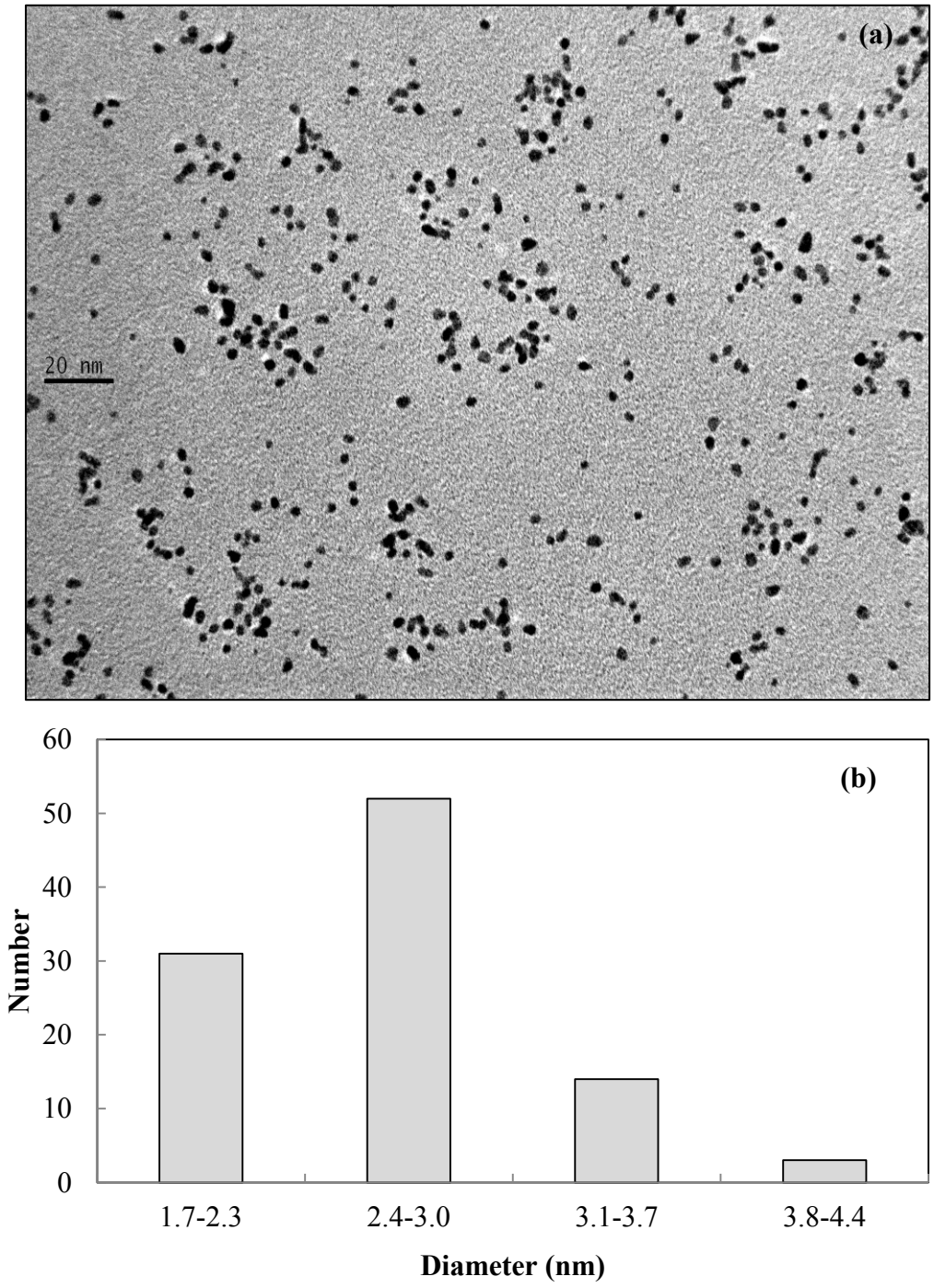

Figure 17. TEM image of (a) PVP/Pt nanoparticles synthesized in ethanol and (b) histogram of the PVP/Pt nanoparticles with an average size of 2.7 ± 0.3 nm in diameter.

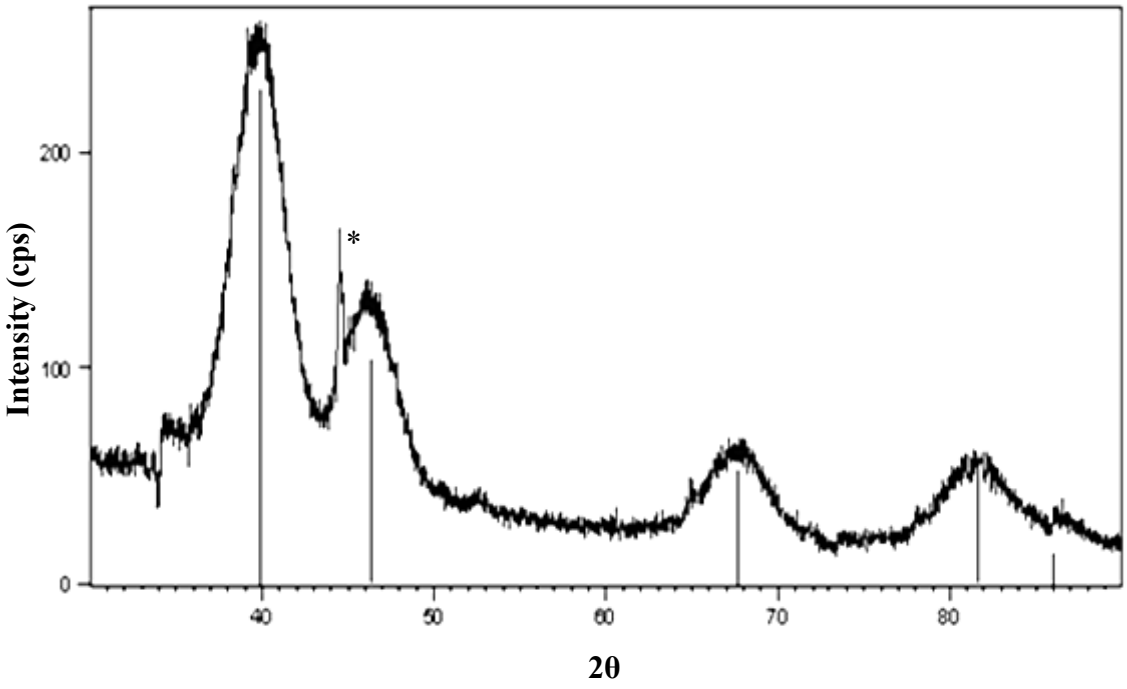

Figure 18. Powder X-ray diffraction pattern showing FCC structure of PVP/Pt nanoparticles synthesized using methanol. Background (*) arising from the double-sided tape used to hold the PVP/Pt nanoparticles.

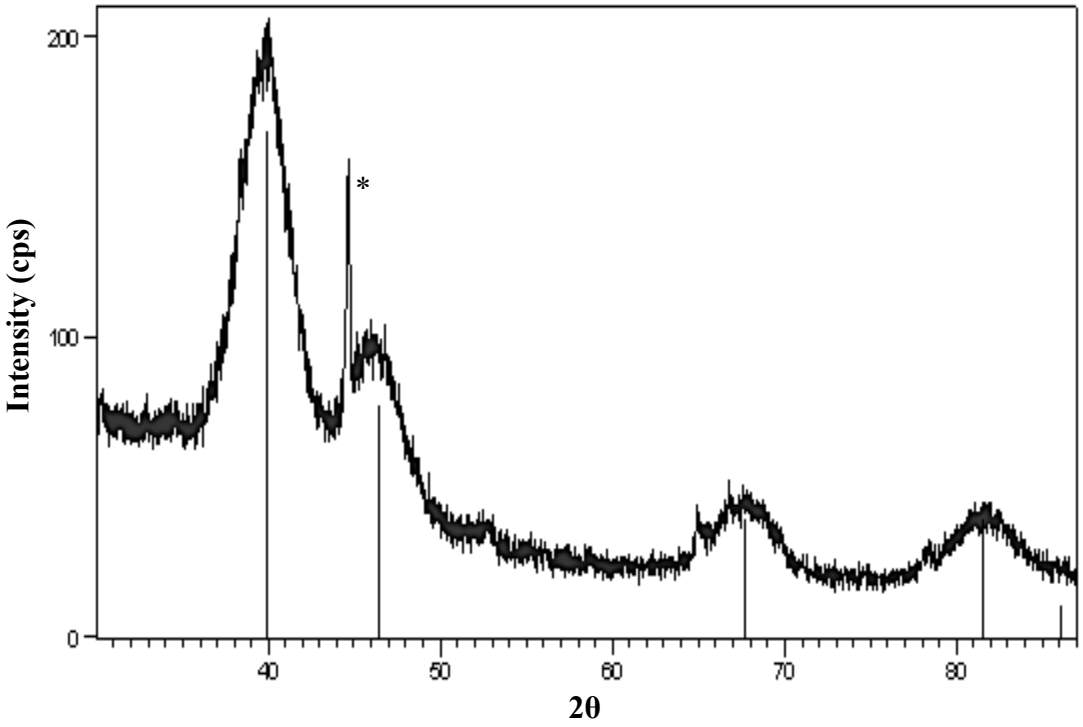

Figure 19. Powder X-ray diffraction pattern showing FCC structure of PVP/Pt nanoparticles synthesized using ethanol. Background (*) arising from the double-sided tape used to hold the PVP/Pt nanoparticles.

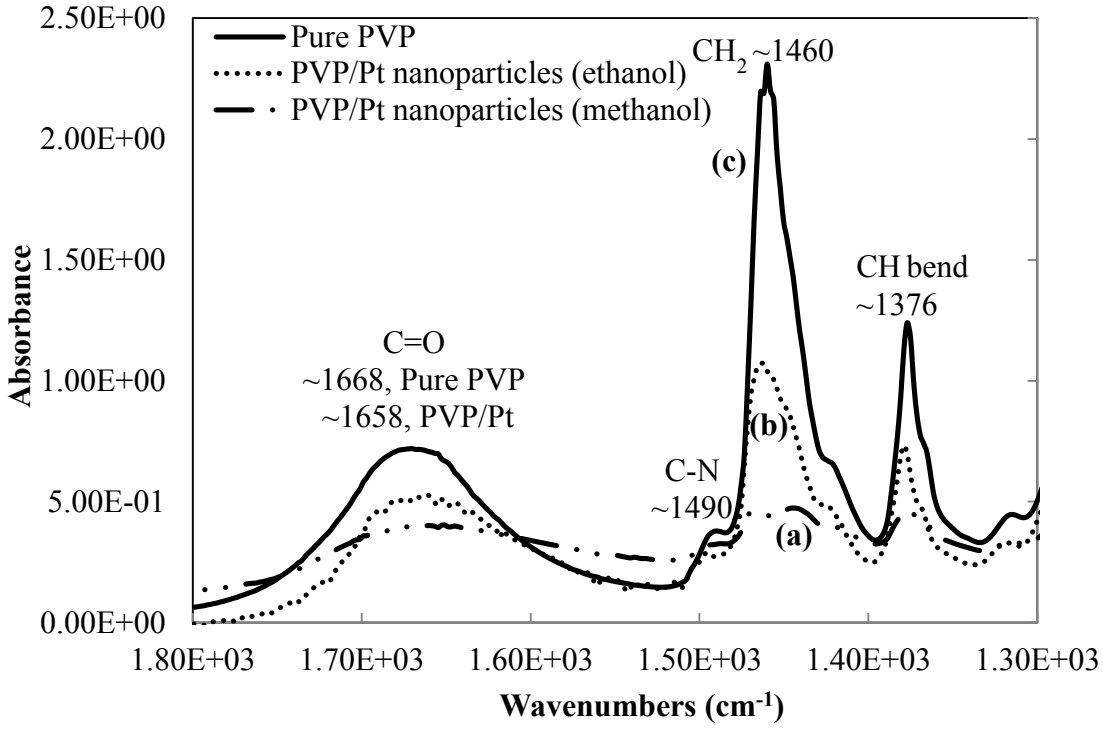

Figure 20. FTIR spectra of (a) PVP/Pt nanoparticles synthesized in methanol, (b) PVP/Pt nanoparticles synthesized in ethanol and (c) pure PVP.

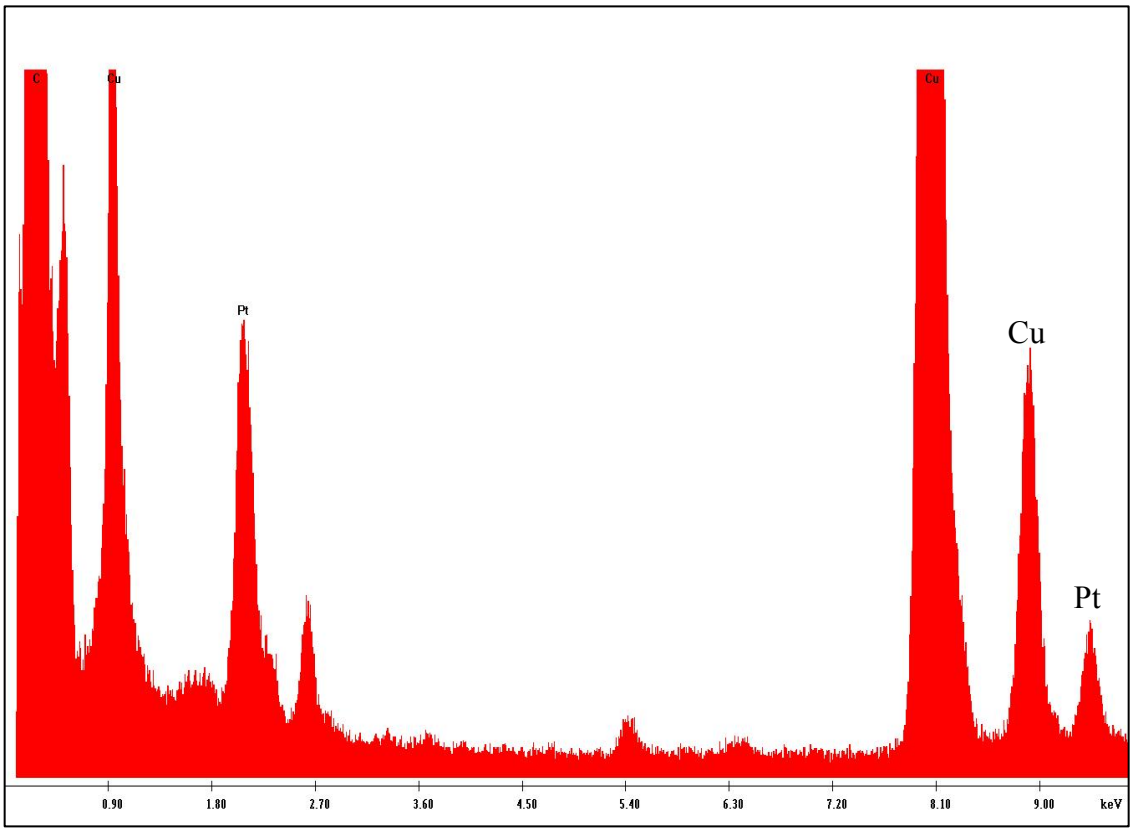

keV

Figure 21. EDS spectra of PVP/Pt nanoparticles synthesized in methanol.

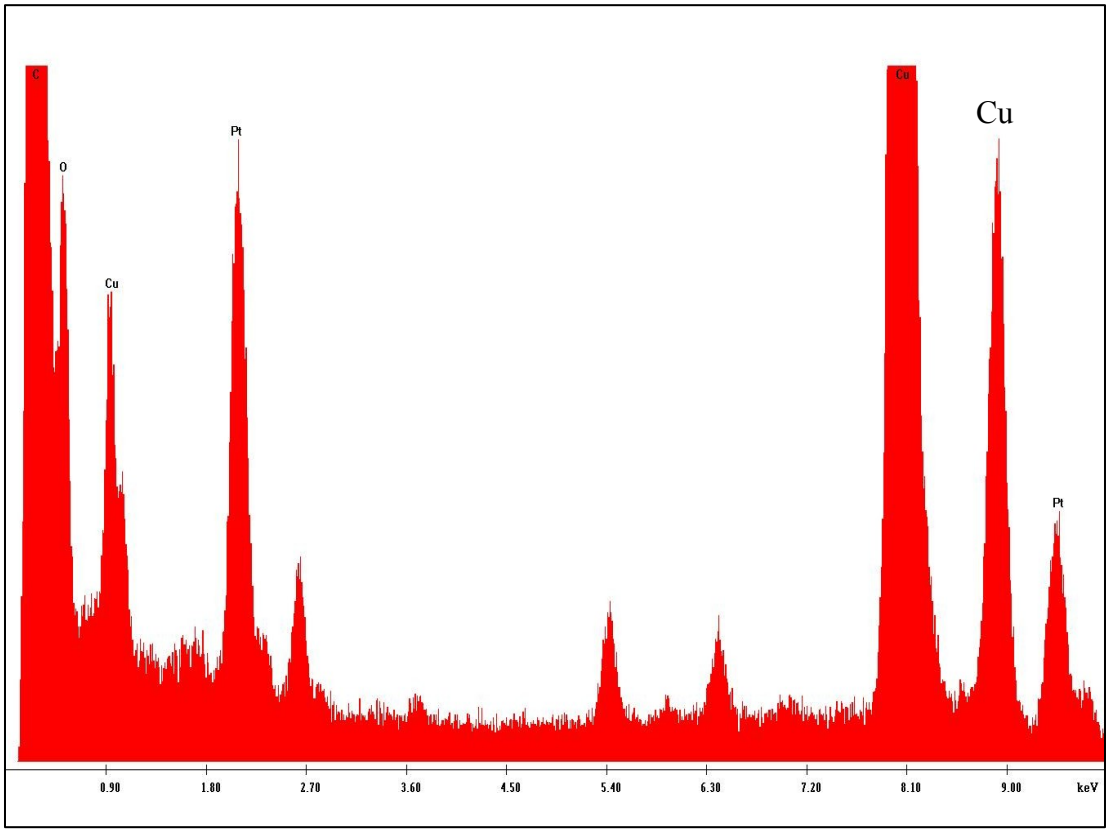

Figure 22. EDS spectra of PVP/Pt nanoparticles synthesized in ethanol.

3.2. Characterization of PVP/Ir Nanoparticles

The PVP/Ir nanoparticles were synthesized in a similar manner. Instead of using dihydrogen hexachloroplatinate (IV) hexahydrate, a 0.006 M dihydrogen hexachloroiridate (IV) hydrate was dissolved in 20 mL of distilled water to which 0.133 g PVP was added. In this method 95% ethanol was used as the solvent. Figure 23 shows the electronic spectrum of a 95% ethanol solution of 1.2×10^{-5} M in PVP and 6.14×10^{-4} M in H_2IrCl_6 before refluxed (solid line). The solution is brownish-red and exhibits H_2IrCl_6 charge transfer bands at 430 nm and 488 nm. After refluxing for 1 hour, the solution turned colorless, and then gradually becomes light yellow, and finally turns dark brown. This change in color is an indication that a chemical reaction has taken place.

To adsorb the Ir nanoparticles into the porous Vycor glass, the particle size must be $\leq 10 \pm 1$ nm. So, to determine the size, TEM analyses were used. TEM images of the PVP/Ir nanoparticles (Figure 24a) were recorded on the same system used for the PVP/Pt nanoparticles. The particles do not look aggregated and from the scale bar located on the bottom right corner of the image, the particles appear much smaller than the particles obtained for the PVP/Pt nanoparticles. One hundred particles were selected and the particle sizes were measured and a histogram was plotted. The average size of the Ir nanoparticles was obtained from highest bar in the histogram labeled 1.5-2.1 nm (Figure 24b).

The crystal structure of the Ir particles was examined by XRD analyses. The XRD pattern of the PVP/Ir nanoparticles revealed a broad peak at 40.8^{o}, followed by lower intensity reflections at 47.4^{o}, 69.3^{o} and 83.6^{o} (Figure 25). Nevertheless, the PVP/Ir

samples being measured, matches the reference pattern of Ir from the XRD database by the appearance of the stick patterns. The crystal system of the Ir particles was found to be face-centered cubic obtained from the reference pattern parameters in the XRD database.

FTIR spectra of the Ir nanoparticles capped with PVP, shows similar vibrations to those of the PVP/Pt nanoparticles (Figure 26). Vibrations at 1668 cm^{-1} for C=O, 1490 cm^{-1} for C-N, 1460 cm^{-1} for CH_2 and 1376 cm^{-1} for CH are all detected in the spectra for the Ir nanoparticles capped with PVP. The assigned bands of the PVP/Ir nanoparticles show a reduction in intensity in comparison to the intensity of the pure PVP. The C=O vibration at 1668 cm^{-1} for the capped Ir nanoparticles with the PVP, is shifted to 1658 cm^{-1}. This shift to lower frequencies and the reduction in intensity of the capped Ir nanoparticles indicates that the C=O group is attached to the Ir nanoparticle.

To confirm the identity of the Ir nanoparticles in the sample, an EDS analysis was utilized. The EDS spectra reveal strong bands of carbon, copper and iridium. The Ir bands are located at *ca.* 1.98, 9.00 and 10.63 keV confirms the presence of Ir (Figure 27).

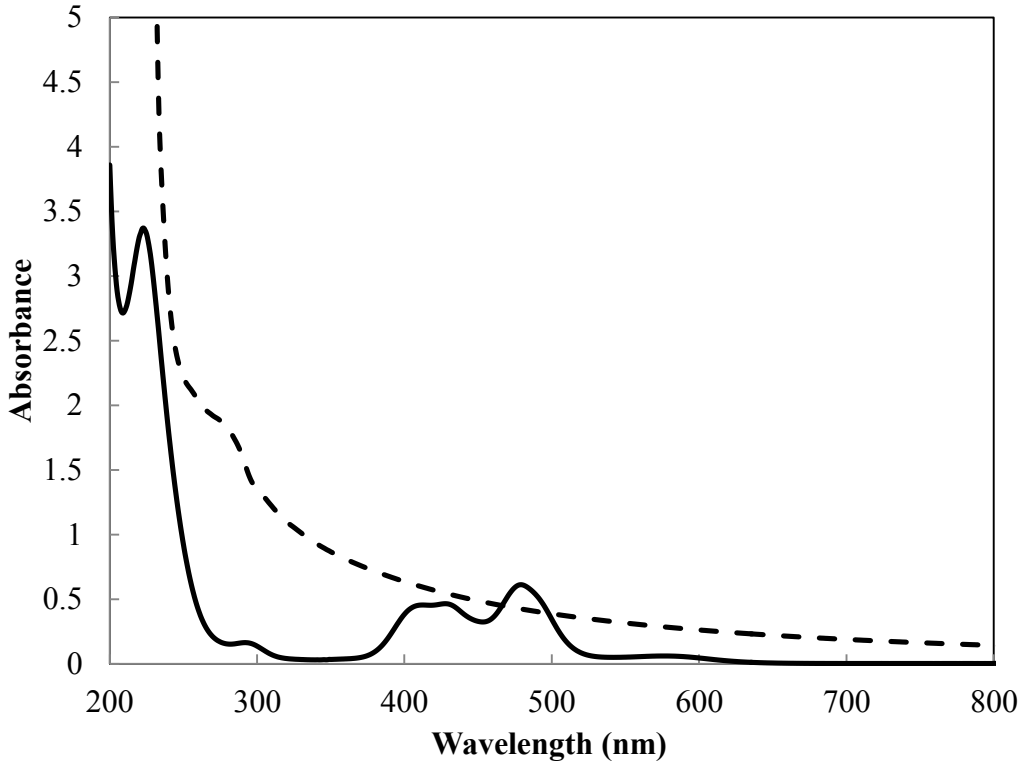

Figure 23. Absorption spectra of PVP/H_2IrCl_6 solution before reflux (——) and PVP/Ir nanoparticles after reflux (– – –) synthesized in ethanol.

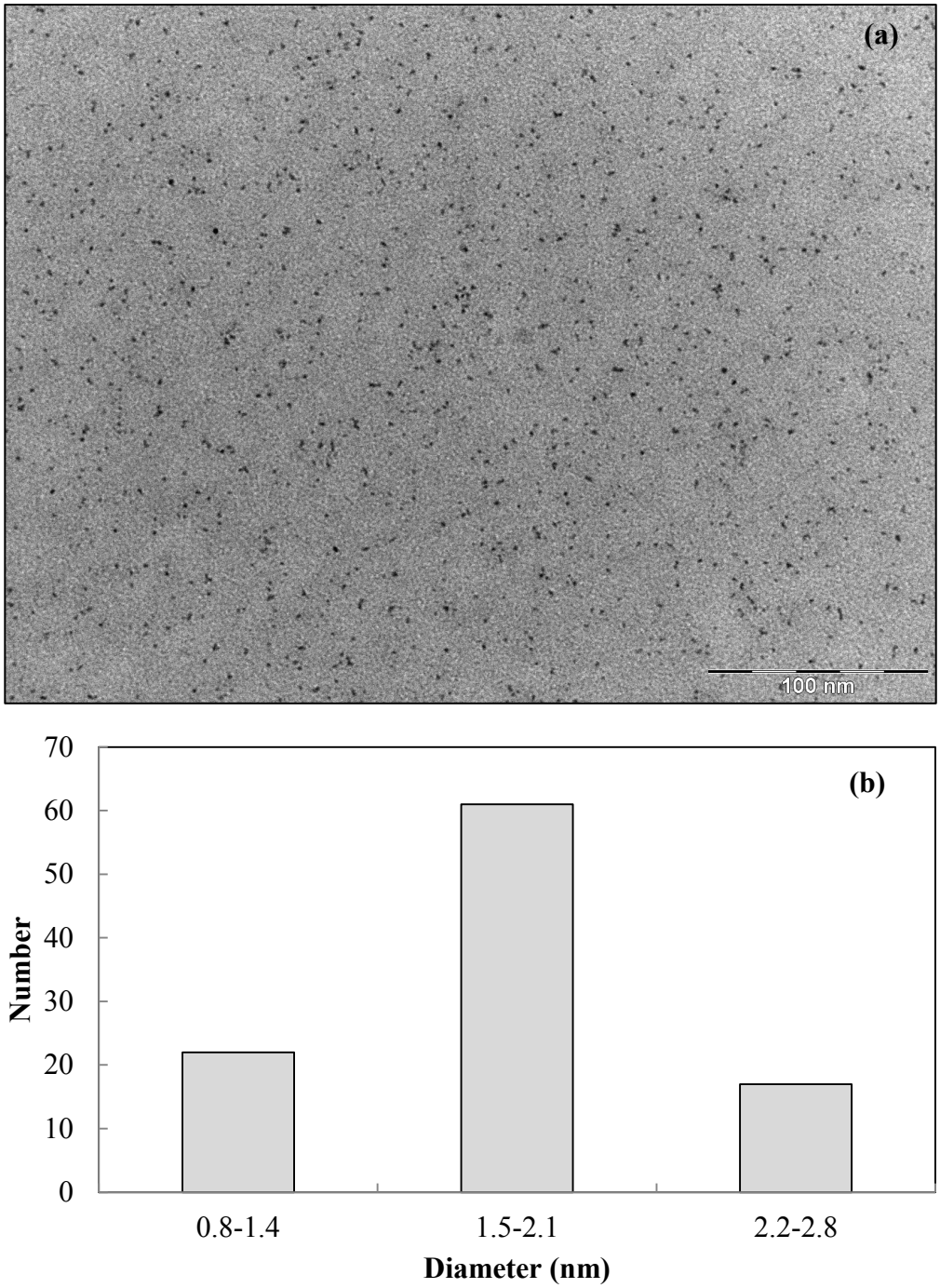

Figure 24. TEM image of (a) PVP/Ir nanoparticles synthesized in ethanol and (b) histogram of the PVP/Ir nanoparticles with an average size of 1.8 ± 0.3 nm in diameter.

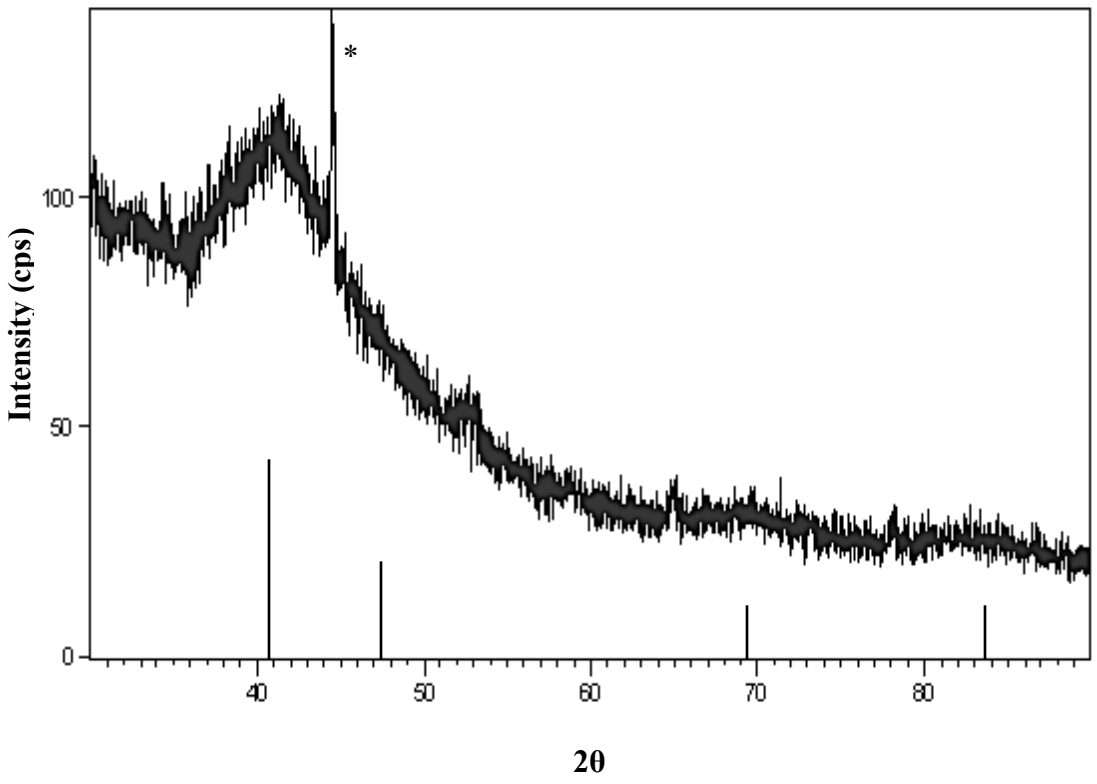

Figure 25. Powder X-ray diffraction pattern showing FCC structure of PVP/Ir nanoparticles synthesized using ethanol. Background (*) arising from the double-sided tape used to hold the PVP/Ir nanoparticles.

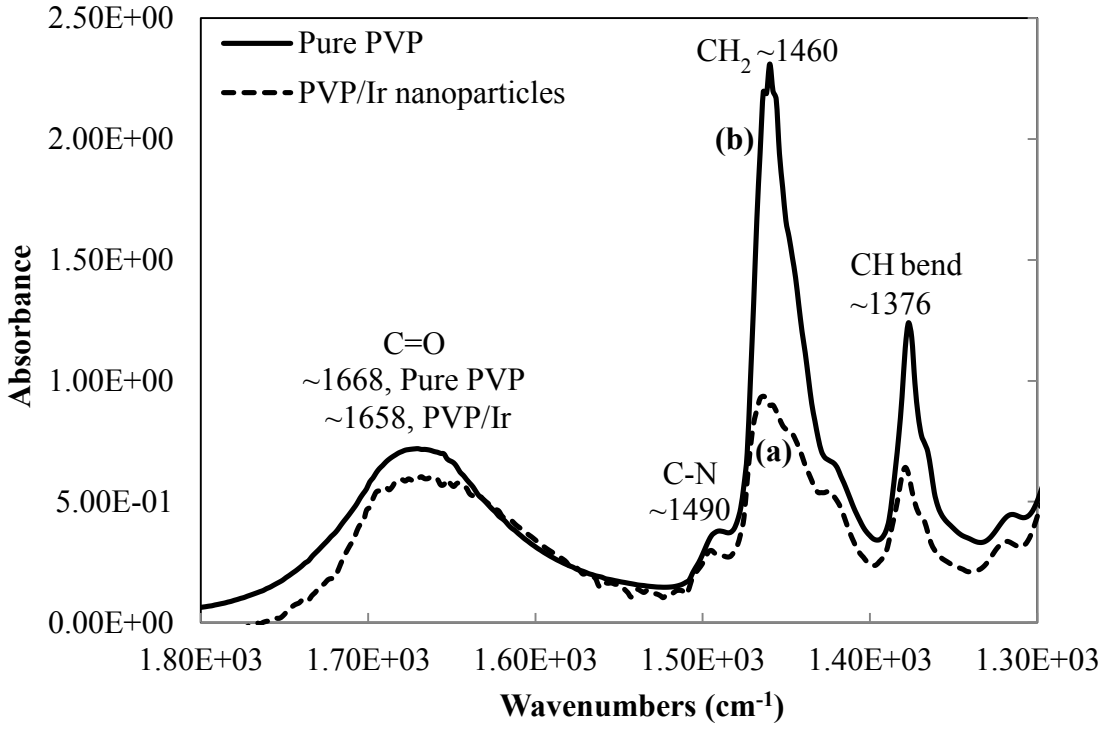

Figure 26. FTIR spectra of (a) PVP/Ir nanoparticles synthesized in ethanol and (b) pure PVP.

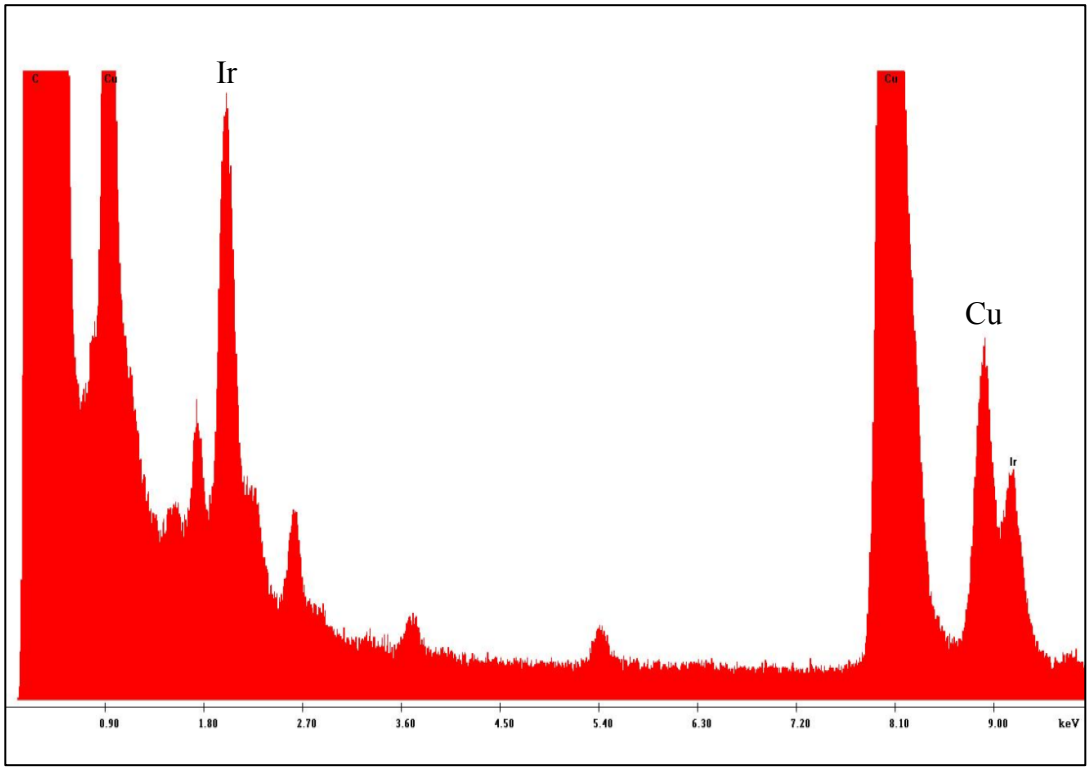

keV

Figure 27. EDS spectra of PVP/Ir nanoparticles synthesized in ethanol.

3.3. Characterization of PVP/Pt-Ir Nanoparticles

Figure 28 shows the UV-vis absorption spectra of the ethanol solution of PVP, H_2PtCl_6 and H_2IrCl_6 before reflux (solid line). The band at 268 nm is due to H_2PtCl_6 while the charge transfer bands of H_2IrCl_6 are at 430 nm and 500 nm. After reflux, the sample solution was dark brown and exhibits a shoulder in the absorption spectra at *ca.* 280 nm (Figure 28, dashed line). To determine the size of the PVP/Pt-Ir particles, TEM images of the PVP/Pt-Ir nanoparticles were analyzed as previously described and the corresponding histogram are shown in Figure 29. The TEM images shows particles of 2-4 nm diameter estimated from the scale bar with some polydispersity (Figure 29a). A hundred particles were randomly picked and their sizes were measured and exported to Microsoft Excel 2010 for analysis. The highest bar in the histogram with sizes ranging from 1.6-2.2 nm (Figure 29b) was used to calculate the average particle size of the Pt-Ir in the sample.

The reference patterns for Pt and Ir which are displayed as stick patterns observed from the XRD database (Figure 30), matches the broad peaks attributed to the PVP/Pt-Ir nanoparticles, suggesting a mixture of Pt and Ir are present in the PVP/Pt-Ir nanoparticles sample. The Pt-Ir nanoparticles exhibited a face-centered cubic (FCC) crystal structure obtained from the parameters of the Pt and Ir reference patterns from the XRD database.

Figure 31 shows the FTIR spectra of the Pt-Ir nanoparticles capped with PVP, with vibrations assigned to the C=O (1668 cm^{-1}), C-N (1490 cm^{-1}), CH_2 (1460 cm^{-1}) and CH (1376 cm^{-1}), similar to the vibrations of the previously described individual PVP/Pt and PVP/Ir nanoparticles. The C=O absorption of the PVP capped Pt-Ir is reduced in

intensity in comparison to the C=O absorption of the pure PVP and is shifted to 1658 cm^{-1}. This carbonyl shift to lower frequencies and the reduction in intensity, also suggests that the Pt-Ir nanoparticles is attached to the C=O group of the PVP.

EDS analysis was used to confirm the presence and identity of the platinum and iridium nanoparticles generated (Figure 32). EDS spectra identified C, Cu, Cl, Pt and Ir bands. The C and Cu bands are from the carbon coated copper grids and the Cl band is from the synthesis. In fact, the spectra confirm the existence of Pt and Ir particles with band position at *ca.* 2.05, 9.41 and 11.01 keV attributed to Pt and bands at *ca.* 9.00 and 10.63 keV attributed to Ir (Figure 32).

How can one distinguish if Pt-Ir is a core shell material or an alloy? High resolution transmission electron microscopy (HRTEM) was used to determine if the PVP/Pt-Ir nanoparticle is a core shell material or an alloy, which is the bonding of two or more elements[107] (Figure 33). The image is important because it shows that the nanoparticles are close to circular and crystalline. The experimental Pt-Ir lattice spacing of 2.20 Å was estimated from the scale bar provided and is within 0.06 Å and 0.01 Å of the calculated lattice spacing obtained from the reference pattern of 2.26 Å (111) for Pt and 2.21 Å (111) for Ir from the XRD database. The lattice spacing from the experimental diffraction pattern of the Pt-Ir nanoparticle in Figure 33 is closer to the lattice spacing of Ir than to the lattice spacing of Pt, suggesting that the diffraction pattern displayed may be of PVP/Ir nanoparticles. Since, TEM image of the PVP/Pt-Ir nanoparticles exhibit an average particle size of 1.9 ± 0.3 nm in diameter, which is within the average particle size of the individual Pt of 3.1 ± 0.4 nm and individual Ir of 1.8 ± 0.3

nm, and EDS and XRD pattern confirms the presence of Pt and Ir in the sample, the nanoparticles shown in Figure 29a, are nanoparticles made up of a mixture of individual Pt and individual Ir nanoparticles.

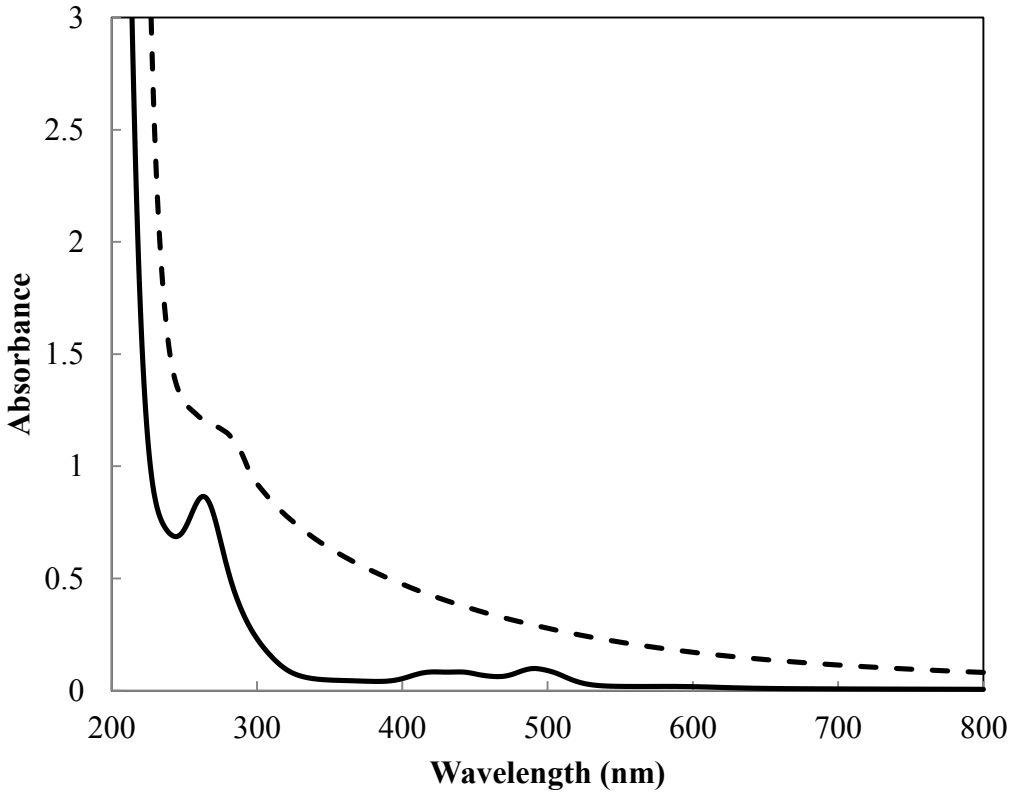

Figure 28. Absorption spectra of PVP/Pt(IV)-Ir(IV) solution before reflux (——) and PVP/Pt-Ir nanoparticles after reflux (– – –) synthesized in ethanol.

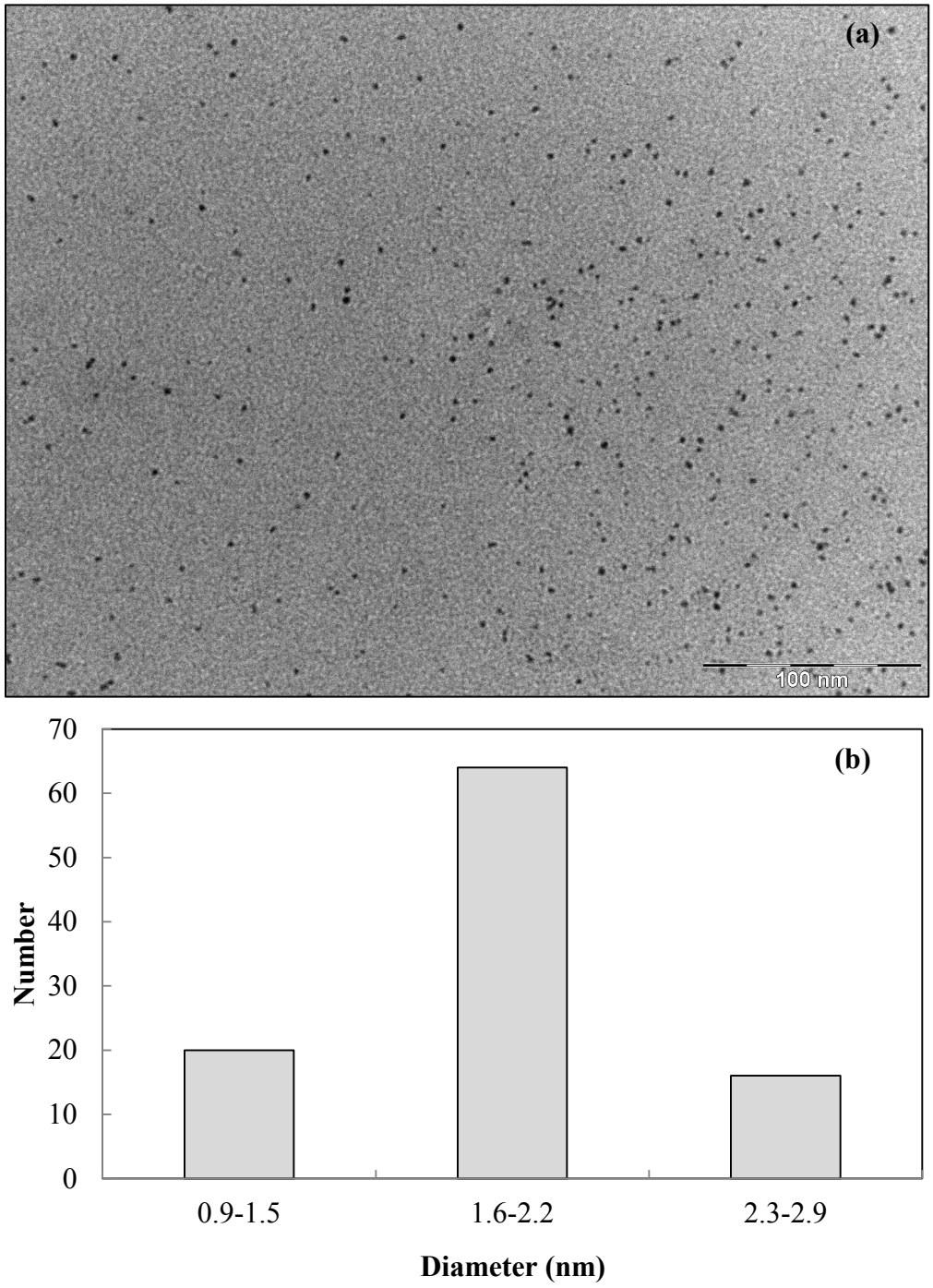

Figure 29. TEM image of (a) PVP/Pt-Ir nanoparticles synthesized in ethanol and (b) histogram of the PVP/Pt-Ir nanoparticles with an average size of 1.9 ± 0.3 nm in diameter.

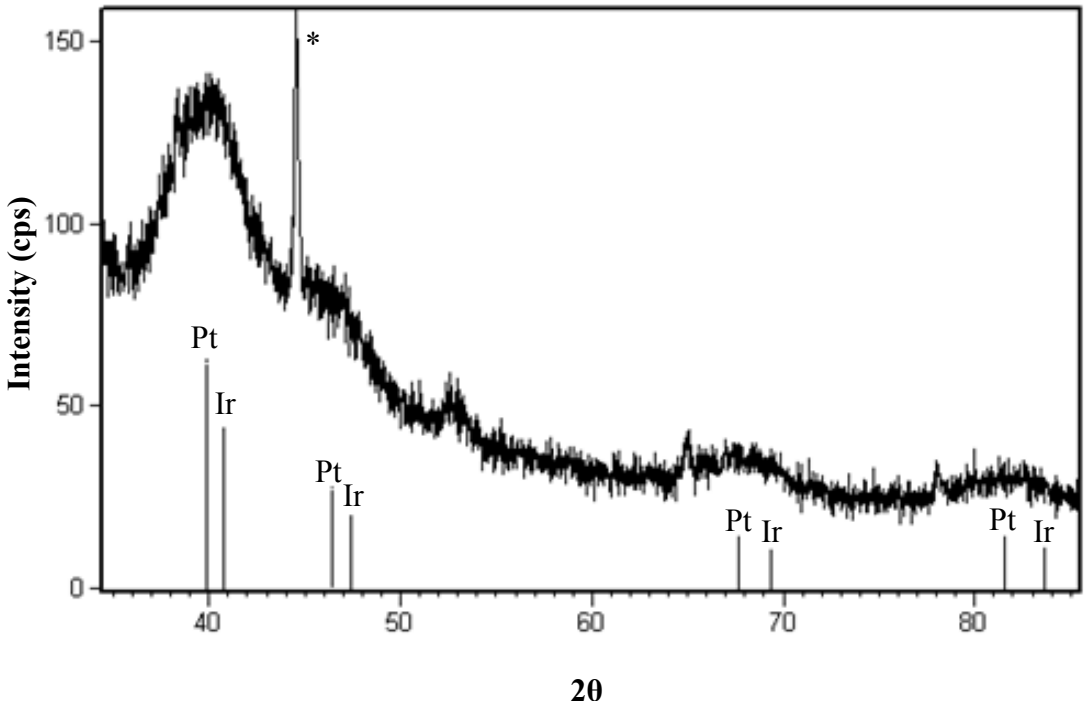

Figure 30. Powder X-ray diffraction pattern showing FCC structure of PVP/Pt-Ir nanoparticles synthesized using ethanol with reference stick patterns corresponding to Pt and Ir nanoparticles. Background (*) arising from the double-sided tape used to hold the PVP/Pt-Ir nanoparticles.

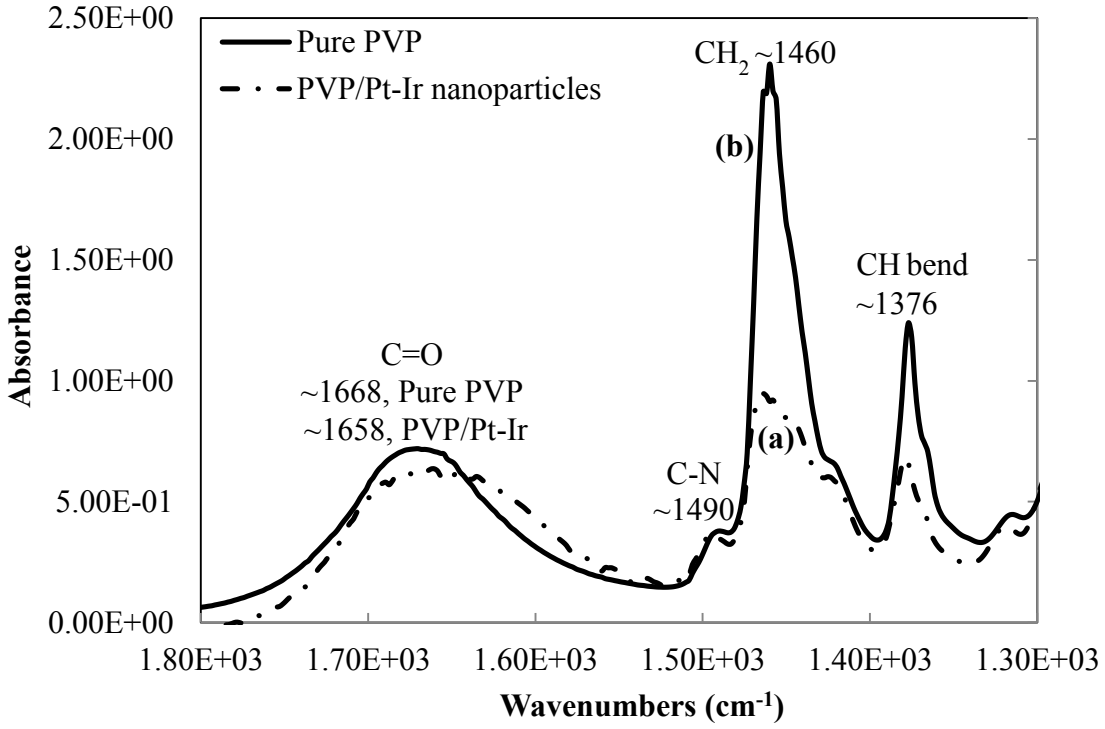

Figure 31. FTIR spectra of (a) PVP/Pt-Ir nanoparticles synthesized in ethanol and (b) pure PVP.

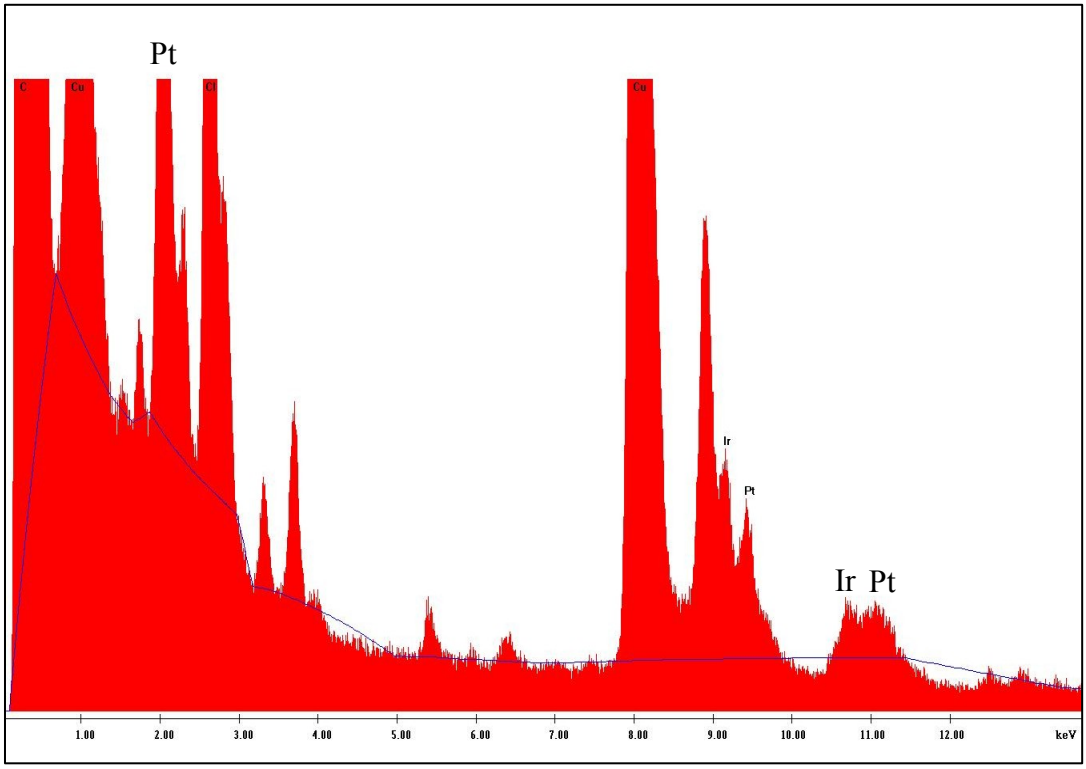

Figure 32. EDS spectra of PVP/Pt-Ir nanoparticles synthesized in ethanol.

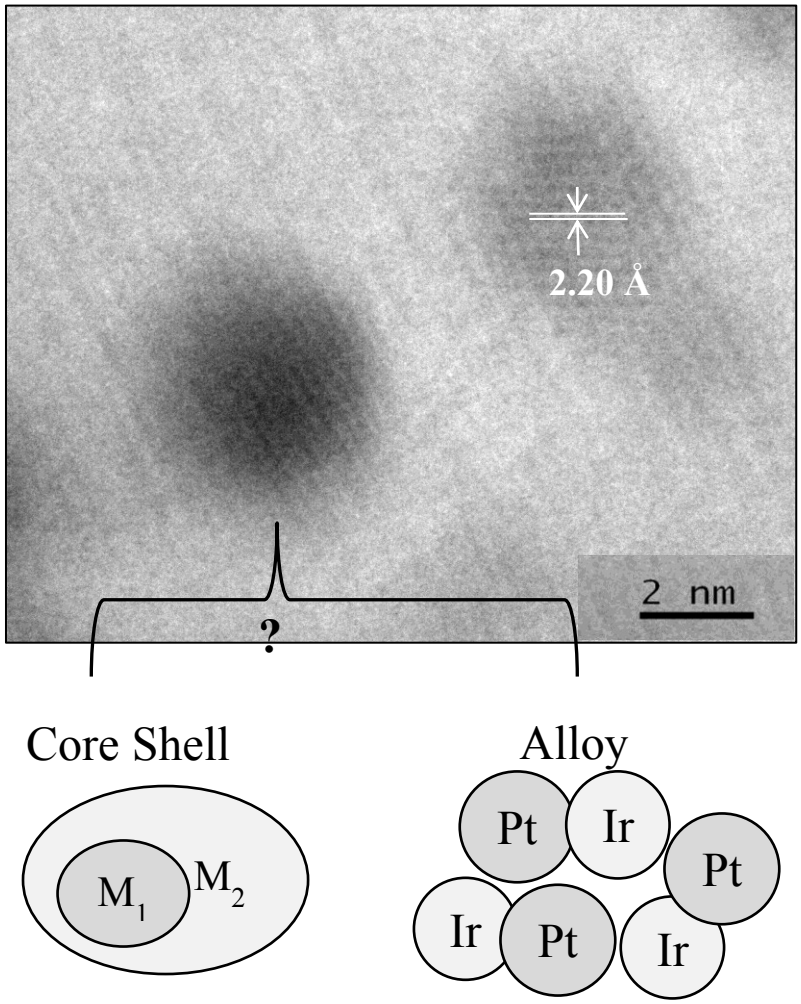

Figure 33. HRTEM image of PVP/Pt-Ir nanoparticles synthesized in ethanol.

3.4. Impregnation of PVG with PVP/Pt, PVP/Ir and PVP/Pt-Ir nanoparticles

To determine the molar concentration of the Pt, Ir and Pt-Ir nanoparticles in solution, the number of Pt or Ir atoms per nanoparticle, N was calculated from the equation provided by Liu and co-workers which is described as[108]

$$N = (\pi\rho * D^3 * N_A)/(6M) \quad (2)$$

where ρ is the density[109] of FCC Pt or Ir, D (cm) is the average core diameter of the Pt or Ir nanoparticle, N_A is Avogadro's constant and M is the molecular weight of the Pt or Ir. The actual concentration, C for the Pt, Ir and Pt-Ir nanoparticles which is summarized in Table I is calculated by the equation[108]

$$C = (N_{total} * N_A)/(NVN_A) \quad (3)$$

where N_{total} is the initial amount of Pt^{4+} or Ir^{4+} salt added in moles, N is the number of Pt or Ir atoms per nanoparticle and V is the volume of the reaction solution in liter.

Table I. Measured and calculated concentration of Pt, Ir and Pt-Ir nanoparticles

Metal nanoparticles	Average diameter (nm)	Measured concentration of salt (M)	Calculated concentration of nanoparticle (M)	Concentration impregnating nanoparticle solution (M)
Pt (methanol)	3.1 ± 0.4	(6.15±0.02)E-4	(6.58±0.02)E-7	(3.29±0.05)E-7
Pt (ethanol)	2.7 ± 0.3	(5.99±0.02)E-4	(9.45±0.03)E-7	(4.73±0.07)E-7
Ir	1.8 ± 0.3	(6.14±0.03)E-4	(3.36±0.02)E-6	(1.68±0.03)E-6
Pt-Ir	1.9 ± 0.3	(3.10±0.01)E-4	(2.92±0.01)E-6	(2.92±0.03)E-6

Solutions of PVP/Pt and PVP/Ir nanoparticles to impregnate Corning's code 7930 porous Vycor glass were prepared by dispersing 15 ml of an aliquot of the PVP/M np's in 15 ml

of either methanol or 95% ethanol. A 30 ml of an aliquot of the PVP/Pt-Ir nanoparticles solution was pipetted from the PVP/Pt-Ir ethanol stock solution and used without any further dilution. Based on the amount of the H_2PtCl_6 or H_2IrCl_6 used in the preparation, the concentration of the nanoparticles was calculated and the results tabulated in Table I.

In the impregnation experiments, two types of PVG were used. The unpolished PVG with approximate dimensions of 19 mm x 19 mm x 5 mm, and the polished PVG with dimensions of 25 mm x 25 mm x 2 mm were weighed and placed upright in glass Coplin Staining Jars and either 15 ml or 30 ml of the impregnating solution was added. The jar was then covered and allowed to stand at room temperature for 24 hours. At that point, the PVG was removed and placed in the vacuum oven and dried at room temperature. The method was repeated twice to adsorb more of the nanoparticles into the glasses, and adsorption was monitored by absorption spectroscopy. As shown in Figure 34, the absorbance at *ca.* 280 nm increases after each exposure of the PVG to the impregnating solution.

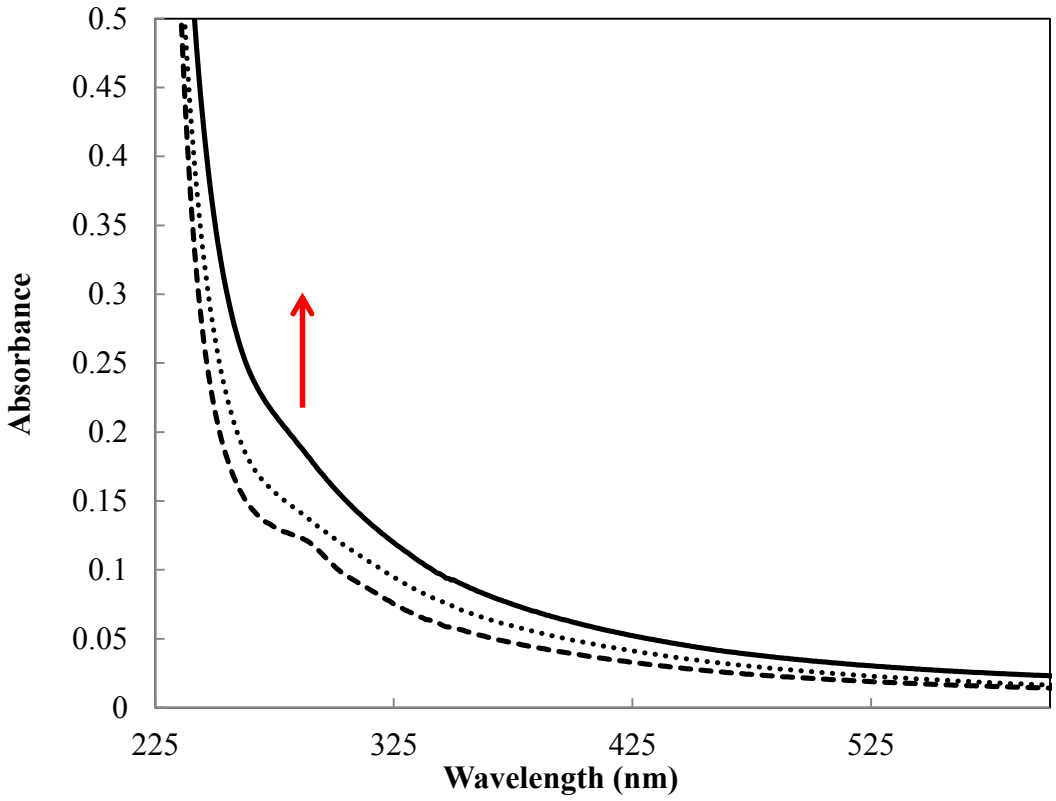

Figure 34: Absorption spectra of impregnated PVG with PVP/Pt nanoparticles synthesized in methanol after first (▬ ▬ ▬), second (·····) and third (▬▬) drying in a vacuum oven at room temperature.

3.4.1 EXAFS Spectroscopy

To study the structural and electronic properties of PVP/Pt, PVP/Ir and PVP/Pt-Ir nanoparticles before and after adsorption into porous Vycor glass, XANES and EXAFS spectroscopy were employed. All XANES and EXAFS spectra were referenced to Pt foil and Ir foil. EXAFS is an interference effect between an excited electron wave and a back scattered electron wave from the nearest neighbor atoms that produces an oscillation in the raw spectral data which represents an absorption coefficient as a function of photon energy E. The photoelectron is ejected from the atom with a wavelength[110] $\lambda = 2\pi/k$, where k is the photoelectron wavevector defined as[111]

$$k = (2m/\hbar^2(E - E_o))^2 \quad (4)$$

where m is the electron mass, $\hbar = h/2\pi$ where h is Planck's constant, E is incident photon energy and E_o is the threshold energy of that absorption edge. The EXAFS function $\chi(E)$ is normalized to the smooth background absorptions μ_o (E) and subtracted from the absorption coefficient of the atom μ (E) which is the given by[111]

$$\chi(E) = (\mu(E) - \mu_o(E)/\mu_o(E)) \quad (5)$$

To obtain the EXAFS function in k space, $\chi(E)$ is converted into $\chi(k)$ by the equation[112]

$$\chi(k) = \Sigma\ (N_j S_j(k)*F_j(k)*\exp(-2\sigma_j^2k^2)*\exp(-2r_j/\lambda(k))(\mathrm{Sin}(2k_{rj} + \varnothing_{ij}(k))/kr_j^2) \quad (6)$$

where $F_j(k)$ is the backscattering amplitude, N_j is the coordination number of the central atom, σ_j is the Debye-Waller factor, r_j is the distance from the absorber to the neighboring atom. $\varnothing_i$ (k) is the central atom phase shift, $\varnothing_j$ (k) is the backscattering phase shift, exp(-$2r_j/\lambda(k)$) is due to inelastic scattering and S_i (k) is the amplitude reduction factor. $\chi(k)$ is

composed of sine waves, so the experimental data are Fourier transformed from *k* to *R* space by multiplying by a window function, $w(k)$ to determine the radial distribution function of Pt, Ir and Pt-Ir nanoparticles before and after adsorption into PVG. A window function is a filtering window that selects the *k* range to be transformed, and is used to filter out the first-neighbor shell from interference caused by scattering from the neighboring atoms.[113]

3.4.2 PVP/Pt Nanoparticles

To examine PVG glass impregnated with PVP/Pt nanoparticles, UV-vis absorption spectroscopy was utilized. Figures 35a and 36a shows the absorption spectra of the PVG before (solid line) and after impregnation (dashed line) with the PVP/Pt nanoparticles. As previously described, the impregnated PVG's with the PVP/Pt nanoparticles are dried in a vacuum oven at room temperature. A comparison of Figures 35 and 36 shows that adsorption is independent of whether the PVP/Pt nanoparticles were prepared by methanol or ethanol reduction. The absorption spectra of the clean PVG and impregnated PVG do not exhibit any bands in the visible region. Inset on the upper right corner of Figure 35a shows an image of a clean PVG (left image) and a PVG impregnated with PVP/Pt nanoparticles (right image). But after the impregnated PVG spectra were subtracted from the clean PVG spectra, a very weak intensity band with a broad shoulder is observed at *ca.* 280 nm (Figures 35b and 36b) which may be attributable to the excitation of interband transition of the Pt nanoparticles.[114,115] A larger image of the clean PVG before impregnation (left image) and after impregnation of the PVP/Pt nanoparticles into the PVG (right image) is shown in Figures 37. The left image

is transparent and the right image of the PVG is light brown. The light brown color of the PVG establishes that the PVP/Pt nanoparticles adsorbed into the glass. But the appearance of the change in color from transparent to light brown does not show if the oxidation state of the Pt nanoparticles in the glass remained unaffected.

To confirm the presence and the oxidation state of Pt nanoparticles in the glass, XANES analyses were employed. The normalized x-ray absorption near edge structure (XANES) in Figure 38 shows that the platinum foil, which is the reference material, exhibits an L_3-edge energy or threshold energy at 11563.0 ± 0.3 eV, which is 1 eV lower than the published value of 11564 eV.[116] The threshold energy value or edge energy, $E_{0,}$ for the Pt foil and the PVP/Pt nanoparticles before and after impregnation into PVG, are obtained from the first maximum of the first derivative spectra,[117] indicated by the red dashed vertical line in the spectrum (Figure 39). Pt foil contains atoms in the zero oxidation state, and crystallizes in a face-centered cubic (FCC) crystal system. The PVP/Pt nanoparticles, the PVP/Pt in the polished PVG and the PVP/Pt in rolled PVG were compared with the Pt foil to confirm its presence in PVG, and to examine the change in oxidation state of the Pt nanoparticles upon adsorption. In the derivative spectra, there is a 1.2 eV shift to lower energy for the PVP/Pt nanoparticles before impregnation into PVG, but this is due to experimental error, because no shift to higher energy is observed for the PVP/Pt nanoparticles in the impregnated glass, even though the glass can behave as an oxidizing matrix. The absence of a pre-edge absorption and the absence of a shift to higher energies to the right of the XANES spectrum indicate that the Pt nanoparticles in the glass are not oxidized. The normalized XANES spectrum in

Figure 38 for the PVP/Pt nanoparticles impregnated into the rolled PVG, shows some fluctuation in the data (circled in red) at the absorption edge between 11520-11550 eV. This fluctuation is due to experimental error, because other samples that were previously examined did not exhibit any variation in the XANES spectra in the absorption edge region. The oscillatory variation observed in the post-edge region in the spectra is due to the interaction of the absorbing atom with the neighboring atom, *i.e.,* the EXAFS spectrum. A smooth decay will be observed in the absence of a near neighbor atom interaction, thereby precluding information such as metal-metal bond length will not be available.

Due to the presence of the neighboring atom, the radial distance of the Pt-Pt bond length is obtained. The Fourier transform magnitude *vs.* the radial distance (Å) of the EXAFS data of Pt foil and the PVP/Pt nanoparticles before and after adsorption into the PVG are depicted in Figures 40-43. The first and highest peak in the spectrum represents the first-neighbor shell. The second minor peak represents the second-neighbor shell and the other peaks at larger *R* (distance from the absorber atom) values arise from higher ordered shells.[118] The Pt-Pt bond length is represented by the vertical dashed line, which yields a Pt-Pt bond length of 2.06 ± 0.01 Å for Pt foil, 2.04 ± 0.01 Å for PVP/Pt nanoparticles, 2.04 ± 0.01 Å for PVP/Pt nanoparticles impregnated into polished PVG and 2.04 ± 0.01 Å for PVP/Pt nanoparticles impregnated into rolled PVG. All the bond lengths recorded for the PVP/Pt nanoparticles with and without the PVG are within experimental error of the bond length of the Pt foil.

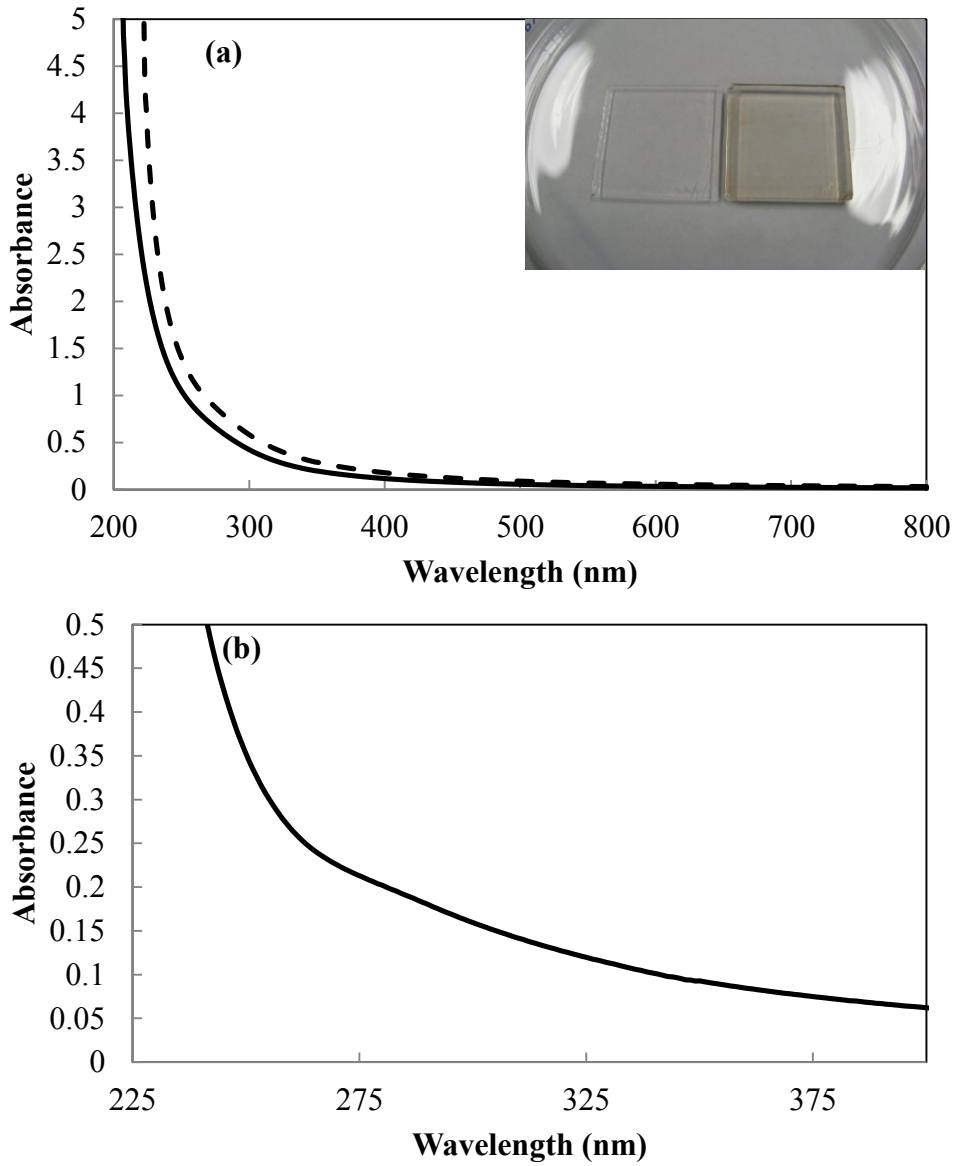

Figure 35. Absorption spectra of (a) PVG before (——) and after adsorption and drying (– – –) with PVP/Pt nanoparticles synthesized in methanol. The inset shows the PVG sample before and after impregnation with the PVP/Pt nanoparticles. The difference spectrum (b) of the adsorbed PVP/Pt nanoparticles obtained by subtraction of the spectra shown above.

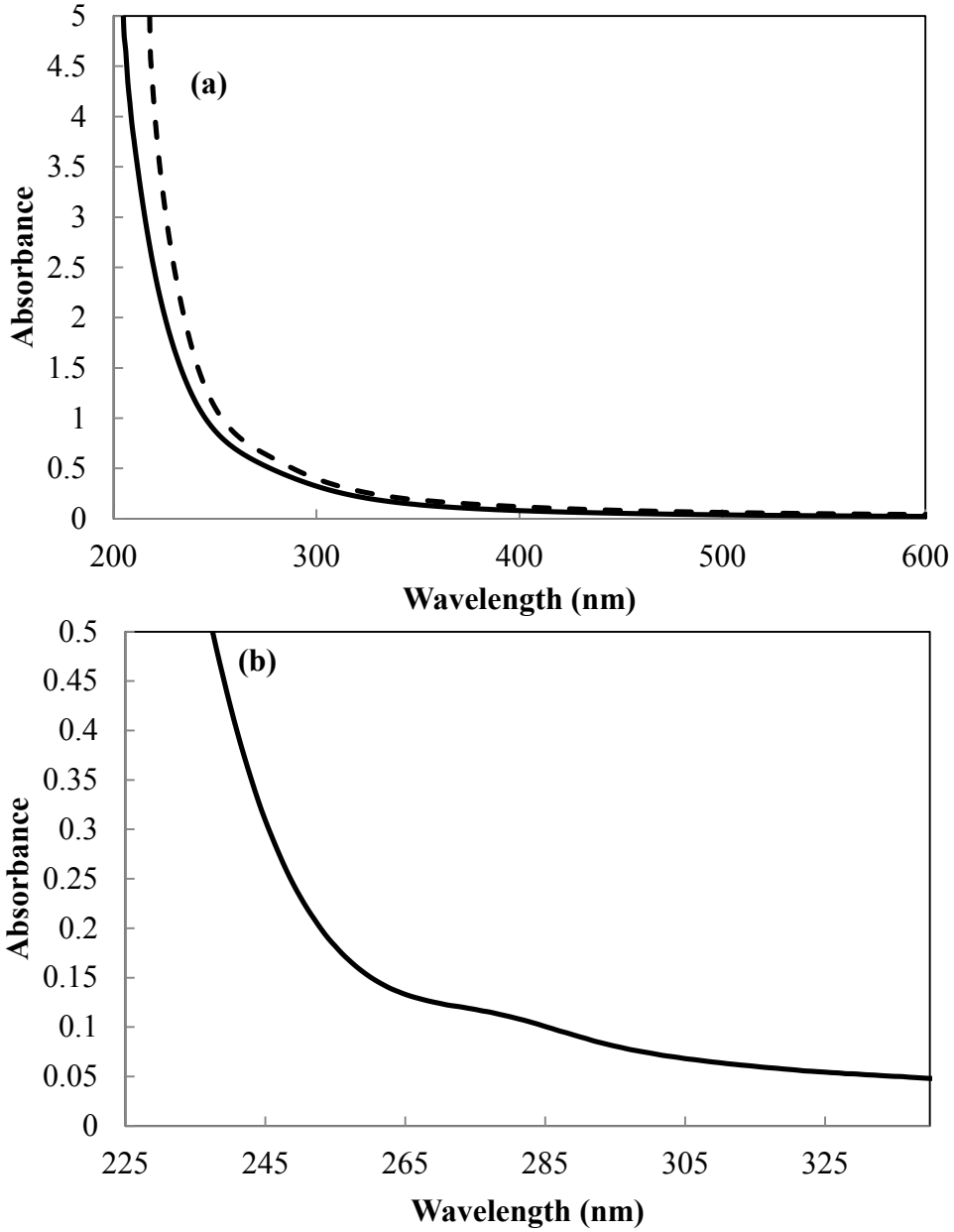

Figure 36. Absorption spectra of (a) PVG before (——) and after adsorption and drying (– – –) with PVP/Pt nanoparticles synthesized in ethanol. The inset shows the PVG sample before and after impregnation with the PVP/Pt nanoparticles. The difference spectrum (b) of the adsorbed PVP/Pt nanoparticles obtained by subtraction of the spectra shown above.

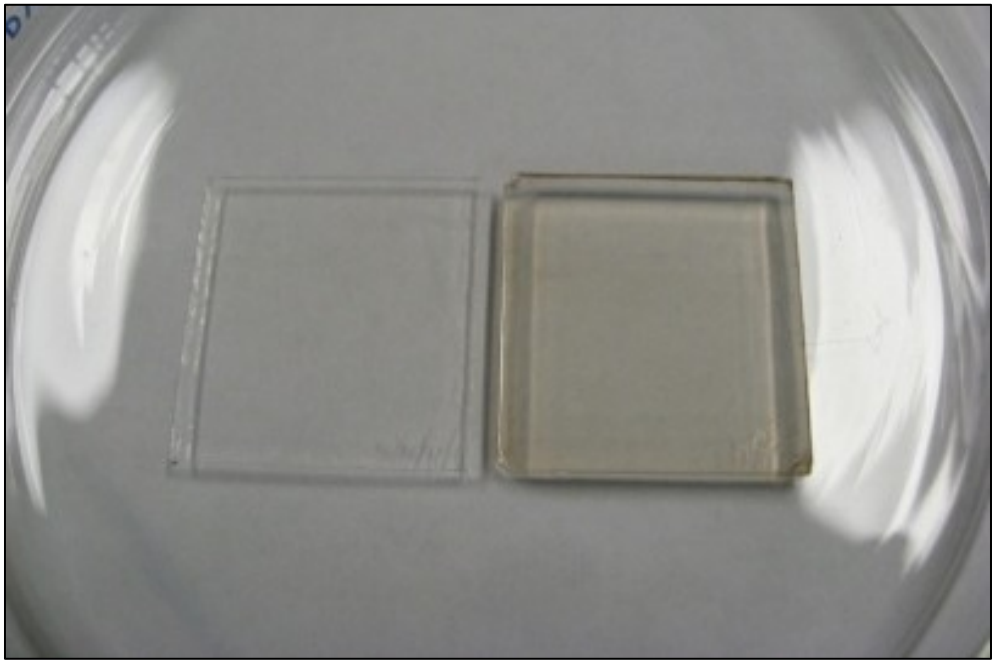

Figure 37. Image of clean PVG (left) and PVP/Pt nanoparticles synthesized in methanol adsorbed into PVG (right).

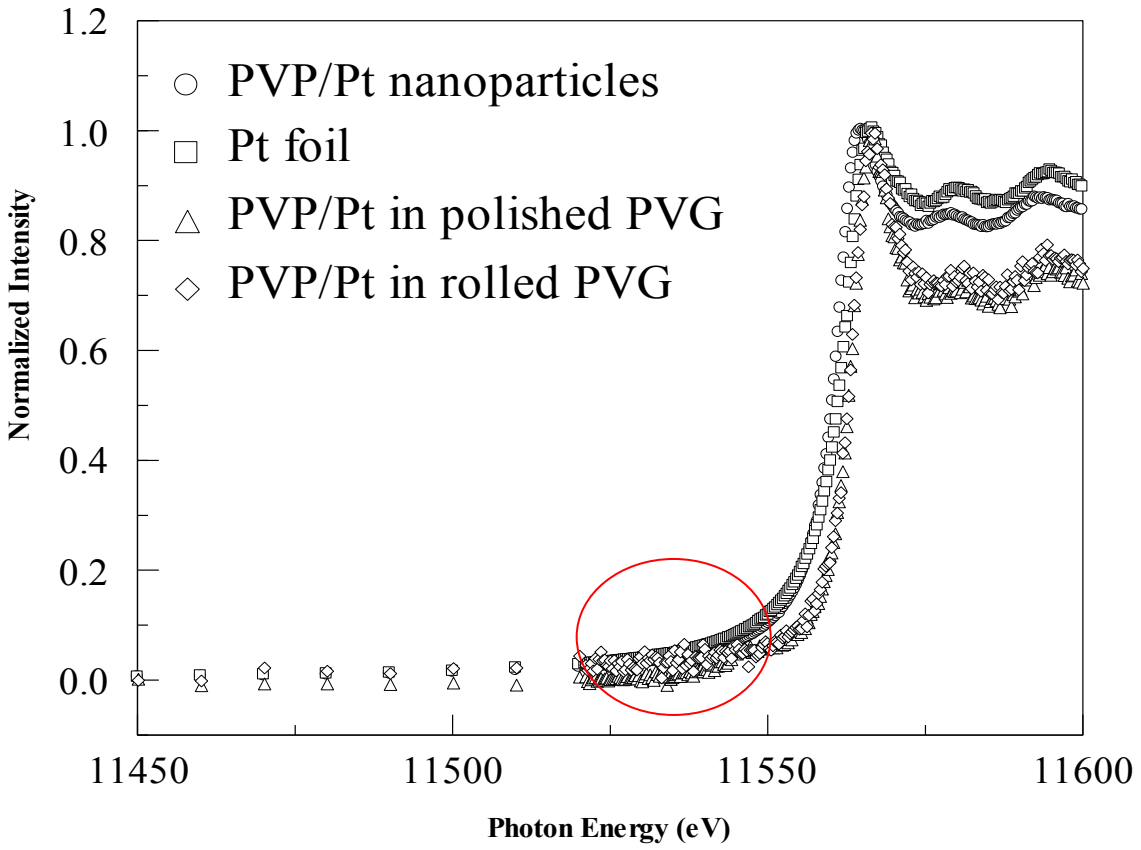

Figure 38. Normalized XANES spectra of PVP/Pt nanoparticles before adsorption into PVG (○), PVP/Pt nanoparticles after adsorption into polished PVG (Δ) and PVP/Pt nanoparticles after adsorption into rolled PVG (◇) when compared to Pt foil (□).

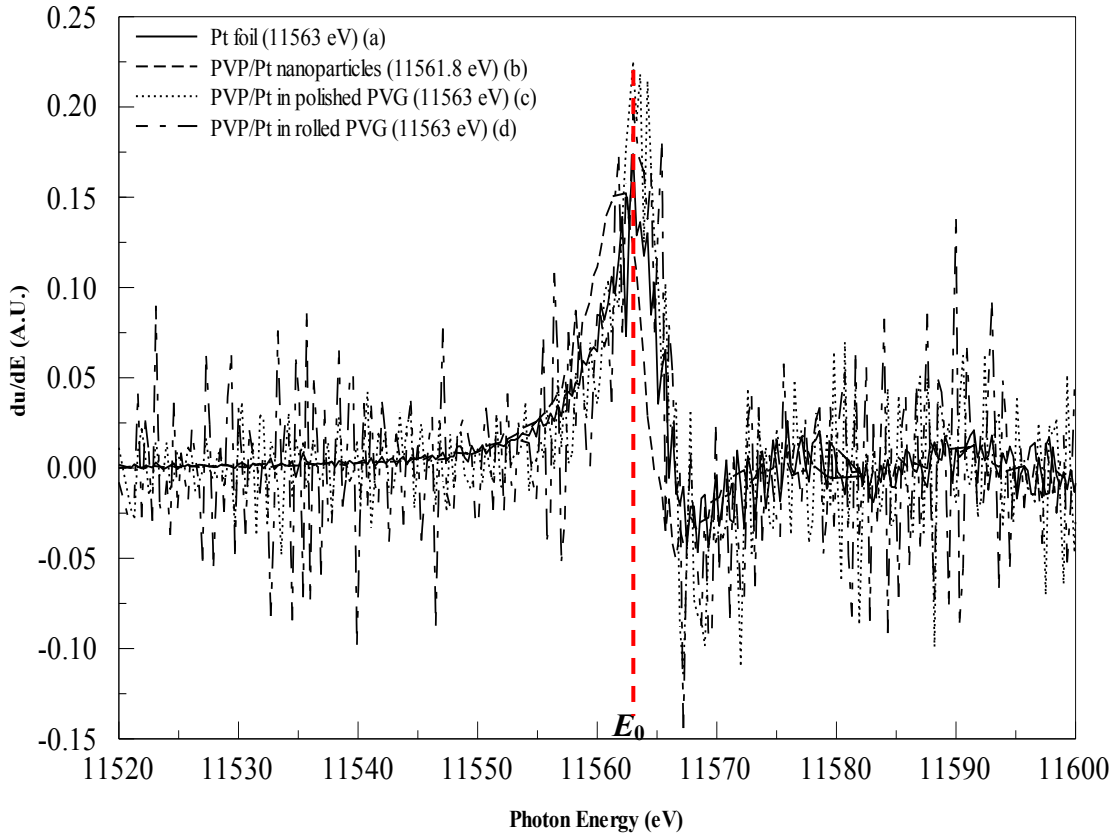

Figure 39. First derivative spectra of (a) Pt foil, (b) PVP/Pt nanoparticles before adsorption into rolled and polished PVG, (c) PVP/Pt nanoparticles after adsorption into polished PVG and (d) PVP/Pt nanoparticles after adsorption into rolled PVG.

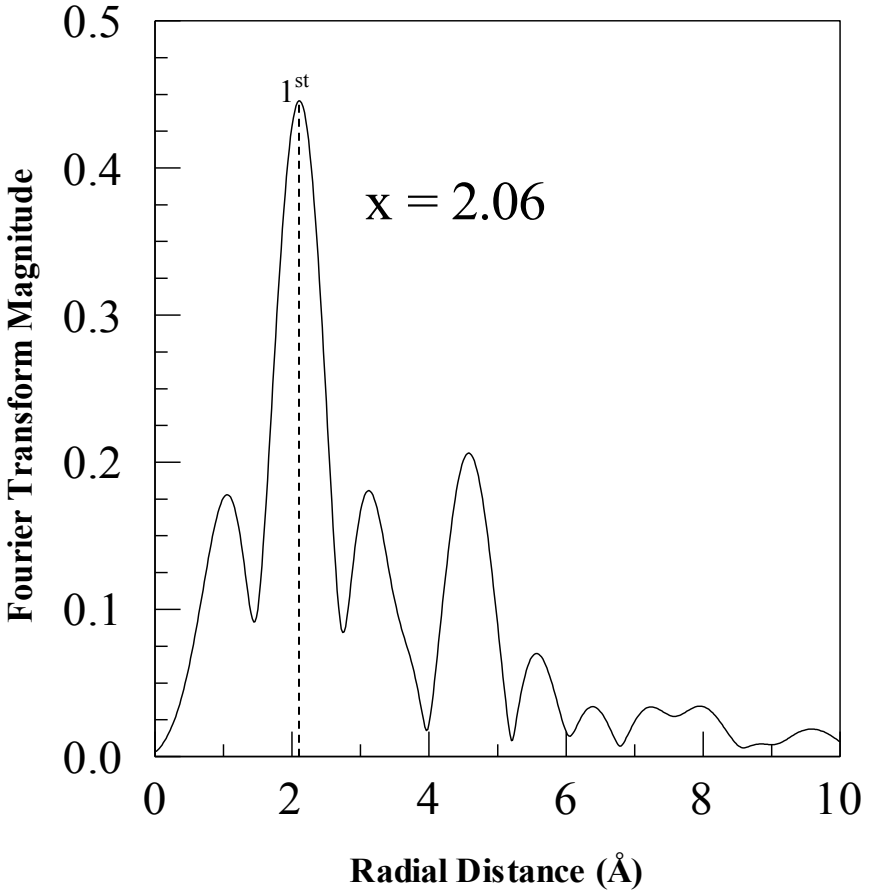

Figure 40. Fourier transform of the EXAFS data of Pt foil.

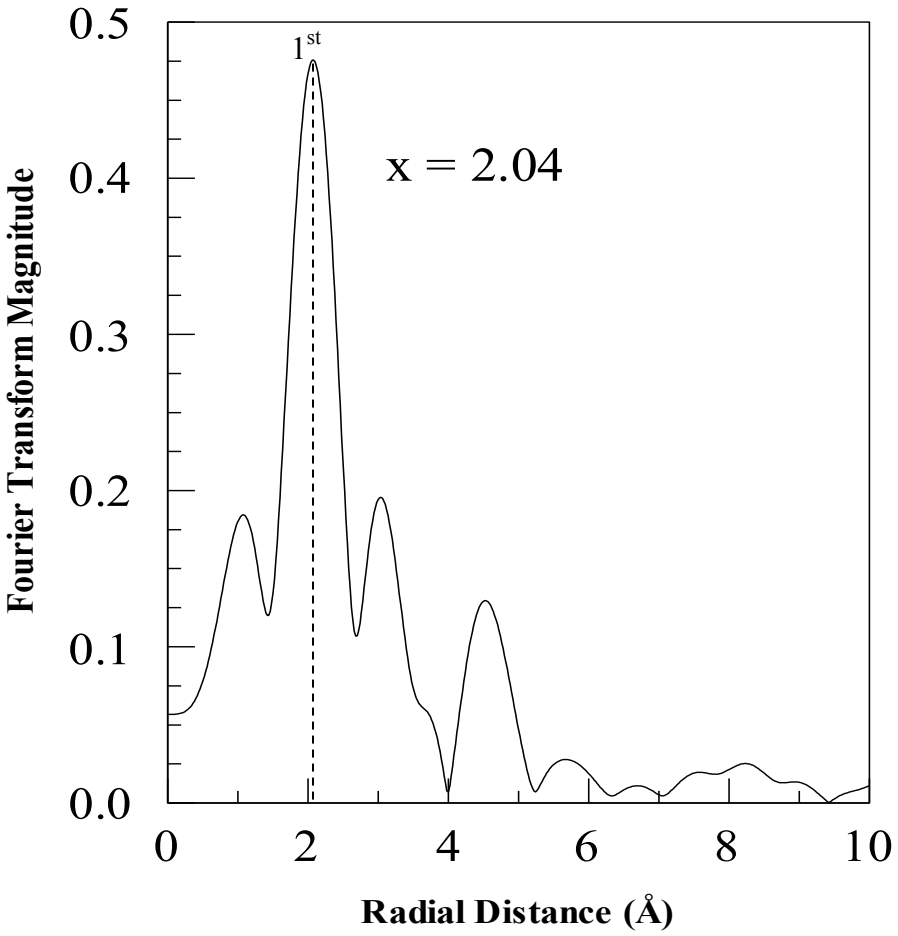

Figure 41. Fourier transform of the EXAFS data of PVP/Pt nanoparticles before adsorption into PVG.

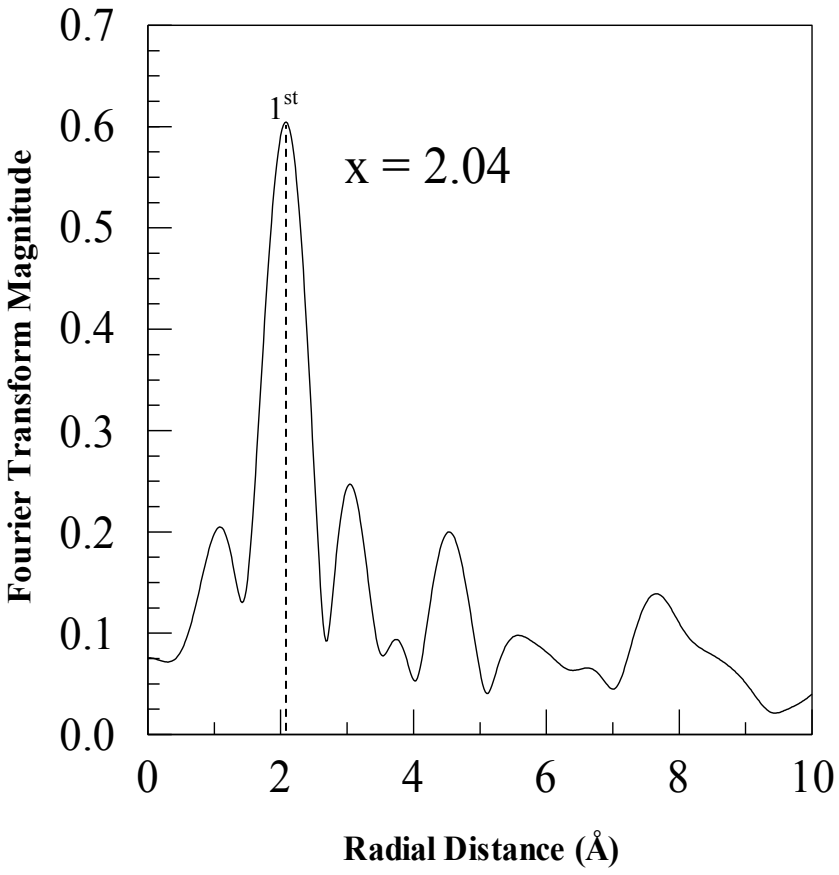

Figure 42. Fourier transform of the EXAFS data of PVP/Pt nanoparticles adsorbed into polished PVG.

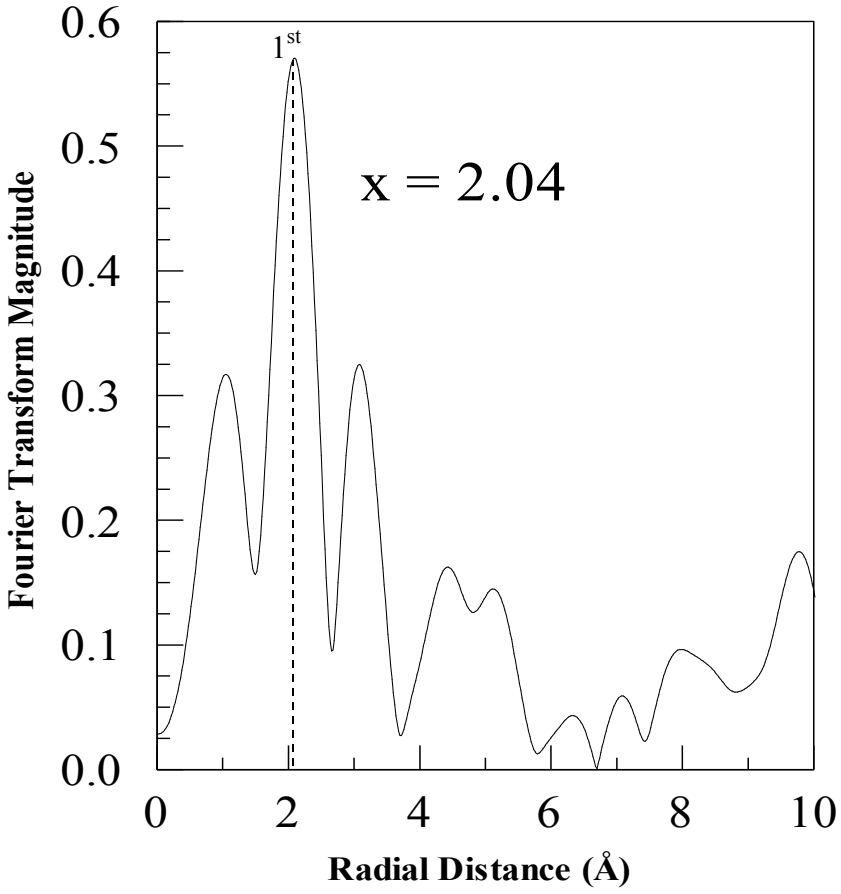

Figure 43. Fourier transform of the EXAFS data of PVP/Pt nanoparticles adsorbed into rolled PVG.

3.4.3 PVP/Ir Nanoparticles

UV-visible absorption spectra were recorded to analyze the PVP/Ir nanoparticles impregnated into the PVG. Figure 44a shows the absorption spectrum of clean PVG (solid line) and PVG impregnated (dashed line) with the PVP/Ir nanoparticles. The spectra are similar, yet the color of the samples (inset) clearly shows that PVG is impregnated with the PVP/Ir nanoparticles. After spectral subtraction of the clean PVG from the impregnated PVG, a very broad shoulder is observed at *ca.* 280 nm (Figure 44b). A larger image of the impregnated PVG (Figure 45) verifies that the PVP/Ir nanoparticles impregnate PVG. To further characterize the adsorbed PVP/Ir nanoparticles, XANES and EXAFS measurements were employed.

Normalized XANES spectra of Ir foil, PVP/Ir nanoparticles and PVP/Ir nanoparticles adsorbed into polished PVG are shown in Figure 46. The EXAFS spectra of the PVP/Ir nanoparticles before and after impregnation into the PVG agree with that of Ir foil. The Ir foil L_3-edge energy or threshold energy is 11214.0 ± 0.3 eV, which is 1 eV lower than the reported value of 11215 eV.[116] There is no evidence showing a pre-edge absorption and no distinct shift of the peak maximum to higher energies is observed in the first derivative spectrum (Figure 47) suggestive of oxidation of the nanoparticles. The normalized XANES spectra in Figure 46 for the PVP/Ir nanoparticles impregnated into the polished PVG also show fluctuation at the absorption edge between 11180-11210 eV (circled in red) similar to that of the fluctuation observed for PVP/Pt nanoparticles impregnated into the rolled PVG at the absorption edge region. This is also due to experimental error because from the previous spectra, which show the adsorption of

PVP/Pt nanoparticles into polished PVG (Figure 38), there is no distinct fluctuation with the polished the PVG.

Figures 48-50 show the radial distribution function of Ir foil and PVP/Ir nanoparticles before and after adsorption into polished PVG, respectively. The shapes of the strongest peaks are similar and closely resemble the Pt nanoparticles previously described. The Ir-Ir bond length extracted from the EXAFS spectra peak maximum is 2.04 ± 0.01 Å for Ir foil, 1.74 ± 0.01 Å for PVP/Ir nanoparticles before impregnation into PVG and 1.74 ± 0.01 Å for PVP/Ir nanoparticles adsorbed into polished porous Vycor glass. The bond lengths of 1.74 ± 0.01 Å for the PVP/Ir nanoparticles before and after impregnation into the PVG are smaller than the bond length of the Ir foil. This may be due to the small sizes of the PVP/Ir nanoparticles of 1.8 ± 0.3 nm in diameter and the larger surface area.

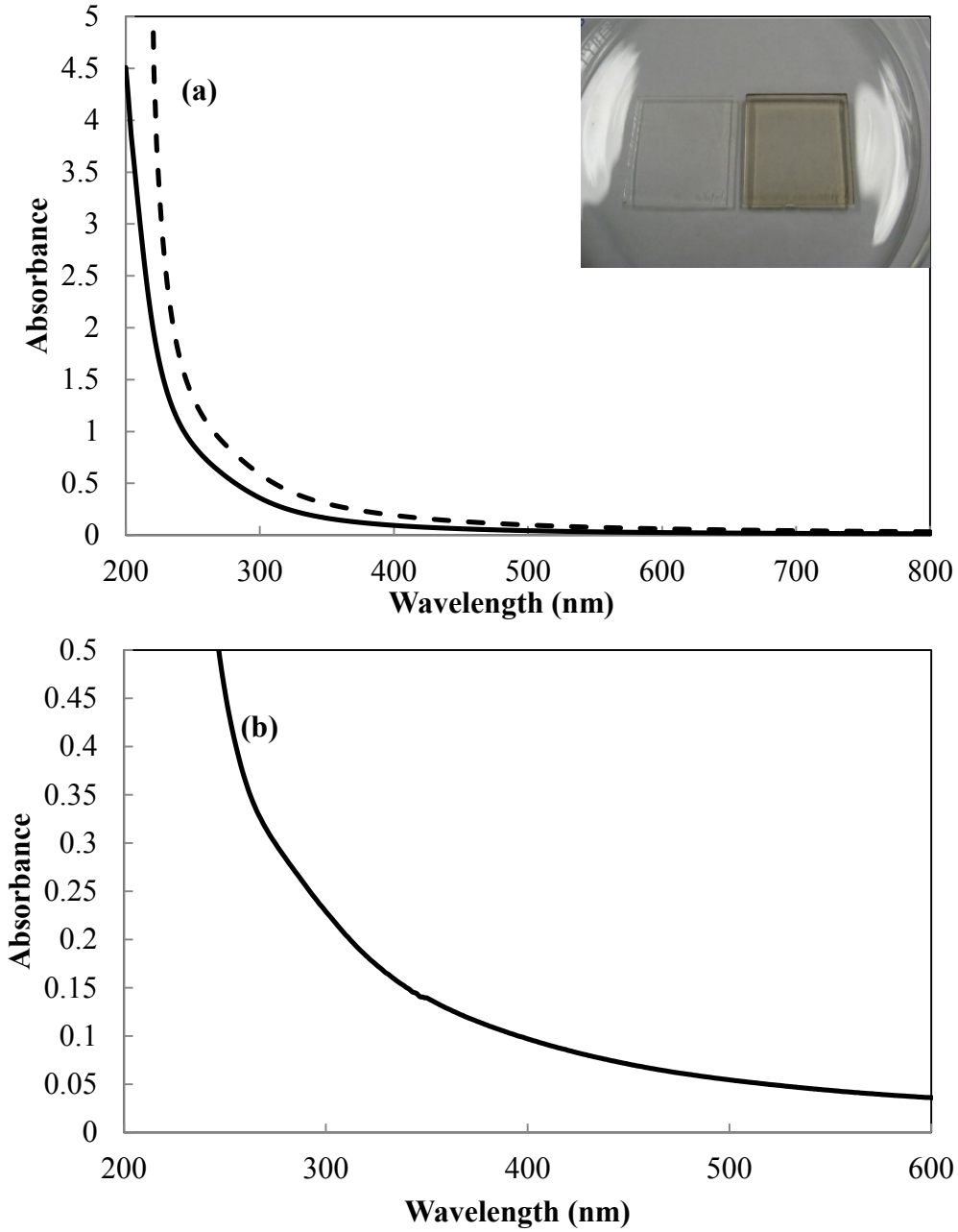

Figure 44. Absorption spectra of (a) PVG before (——) and after adsorption and drying (– – –) with PVP/Ir nanoparticles synthesized in ethanol. The inset shows the PVG sample before and after impregnation with the PVP/Ir nanoparticles. The difference spectrum (b) of the adsorbed PVP/Ir nanoparticles obtained by subtraction of the spectra shown above.

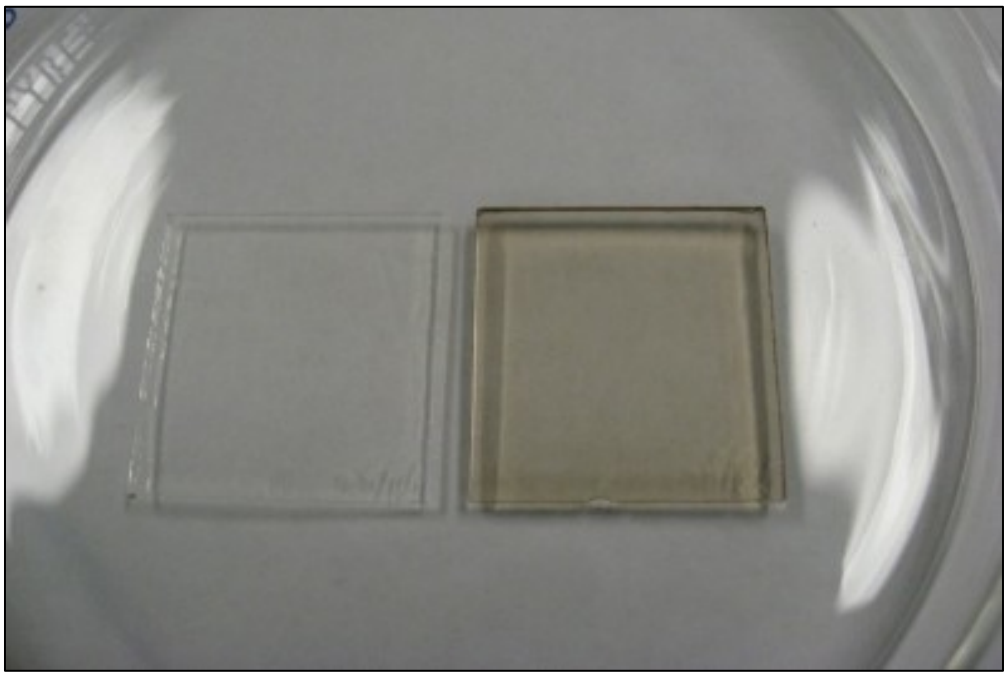

Figure 45. Image of clean PVG (left) and PVP/Ir nanoparticles synthesized in ethanol adsorbed into PVG (right).

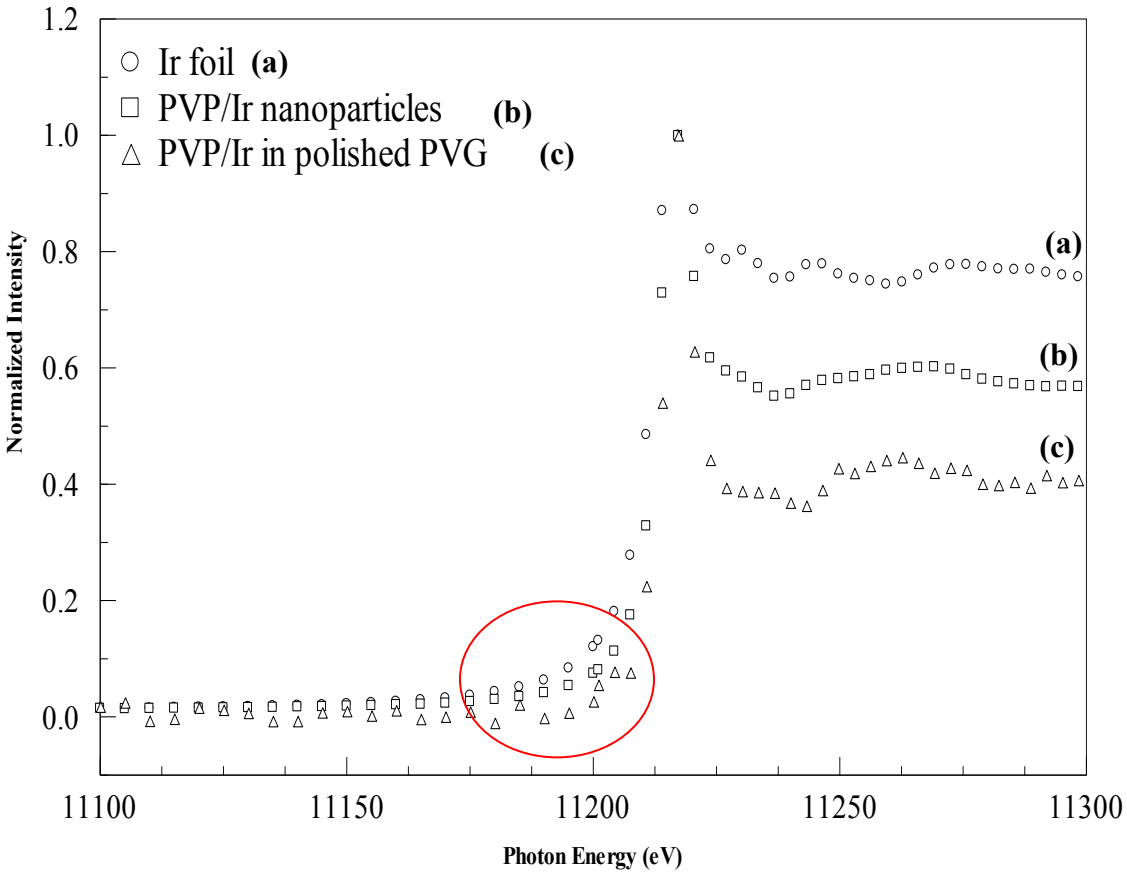

Figure 46. Normalized XANES spectra of (a) Ir foil (○), (b) PVP/Ir nanoparticles before impregnation into PVG (□), and (c) PVP/Ir nanoparticles after impregnation into polished PVG (Δ).

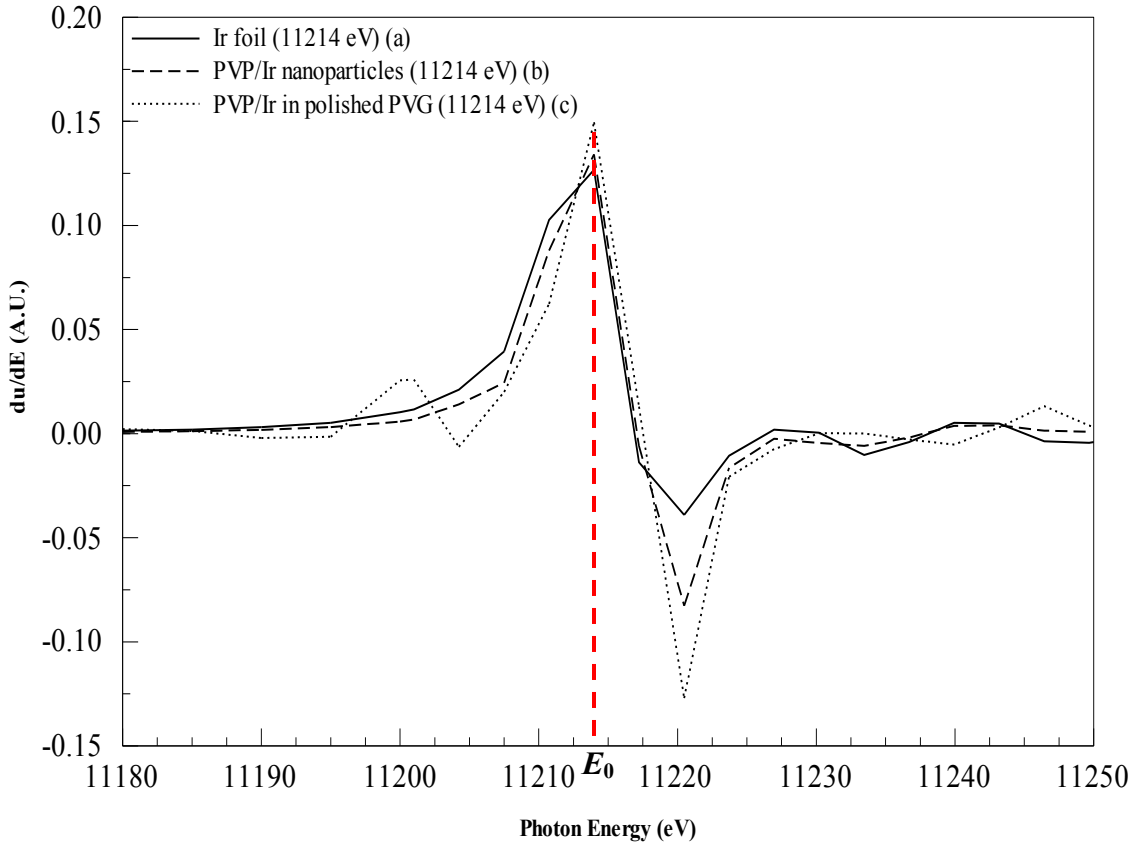

Figure 47. First derivative spectra of (a) Ir foil, (b) PVP/Ir nanoparticles before impregnation into polished PVG and (c) PVP/Ir nanoparticles after impregnation into polished PVG.

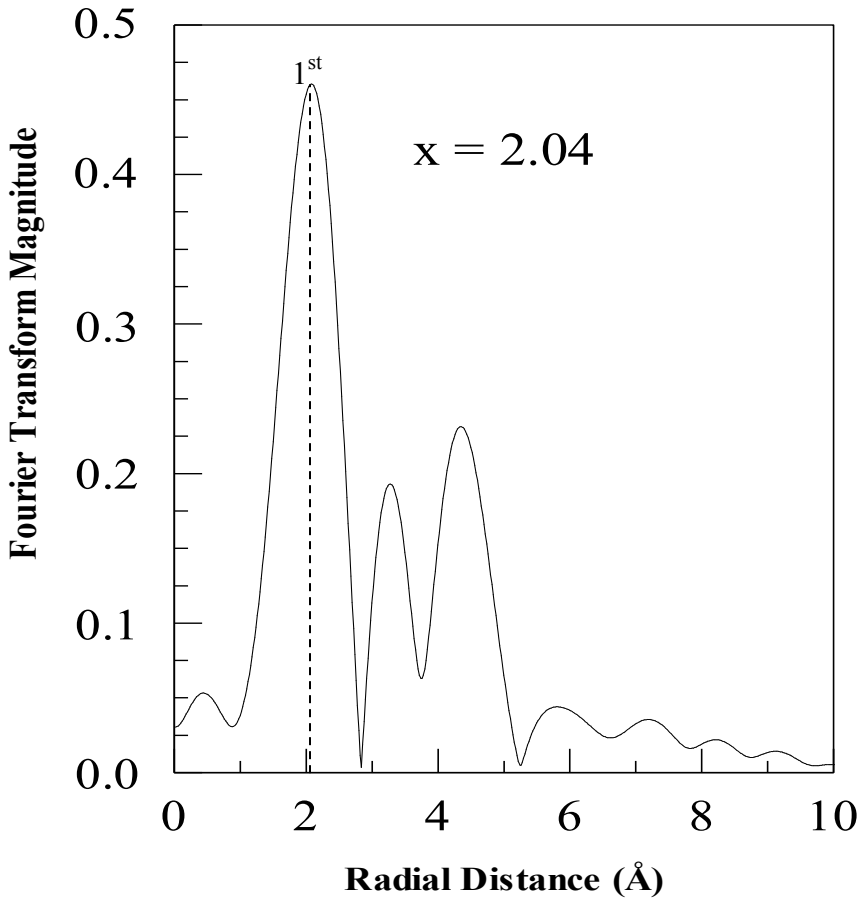

Figure 48. Fourier transform of the EXAFS data of Ir foil.

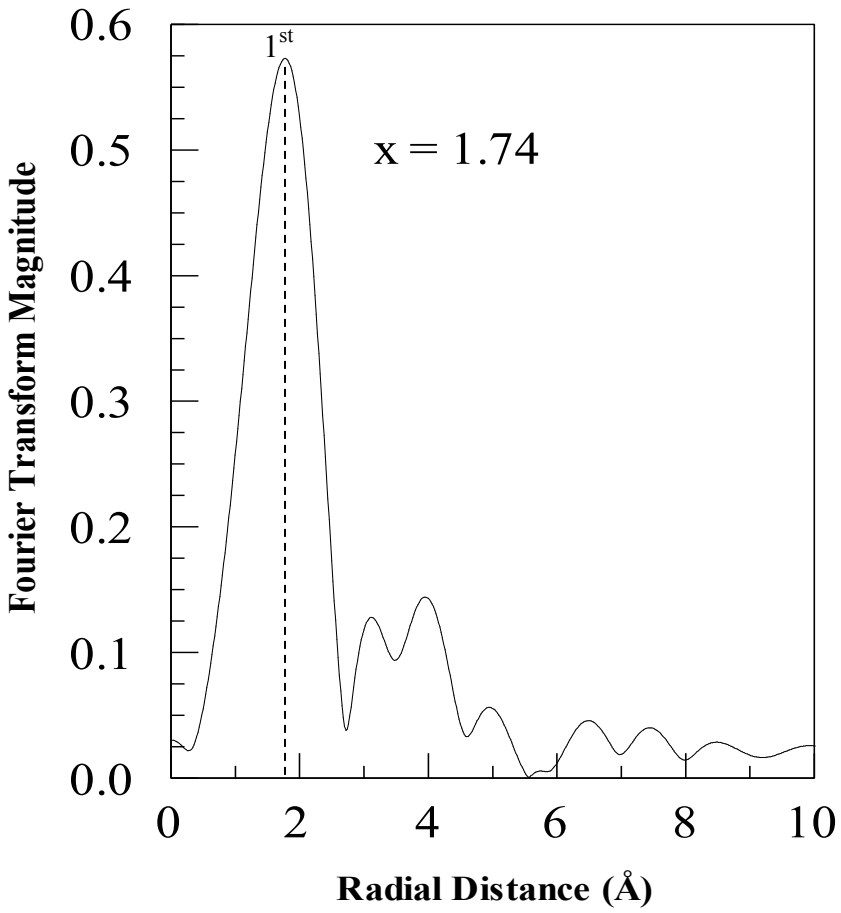

Figure 49. Fourier transform of the EXAFS data of PVP/Ir nanoparticles before adsorption into polished PVG.

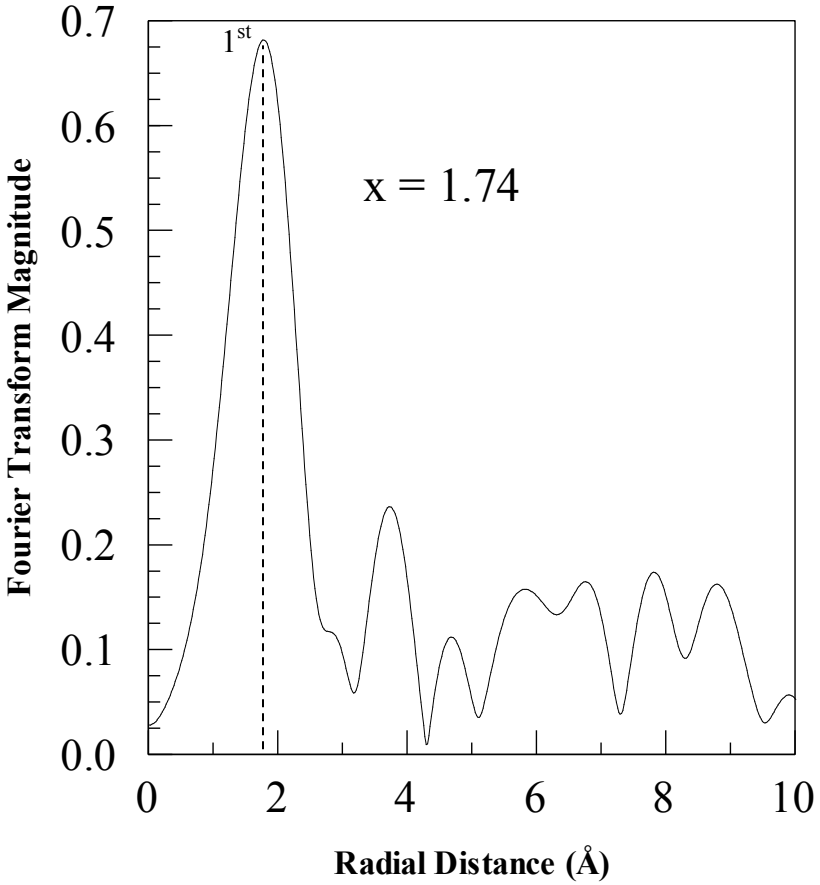

Figure 50. Fourier transform of the EXAFS data of PVP/Ir nanoparticles after adsorption into polished PVG.

3.4.4 PVP/Pt-Ir Nanoparticles

Absorption spectroscopy in the 200-800 nm wavelength region was used to examine the adsorbed nanoparticles. As found with both the PVP/Pt and PVP/Ir nanoparticles, the PVP/Pt-Ir nanoparticles embedded in the porous Vycor glass show a characteristic band at *ca.* 280 nm. Figure 51a shows the absorption spectra of porous Vycor glass before (solid line) and after impregnation (dashed line) with PVP/Pt-Ir nanoparticles. After subtracting the spectrum of PVG, a weak shoulder appeared around *ca.* 280 nm (Figure 51b) resembling the band of the individual Pt or Ir nanoparticles. An alloy of Pt-Ir foil (80:20 wt%, Alfa Aesar) was used as a reference material for comparison with PVP/Pt-Ir nanoparticles before and after adsorption into the PVG. The Pt-Ir foil was produced from an ingot of platinum and iridium, rolled to size and cut. Based on the bond length information obtained with Pt and Ir from the PVP/Pt-Ir nanoparticles, a conclusion can be reached on whether or not the PVP/Pt-Ir nanoparticles is a core-shell material, an alloy, or a mixture composed of two separate phases of platinum and iridium nanoparticles. The EXAFS of platinum and iridium were analyzed separately to prevent overlap from neighboring atom since the L_3-edge energy of platinum (11564 eV) and iridium (11215 eV) is close in proximity. The energy ranges of the platinum were truncated at 11600-11800 eV and iridium were truncated at 11250-11400 eV for data analysis.

The x-ray absorption spectra of Pt-Ir foil (80:20 wt%), PVP/Pt-Ir nanoparticles and PVP/Pt-Ir nanoparticles impregnated into the polished PVG are depicted in Figure 52. The PVP/Pt-Ir nanoparticles with and without the glass resembles the spectra

of the Pt-Ir foil, which confirms the presence of Pt-Ir nanoparticles and Pt-Ir nanoparticles embedded in the glass. Figure 53 illustrates the normalized XANES spectra of the Pt portion from PVP/Pt-Ir nanoparticles before and after adsorption into the polished porous Vycor glass. However, a gap or spacing is observed in the absorption edge region of 11540-11560 eV, circled in red, between the Pt portion from the Pt-Ir foil and the Pt portion from PVP/Pt-Ir nanoparticles in the XANES spectra. This may be due to small changes in the chemical environment. The edge energy (E_0) is 11563.0 ± 0.3 eV for Pt obtained from the first maximum of the first derivative spectrum (Figure 54). The Pt-Ir nanoparticle spectrum does not show any type of shift to higher energies or any pre-edge absorption when compared to the Pt-Ir foil. Figure 55 shows the radial distribution function of the Pt portion from the Pt-Ir foil absorption data and the Pt portion from the PVP/Pt-Ir nanoparticles absorption data before (Figure 56) and after adsorption (Figure 57) into polished PVG. The Fourier transform of the EXAFS data of the Pt portion from the Pt-Ir foil exhibit a bond length of 2.06 ± 0.01 Å obtained from the peak maximum shown by the dashed line, and has an exact bond length as the Pt foil previously mentioned. The Pt-Pt bond length for the PVP/Pt-Ir nanoparticles before adsorption into PVG is 2.04 ± 0.01 Å and after impregnation is also 2.04 ± 0.01 Å. The bond lengths are identical to the bond lengths of the individual Pt nanoparticles. The only difference in the Fourier transform spectra of the Pt portion from the Pt-Ir foil in Figure 55 to the individual Pt nanoparticles in Figure 41 is the absence of the second-neighbor shell. This consistency in the data analyses is remarkable, as it shows that Pt nanoparticles are

present in the sample being analyze with no change in the oxidation state of the Pt embedded in the silica matrix.

The Ir contribution from the PVP/Pt-Ir nanoparticles was also analyzed to determine if the iridium was oxidized and bonded to platinum or iridium. Figure 58 shows the XANES spectra of the Ir portion from PVP/Pt-Ir nanoparticles before and after adsorption into the porous Vycor glass. The edge energy (E_0) in the spectra of the Ir portion from the PVP/Pt-Ir nanoparticles with and without the PVG is 11214.0 ± 0.3 eV, also obtained from the first maximum of the first derivative spectra (Figure 59), and identical to the Ir portion from the Pt-Ir foil. So, there is no evidence of a pre-edge absorption or shift in the peak maximum to higher energies. Figures 60-62 show the radial distribution function of Ir from the Pt-Ir foil and the Ir particles from the PVP/Pt-Ir nanoparticles before and after adsorption into polished PVG, respectively. The Ir-Ir bond distance is 2.04 ± 0.01 Å for the Ir portion from the Pt-Ir foil, 1.74 ± 0.01 Å for the Ir portion from the PVP/Pt-Ir nanoparticles before adsorption into PVG and 1.74 ± 0.01 Å after adsorption in the glass. These Ir-Ir bond lengths of 1.74 ± 0.01 Å from the Pt-Ir nanoparticles before and after impregnation into PVG are identical to the Ir-Ir bond length of the individual Ir of 1.74 ± 0.01 Å from the PVP/Ir nanoparticles before and after impregnation into the polished PVG (Figures 49 and 50). The only difference in the Fourier transform spectra of Ir in Figure 60 to the individual Ir nanoparticles in Figure 49 is the magnitude of the second-neighbor shell and higher ordered shells is higher.

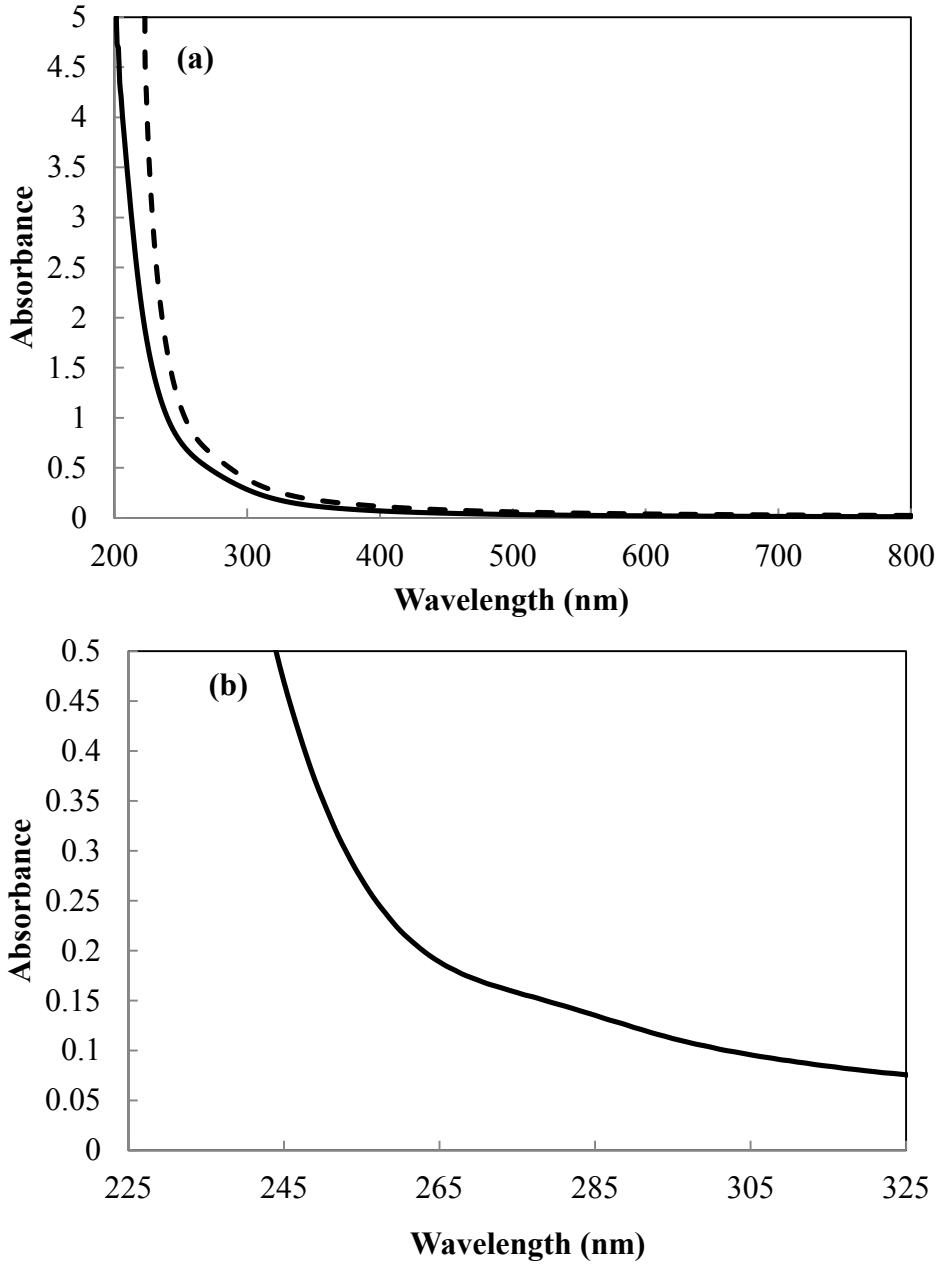

Figure 51. Absorption spectra of (a) PVG before (——) and after impregnation and drying (– – –) with PVP/Pt-Ir nanoparticles synthesized in ethanol. The difference spectrum (b) of the adsorbed PVP/Pt-Ir nanoparticles obtained by subtraction of the spectra shown above.

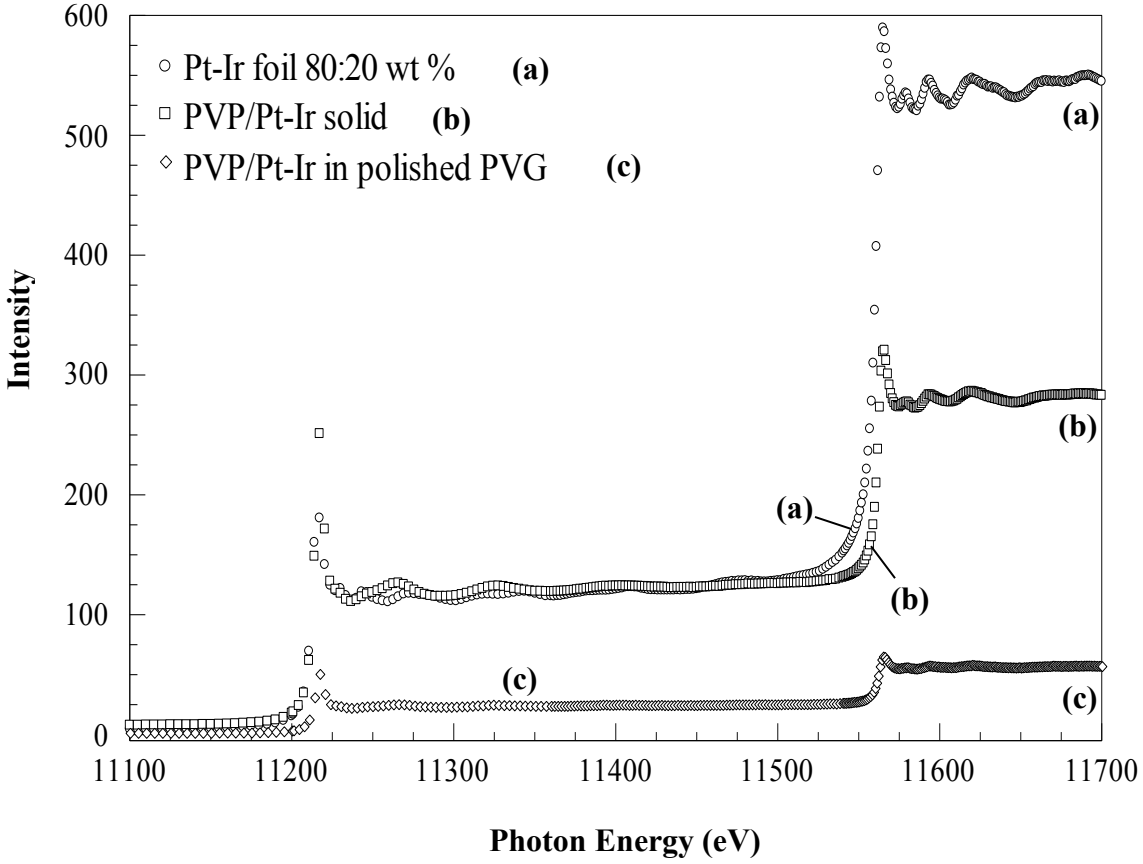

Figure 52. X-ray absorption (XANES and EXAFS) spectra of (a) Pt-Ir foil (○), (b) PVP/Pt-Ir before adsorption into PVG (□) and (c) PVP/Pt-Ir nanoparticles impregnated into polished PVG (◇).

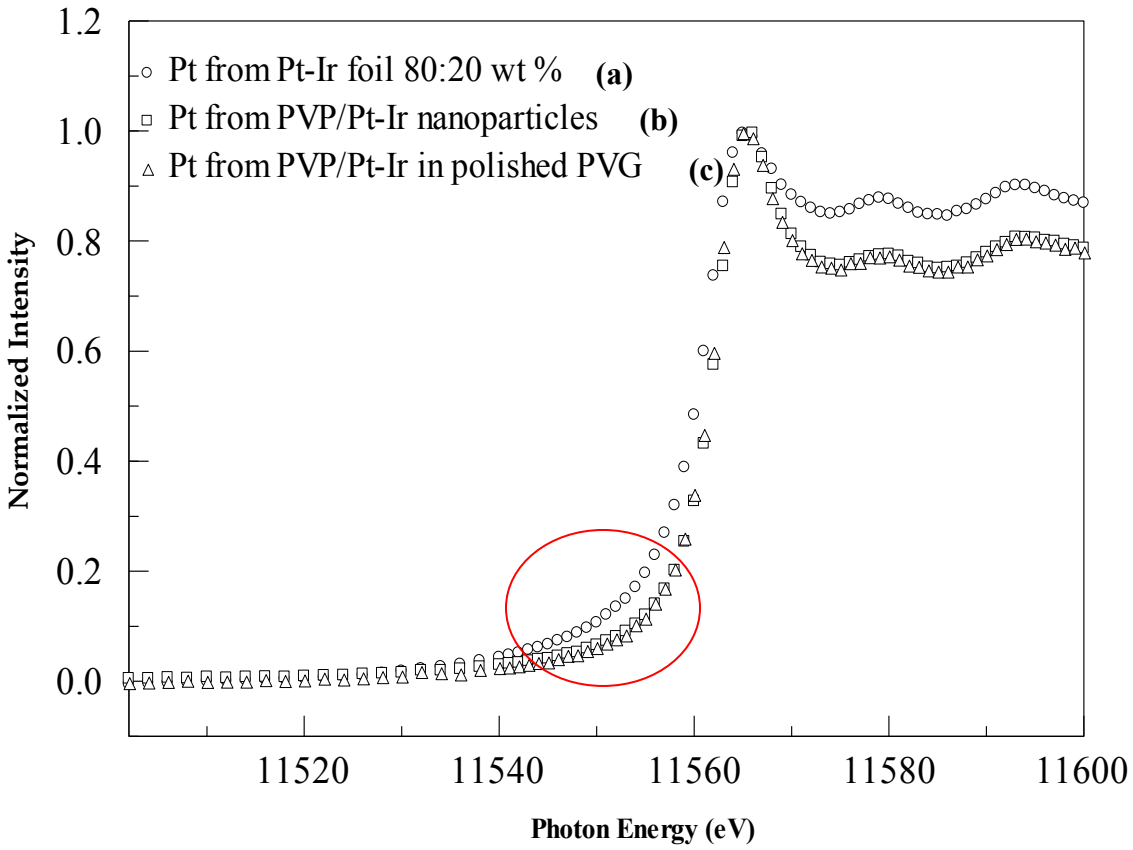

Figure 53. Normalized XANES spectra of (a) Pt portion from the Pt-Ir foil (○), (b) Pt portion from the PVP/Pt-Ir nanoparticles before impregnation into PVG (□) and (c) Pt portion from PVP/Pt-Ir nanoparticles after adsorption into polished PVG (Δ).

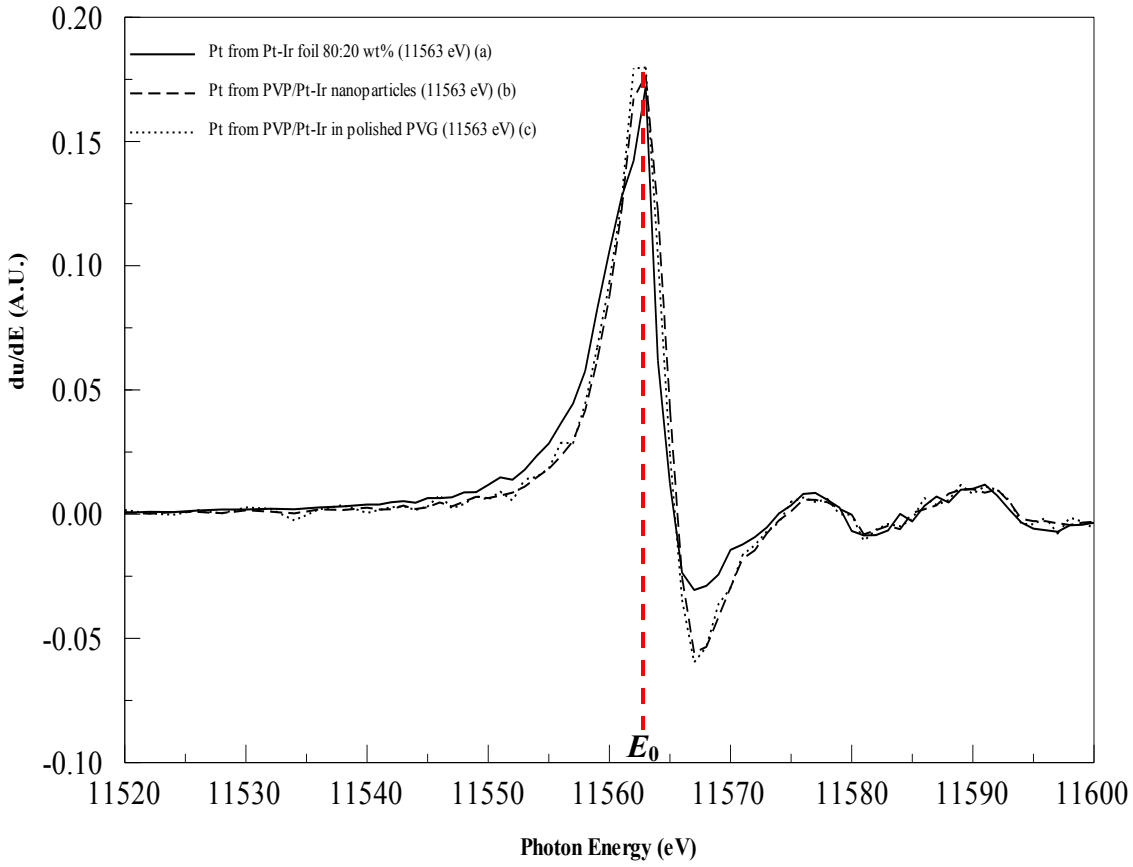

Figure 54. First derivative spectra of (a) Pt portion from the Pt-Ir foil, (b) Pt portion from the PVP/Pt-Ir nanoparticles before impregnation into PVG and (c) Pt portion from PVP/Pt-Ir nanoparticles after adsorption into polished PVG.

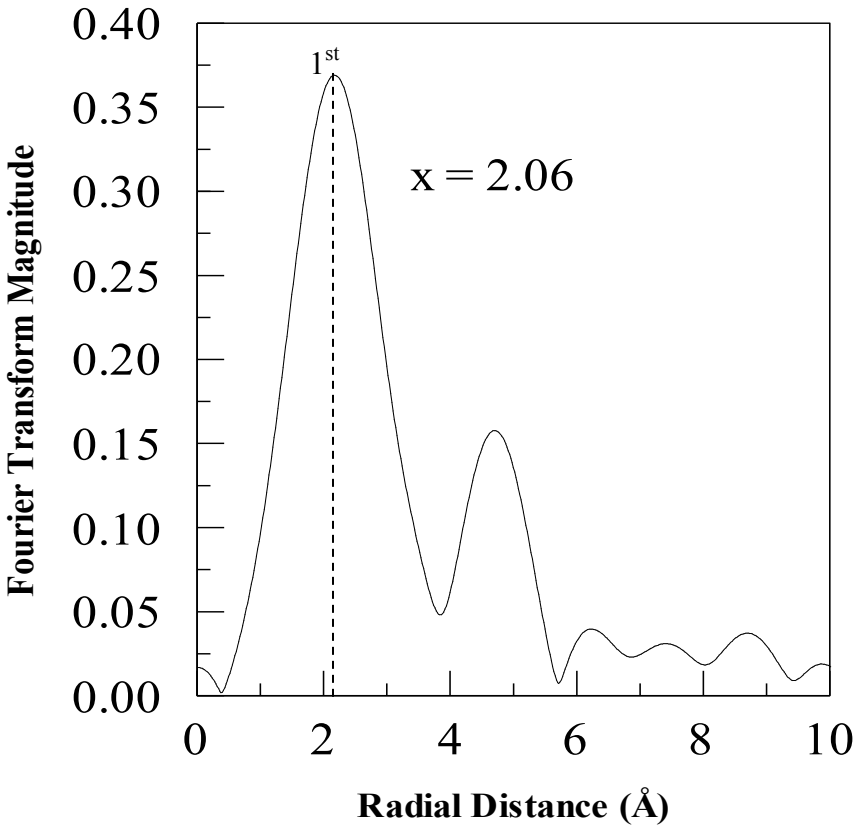

Figure 55. Fourier transform of the EXAFS data of the Pt portion from Pt-Ir foil (80:20 wt%).

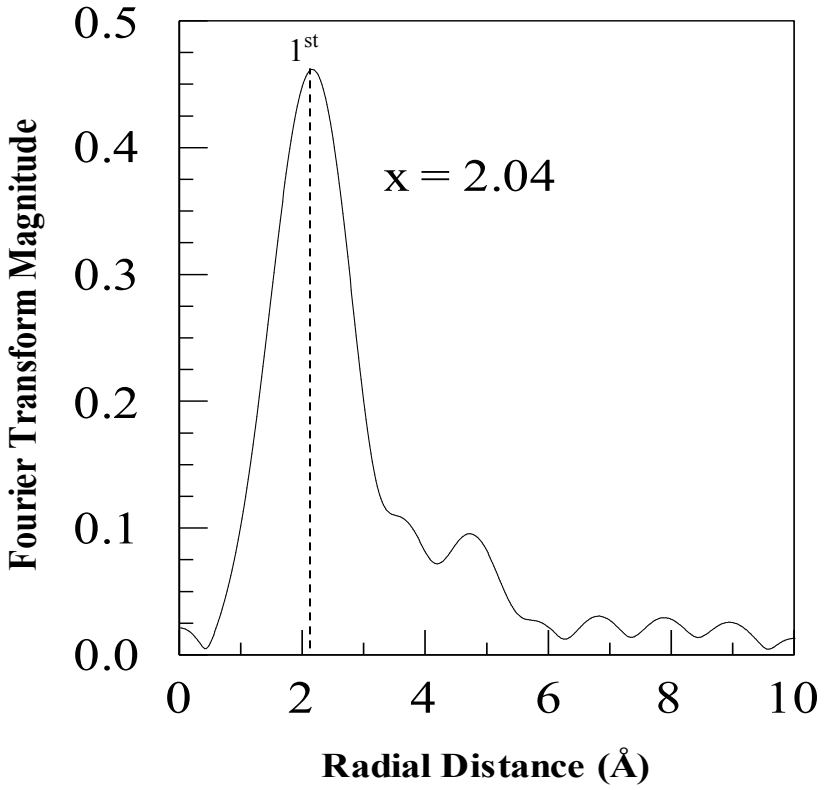

Figure 56. Fourier transform of the EXAFS data of the Pt portion from PVP/Pt-Ir nanoparticles before adsorption into polished PVG.

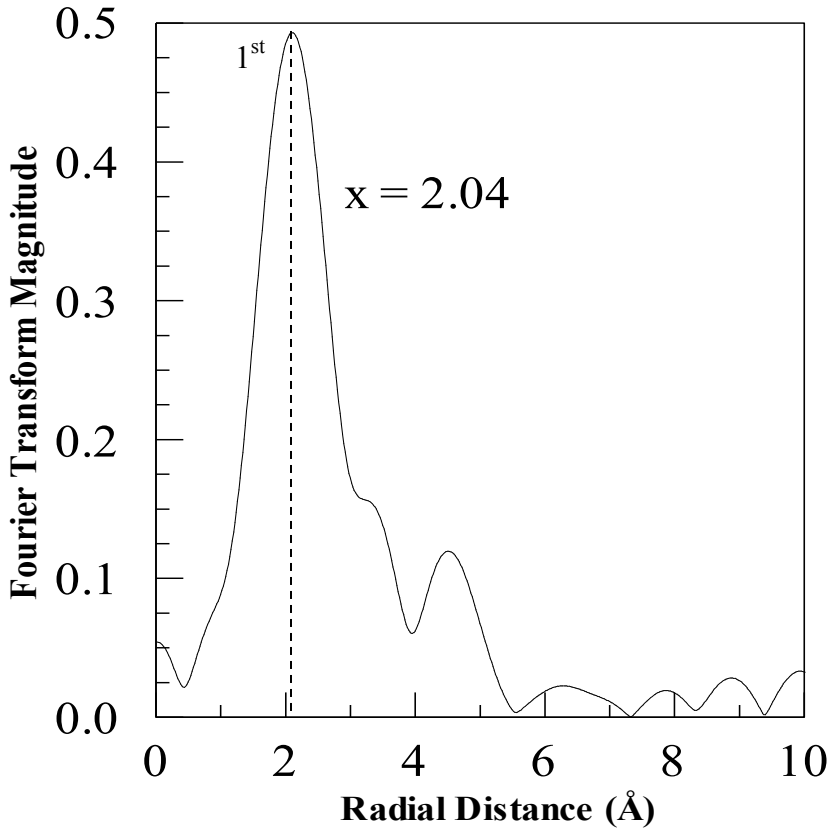

Figure 57. Fourier transform of the EXAFS data of the Pt portion from PVP/Pt-Ir nanoparticles after adsorption into polished PVG.

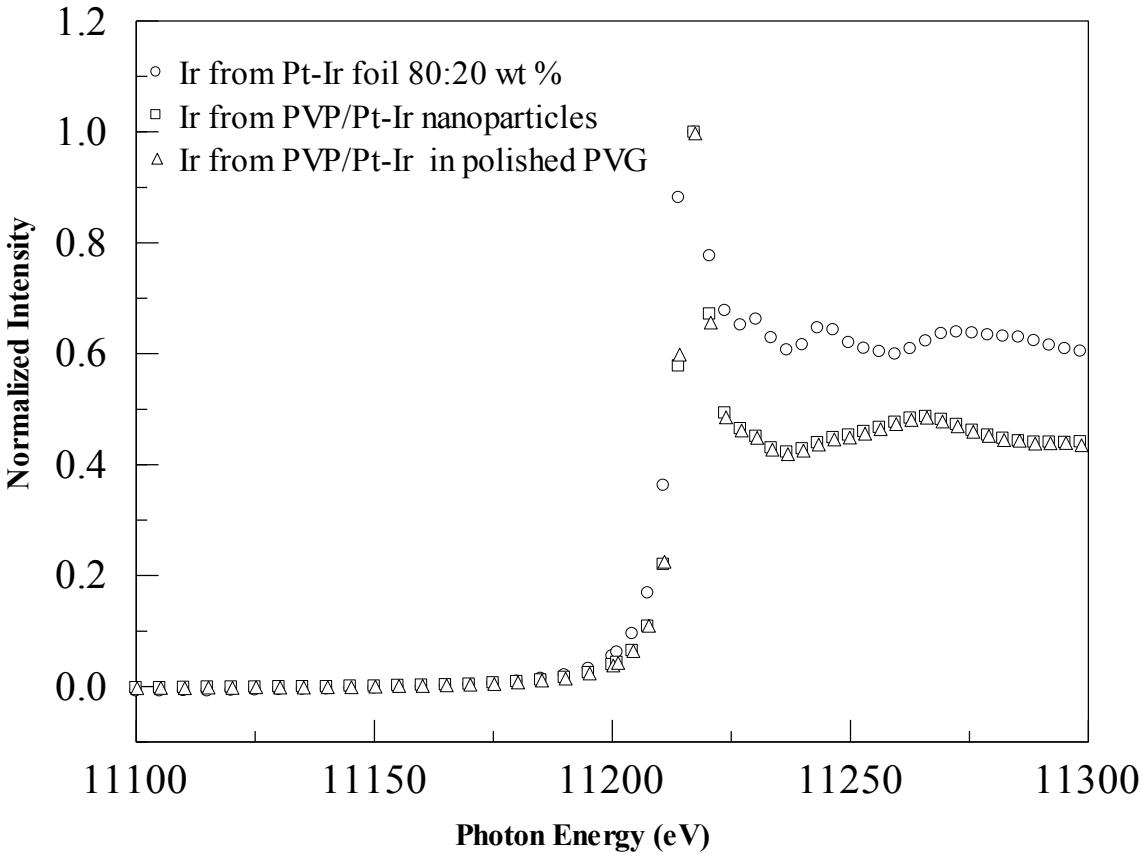

Figure 58. Normalized XANES spectra of Ir portion from the Pt-Ir foil (○), Ir portion from PVP/Pt-Ir nanoparticles before (□) and after adsorption into polished PVG (Δ).

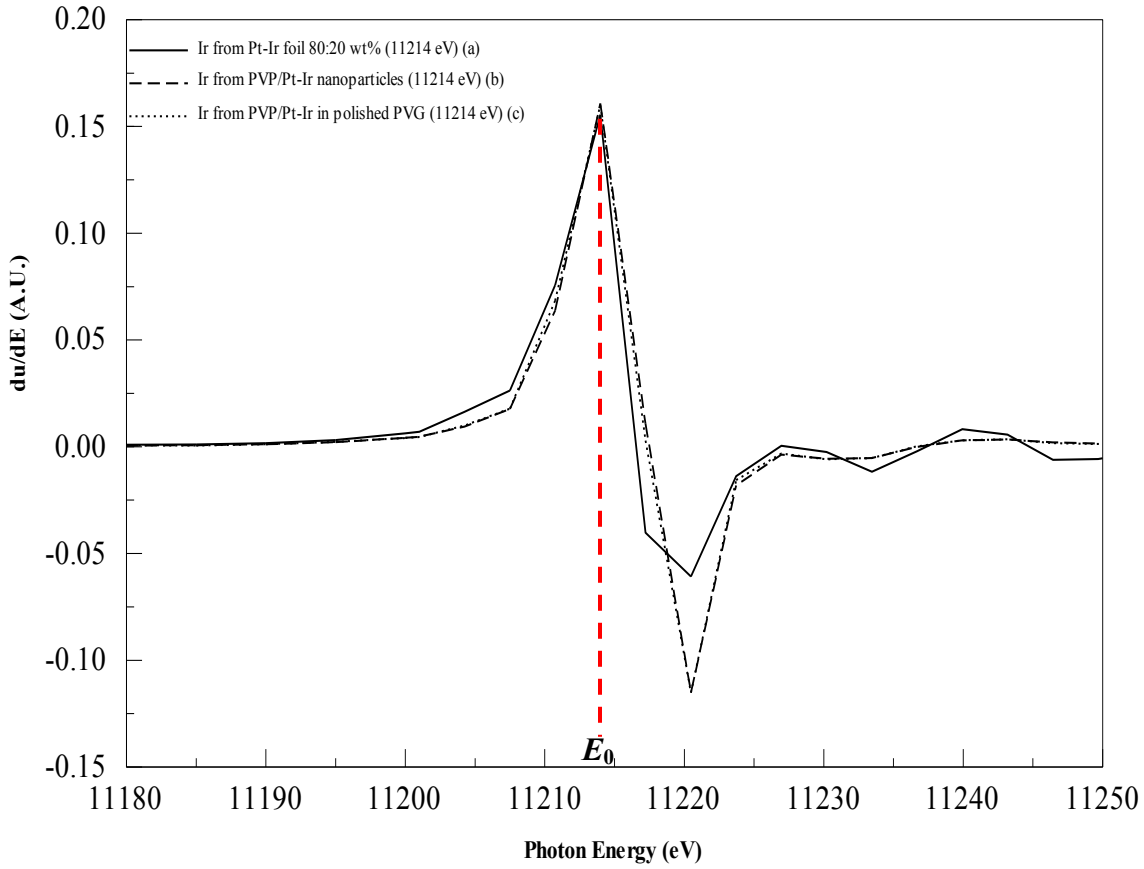

Figure 59. First derivative spectra of (a) Ir portion from the Pt-Ir foil, (b) Ir portion from the PVP/Pt-Ir nanoparticles before impregnation into PVG and (c) Ir portion from PVP/Pt-Ir nanoparticles after adsorption into polished PVG.

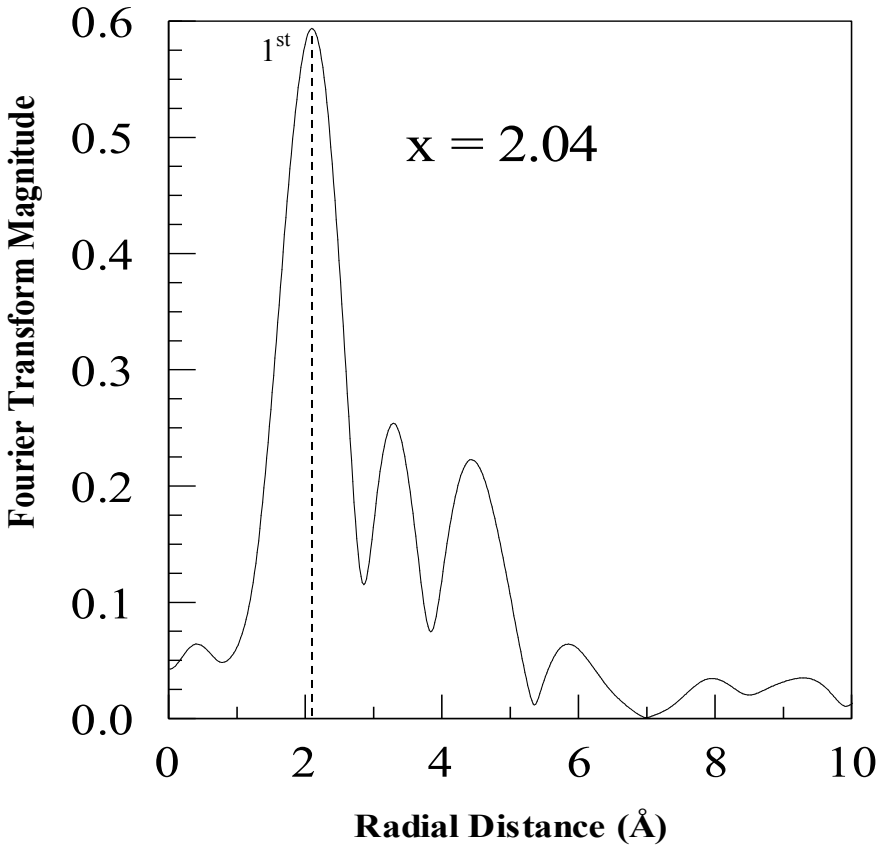

Figure 60. Fourier transform of the EXAFS data of the Ir portion from Pt-Ir foil (80:20 wt%).

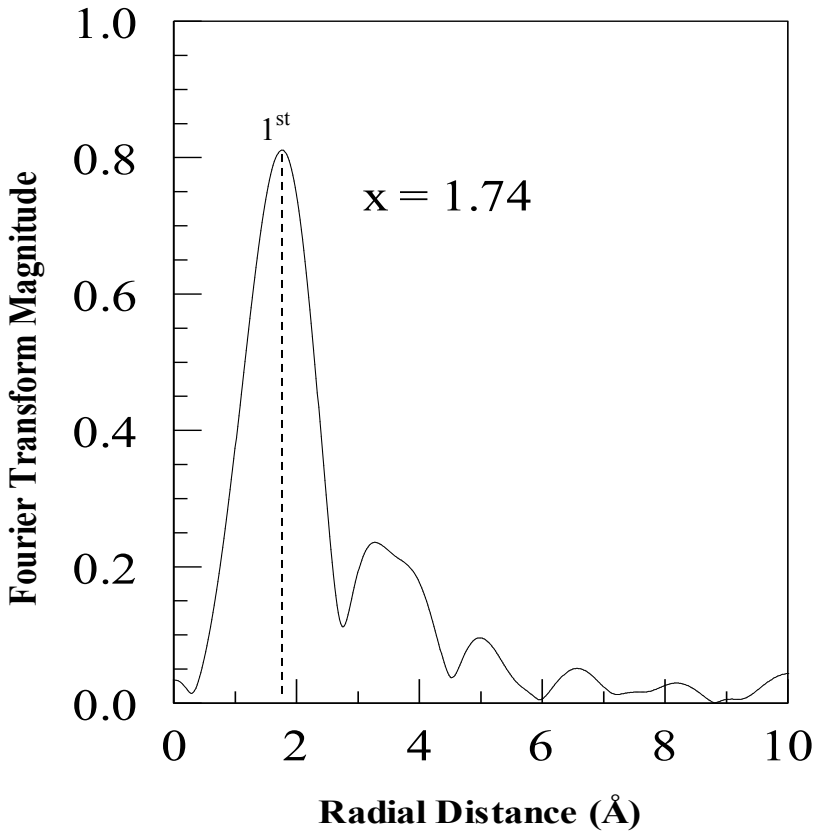

Figure 61. Fourier transform of the EXAFS data of the Ir portion from PVP/Pt-Ir nanoparticles before adsorption into polished PVG.

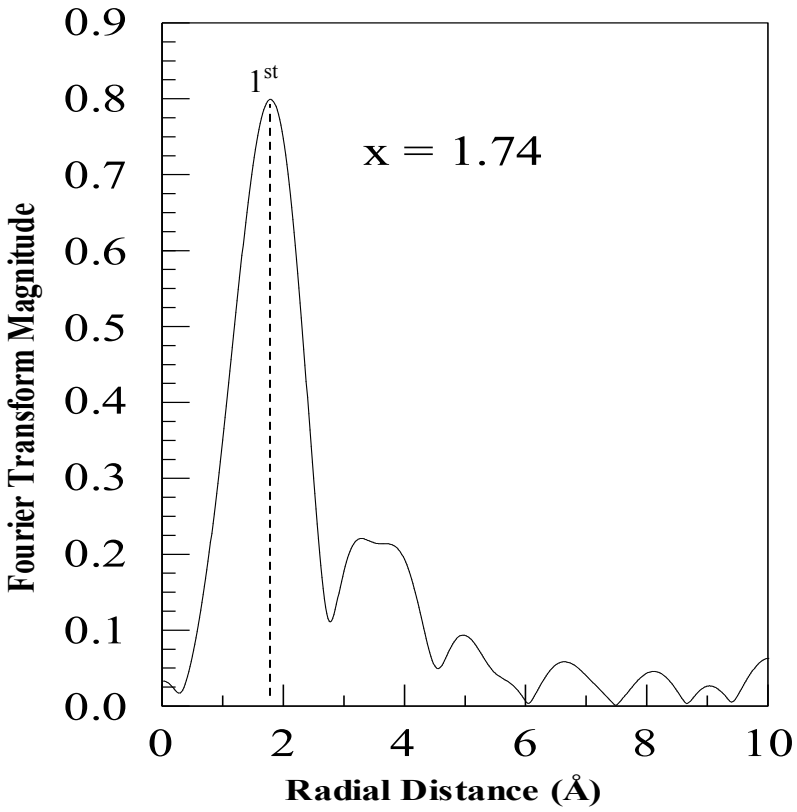

Figure 62. Fourier transform of the EXAFS data of the Ir portion from PVP/Pt-Ir nanoparticles after adsorption into polished PVG.

3.5. PVP removal from adsorbed PVP/Pt nanoparticles in PVG

The amount of Pt nanoparticles present in 15 ml PVP/Pt (synthesized in methanol) stock solution is 5.12 x 10^{-6} g. The amount was calculated using the initial concentration of 6.58 x 10^{-7} M (Table I) of the Pt nanoparticles multiplied by the volume of 0.2 liter of the reaction solution and the molecular weight of 517.91 g/mol of the Pt^{4+} salt. The amount of Pt nanoparticles adsorbed into the PVG could not be determined spectroscopically because no distinct absorption band attributable to the nanoparticles beyond the absorption of PVG is present in the spectrum. Nonetheless, impregnation causes the PVG samples to become light brown which clearly establishes that the nanoparticles adsorbed into PVG. Our goal was to create a stable matrix for the PVP/Pt nanoparticles, so by accomplishing the impregnation of PVP/Pt nanoparticles in the porous Vycor glass, we focused on stripping off the polymer. We wanted to determine if the presence of the PVP cap on the nanoparticles would hinder their reactivity, specifically their interaction with Ru(II) diimines complexes. And more specifically, if we removed the PVP surfactant from around the Pt adsorbed in PVG, will the Pt coordinate to a diimine ligand?

If a shift to higher energy is seen when compared to the Pt foil, the oxidation state of the Pt particles in the PVG and after PVP removal will increase. EXAFS and XANES measurement on the PVP/Pt nanoparticles in the porous Vycor glass and after PVP removal were measured with Pt foil as a standard. Pt foil, which has an oxidation state of zero, was used for comparison with the PVP/Pt nanoparticles produced to confirm the presence of Pt^0 and to determine the Pt-Pt bond length. After adsorption of the PVP/Pt

nanoparticles into Corning's code 7930 porous Vycor glass, the PVG was placed inside a small Soxhlet extraction apparatus (Chemglass) connected to a condenser (Chemglass) and a round bottom flask (Sigma Aldrich) with a heating mantle (Glas-Col) and a power controller (Glas-Col). A 100 ml aliquot of distilled water was placed in the round bottom flask, heated to reflux, and the samples extracted for a total of 4 days. As the water is heated, the vapor goes up the distillation arm of the Soxhlet apparatus and condenses back down into the extraction thimble holding the PVG sample. When the bottom of the extraction apparatus holding the sample is filled with water, a siphon is created and the water goes up the side arm of the extraction apparatus and is emptied back into the round bottom flask. The cycling process is repeated many times until heating is stopped.

The extracted PVP contained in the round bottom flask was placed into an evaporation dish and dried in air. The dried PVP extracted was scraped out with a spatula, collected and weighed. The extraction procedure was repeated twice. Even though more PVP was isolated after the second extraction, the amount extracted did not decline as expected. Instead the weight of the PVP isolated did not decrease with each extraction, but the apparent weight of PVP increased and decreased. In addition to the variation in the amount of PVP extracted, the total weight of PVP extracted exceeded the amount of PVP used in the preparation of the nanoparticles clearly indicating a problem.

Figure 63 shows the normalized XANES spectra of the Pt foil L_{III}-edge in which the oxidation state is zero and the Pt adsorbed into PVG before and after removal of the PVP surfactant. The XANES region is the rise in absorption coefficient at 50 eV before and 50 eV after the Pt L_{III}-edge absorption region.[116] The absorption region between

11540-11555 eV in the XANES spectra of the PVP/Pt nanoparticles impregnated into the rolled PVG before PVP removal, shows some fluctuations in the data points, circled in red. This fluctuation is also due to experimental error, because the same piece of rolled glass was used for the extraction of the PVP from the adsorbed PVP/Pt nanoparticles in PVG, and there are no visible fluctuations in the XANES spectra after PVP removal.

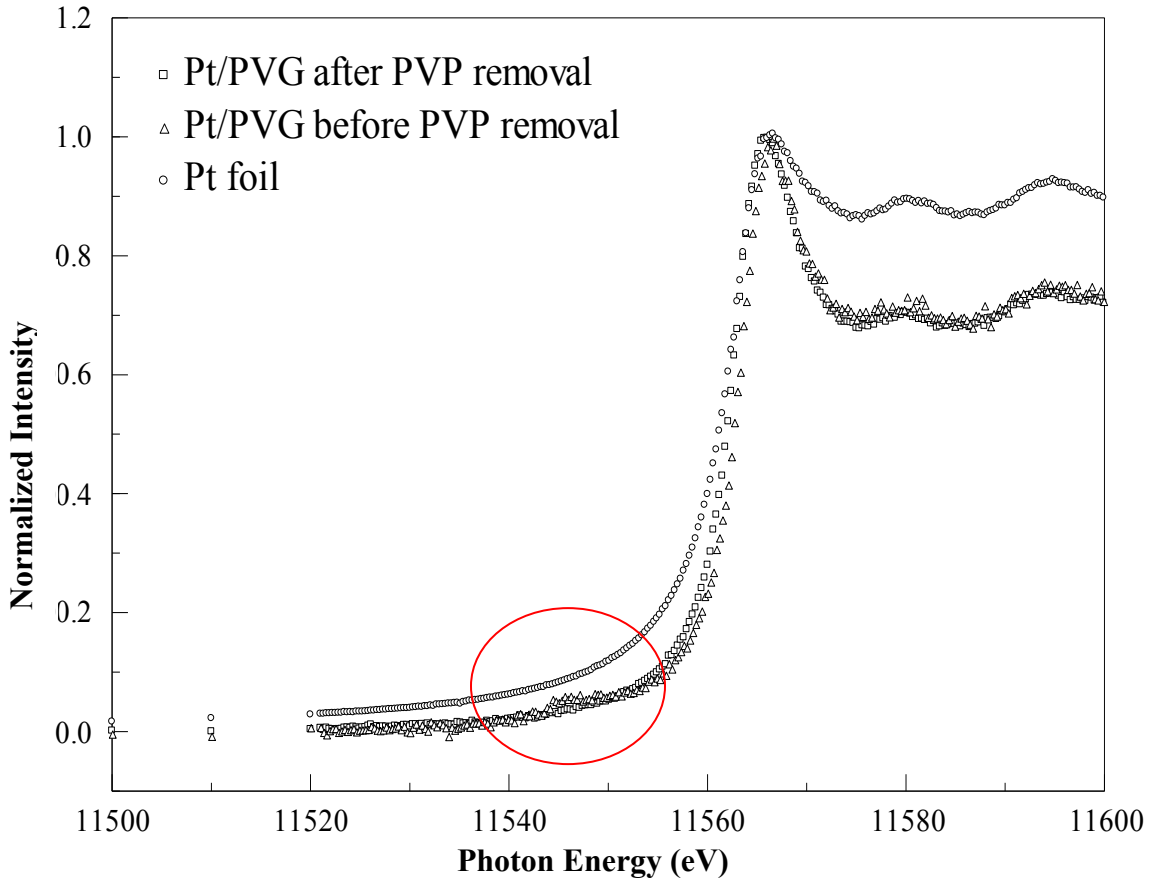

Figure 63. Normalized XANES spectra of PVP/Pt nanoparticles in PVG before (Δ) and after (□) PVP removal when compared to Pt foil (○).

The edge energy (E_0) is 11563.0 ± 0.3 eV for all three samples displayed in Figure 64, which indicates that there is no shift to higher energies of the peak maximum in the derivative spectra. The experimental EXAFS values for the average Pt-Pt bond length of

the Pt in the Pt foil is 2.06 ± 0.01 Å (Figure 40) and 2.04 ± 0.01 Å for the Pt nanoparticles in the PVP/Pt adsorbed into PVG (Figures 42 and 43). The Pt-Pt bond distance of PVP/Pt nanoparticles in the PVG after PVP removal is 2.02 ± 0.01 Å (Figure 65), which is within experimental error of the Pt-Pt distance in the PVP/Pt nanoparticles prior to PVP extraction.

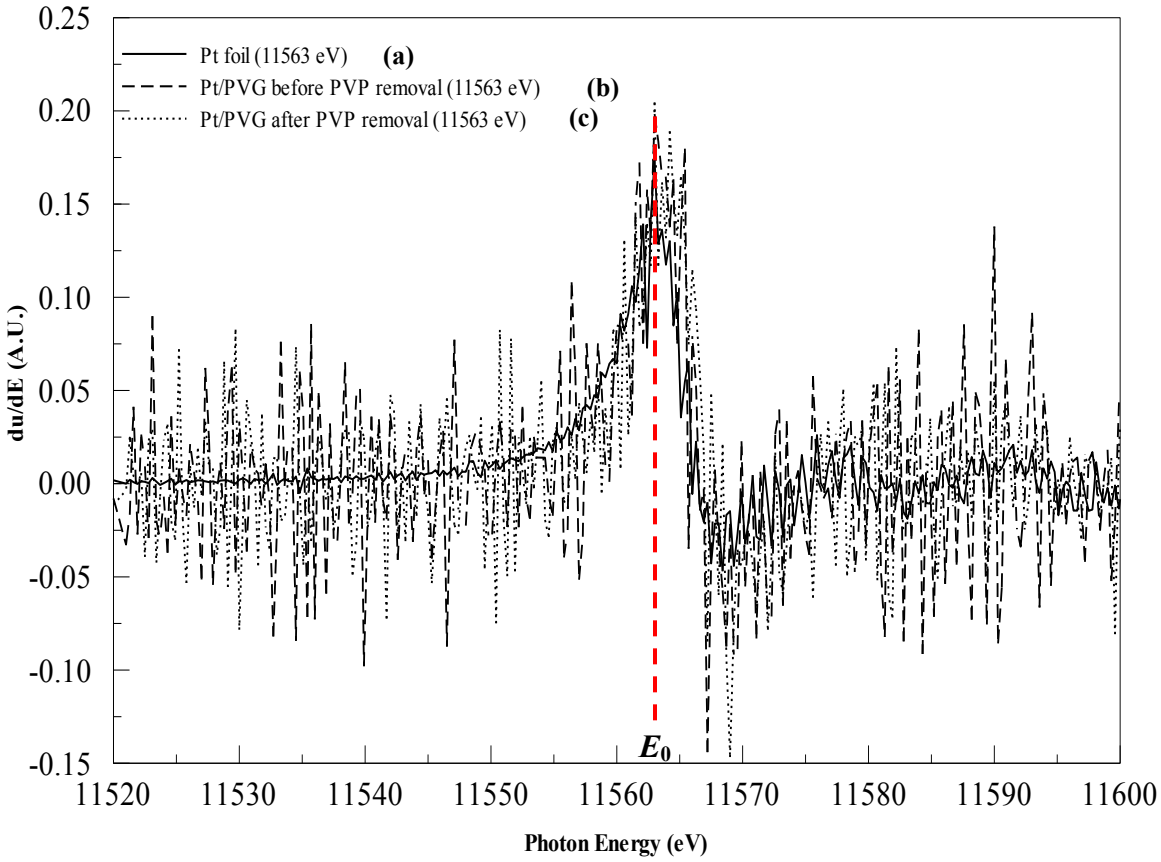

Figure 64. First derivative spectra of (a) Pt foil, (b) PVP/Pt nanoparticles impregnated into rolled PVG before PVP removal and (c) PVP/Pt nanoparticles impregnated into rolled PVG after PVP removal.

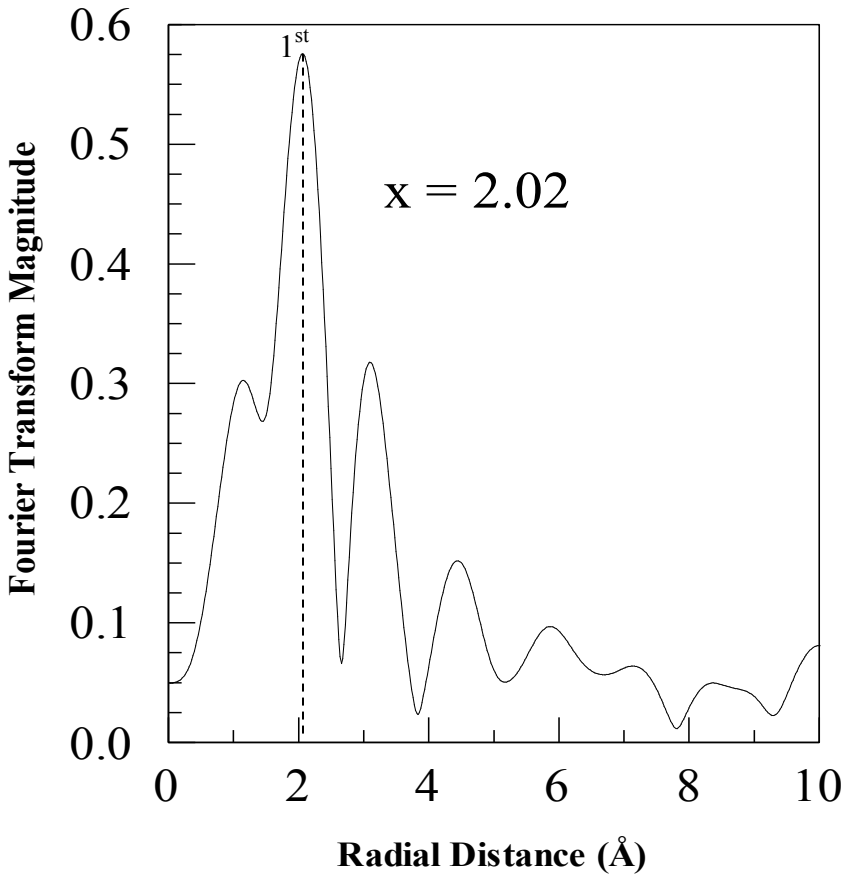

Figure 65. Fourier transform of the EXAFS data of PVP/Pt nanoparticles in rolled PVG after PVP removal.

To determine the degree of aggregation of the Pt nanoparticles, the UV-vis absorption spectra were recorded before and after extraction. Figure 66 shows the electronic spectra of PVP/Pt nanoparticles adsorbed into the PVG (solid line) and after removal of the PVP (dashed line) by water extraction. Absorption spectra show a broad shoulder at *ca.* 280 nm, similar to that present in the PVP/Pt nanoparticles after their preparation (Figure 13), indicating the formation of Pt clusters.[114,115]

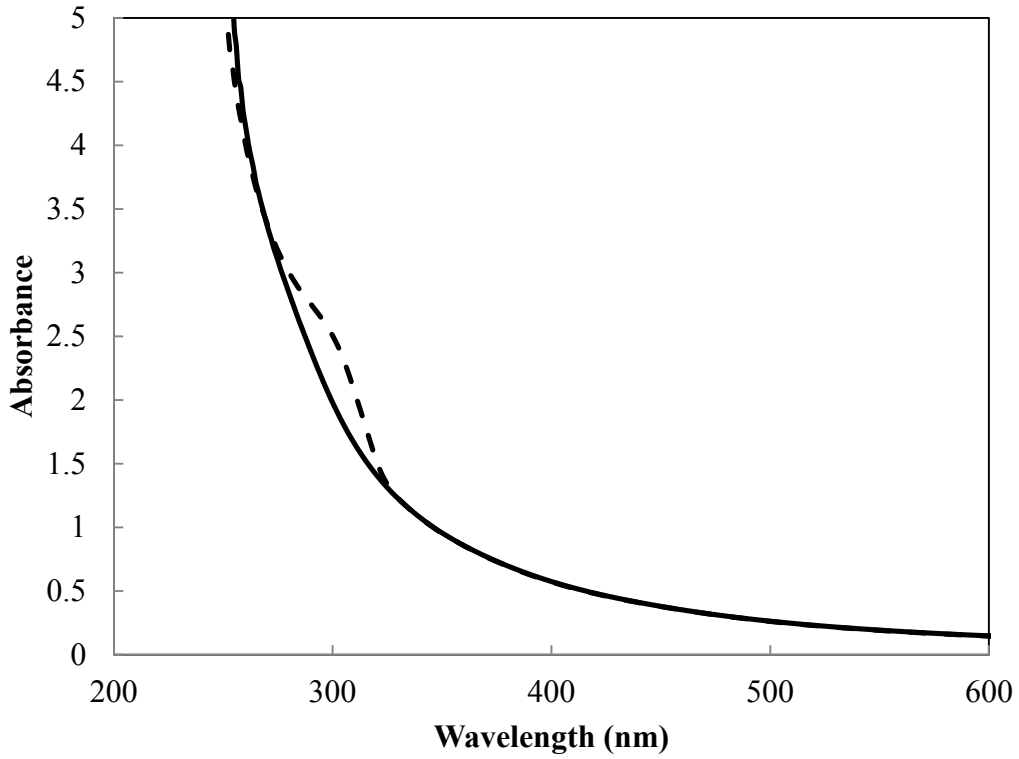

Figure 66. Absorption spectra of PVP/Pt nanoparticles in PVG before (——) and after (– – –) PVP extraction.

To identify and resolve the problem with the increased weight of the so-called dried PVP, FTIR spectroscopy was applied. Figure 67 shows the FTIR spectra of the extracted PVP and pure PVP. FTIR spectra detected CH (~1376 cm^{-1}), CH_2 (~1460 cm^{-1}), C-N (~1490 cm^{-1}), and C=O vibrations. The pure PVP has a medium intensity vibration at 1668 cm^{-1} which corresponds to the υ(C=O) stretch.[105] The extracted PVP shows a carbonyl shifted from 1668 to 1632 cm^{-1}. The shift of the carbonyl absorption is due to hydrogen bonding,[119] suggesting that the extracted PVP was absorbing water from the atmosphere. Indeed, heating the extracted PVP confirmed that the increased weight is due to water adsorption.

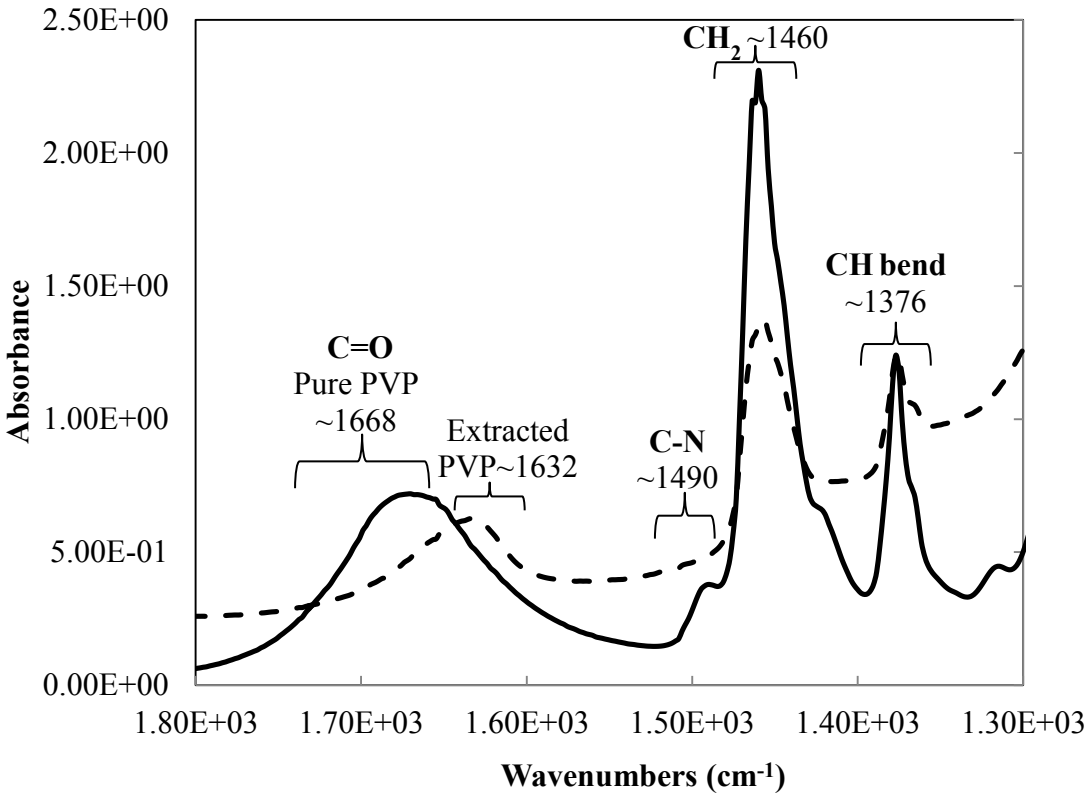

Figure 67. IR spectra of extracted PVP (- - -·) *vs.* pure PVP (——).

To quantitate the amount of PVP extracted, the absorbed water had to be removed. Because PVP is hygroscopic[19] and therefore has the capability to absorb water from the atmosphere, after the initial drying under air, the extracted PVP was placed in a vacuum oven and heated at 50 ^{o}C for five days. Table II summarizes the weight of the empty crucible and the weight of the wet PVP.

Table II. Extracted PVP heated at 50 ^{o}C vacuum oven after 5 days

Sample #	Wt. of empty crucible (g)	Wt. of crucible and PVP (g)	Wt. of extracted PVP (g)	Wt. crucible and extracted PVP after 5 days @ 50^{o}C in vacuum oven (g)	Wt. of extracted PVP (g) after drying	% Extracted PVP
Pt/meth in rolled PVG						
PVG 1	11.7311	11.7487	0.0176	11.7359	0.0048 ± 0.0004	48 ± 4
PVG 20	11.9137	11.9256	0.0119	11.9194	0.0057 ± 0.0004	57 ± 4
PVG 25	12.0031	12.0164	0.0133	12.0075	0.0044 ± 0.0004	44 ± 4
PVG 26	11.2733	11.2809	0.0076	11.2780	0.0047 ± 0.0004	47 ± 4
PVG 28	10.5498	10.5622	0.0124	10.5549	0.0051 ± 0.0004	51 ± 4
					0.0049 ± 0.0004	**49 ± 4**

After drying the PVP, the average weight of the PVP extracted from five pieces of rolled PVG were measured to be 0.0049 ± 0.0004 g. Since previous studies show that PVP can be heated to 70 ^{o}C without decomposition,[119] the extracted PVP was heated again in the vacuum oven (Precision by GCA Corporation, Model 29) for a period of 9 and 10 days but at 70 ^{o}C, until it achieved a constant weight (Tables III and IV). After drying the PVP at 70 ^{o}C, the average weight of the extracted PVP was 0.0046 ± 0.0004 g. These studies show that the water was removed when more heat was applied at a longer period.

Table III. Extracted PVP heated at 70 ^{o}C in a vacuum oven after 9 days

Sample #	Wt. crucible and extracted PVP after 9 days @ 70 ^{o}C in vacuum oven (g)	Wt. of extracted PVP (g) after drying	% Extracted PVP
Pt/meth rolled PVG			
PVG 1	11.7357	0.0046 ± 0.0004	46 ± 4
PVG 20	11.9190	0.0053 ± 0.0004	53 ± 4
PVG 25	12.0073	0.0042 ± 0.0004	42 ± 4
PVG 26	11.2777	0.0044 ± 0.0004	44 ± 4
PVG 28	10.5544	0.0046 ± 0.0004	46 ± 4
		0.0046 ± 0.0004	**46 ± 4**

Table IV. Extracted PVP heated at 70 ^{o}C in a vacuum oven after 10 days

Sample #	Wt. crucible and extracted PVP after 10 days @ 70 ^{o}C in vacuum oven (g)	Wt. of extracted PVP (g) after drying	% Extracted PVP
Pt/meth rolled PVG			
PVG 1	11.7357	0.0046 ± 0.0004	46 ± 4
PVG 20	11.9190	0.0053 ± 0.0004	53 ± 4
PVG 25	12.0072	0.0041 ± 0.0004	42 ± 4
PVG 26	11.2777	0.0044 ± 0.0004	44 ± 4
PVG 28	10.5542	0.0044 ± 0.0004	46 ± 4
		0.0046 ± 0.0004	**46 ± 4**

To be certain that a sufficient amount of the water was removed, a final heating at 70 ^{o}C of the extracted PVP was performed under vacuum for a total of 13 days. The dried extracted PVP produced a weight of 0.0046 ± 0.0004 g which confirmed that a constant weight was achieved, and the maximum amount of water removed from the extracted PVP (Table V).

Table V. Extracted PVP heated at 70 ^{o}C in a vacuum oven after 13 days

Sample #	Wt. crucible and extracted PVP after 13 days @ 70 ^{o}C in vacuum oven (g)	Wt. of extracted PVP (g) after drying	% Extracted PVP
Pt/meth rolled PVG			
PVG 1	11.7357	0.0046 ± 0.0004	46 ± 4
PVG 20	11.9190	0.0053 ± 0.0004	53 ± 4
PVG 25	12.0072	0.0041 ± 0.0004	41 ± 4
PVG 26	11.2777	0.0044 ± 0.0004	44 ± 4
PVG 28	10.5542	0.0044 ± 0.0004	44 ± 4
		0.0046 ± 0.0004	**46 ± 4**

3.6. $[Ru(bpy)_2(dpp)]^{2+}$ complex in PVG with PVP/Pt Nanoparticles

Since extraction of the PVP from the adsorbed Pt in the porous Vycor glass was achieved, the PVG samples containing the stripped Pt were dried and then impregnated with 1 x 10^{-5} M $[Ru(bpy)_2(dpp)]^{2+}$ in acetonitrile to investigate their chemistry. Figure 68a shows the absorption spectra of $[Ru(bpy)_2(dpp)]^{2+}$ complex impregnated into the PVG with the stripped PVP/Pt nanoparticles after subtraction of the spectrum of PVG. The amount of $[Ru(bpy)_2(dpp)]^{2+}$ complex loaded into the glass is 8.4 x 10^{-8} mol/g. The absorption spectrum exhibited a peak at 420 nm and another at 470 nm.[85] These peaks are characteristic of the metal-to-ligand charge transfer (MLCT) bands to bpy and to dpp, respectively.

The peaks were resolved by fitting to a Gaussian Function using Origin Lab 7.0 (Figure 68b). The Gaussian Function is given by the equation

$$y = y0 + (A/(w*\text{sqrt}(\pi/2)))*\exp(-2*((x-xc)/w)\text{^}2) \quad (7)$$

where $y0$ is the baseline offset, A is the area under the peak, xc is the center of the peak and w is the width of the peak described as,

$$w = w1/\text{sqrt}(\ln(4)) \quad (8)$$

where $w1$ is the width of the peak at half height. The raw data collected from the absorption spectra (Figure 68a) were converted to an ASCII file and imported into Origin Lab 7.0 program. The x and y data values were then highlighted and plotted with scatter analysis. Using the "Analysis" button on the tool bar, the "Gaussian Function" was selected from the "Fit Multiple Peaks" section. The peaks of interest were selected and a fit of the raw data were obtained with the resolved peaks.

The absence of new bands or shoulder on existing bands implies no interaction of the stripped Pt nanoparticles in PVG with the $[Ru(bpy)_2(dpp)]^{2+}$. To further examine the reactivity of the nanoparticles in PVG, the unstripped PVP/Pt nanoparticles adsorbed into the glass were also impregnated with $[Ru(bpy)_2(dpp)]^{2+}$ complex with a loading of 5.7 x 10^{-8} mol/g. Absorption spectra detected the MLCT bands at 420 nm for bpy and 470 nm bands for dpp (Figure 69a). Gaussian fits of the MLCT transitions (Figure 69b) gave no evidence of either a new distinct absorption or a shoulder to suggest an interaction between $[Ru(bpy)_2(dpp)]^{2+}$, with either the stripped PVP/Pt nanoparticles or with those nanoparticles containing the full PVP cap.

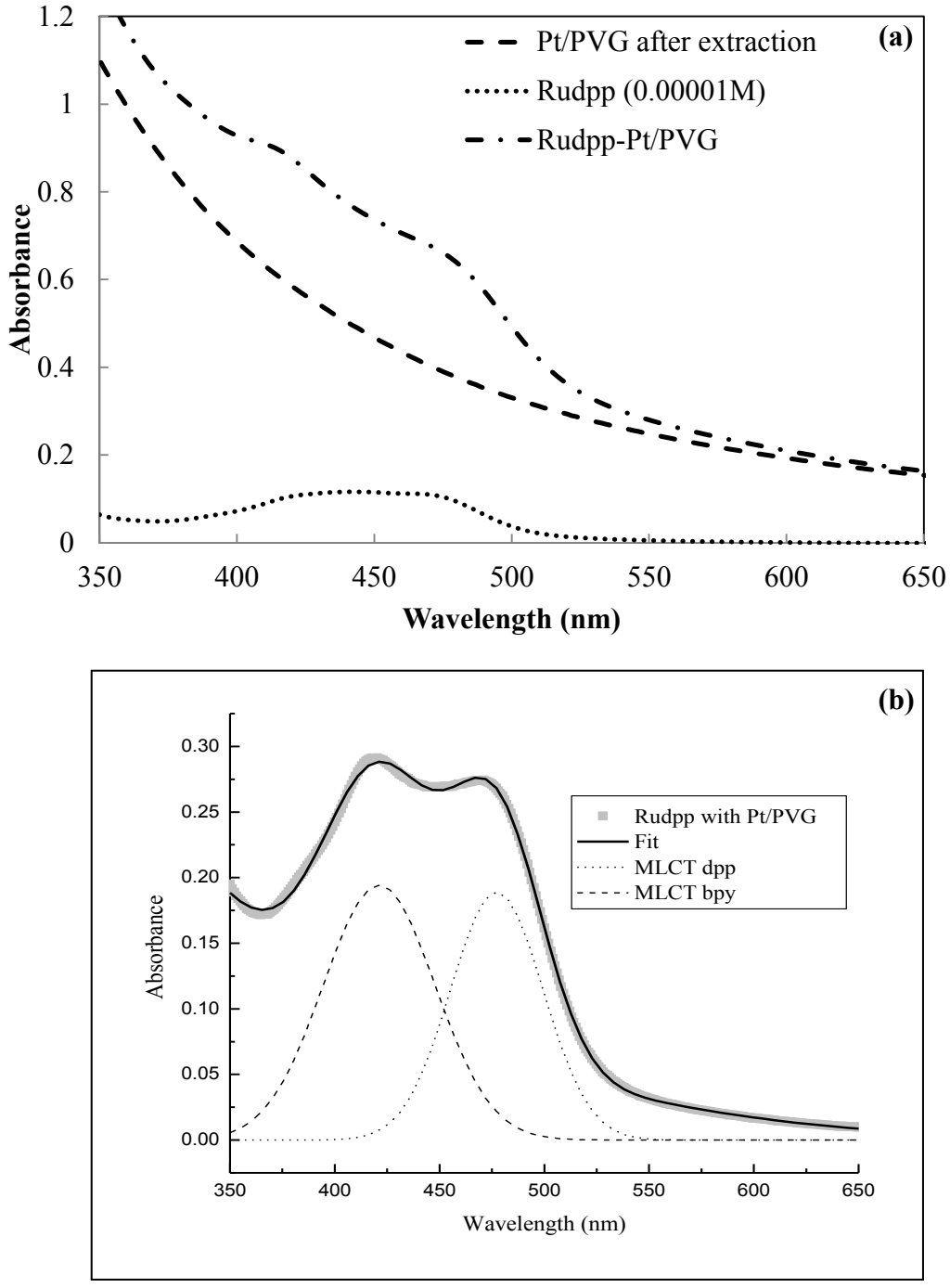

Figure 68. Absorption spectra of (a) 1 x 10^{-5} M $[Ru(bpy)_2(dpp)]^{2+}$ in acetonitrile (·····), stripped PVP/Pt nanoparticles in PVG (– – –) and $[Ru(bpy)_2(dpp)]^{2+}$ with the stripped PVP/Pt nanoparticles adsorbed into PVG (– · –) and (b) Resolved spectra of $[Ru(bpy)_2(dpp)]^{2+}$ with "stripped" PVP/Pt nanoparticles adsorbed into PVG by subtracting the spectra shown above.

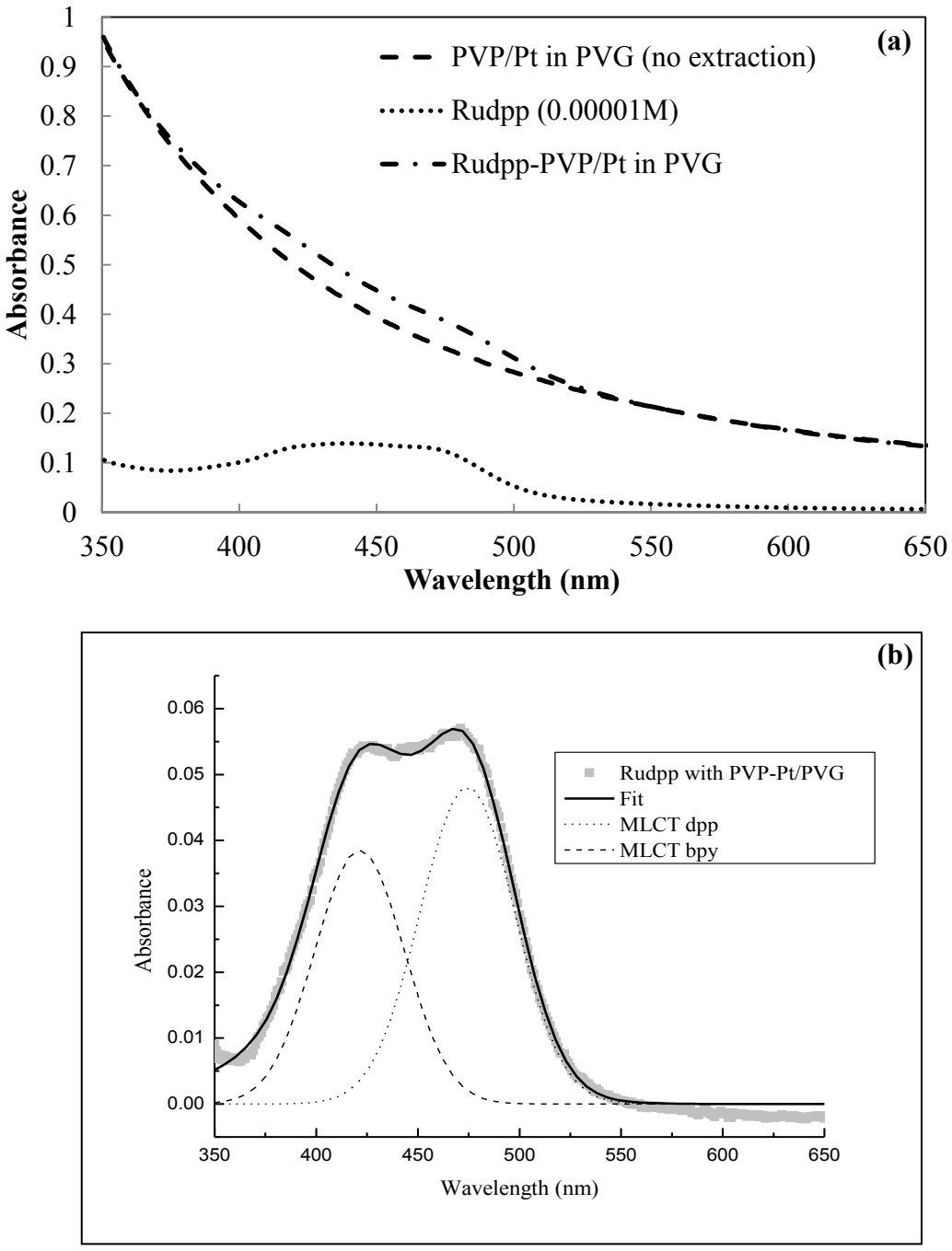

Figure 69. Absorption spectra of (a) 1 x 10^{-5} M $[Ru(bpy)_2(dpp)]^{2+}$ in acetonitrile (·····), unstripped PVP/Pt nanoparticles in PVG (– – –) and $[Ru(bpy)_2(dpp)]^{2+}$ with the unstripped PVP/Pt nanoparticles adsorbed into PVG (– · – ·) and (b) Resolved spectra of $[Ru(bpy)_2(dpp)]^{2+}$ with unstripped PVP/Pt nanoparticles adsorbed into PVG by subtracting the spectra shown above.

3.7. $[Ru(bpy)_2(ppz)]^{2+}$ complex in PVG with PVP/Pt Nanoparticles

There was no interaction of the $[Ru(bpy)_2(dpp)]^{2+}$ complex with the stripped Pt nanoparticles adsorbed in the glass. So we decided to conduct another experiment using 6.8×10^{-6} M $[Ru(bpy)_2(ppz)]^{2+}$ in acetonitrile as the impregnating solution. Like dpp, ppz contains two peripheral nitrogens that can serve as coordination sites, but unlike dpp, ppz is planar and does not require a structural change for bidentate coordination. The absorption spectrum of the $[Ru(bpy)_2(ppz)]^{2+}$ complex impregnated into the PVG with the stripped Pt nanoparticles after subtracting the spectrum of the glass is depicted in Figure 70a. The absorption spectrum shows the two MLCT bands, one at 420 nm corresponding to the charge transfer to bpy and the other at 480 nm corresponding to the charge transfer to ppz. The MLCT peaks were resolved using a Gaussian Function as described in Section 3.6 (Figure 70b). There was no evidence, however, of a new absorption or shoulder at longer or shorter wavelengths in the UV-vis region to indicate the formation of a new complex or product.

The impregnation of the $[Ru(bpy)_2(dpp)]^{2+}$ and $[Ru(bpy)_2(ppz)]^{2+}$ complexes into the porous Vycor glass with the stripped Pt nanoparticles was accomplished, but there was no evidence showing any kind of interaction between the complexes and the Pt nanoparticles. The results of our experiments in PVG were not what we expected, so the experiments proceeded in a different direction. Since there was no interaction in the glass, we decided to run the experiments in fluid solution. The PVP/Pt nanoparticles solution was mixed with the Ru(II) complexes and absorption and emission spectroscopy was utilized to probe whether an interaction occurred.

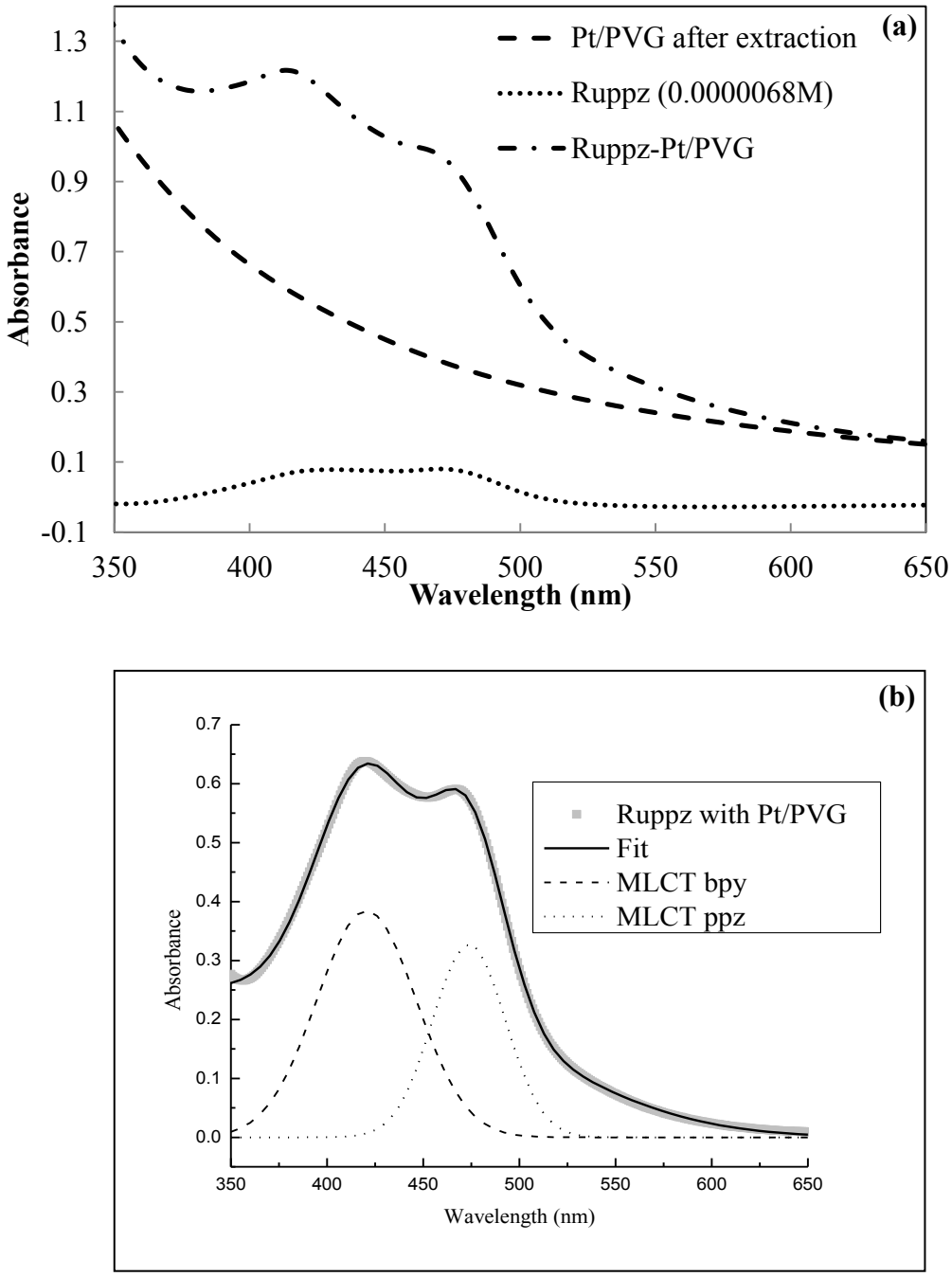

Figure 70. Absorption spectra of (a) 6.8 x 10^{-6} M $[Ru(bpy)_2(ppz)]^{2+}$ in acetonitrile (·····), unstripped PVP/Pt nanoparticles in PVG (– – –) and $[Ru(bpy)_2(ppz)]^{2+}$ with the unstripped PVP/Pt nanoparticles adsorbed into PVG (– · –) and (b) Resolved spectra of $[Ru(bpy)_2(ppz)]^{2+}$ with unstripped PVP/Pt nanoparticles adsorbed into PVG by subtracting the spectra shown above.

3.8. Association of $[Ru(bpy)_2(ppz)]^{2+}$ with PVP/Pt Nanoparticles

3.8.1 Reaction in 80% water-ethanol solution

A simple room temperature experiment between $[Ru(bpy)_2(ppz)]^{2+}$ (1.45×10^{-5} M) and PVP/Pt nanoparticles (9.45×10^{-8} M) was carried out in 80% water-ethanol solution (Figure 71a), leading to the presence of a new band circled in red at 540-nm after the PVP/Pt nanoparticles were subtracted (Figure 71b). This absorption is assigned to a band characteristic of the PVP/Pt nanoparticles and $[Ru(bpy)_2(ppz)]^{2+}$ complex because it is not present in the absorption spectrum of $[Ru(bpy)_2(ppz)]^{2+}$ or the PVP/Pt nanoparticles. PVP/Pt nanoparticles exhibit a tailing absorption through the visible region, but do not exhibit a distinct maximum at 540 nm. Similarly, $[Ru(bpy)_2(ppz)]^{2+}$ exhibits a weak tail on the long wavelength side of 476-nm ppz localized MLCT absorption, but like the nanoparticles does not show the distinct maximum at 540 nm that occurs when the PVP/Pt nanoparticles are added to either a 80% water-ethanol solution or 95% ethanol of $[Ru(bpy)_2(ppz)]^{2+}$. The spectra of $[Ru(bpy)_2(ppz)]^{2+}$ complex with PVP/Pt nanoparticles were resolved using the Gaussian Function from Origin Lab 7.0 program (Figure 72). Resolution of the absorption spectra, shows that band at 540-nm is broad and exist. An experiment with $[Ru(bpy)_2(ppz)]^{2+}$ complex and pure PVP was conducted to ruled out any interaction between the complex and the PVP. Figure 73 shows the resolved absorption spectra of the $[Ru(bpy)_2(ppz)]^{2+}$ complex and pure PVP. Only the MLCT bands were present and there was no evidence of a new band at longer wavelength, λ.

Titrations of an 80% water-ethanol solution 1.1×10^{-5} M in $[Ru(bpy)_2(ppz)]^{2+}$ with PVP/Pt nanoparticles in room temperature, 22 ± 1 ^{o}C, increases the intensity of the

MLCT transitions and the 540-nm band as shown by the arrow in Figure 74. The plot of PVP/Pt nanoparticles absorption at 540 nm *vs.* concentration of PVP/Pt nanoparticles in 80% water-ethanol solution is linear with an extinction coefficient of 1 x 10^6 $M^{-1}cm^{-1}$ (Figure 75a), whereas, the plot of [$Ru(bpy)_2(ppz)^{2+}$-PVP/Pt] solutions at 540 nm as a function of the concentration of PVP/Pt nanoparticles in 80% water-ethanol solution, shows a non-linear dependence with an extinction coefficient of 4.5 x 10^5 $M^{-1}cm^{-1}$ (Figure 75b). Because of the differences in extinction coefficients and the shape of the plot, the 540 nm absorption is due to the [$Ru(bpy)_2(ppz)^{2+}$-PVP/Pt] interaction.

Emission spectra were recorded using a 2 nm slit width and an integration time of 0.5 s at an excitation wavelength of 476 nm to investigate the degree of quenching. As the concentration of the Pt nanoparticles increased, the intensity of the 690-nm $[Ru(bpy)_2(ppz)]^{2+}$ complex decreased (Figure 76) providing further evidence of an interaction between the nanoparticles and the complex. A Stern-Volmer quenching constant, K_{sv}, of 6 x 10^6 M^{-1} was obtained from the slope of the graph (Figure 77), and calculated using the initial intensity, I_o, of the $[Ru(bpy)_2(ppz)]^{2+}$ complex at 690-nm divided by the intensity, I, of the combined $[(bpy)_2Ru(ppz)]^{2+}$ complex with PVP/Pt nanoparticles as a function of the concentration of the PVP/Pt nanoparticles (Figure 77). The shape of the graph is non-linear and exhibits a "step-like" curve. All solutions were deaerated by Argon bubbling for 5 minutes.

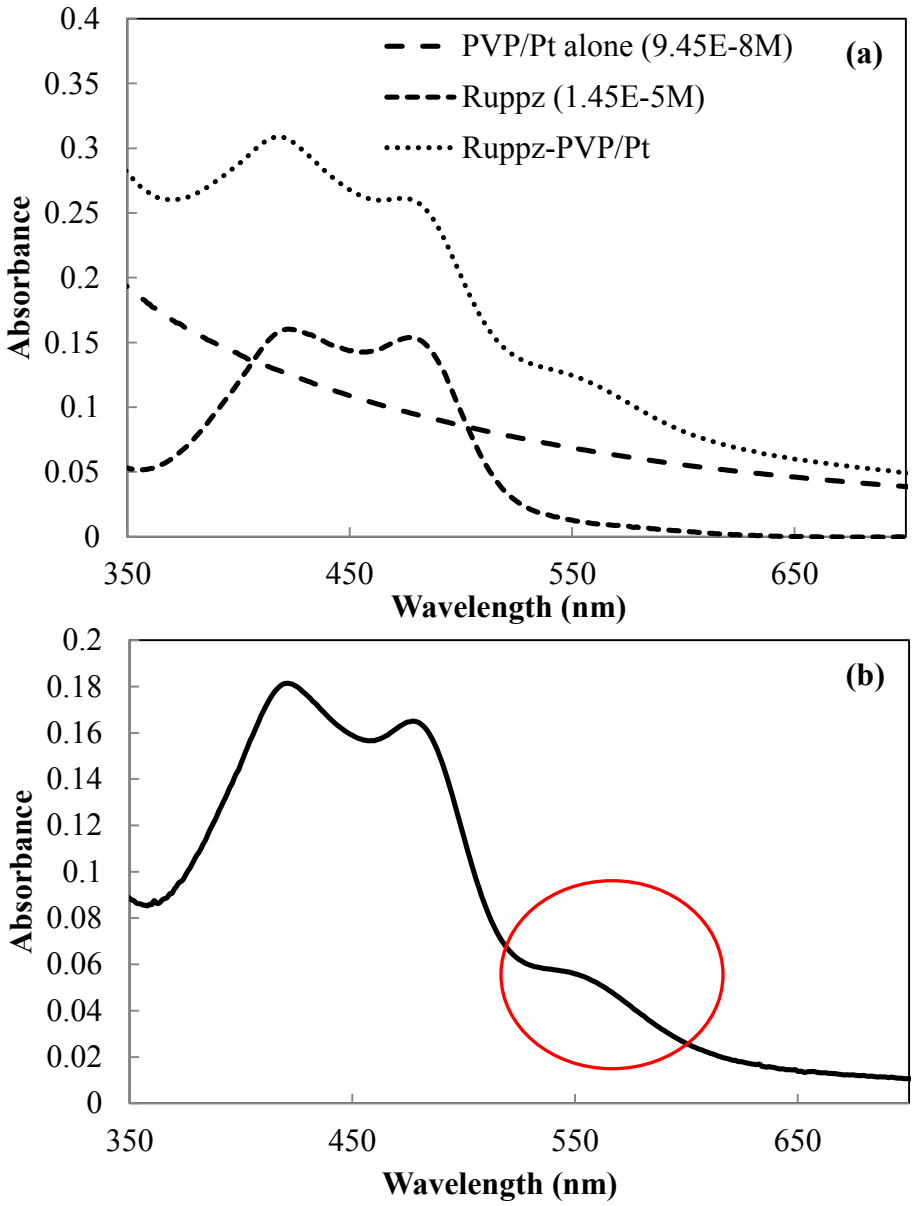

Figure 71. Absorption spectra of (a) reaction between 1.45 x 10^{-5} M $[Ru(bpy)_2(ppz)]^{2+}$ and 9.45 x 10^{-8} M PVP/Pt nanoparticles in 80% water-ethanol solution at room temperature and (b) association of $[Ru(bpy)_2(ppz)]^{2+}$ and PVP/Pt nanoparticles by subtracting the spectra shown above.

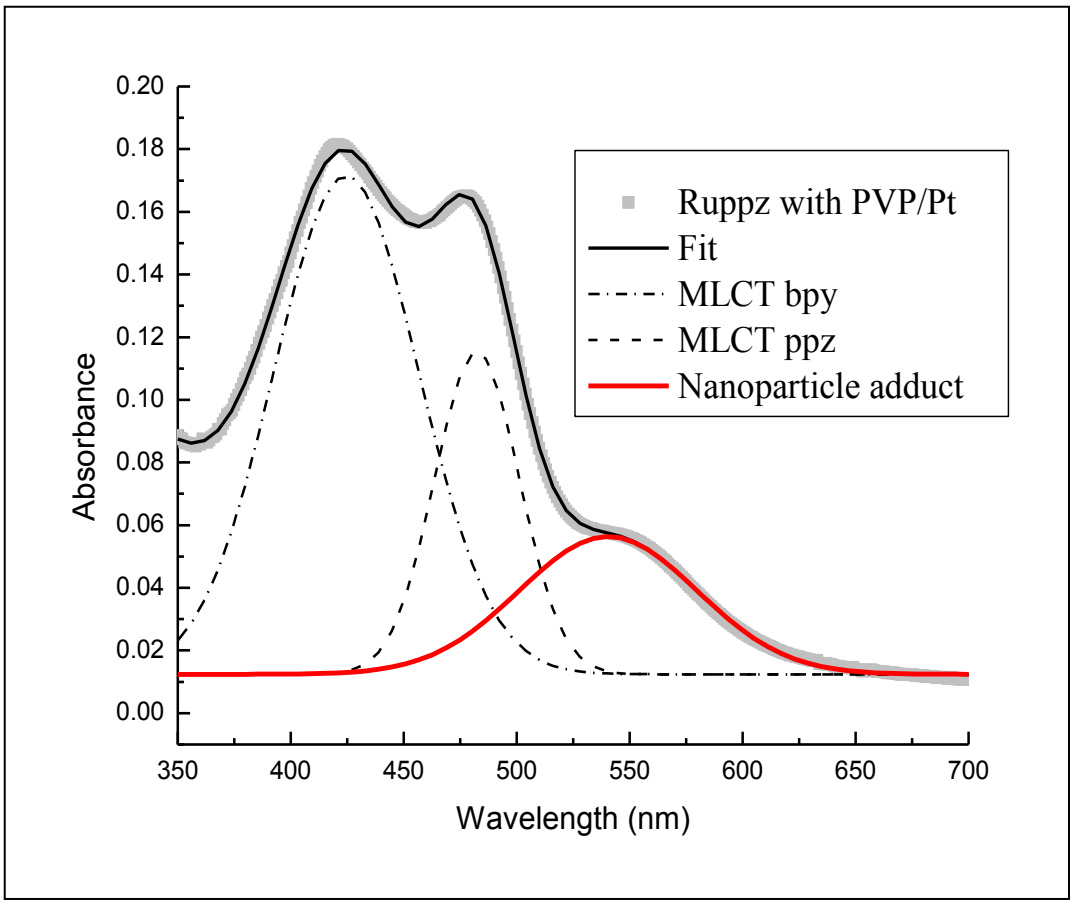

Figure 72. Gaussian Fit using Origin lab 7.0 of the MLCT transition of 1.45 x 10^{-5} M $[Ru(bpy)_2(ppz)]^{2+}$ with 9.45 x 10^{-8} M PVP/Pt nanoparticles in 80% water-ethanol solution at room temperature.

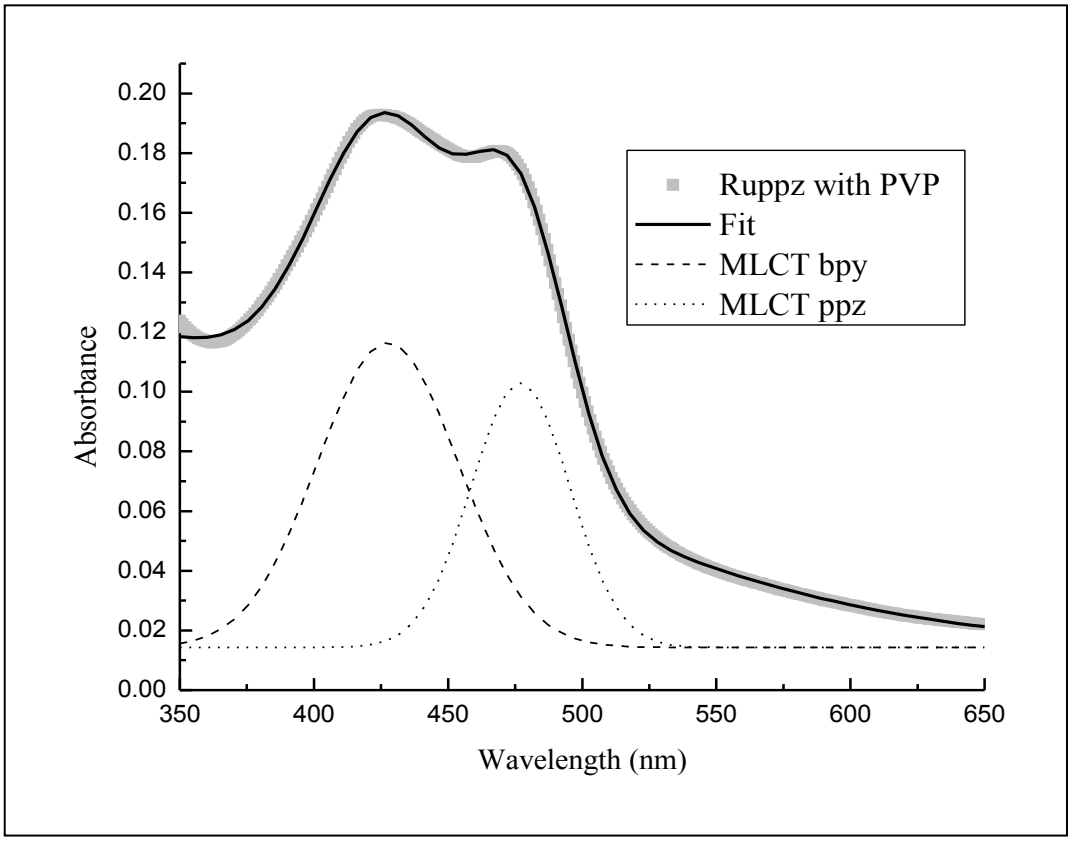

Figure 73. Gaussian Fit using Origin lab 7.0 of the MLCT transition of 2.0 x 10^{-5} M $[Ru(bpy)_2(ppz)]^{2+}$ with 4.0 x 10^{-6} M PVP in 95% ethanol at room temperature.

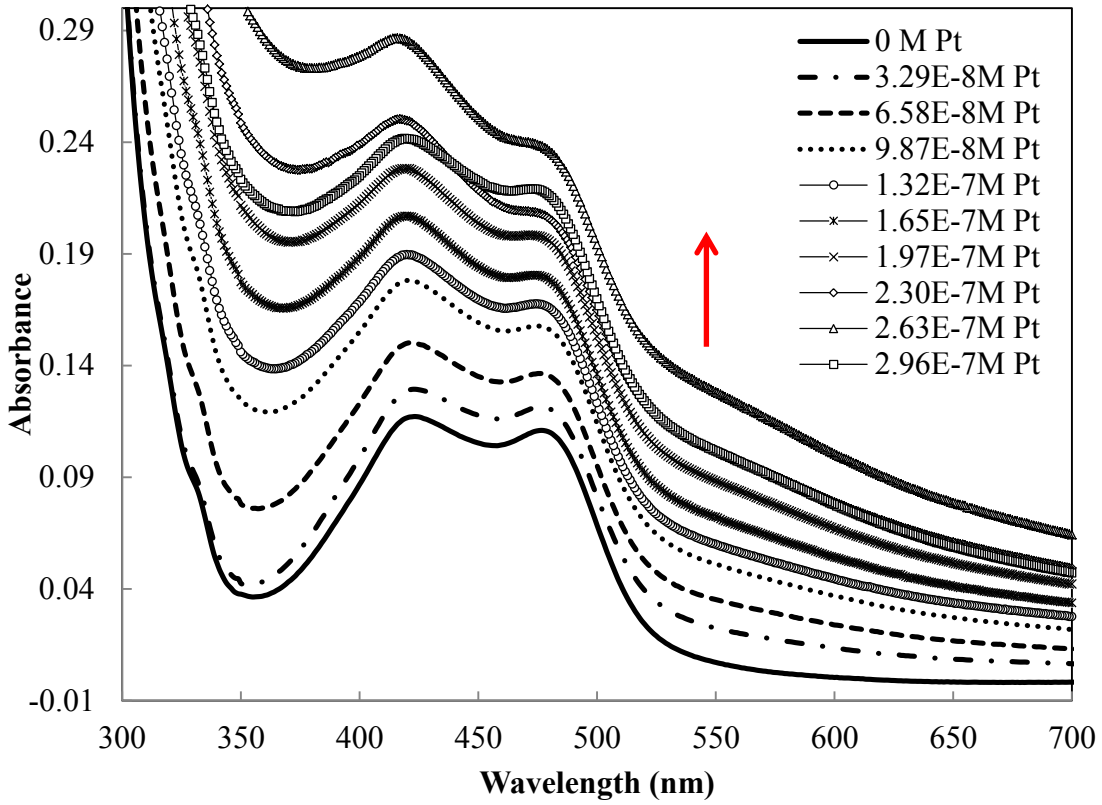

Figure 74. Absorption spectra of 1.1 x 10^{-5} M $[Ru(bpy)_2(ppz)]^{2+}$ with [PVP/Pt] nanoparticles in 80% water-ethanol solution at room temperature.

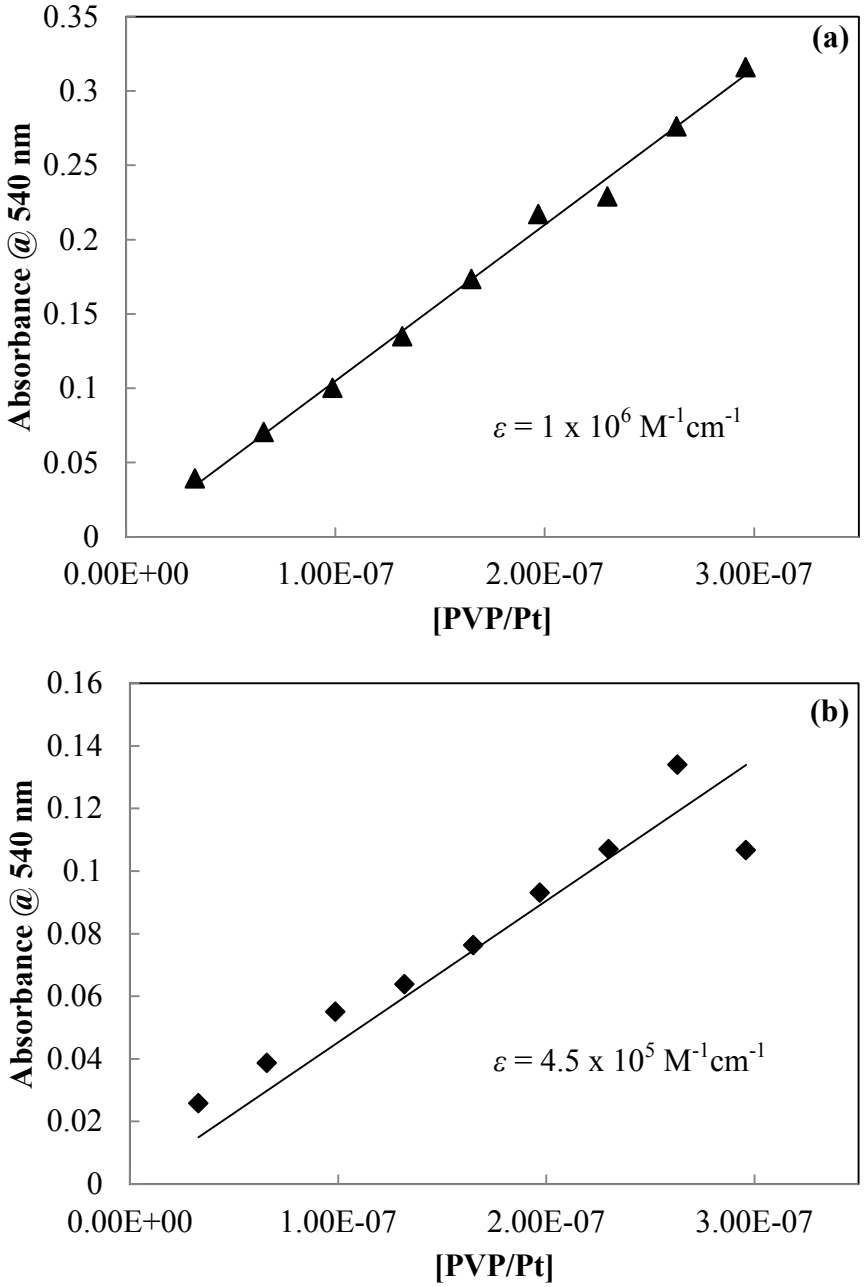

Figure 75. Plot of absorbances at 540 nm *vs.* concentration of (a) PVP/Pt nanoparticles in the absence of 1.1 x 10^{-5} M $[Ru(bpy)_2(ppz)]^{2+}$ in 80% water-ethanol solution, ε = 1 x 10^6 $M^{-1}cm^{-1}$ and (b) PVP/Pt nanoparticles in the presence of 1.1 x 10^{-5} M $[Ru(bpy)_2(ppz)]^{2+}$ in 80% water-ethanol solution, ε = 4.5 x 10^5 $M^{-1}cm^{-1}$.

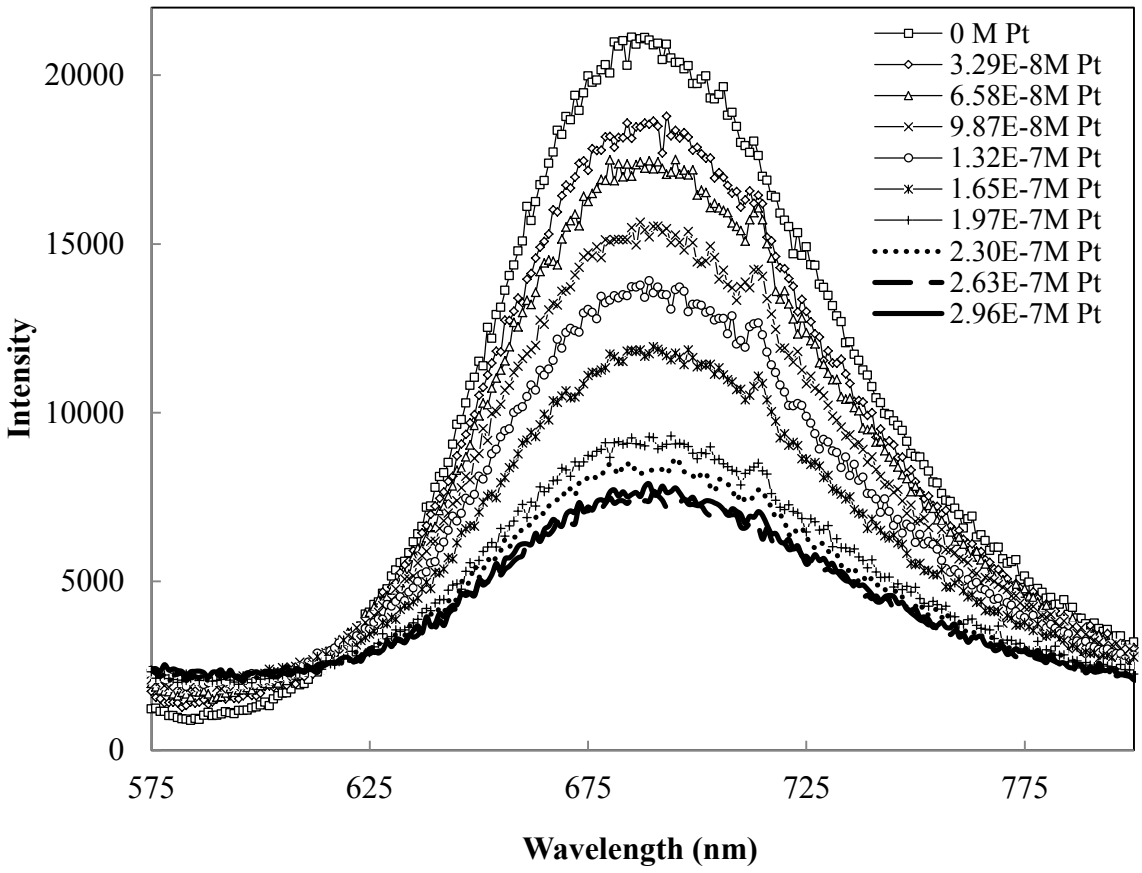

Figure 76. Emission spectra of 1.1 x 10^{-5} M $[Ru(bpy)_2(ppz)]^{2+}$ with [PVP/Pt] nanoparticles in 80% water-ethanol solution at room temperature, with excitation λ of 476 nm. All solutions were deaerated by Argon bubbling for 5 minutes.

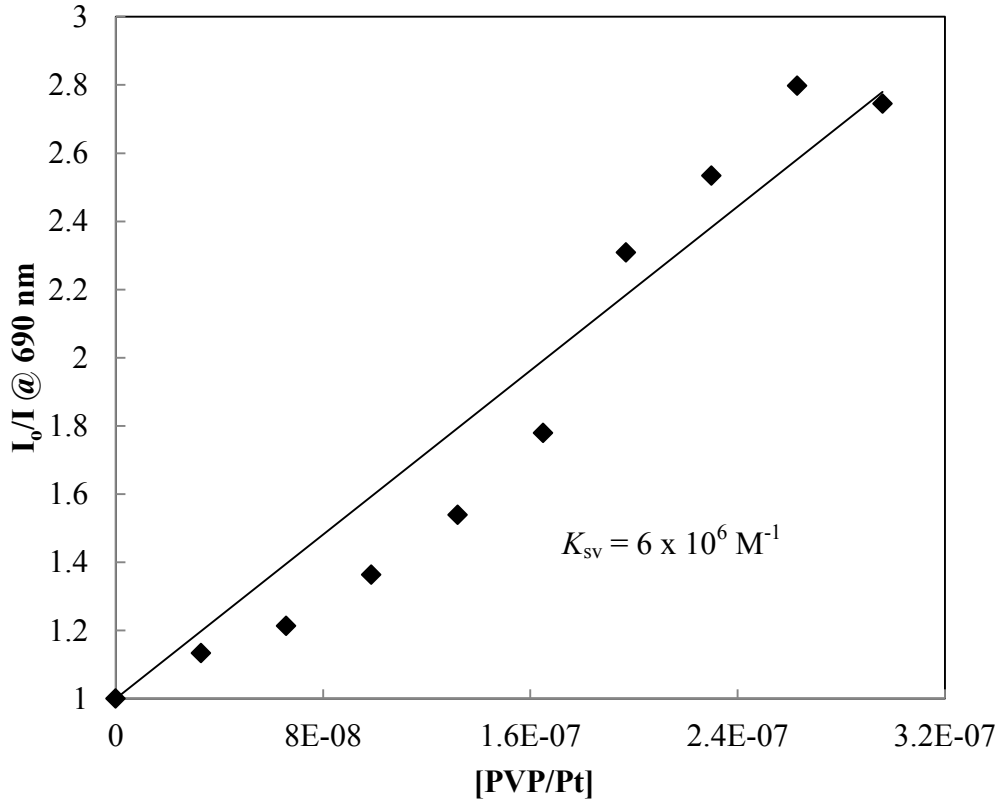

Figure 77. Stern-Volmer Plot of 1.1 x 10^{-5} M $[Ru(bpy)_2(ppz)]^{2+}$ with [PVP/Pt] nanoparticles in 80% water-ethanol solution at room temperature. All solutions were deaerated by Argon bubbling for 5 minutes.

3.8.2 Reaction in 95% ethanol solvent

Titrations of a 95% ethanol solution 1.70 x 10^{-5} M in $[Ru(bpy)_2(ppz)]^{2+}$ with PVP/Pt nanoparticles were conducted at room temperature. Figure 78 shows the appearance of a new shoulder on the low energy side of the ppz MLCT transition similar to the reaction of the $[Ru(bpy)_2(ppz)]^{2+}$ with PVP/Pt nanoparticles in 80% water-ethanol solution. The decline in emission intensity of the $[Ru(bpy)_2(ppz)]^{2+}$ with the addition of PVP/Pt nanoparticles (Figure 79) is evidence that the nanoparticles are interacting with the complex. The sensitivity to the solvent environment shifts the emission peak from 690-nm in 80% water-ethanol solvent to 673-nm in 95% ethanol. Time-resolved lifetime measurements were performed on the $[Ru(bpy)_2(ppz)]^{2+}$ complex in the absence of the quencher in 95% ethanol (Figure 80). The emission decay, which corresponds to how long the molecule stays in the excited state before returning to the ground state, gave a lifetime value of 727 ± 8 ns (Table VI). In conjunction with emission intensity measurements, lifetime measurements are an absolute method to determine static (associational) and dynamic (collisional) quenching. Static quenching occurs when $\tau_o/\tau = 1$, and dynamic quenching occurs when the emission intensity in the absence (F_o) and presence (F) of the quencher equals the lifetime in the absence (τ_0) and presence (τ) of the quencher, *i.e.,* $F_o/F = \tau_o/\tau$.[120] Six lifetime measurements were carried out with the $[Ru(bpy)_2(ppz)]^{2+}$ complex in the presence of the PVP/Pt nanoparticles (quencher). The lifetime values recorded are listed in Table VI. As the concentration of the quencher increases, the lifetime values were lower than the value of the $[Ru(bpy)_2(ppz)]^{2+}$ complex recorded.

Table VI. Lifetime values of 1.70 x 10^{-5} M $[Ru(bpy)_2(ppz)]^{2+}$ with [PVP/Pt] nanoparticles in 95% ethanol at 673-nm

	Sample #	Concentration of PVP/Pt (M)	τ (ns)
1	$[Ru(bpy)_2(ppz)]^{2+}$	0	726.95 ± 8.45
2	$[Ru(bpy)_2(ppz)^{2+}$-PVP/Pt]	1.32 x 10^{-8}	701.86 ± 8.94
3	$[Ru(bpy)_2(ppz)^{2+}$-PVP/Pt]	2.63 x 10^{-8}	689 ± 8.54
4	$[Ru(bpy)_2(ppz)^{2+}$-PVP/Pt]	3.95 x 10^{-8}	719.57 ± 10
5	$[Ru(bpy)_2(ppz)^{2+}$-PVP/Pt]	5.26 x 10^{-8}	712.9 ± 8.98
6	$[Ru(bpy)_2(ppz)^{2+}$-PVP/Pt]	6.58 x 10^{-8}	683.81 ± 8.46
7	$[Ru(bpy)_2(ppz)^{2+}$-PVP/Pt]	7.90 x 10^{-8}	668.41 ± 8.26

Figure 81 shows the Stern-Volmer plot of I_o/I with K_{sv} = 5.0 x 10^6 M^{-1} and τ_o/τ with K_{sv} = 9.2 x 10^5 M^{-1} as a function of the PVP/Pt nanoparticles concentration added to the $[Ru(bpy)_2(ppz)]^{2+}$ complex. The bimolecular quenching constant, k_b, of the interaction between the $[Ru(bpy)_2(ppz)]^{2+}$ complex and PVP/Pt nanoparticles were calculated from the relationship $K_{sv} = k_b\tau$, where τ is the emission lifetime of $*[Ru(bpy)_2(ppz)]^{2+}$ in room temperature 95% ethanol, that has been deaerated by Argon bubbling for five minutes. Substituting the appropriate values yields (1.3 ± 0.1) x 10^{12} $M^{-1}s^{-1}$ for k_b. The value is quite large, since the bimolecular quenching constant of 1 x 10^{10} $M^{-1}s^{-1}$ is the largest value found in aqueous solution.[120]

A plot of an increase in the absorbance at 540-nm of $[Ru(bpy)_2(ppz)]^{2+}$ with PVP/Pt nanoparticles *vs.* the concentration of the PVP/Pt nanoparticles added shows a series of stepwise equilibria (Figure 82).

To determine the stoichiometry or the amount of the $[Ru(bpy)_2(ppz)]^{2+}$ binding to the PVP/Pt nanoparticles, a Job's plot was introduced using the concentrations of 2.4 x 10^{-5} M and 4.8 x 10^{-5} M of $[Ru(bpy)_2(ppz)]^{2+}$, and the concentrations of 2.63 x 10^{-8} M

and 5.26 x 10^{-8} M of the PVP/Pt nanoparticles indicated by the arrow in Figure 82. Job's plots of the absorbance at 540 nm *vs.* the mole fraction of the PVP/Pt nanoparticles yield PVP/Pt/$[Ru(bpy)_2(ppz)]^{2+}$ ratios of < 1 (Figure 83). The error is large, principally due to the uncertainties in the calculation of the nanoparticle concentrations.

TEM of the samples were analyzed to determine the morphology and degree of aggregation of the PVP/Pt nanoparticles in the presence of the $[Ru(bpy)_2(ppz)]^{2+}$ complex. The initial uniform distributions of the individual PVP/Pt nanoparticles (Figure 16a) changes in the presence of $[Ru(bpy)_2(ppz)]^{2+}$ to one showing PVP/Pt aggregates with the level of aggregation proportional to the amount of PVP/Pt nanoparticles added. At low concentration of the nanoparticles, aggregates of 3 or 4 nanoparticles are detected by TEM (Figure 84), while further additions of the nanoparticles in the presence of $[Ru(bpy)_2(ppz)]^{2+}$ leads to larger aggregates of differing shape (Figure 85a). The aggregates appeared close to circular and triangular in shape. The individual PVP/Pt nanoparticles within the aggregates are 3.1 ± 0.4 nm in diameter (Figure 85b), identical to the particle size of the PVP/Pt nanoparticles in the absence of the Ru complex.

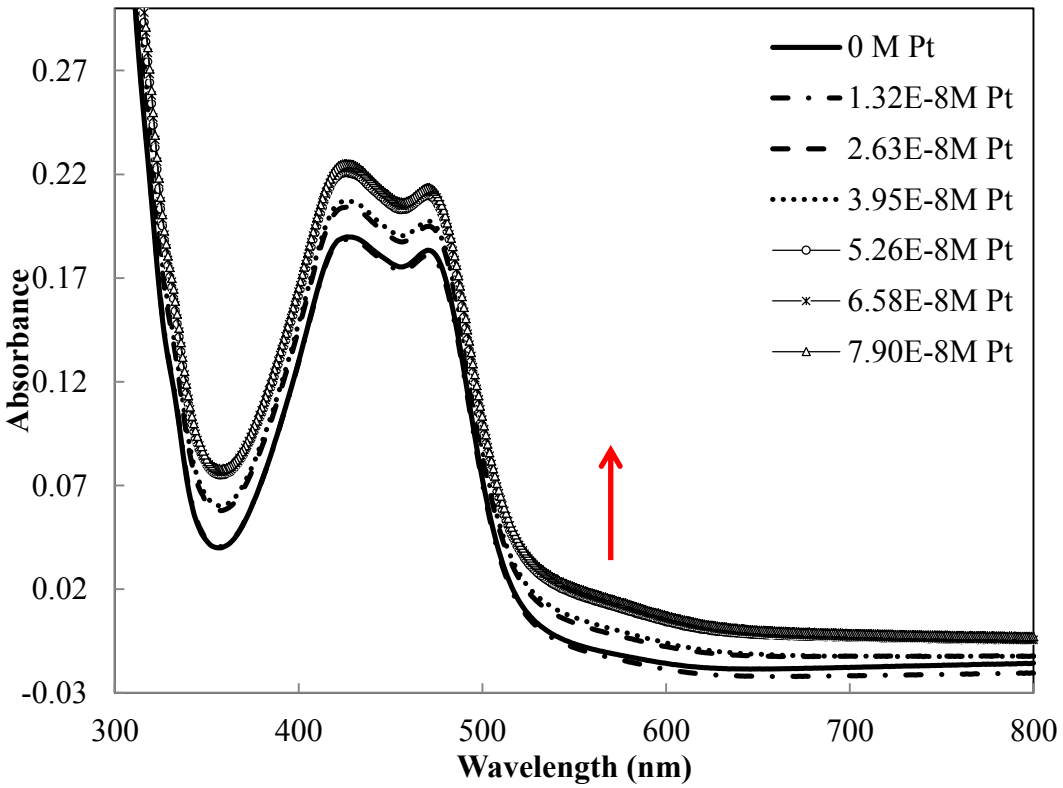

Figure 78. Absorption spectra of 1.70 x 10^{-5} M $[Ru(bpy)_2(ppz)]^{2+}$ with [PVP/Pt] nanoparticles in 95% ethanol solution at room temperature.

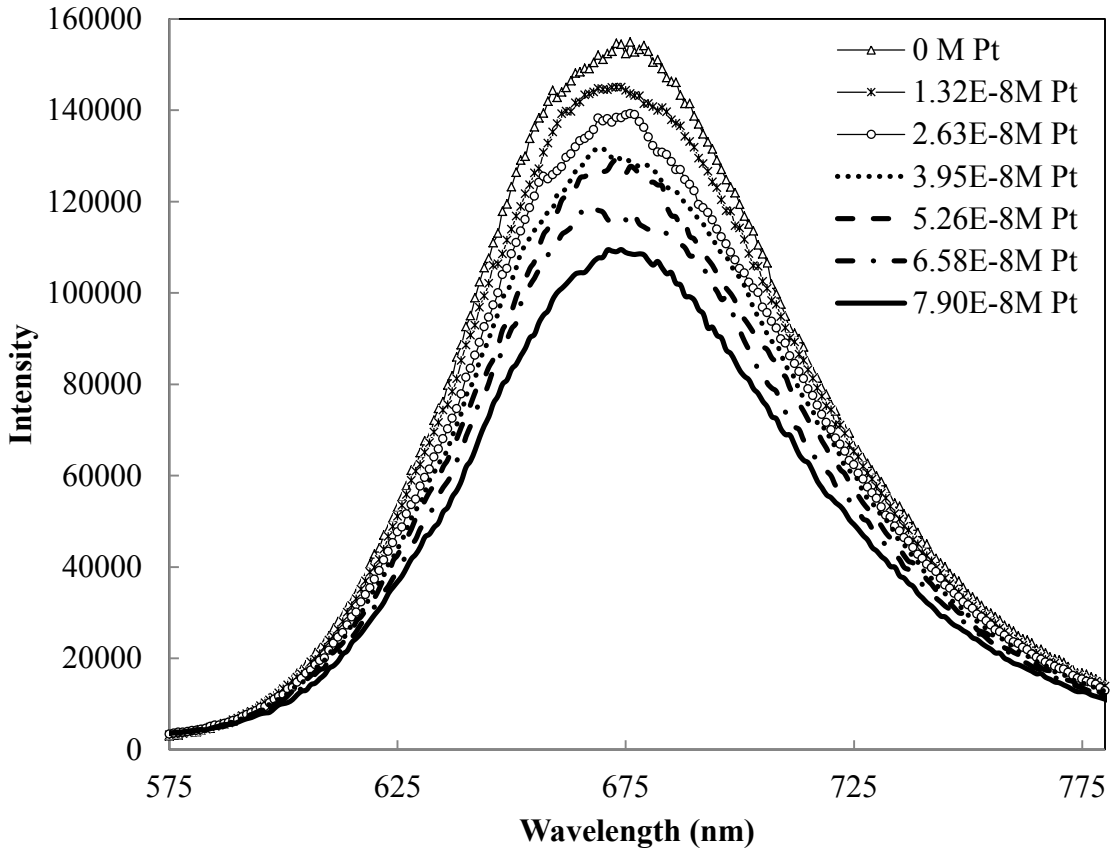

Figure 79. Emission spectra of 1.70 x 10^{-5} M $[Ru(bpy)_2(ppz)]^{2+}$ with [PVP/Pt] nanoparticles in 95% ethanol solution at room temperature, with excitation λ of 476 nm. All solutions were deaerated by Argon bubbling for 5 minutes.

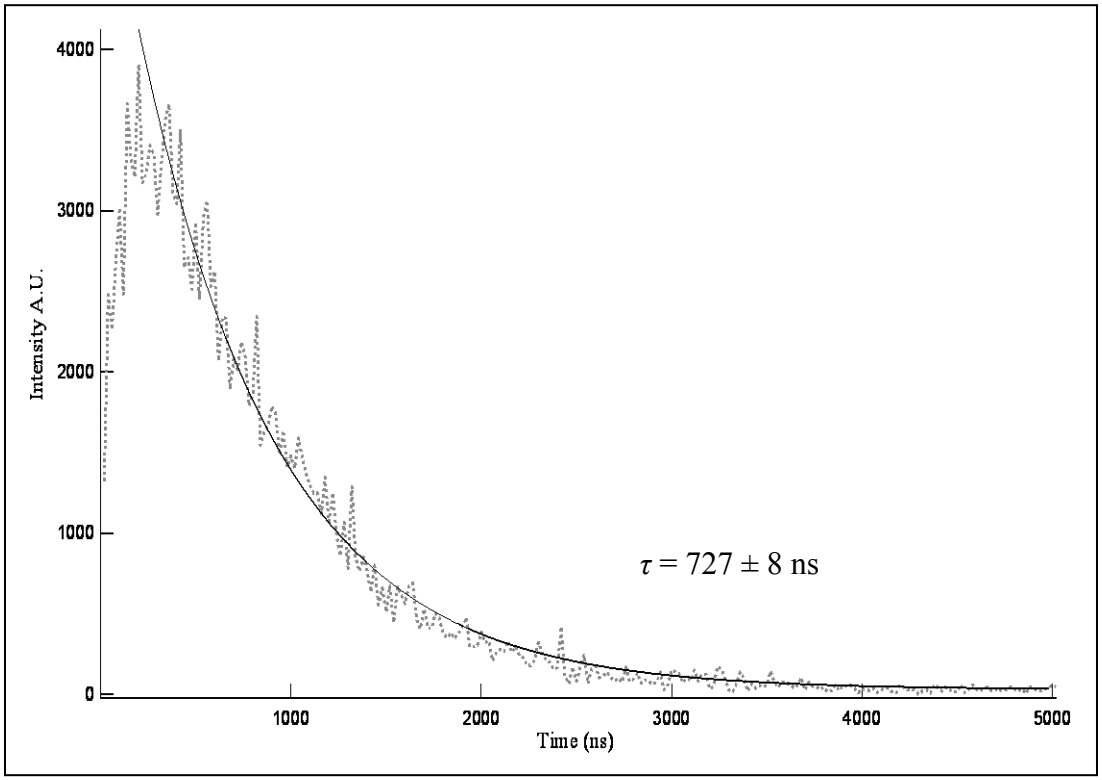

Figure 80. Time-resolved lifetime measurements of 1.70 x 10^{-5} M $[Ru(bpy)_2(ppz)]^{2+}$ complex in 95% ethanol without the quencher (PVP/Pt nanoparticles) at room temperature. The solution was deaerated by Argon bubbling for 5 minutes.

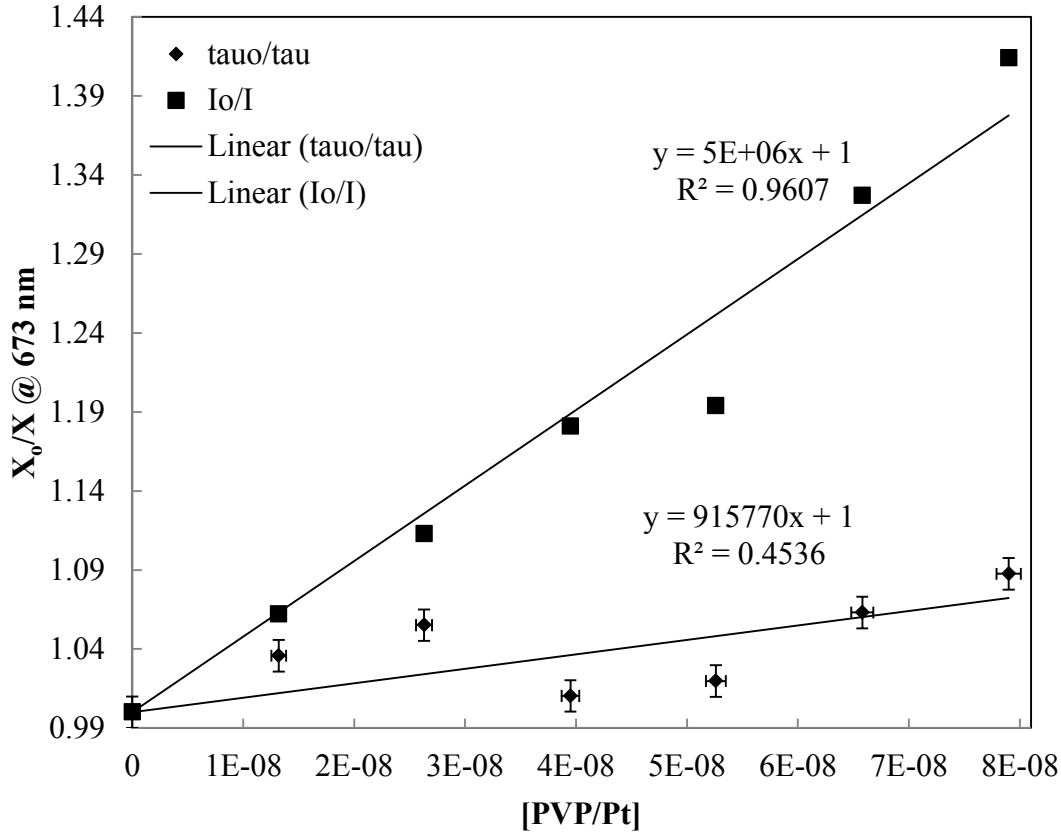

Figure 81. Stern-Volmer Plot of I_o/I and τ_o/τ of 1.70 x 10^{-5} M $[Ru(bpy)_2(ppz)]^{2+}$ with [PVP/Pt] nanoparticles in 95% ethanol solution at room temperature. All solutions were deaerated by Argon bubbling for 5 minutes.

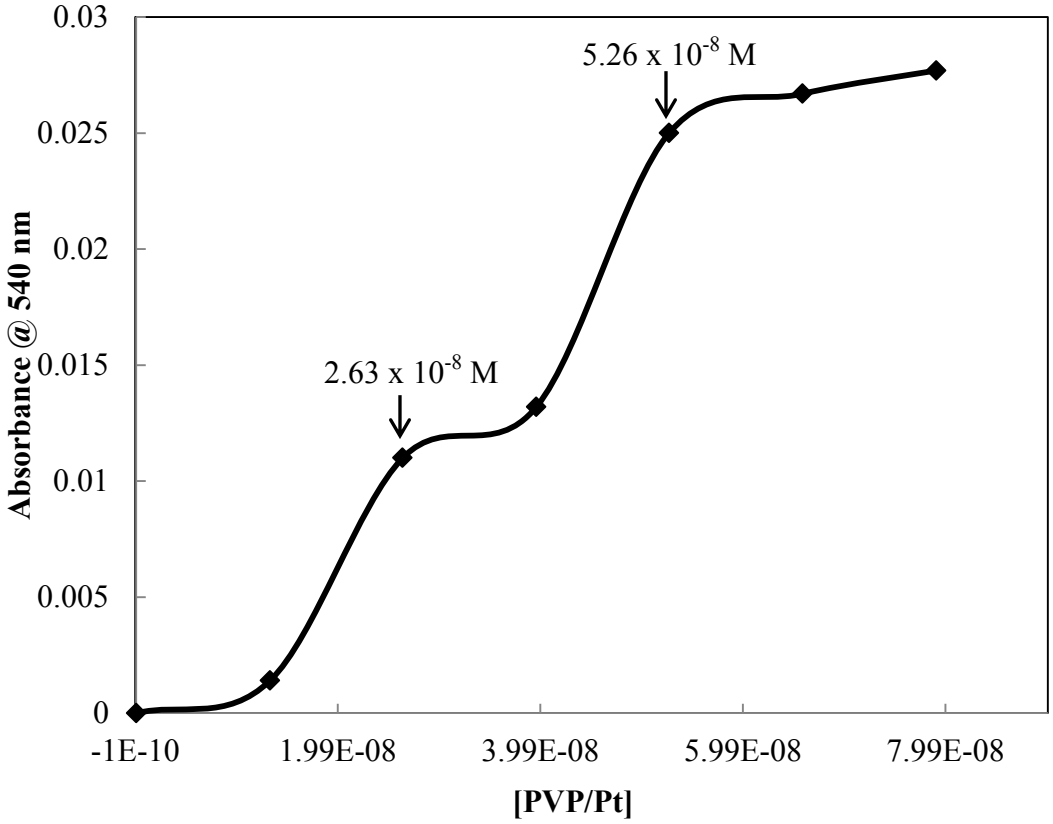

Figure 82. Increase in absorbance at 540 nm as a function of [PVP/Pt] nanoparticles in the presence of 1.70 x 10^{-5} M $[Ru(bpy)_2(ppz)]^{2+}$ in 95% ethanol at room temperature.

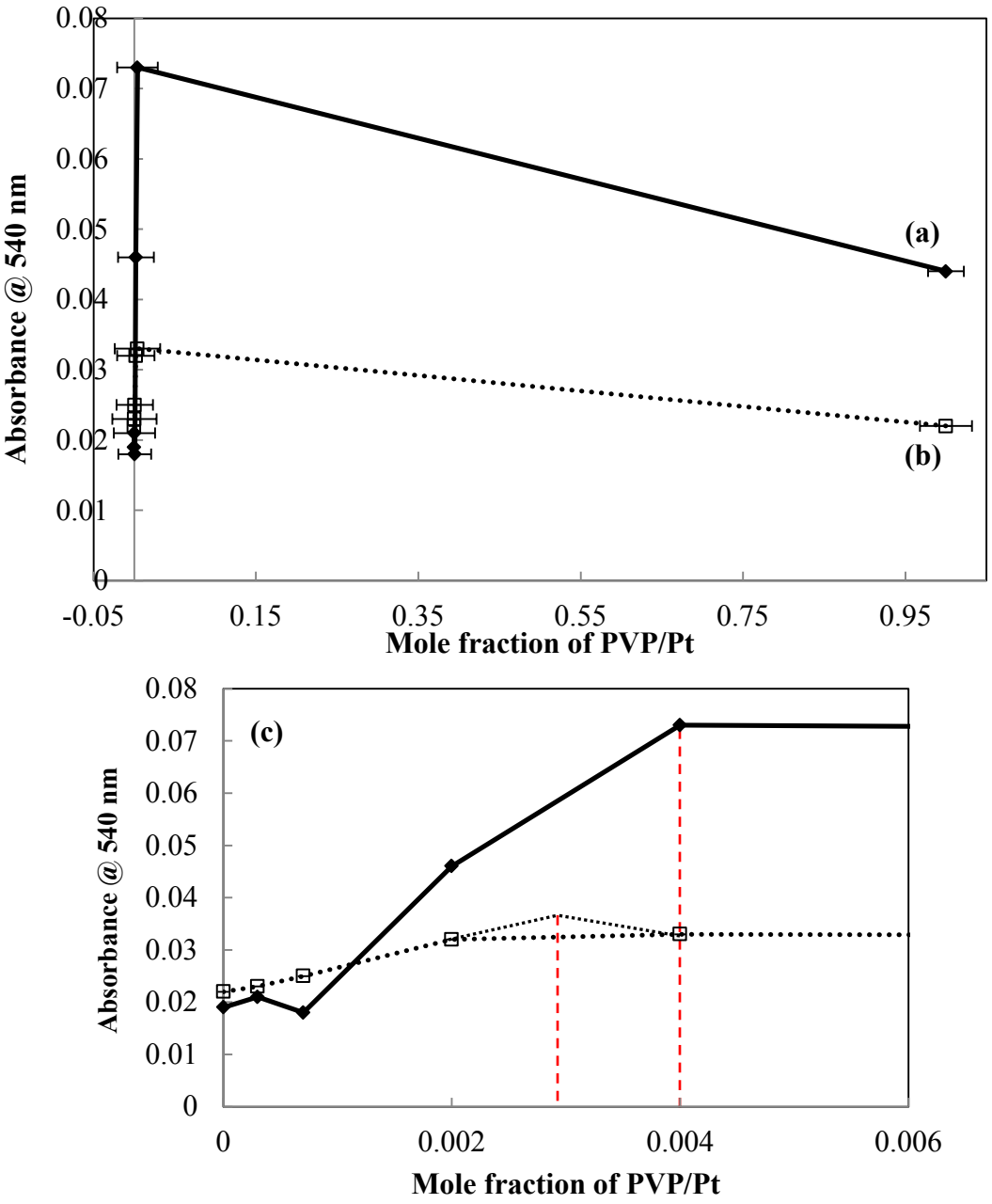

Figure 83. Job's plot showing absorbance at 540 nm *vs.* mole fraction of PVP/Pt nanoparticles in 95% ethanol solution at room temperature for (a) $[Ru(bpy)_2(ppz)]^{2+}$ (4.80E-5 M) with PVP/Pt nanoparticles (5.26E-8 M), (b) $[Ru(bpy)_2(ppz)]^{2+}$ (2.40E-5 M) with PVP/Pt nanoparticles (2.63E-8 M) and (c) larger image of the spectra shown above.

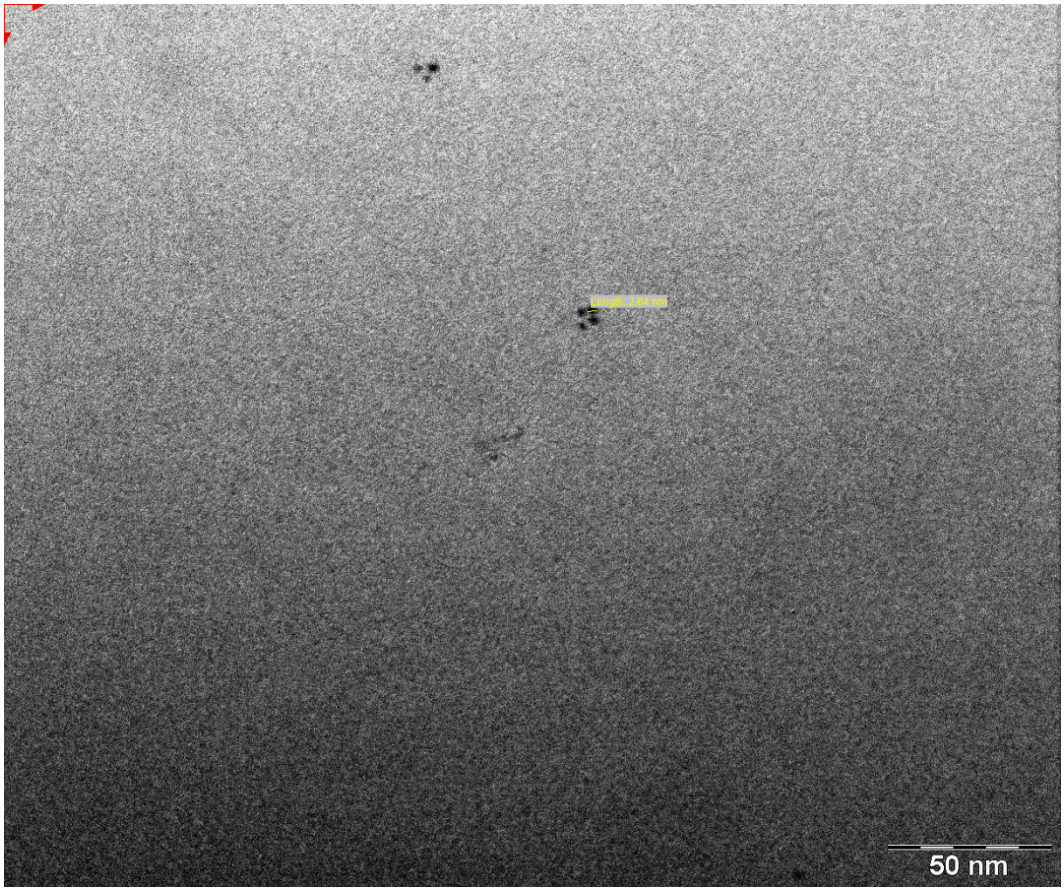

Figure 84. TEM image of 5.26 x 10^{-11} mol PVP/Pt nanoparticles (synthesized in methanol) in the presence of 1.92 x 10^{-7} mol $[Ru(bpy)_2(ppz)]^{2+}$.

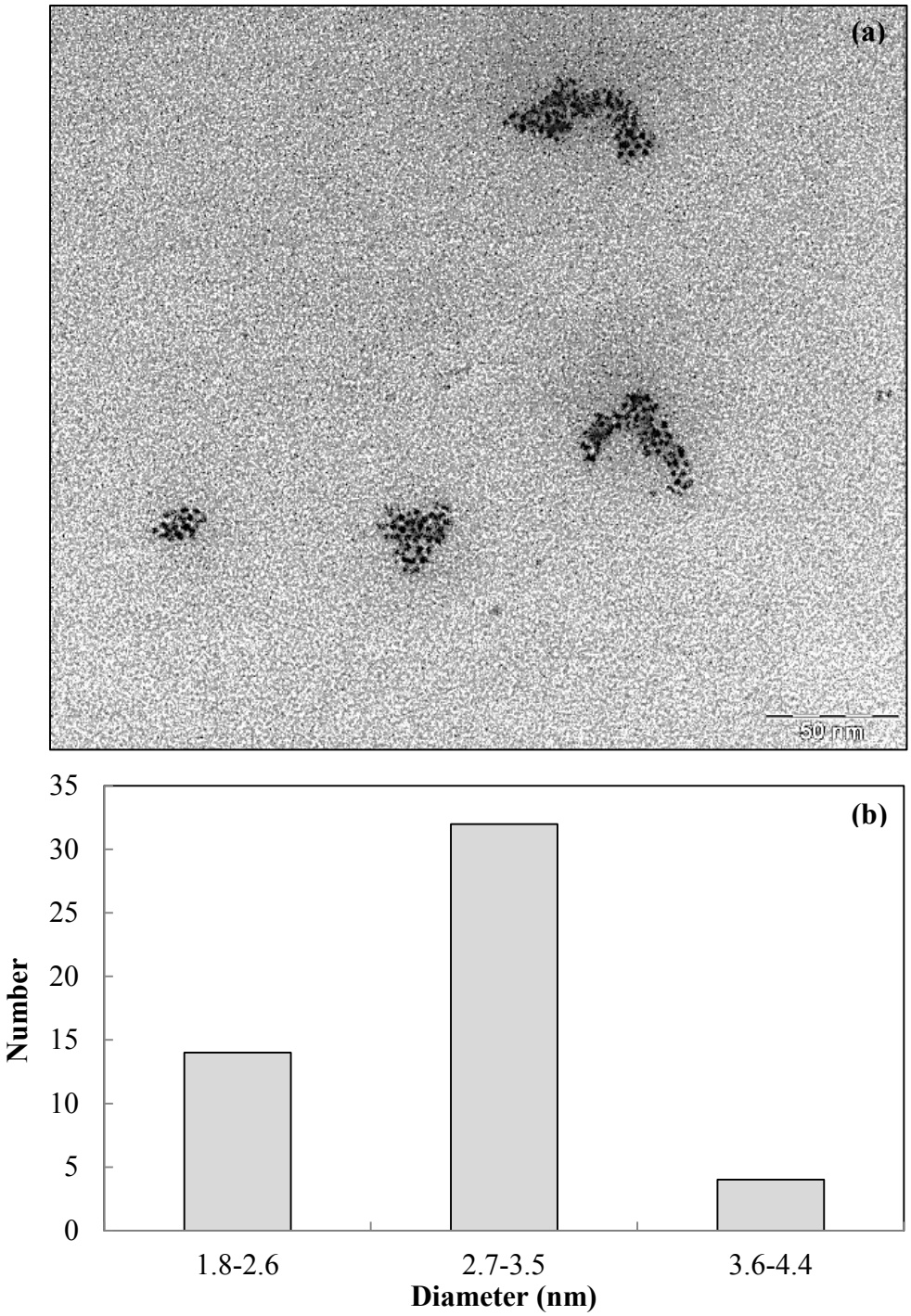

Figure 85. TEM image of (a) 2.10 x 10^{-10} mol PVP/Pt nanoparticles (synthesized in methanol) in the presence of 4.80 x 10^{-8} mol $[Ru(bpy)_2(ppz)]^{2+}$ and (b) histogram of the individual PVP/Pt nanoparticles within the aggregate with an average particle size of 3.1 ± 0.4 nm in diameter.

3.9. Association of $[Ru(bpy)_2(ppz)]^{2+}$ with PVP/Ir Nanoparticles

To date, there has been no report on the association of $[Ru(bpy)_2(ppz)]^{2+}$ with PVP/Ir nanoparticles. We decided to examine the quenching of 1.0 x 10^{-5} M $[Ru(bpy)_2(ppz)]^{2+}$ and 5.6 x 10^{-7} M PVP/Ir nanoparticles in room temperature, 22 ± 1 ^{o}C, 80% water-ethanol solution. Analogous to that found with the PVP/Pt nanoparticles, Figure 86 shows the MLCT transition to bpy and ppz along with a distinct shoulder on the long wavelength side of the ppz MLCT absorption. Three peaks in the spectrum are observed corresponding to the bpy localized MLCT at 420 nm and 480 nm for ppz localized MLCT, as well as a band at 540 nm. Resolution of the spectrum (Figure 87) reveals an absorption at 539 nm, but unlike the spectral changes accompanying the addition of the PVP/Pt nanoparticles to $[Ru(bpy)_2(ppz)]^{2+}$, addition of the PVP/Ir nanoparticles does not reduce the intensity of the ppz localized MLCT relative to that of bpy localized MLCT.

Titration experiments were then conducted for $[Ru(bpy)_2(ppz)]^{2+}$ with PVP/Ir nanoparticles in an 80% water-ethanol solution. The 1.4 x 10^{-5} M $[Ru(bpy)_2(ppz)]^{2+}$ complex was diluted by adding aliquots of PVP/Ir nanoparticles. Because of the addition of the PVP/Ir nanoparticles to the complex, it leads to the appearance of an increase in the 539-nm band on the lower energy side of the ppz ligand (Figure 88).

The quenching of the 690-nm emission of the $[Ru(bpy)_2(ppz)]^{2+}$ complex by PVP/Ir nanoparticles in 80% water-ethanol solution is shown in Figure 89. Stern-Volmer plots of the quenching exhibit a nonlinear dependence suggesting a pre-equilibrium with a K_{sv} of 7.4 x 10^5 M^{-1} (Figure 90). The increase in absorbance at 539-nm as a function of

an increase in concentration of the PVP/Ir nanoparticles added in the presence of the $[Ru(bpy)_2(ppz)]^{2+}$ complex also shows a non-linear dependence and does not exhibit a "step-like" curve (Figure 91), in comparison to the 540-nm absorbance plot as a function of [PVP/Pt] nanoparticles in Figure 82.

A stoichiometry was not determined for the complex with the PVP/Ir nanoparticles but was assumed to have similar nanoparticle aggregation behavior based on the similarities from the 540-nm absorption and the 690-nm emission quenching of $[Ru(bpy)_2(ppz)]^{2+}$ with PVP/Pt nanoparticles in 80% water-ethanol solution. However, a sample containing $[Ru(bpy)_2(ppz)]^{2+}$ with an increase concentration of PVP/Ir nanoparticles added, was chosen and taken to be analyzed by TEM to observe their behavior with the complex. Figure 92a shows the TEM image (scale bar 50 nm) of the PVP/Ir nanoparticles self-assembled in the presence of the $[Ru(bpy)_2(ppz)]^{2+}$ complex. The PVP/Ir nanoparticles within the aggregates in the presence of $[Ru(bpy)_2(ppz)]^{2+}$, have an average particle size of 1.8 ± 0.3 nm, calculated from the highest bar from the histogram labeled 1.5-2.1 nm (Figure 92b). The aggregated $[Ru(bpy)_2(ppz)^{2+}$-PVP/Ir] appeared close to circular in comparison to the PVP/Ir nanoparticles in the absence of the $[Ru(bpy)_2(ppz)]^{2+}$ complex (Figure 24).

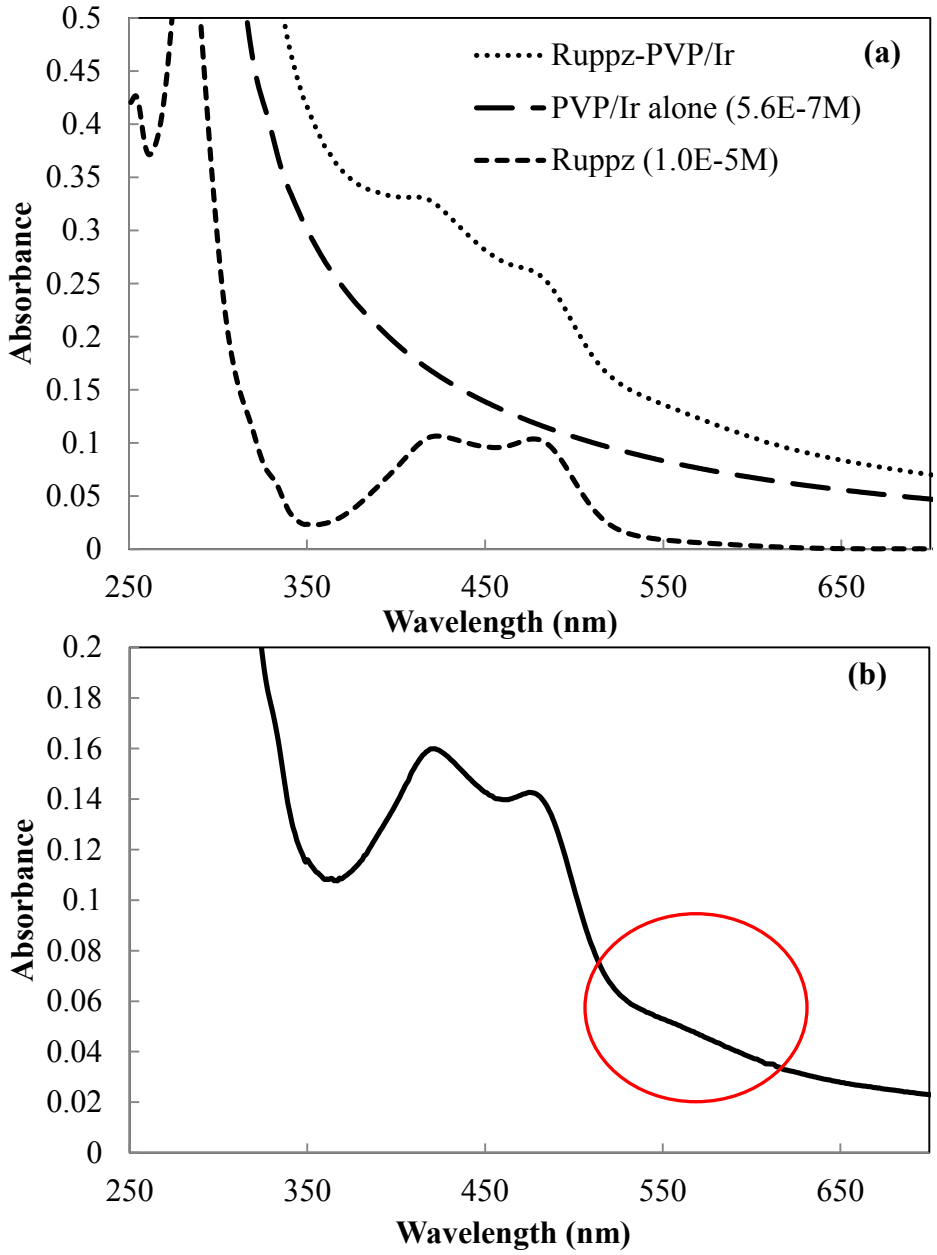

Figure 86. Absorption spectra of (a) reaction between 1.0 x 10^{-5} M $[Ru(bpy)_2(ppz)]^{2+}$ and 5.6 x 10^{-7} M PVP/Ir nanoparticles in 80% water-ethanol solution at room temperature and (b) association of $[Ru(bpy)_2(ppz)]^{2+}$ and PVP/Ir nanoparticles by subtracting the spectra shown above.

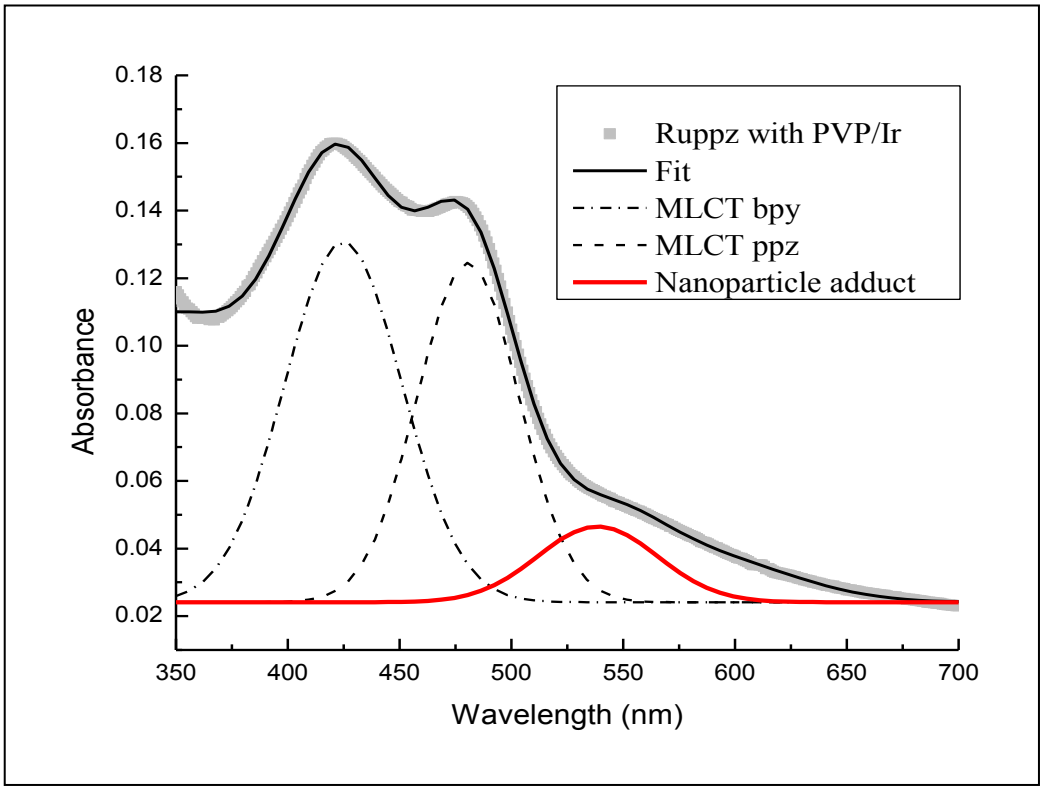

Figure 87. Gaussian Fit using Origin lab 7.0 of the MLCT transition of 1.0 x 10^{-5} M $[Ru(bpy)_2(ppz)]^{2+}$ with 5.6 x 10^{-7} M PVP/Ir nanoparticles in 80% water-ethanol solution at room temperature.

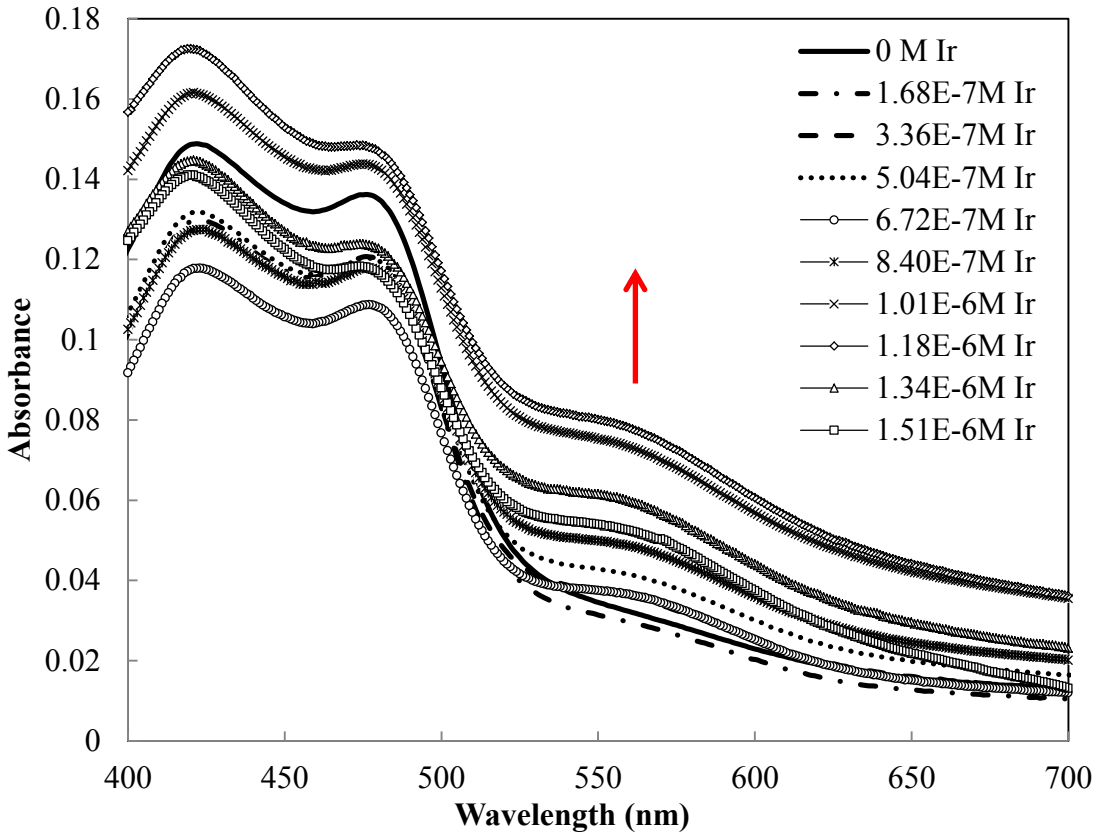

Figure 88. Absorption spectra of 1.4 x 10^{-5} M $[Ru(bpy)_2(ppz)]^{2+}$ with [PVP/Ir] nanoparticles in 80% water-ethanol solution at room temperature.

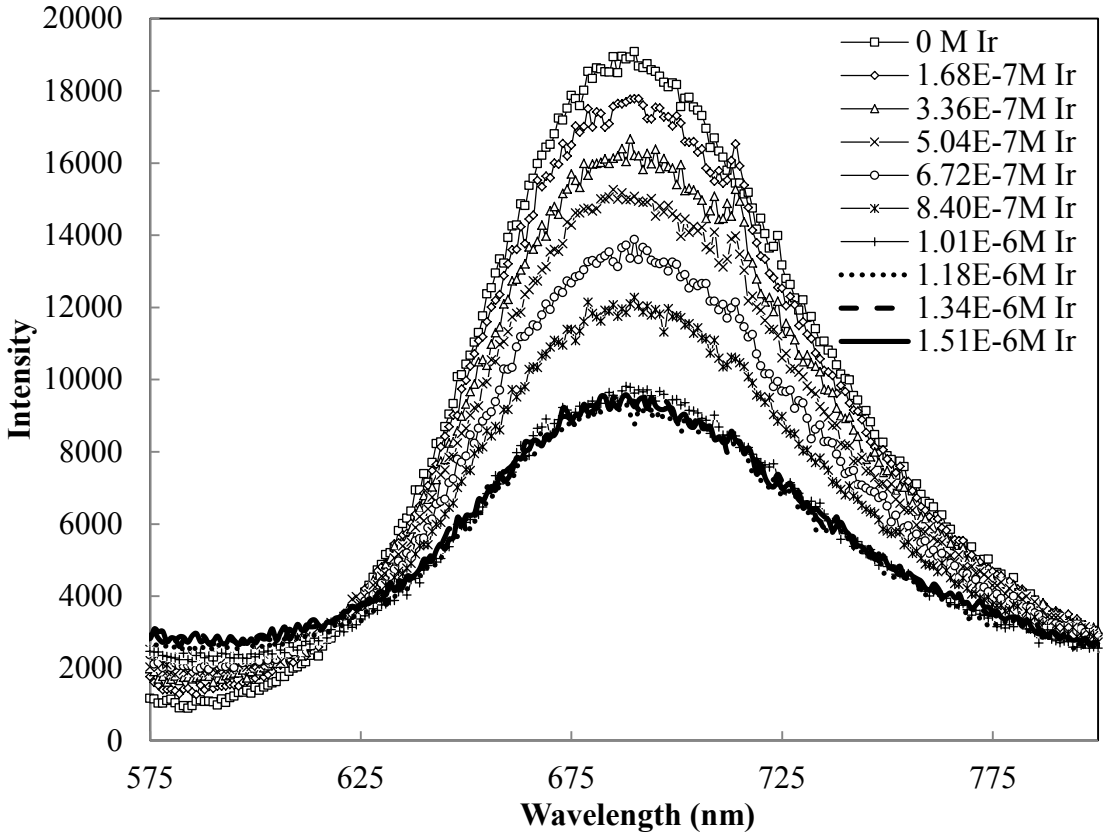

Figure 89. Emission spectra of 1.4 x 10^{-5} M $[Ru(bpy)_2(ppz)]^{2+}$ with [PVP/Ir] nanoparticles in 80% water-ethanol solution at room temperature, with excitation λ of 476 nm. All solutions were deaerated by Argon bubbling for 5 minutes.

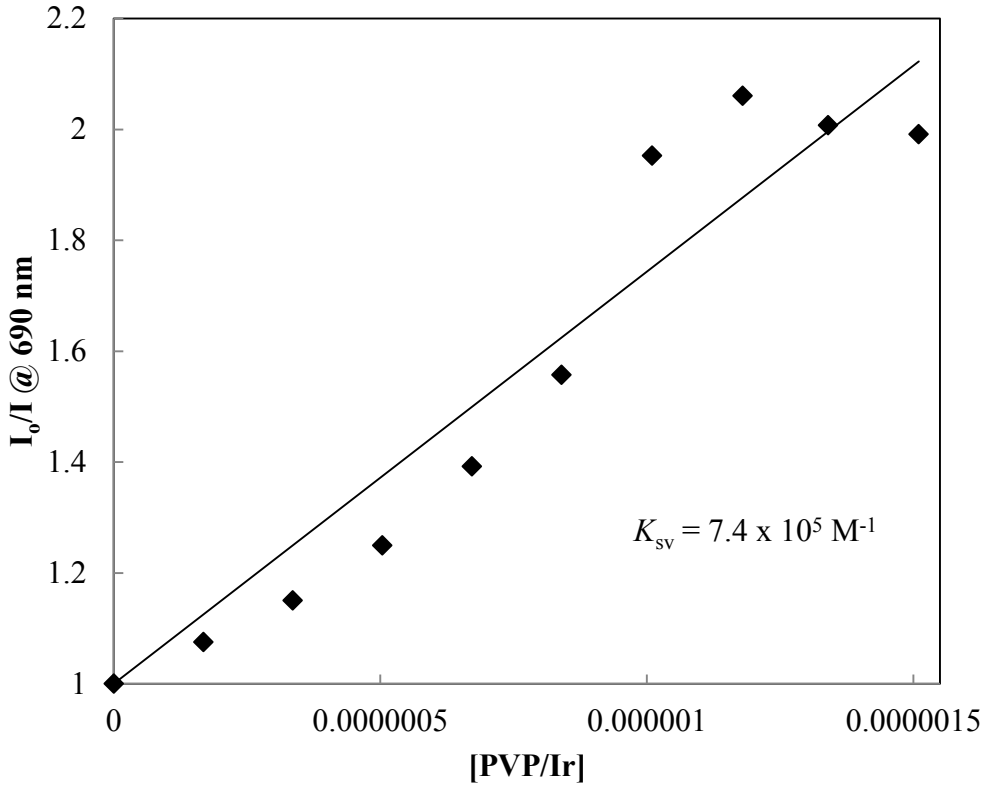

Figure 90. Stern-Volmer Plot of 1.4 x 10^{-5} M $[Ru(bpy)_2(ppz)]^{2+}$ with [PVP/Ir] nanoparticles in 80% water-ethanol solution at room temperature. All solutions were deaerated by Argon bubbling for 5 minutes.

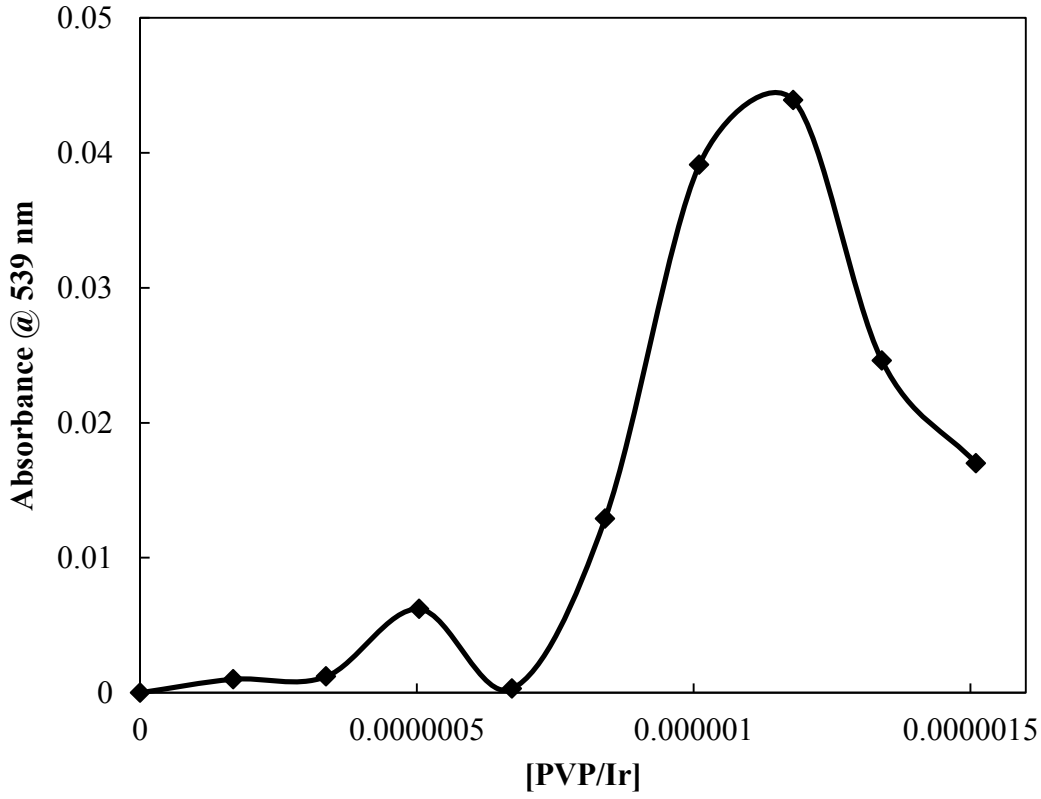

Figure 91. Increase in absorbance at 539 nm as a function of [PVP/Ir] nanoparticles in the presence of 1.4 x 10^{-5} M $[Ru(bpy)_2(ppz)]^{2+}$ in 80% water-ethanol solution.

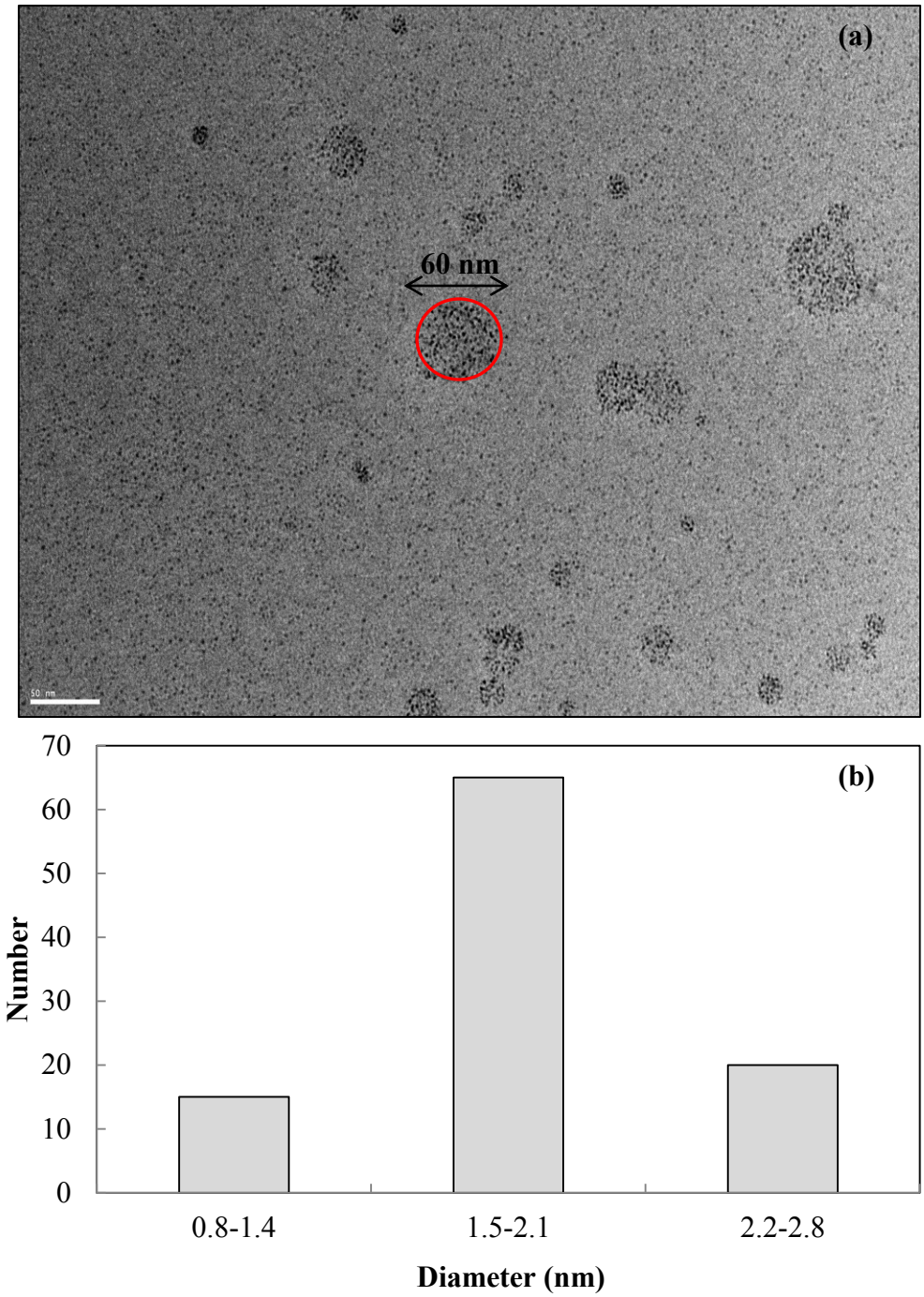

Figure 92. TEM image of (a) 5.6 x 10^{-7} M PVP/Ir nanoparticles (synthesized in ethanol) in the presence of 1.0 x 10^{-5} M $[Ru(bpy)_2(ppz)]^{2+}$ and (b) histogram of the individual PVP/Ir nanoparticles within the aggregate (circled in red) with an average particle size of 1.8 ± 0.3 nm in diameter.

3.10. Association of $[Ru(bpy)_2(ppz)]^{2+}$ with Pt^{2+}

To be certain that the spectral changes observed for the interaction of $[Ru(bpy)_2(ppz)]^{2+}$ with PVP/Pt and PVP/Ir nanoparticles are not due to a trace amount of oxidized Pt or Ir in the nanoparticle solution, a titration experiment was conducted by the addition of a specific amount of K_2PtCl_4 salt to the 2.0 x 10^{-5} M $[Ru(bpy)_2(ppz)]^{2+}$ complex in a sulfuric acid solution adjusted to pH=5. Figure 93 shows the absorption spectra of $[Ru(bpy)_2(ppz)]^{2+}$ with Pt^{2+} salt added. Three intense peaks were detected corresponding to the MLCT to bpy at 420 nm, ppz at 480 nm and the formation of a new band at 555 nm. The absorption of the 555 nm band increased as the concentration of the Pt^{2+} salt added increased.

Quenching of the 690-nm emission of 2.0 x 10^{-5} M $[Ru(bpy)_2(ppz)]^{2+}$ by Pt^{2+} in sulfuric acid solution (Figure 94) exhibits a linear dependence on the concentration of Pt^{2+} salt added with a K_{sv} of 235.4 M^{-1} (Figure 95).

A plot of increase in absorbance at 555 nm *vs.* the concentration of the Pt^{2+} salt is consistent with a single equilibrium fitted to a nonlinear, least-squares equation[121] modeled for one equilibrium (Figure 96).

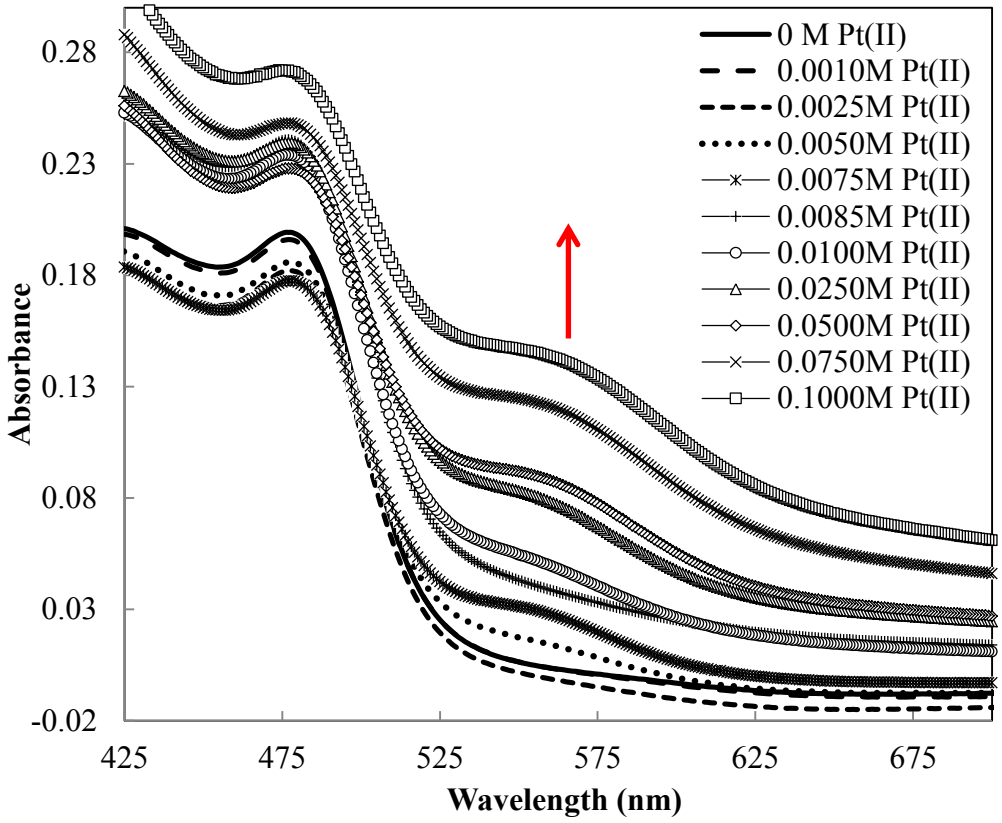

Figure 93. Absorption spectra of 2.0 x 10^{-5} M $[Ru(bpy)_2(ppz)]^{2+}$ with $[K_2PtCl_4]$ salt in sulfuric acid solution adjusted to pH=5 at room temperature.

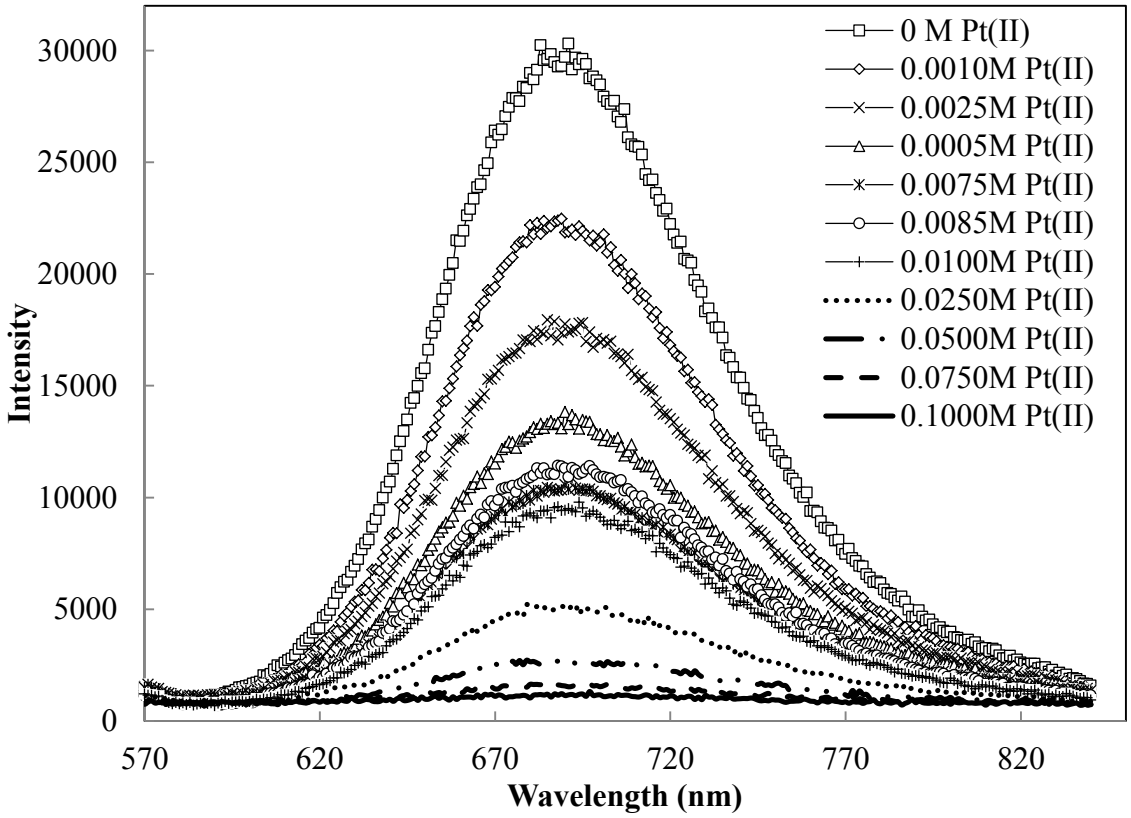

Figure 94. Emission spectra of 2.0 x 10^{-5} M $[Ru(bpy)_2(ppz)]^{2+}$ with $[K_2PtCl_4]$ salt in sulfuric acid solution adjusted to pH=5 at room temperature, with excitation λ of 476 nm. All solutions were deaerated by Argon bubbling for 5 minutes.

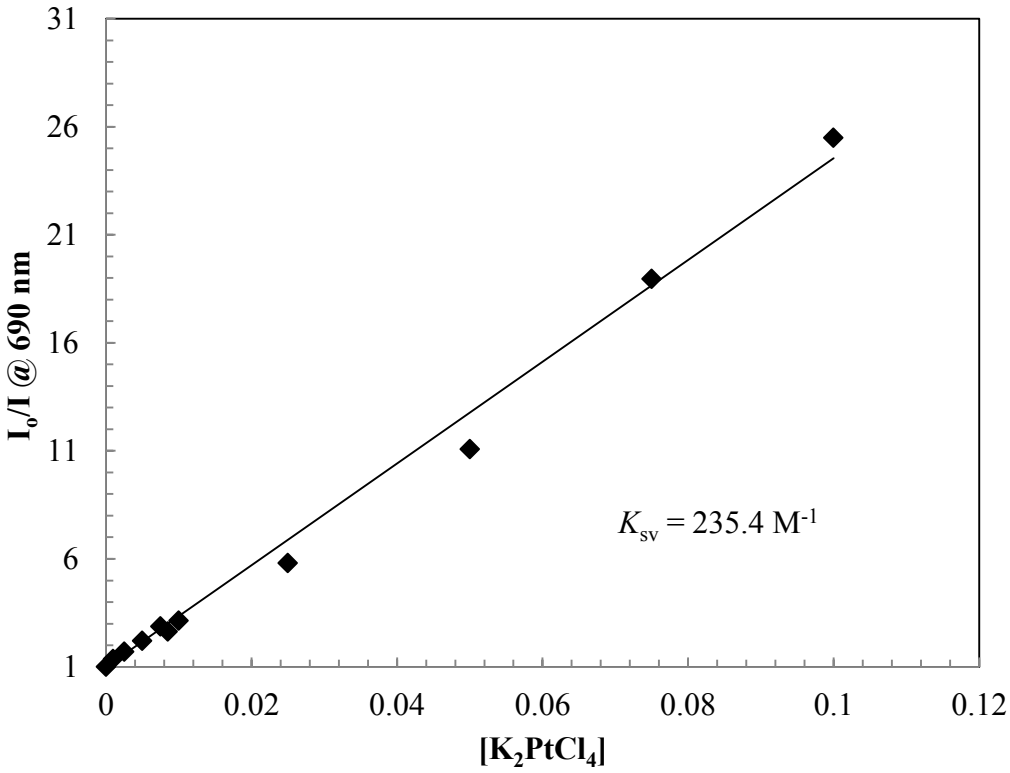

Figure 95. Stern-Volmer Plot of 2.0 x 10^{-5}M $[Ru(bpy)_2(ppz)]^{2+}$ with $[K_2PtCl_4]$ salt in sulfuric acid solution adjusted to pH=5 with K_{sv} = 235.4 M^{-1}. All solutions were deaerated by Argon bubbling for 5 minutes.

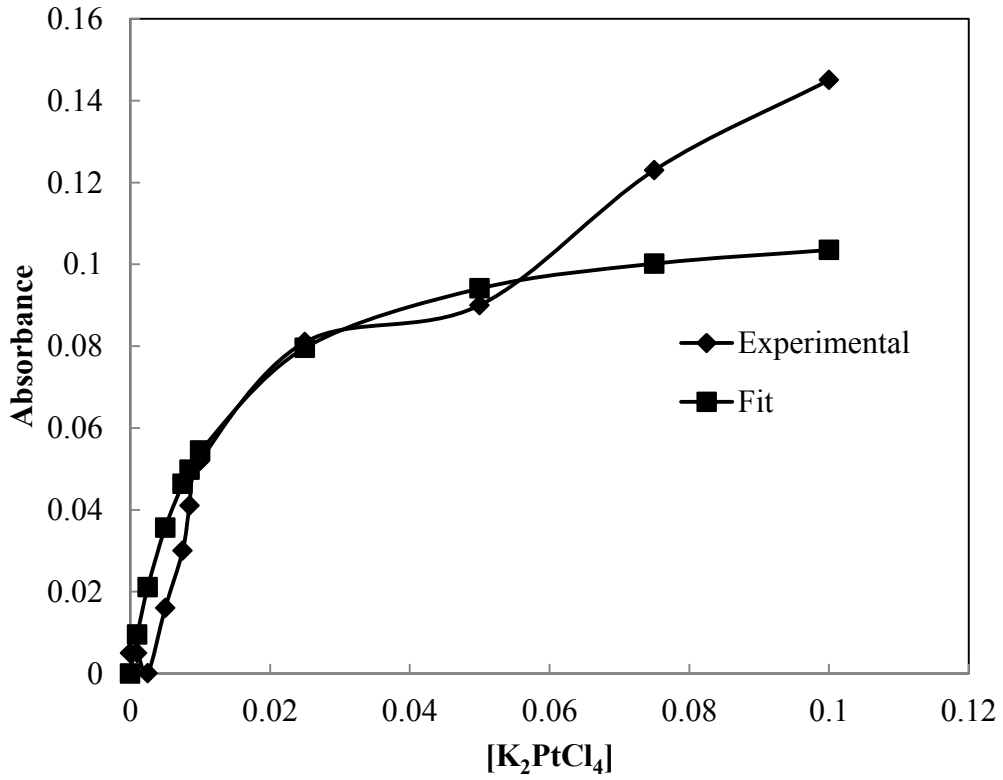

Figure 96. Increase in absorbance at 555 nm as a function of $[K_2PtCl_4]$ salt in the presence of 2.0 x 10^{-5} M $[Ru(bpy)_2(ppz)]^{2+}$ in sulfuric acid solution adjusted to pH=5.

3.11. Association of $[Ru(bpy)_2(dpp)]^{2+}$ with PVP/Pt Nanoparticles

The association of $[Ru(bpy)_2(ppz)]^{2+}$ with PVP/Pt and PVP/Ir nanoparticles in 95% ethanol and 80% water-ethanol solutions produced a new peak at 540 nm and 539 nm, respectively. We wanted to examine if the same type of interaction would take place when $[Ru(bpy)_2(dpp)]^{2+}$ was mixed with PVP/Pt nanoparticles. The chemistry of $[Ru(bpy)_2(dpp)]^{2+}$ (1.00×10^{-4} M) with PVP/Pt nanoparticles (7.88×10^{-7} M) were carried out in distilled water at room temperature. Parts a and b of Figure 97 illustrate the absorption spectra of $[Ru(bpy)_2(dpp)]^{2+}$ with PVP/Pt nanoparticles before and after the PVP/Pt nanoparticles were subtracted. The reaction with the dpp ligand showed a weak intensity shoulder on the low energy side of the dpp MLCT transition. The new band position appeared to be at the same location as the 540-nm and 539-nm bands observed for the interaction of $[Ru(bpy)_2(ppz)]^{2+}$ by PVP/Pt and PVP/Ir nanoparticles. The resolved spectrum in Figure 98 illustrate the appearance of the MLCT bands at 420 nm for bpy, 470 nm for dpp and a 528-nm band indicating an interaction between the $[Ru(bpy)_2(dpp)]^{2+}$ complex and the Pt nanoparticles. To rule out any contribution from the PVP polymer, a reaction between the complex and pure PVP was conducted. Gaussian fit of the absorption spectra show no evidence of a new band at longer wavelength (Figure 99). As seen in Figure 100a, the TEM micrograph shows the PVP/Pt nanoparticles aggregate with the addition of the $[Ru(bpy)_2(dpp)]^{2+}$ complex. The PVP/Pt nanoparticles within the aggregates have an average size of 2.7 ± 0.3 nm obtained from the histogram in Figure 100b. The PVP/Pt aggregates, exhibit a close to circular shape and the remaining Pt clusters does not possess any type of specific shape.

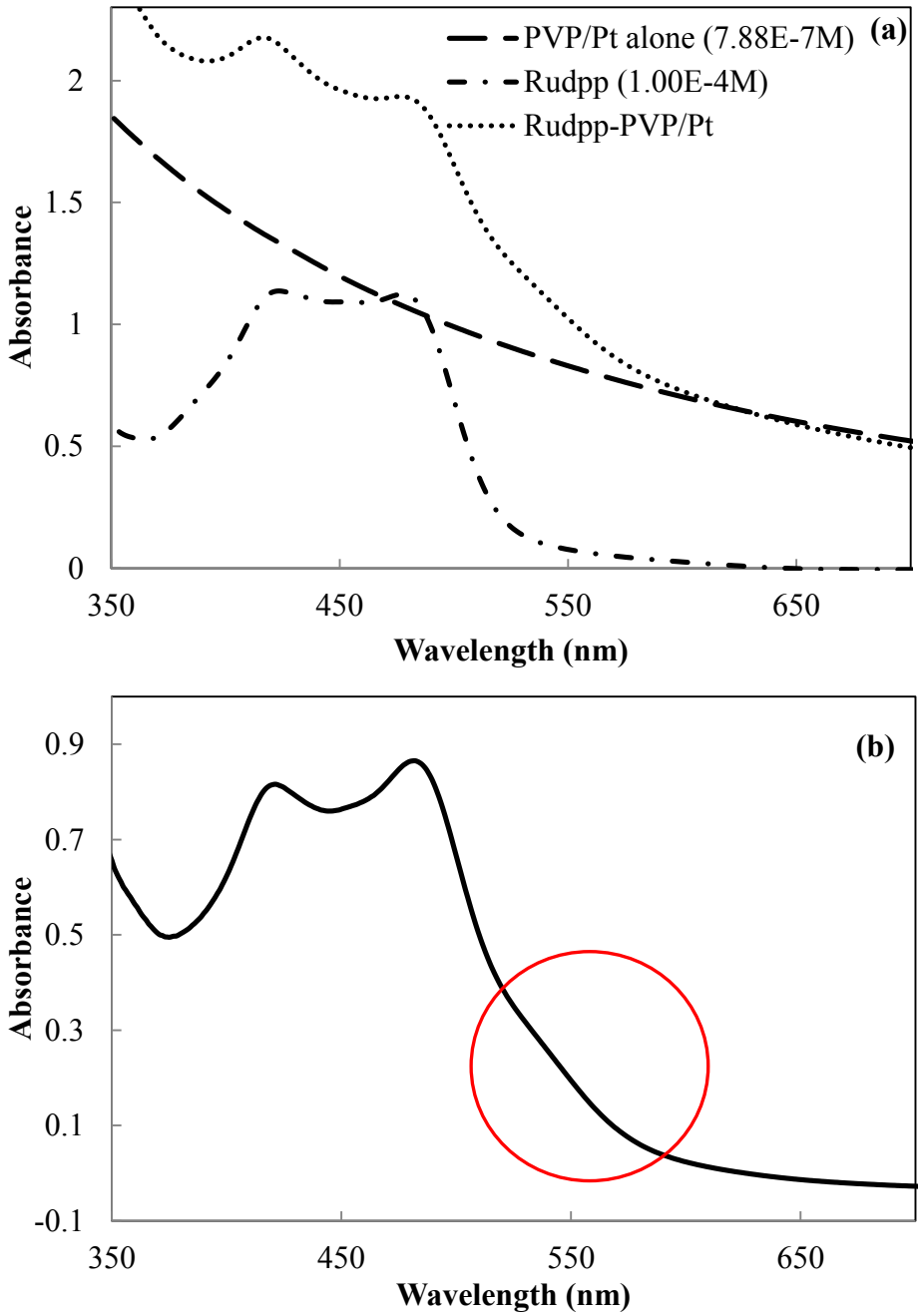

Figure 97. Absorption spectra of (a) reaction between 1.00 x 10^{-4} M $[Ru(bpy)_2(dpp)]^{2+}$ and 7.88 x 10^{-7} M PVP/Pt nanoparticles (synthesized in 95% ethanol) in distilled water at room temperature and (b) association of $[Ru(bpy)_2(dpp)]^{2+}$ and PVP/Pt nanoparticles by subtracting the spectra shown above.

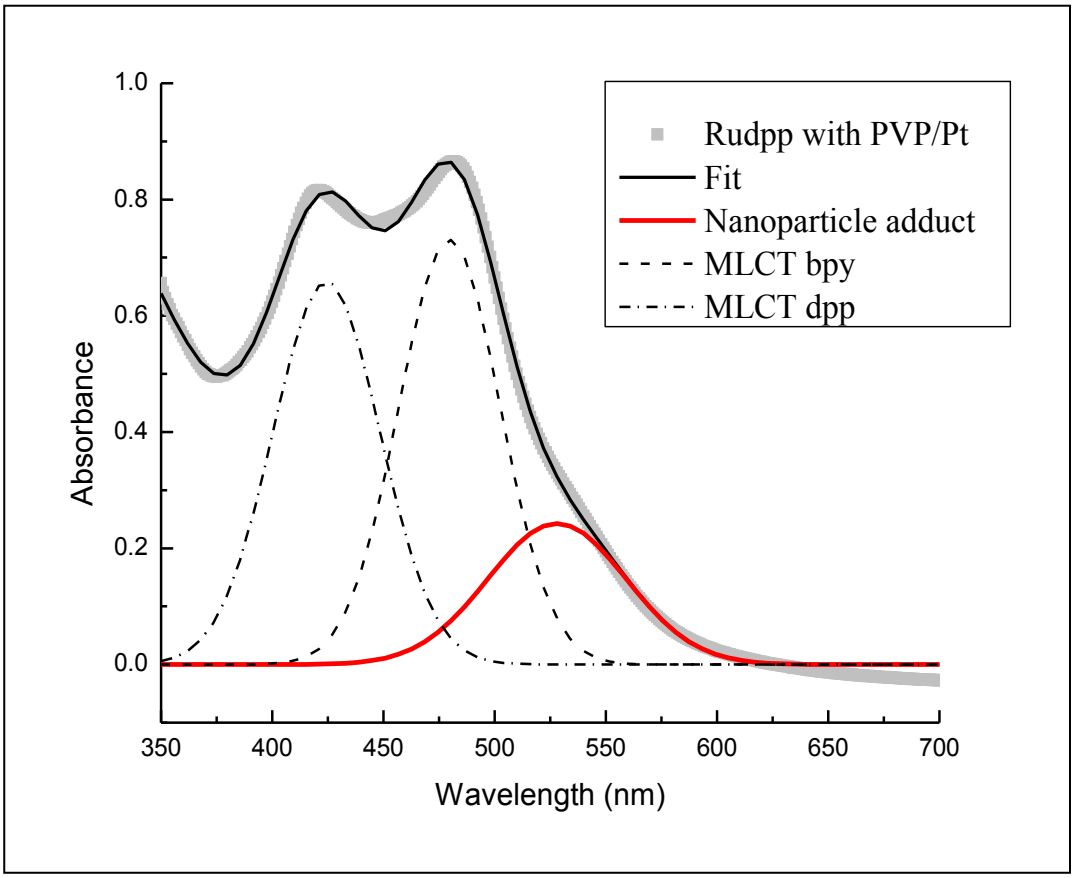

Figure 98. Gaussian Fit using Origin lab 7.0 of the MLCT transition of 1.00 x 10^{-4} M $[Ru(bpy)_2(dpp)]^{2+}$ with 7.88 x 10^{-7} M PVP/Pt nanoparticles in distilled water at room temperature.

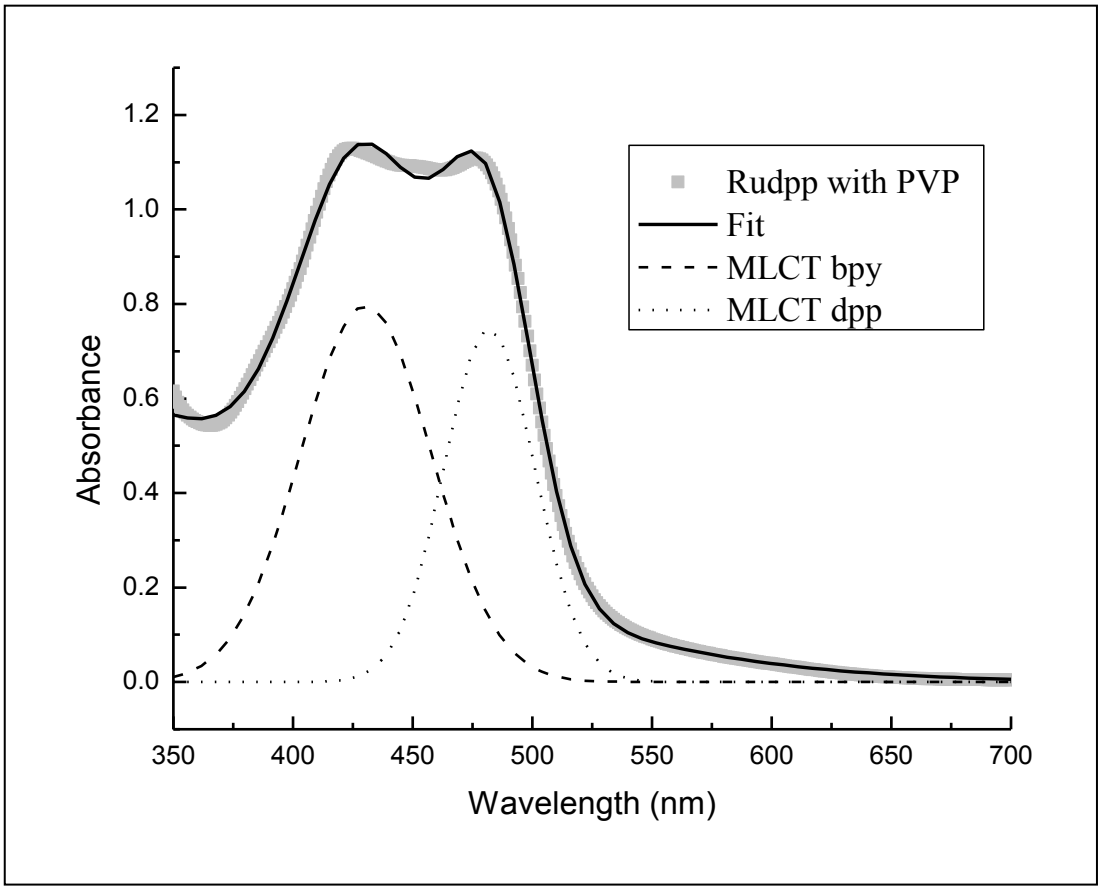

Figure 99. Gaussian Fit using Origin lab 7.0 of the MLCT transition of 1.0 x 10^{-4} M $[Ru(bpy)_2(dpp)]^{2+}$ with 1.0 x 10^{-5} M PVP in distilled water at room temperature.

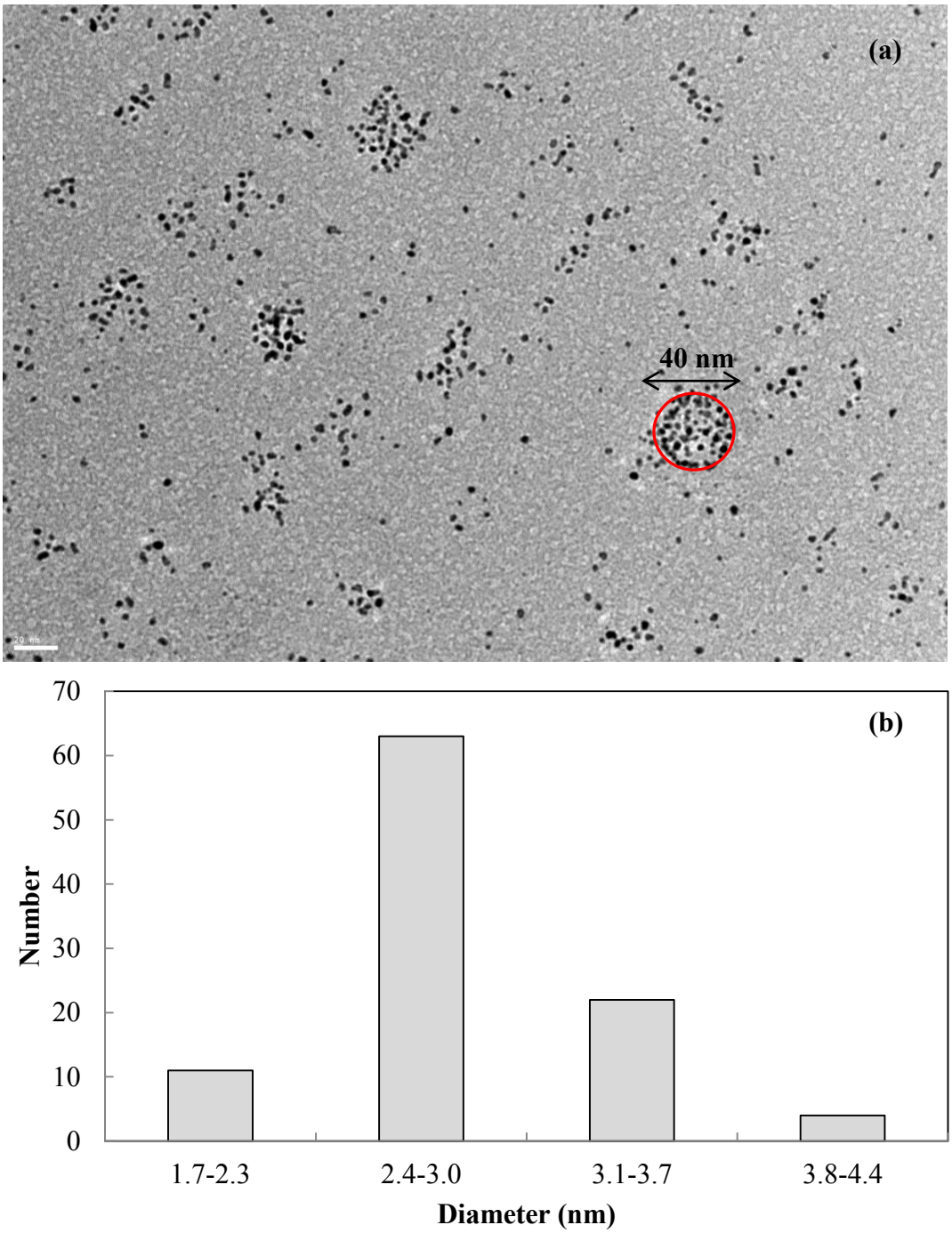

Figure 100. TEM image of (a) 7.88 x 10^{-7} M PVP/Pt nanoparticles (synthesized in ethanol) in the presence of 1.00 x 10^{-4} M $[Ru(bpy)_2(dpp)]^{2+}$ and (b) histogram of the individual PVP/Pt nanoparticles within the aggregate (circled in red) with an average particle size of 2.7 ± 0.3 nm in diameter.

Chapter 4

4. DISCUSSION

4.1. Characterization of PVP/Pt Nanoparticles

The absence of any indication of H_2PtCl_6 in the reaction mixture and the washings of the nanoparticles, the absence of any indication of higher energy absorptions in the XANES spectra, along with the Pt-Pt spacing (Figure 16a inset) that agree with the literature values of the Pt-Pt lattice spacing in the pure Pt metal, establish that the Pt^{4+} ions are completely reduced to Pt^0. However, the absorption spectra of the PVP/Pt nanoparticles after preparation in Figures 13 and 14 (dashed line), exhibits a shoulder at *ca.* 280 nm with an extinction coefficient > 10^6 M^{-1} cm^{-1}, whereas the PVP/Pt shoulder completely disappears in the nanoparticles produced by Rioux et al.[18] Although the 268 nm absorption of H_2PtCl_6 disappears on formation of the Pt nanoparticles, the presence of the shoulder at 280 nm in the vicinity of the absorption of H_2PtCl_6 raises the possibility of not only Pt^{4+}, but also other oxidation states of Pt nanoparticles. Chytil and co-workers,[115] on the other hand, reported a broad shoulder at *ca.* 260-280 nm for Pt nanoparticles after reduction of K_2PtCl_4 and suggest that this is due to the presence of Pt clusters from the excitation of interband transition. Interband (sp-d) transition is a characteristic property of a metallic particle[114,115] and is a transition between the valence band (VB), which leaves a hole in the VB and the conduction band (CB), which places the promoted electron in the CB. It is assumed that the shoulder observed at *ca.* 280 nm in methanol and ethanol (Figures 13 and 14) for the PVP/Pt nanoparticles after preparation is not due to oxidize Pt. Nor is it due to PVP, since PVP has no spectral

signature in the UV-vis region (Figure 15). Rather, as originally assigned by Chytil and co-workers,[115] the shoulder at 280 nm is assigned to Pt^0 clusters on the nanoparticles.

TEM images of the synthesized PVP/Pt nanoparticles deposited onto carbon coated Cu grids and dried in air, show individual particles (Figures 16a and 17a) that appear to be circular. The particle sizes measured with the Image J software and converted to a histogram (Figures 16b and 17b), showed that the size distribution obtained was 3.1 ± 0.4 nm when reduced by methanol (Figure 16b), and 2.7 ± 0.3 nm when reduced by ethanol (Figure 17b). Both are within experimental error of the published values of 2.9 nm and 2.6 nm for reduction with methanol and ethanol, respectively.[18]

The peaks observed in the XRD pattern at 39.9°, 46.4°, 67.7°, 81.6°, and 86.0° (Figures 18 and 19) which correspond to reflections from (111), (200), (220), (311), (222) planes are similar to those of bulk Pt,[122] establishing that regardless of solvent, the alcoholic reduction yields crystalline Pt nanoparticles. The average particle sizes, 28.1 ± 0.1 Å with methanol, and 26.5 ± 0.1 Å with 95% ethanol were calculated using *FWHM* of the XRD peaks in Scherrer's equation.[104] The diameter, B, of the particles is calculated from the equation

$$B = K\lambda/(L \cos \chi/2), \tag{9}$$

where $K = 0.93$ is a constant obtained from the equation,

$$2(\ln 2/\pi)^{1/2} \tag{10}$$

λ, 1.54 Å, is the wavelength of the incident radiation, $\chi/2$ is the Bragg angle in degrees,

$30^o \leq 2\theta \leq 90^o$, and L is the linear dimension of the particle converted to radian using the full width at half maximum (*FWHM*) value given by

$$L = (FWHM \times \pi)/180 \quad (11)$$

The EDS spectra in Figures 21 and 22, correspond to the x-ray energy is similar to the EDS spectra from Xu and co-workers,[123] and establishes the presence of Pt in the isolated nanoparticles.

4.2. Characterization of PVP/Ir Nanoparticles

The absorption spectrum of the PVP/Ir nanoparticles exhibits a broad shoulder at *ca.* 280 nm (ε = 1 x 10^6 $M^{-1}cm^{-1}$) (dashed line) without any indication of the charge transfer bands in the visible region (Figure 23). The absence of the charge transfer bands of H_2IrCl_6, and the absence of a shift to higher energy in the XANES spectra, suggests that the Ir^{4+} ions are completely reduced to Ir^0 by the alcoholic reduction preparation, *i.e.,* the shoulder at *ca.* 280 nm is not due to Ir^{4+}. For example, Creighton and Eadon[114] calculated the absorption spectrum of 10-nm diameter Ir particles in a dielectric medium with a refractive index equal to that of water, and found a shoulder at *ca.* 350 nm. The authors assign the 350-nm band to Ir clusters. Keep in mind that the PVP/Ir nanoparticles prepared in our laboratory with an average particle diameter of 1.8 ± 0.3 nm exhibit a shoulder at *ca.* 280 nm (Figure 23). So, the presence of the 280 nm band in the absorption spectrum of the PVP/Ir nanoparticles is dependent on particle size and is not due H_2IrCl_6 salt remaining in the sample.

Transmission electron microscopy (TEM) images of the PVP/Ir nanoparticles show discrete particles (Figure 24a) and the TEM histogram (Figure 24b) yield an

average particle size of 1.8 ± 0.3 nm in diameter. The HRTEM image of the PVP/Pt-Ir nanoparticles previously described (Figure 33), show a lattice distance of 2.20 Å from the diffraction pattern observed. This value is within experimental error of the calculated lattice spacing of 2.21 Å for bulk Ir.[124] So, the PVP/Ir nanoparticle does appear to be as crystalline as the PVP/Pt nanoparticles.

The PVP/Ir XRD pattern produced one broad peak at 40.8°, and three low intensity peaks at 47.4°, 69.3° and 83.6° (Figures 25) which corresponds to the reflections from (111), (200), (220), (311) planes, respectively.[124] The particle size calculated from the peak at 40.8° using the *FWHM* in Scherrer's equation,[104] 20.2 Å, is within experimental error of the particle size obtained from the TEM image.

The EDS spectrum in Figure 27 agrees with the results of the EDS spectra by Chrisanti,[125] and confirms the presence of Ir in the isolated nanoparticles.

4.3. Characterization of PVP/Pt-Ir Nanoparticles

After refluxing the PVP/H_2PtCl_6 and PVP/H_2IrCl_6 salts, the absorption spectrum (dashed line) shows a shoulder at *ca.* 280 nm (Figure 28). The presence of the shoulder at *ca.* 280 nm in the vicinity of the absorption of H_2PtCl_6 suggests that there might be unreduced H_2PtCl_6 salt in the sample, but according to Chytil and co-workers,[115] in Section 4.1, the shoulder observed at *ca.* 280 nm is attributable to the interband transitions from the formation of Pt clusters and not due to oxidized Pt. The absence of the lower energy Ir charge transfer bands, and assuming the shoulder observed at *ca.* 280 nm is due to Pt^0, suggests that the PVP/H_2PtCl_6 and PVP/H_2IrCl_6 salts have been reduced to the zero charge state PVP/Pt-Ir nanoparticles.

Aggregation of the PVP/Pt-Ir nanoparticles was analyzed by TEM. Individual particles appear spherically shaped (Figure 29a). The average particle size of 1.9 ± 0.3 nm was obtained from the histogram (Figure 29b). Because of the similarities in the densities of 21.450 g/cm^3 for Pt and 22.560 g/cm^3 for Ir,[109] HRTEM failed to identify if a core shell material was present in the PVP/Pt-Ir sample. If the densities between Pt and Ir were much further apart, the electron beam would penetrate the sample depending on its density and a combination of darker and lighter areas in the image would be observed in the nanoparticle, to indicate a core shell material.

The powder x-ray diffraction pattern of the PVP/Pt-Ir nanoparticles (Figure 30) exhibit four peaks at 39.9^o, 46.4^o, 67.7^o, and 81.6^o for Pt, and four peaks at 40.8^o, 47.4^o, 69.3^o and 83.6^o for Ir. These are within experimental error of the reflections from FCC Pt and Ir and correspond to the reflections from the (111), (200), (220) and (311) planes.[126,127] The average particle size of the Pt-Ir nanoparticles calculated from the peak at 39.9^o for Pt and 40.8^o for Ir is 21.9 Å, within experimental error of the size obtained from the TEM histogram of the PVP/Pt-Ir nanoparticles.

EDS analysis establishes that Pt and Ir are present in the nanoparticle sample (Figure 32), similar to that in previously published data.[128] However, XANES and EXAFS failed to distinguish whether the PVP/Pt-Ir nanoparticle is a core shell or an alloy.

The HRTEM image shows a diffraction pattern corresponding to Ir (Figure 33), the experimental Ir-Ir lattice distance of 2.20 Å is within 0.01 Å of the calculated Ir-Ir lattice spacing of 2.21 Å for bulk Ir,[124] and XRD and EDS analyses confirm the presence

of Pt and Ir in the sample. This establishes that the PVP/Pt-Ir nanoparticles are composed of a mixture of individual Pt and individual Ir nanoparticles.

4.4. Adsorption of PVP/Pt Nanoparticles into PVG

The appearance of a shoulder at *ca.* 280 nm in the absorption spectra obtained by subtraction of the PVG background after adsorption of the PVP/Pt nanoparticles (Figures 35b and 36b), suggests that the PVP/Pt nanoparticles, whether synthesized in methanol or ethanol, will adsorb into the porous Vycor glass without oxidation or further aggregation. Also, the light brown appearance after exposing the PVG to a solution of the PVP/Pt nanoparticles establishes adsorption of the nanoparticles into the glass.

EXAFS was used to determine the metal-metal bond length and identification of the nanoparticles. EXAFS is advantageous over conventional XRD because synchrotron radiation energy range is tunable and has higher intensity (10^6 times) than from x-ray tubes, less time is required to run a sample (10-15 minutes), a trace amount of sample is required for detection, and liquid, solid (crystalline and amorphous materials), and gaseous samples may be used.[118] XRD measurements are limited to crystalline solid samples, relatively large amounts of sample are needed, and it takes much longer, *ca.* 2-8 hours to obtain the best signal-to noise ratio.[118]

XANES was used to determine the oxidation state of the adsorbed PVP/Pt nanoparticles in the glass. Figure 38 shows the normalized XANES spectra of the Pt foil and the PVP/Pt nanoparticles before and after adsorption into the polished and rolled porous Vycor glasses. Take into account, Corning's code 7930 porous Vycor glass has a pore size of 10 ± 1 nm,[53] and the PVP/Pt nanoparticles have an average particle size of

3.1 ± 0.4 nm in diameter, so the nanoparticles can impregnate the glass. The PVP/Pt nanoparticles before and after impregnation into the PVG exhibited threshold energies at 11561.8 ± 0.3 eV and 11563.0 ± 0.3 eV, respectively. The PVP/Pt nanoparticle edge energy is shifted to lower energy than the foil, which contains only Pt^0, therefore the 1.2 ± 0.6 eV shift to the left of the absorption edge region of the PVP/Pt nanoparticles before impregnation is attributed to experimental errors. XANES analysis was also performed on the H_2PtCl_6 salt used in this project. H_2PtCl_6 exhibited a threshold energy at 11567.0 ± 0.3 eV, obtained from the first maximum of first derivative spectra. The threshold energy of the Pt^{4+} salt is shifted to 4 eV in comparison the Pt foil. The foil has an oxidation state of zero and it is exactly the same energy as the PVP/Pt nanoparticles impregnated in the glass, so we can conclude that there is no change to the oxidation state of zero in the PVP/Pt nanoparticles before impregnation into the porous Vycor glass because the threshold energy of the PVP/Pt nanoparticles do not shift to higher energies.

For example, Bera and co-workers[117] presented the XANES spectra of Pt metal (Pt^0), Pt acetyl acetonate (Pt^{2+}) and platinum oxide (Pt^{4+}). The edge energy determined from the XANES spectra shifted to higher energies with increasing oxidation state of the Pt. It was found to be 11561.0 eV for Pt metal, and it was shifted to 11561.9 and 11562.9 eV for Pt^{2+} and Pt^{4+}, respectively. Therefore the change to higher energy as a function of an increase in oxidation state of the Pt^0 to Pt^{2+} to Pt^{4+} is approximately 1 and 2 eV. The Pt-Pt bond distance is 2.758 ± 0.004 Å for Pt^0, 3.040 Å for Pt^{2+} and 3.153 ± 0.002 Å for Pt^{4+} with coordination numbers at 12, 4 and 3.7, respectively.[117] Consequently, as the Pt oxidation state increases, the Pt-Pt bond distance also increased as a function of the

decrease in coordination numbers.

Silica has the ability to oxidize metal atoms or small aggregates of metals because of the water molecules present in the glass. The oxidation state of zero of the PVP/Pt nanoparticles adsorbed into the PVG was not affected by the water molecules since no shift to higher energies is observed in comparison to the Pt foil. This could be due to the PVP surfactant protecting the core platinum nanoparticle from being oxidized. The PVP/Pt nanoparticles before and after adsorption into the PVG retained their zero oxidation state by this simple solution adsorption technique.

Figures 40-43 show the Fourier transform of the EXAFS data of Pt foil and PVP/Pt nanoparticles before and after impregnation into polished and rolled PVG. The strongest peak in the spectrum represents the first-neighbor shell and the Pt-Pt bond distance is obtained from it without the phase shift correction. Phase shift occurs due to coulomb interaction when the photoelectron travels back and forth between the neighboring atoms and the central atom. In addition, there is also a backscattering contribution.[113] The phase shift causes the sine wave or oscillation from the interaction of the neighboring atom and the central atom to shift the origin of the wave, *i.e.,* it no longer starts at $k = 0$. The phase shift correction is constant for same type of central atoms and near neighbor atoms. To obtain the true bond distance of the Pt-Pt nanoparticles, the phase shift must be corrected.[129,130] This is done by subtracting the experimental bond length of the Pt foil of 2.06 ± 0.01 Å obtained from the EXAFS fitting (Figure 40) from the bulk Pt value of 2.78 Å found in the literature.[131] The result from the subtraction is then added to the experimental data of the Pt-Pt bond distance obtained from the

strongest peak in the Fourier transform of the EXAFS data of the PVP/Pt nanoparticles before and after adsorption into the polished and rolled PVG (Figures 41-43). The true bond distance after the phase shift correction for the PVP/Pt nanoparticles before and after adsorption into the glass is 2.76 ± 0.01 Å which is within experimental error of the Pt foil of 2.78 ± 0.01 Å. EXAFS data confirms that before and after impregnation of the PVP/Pt nanoparticles into the silica matrix, the Pt-Pt bond distance of the PVP/Pt nanoparticles does not change.

4.5. Adsorption of PVP/Ir Nanoparticles into PVG

The light brown appearance of the PVG (Figure 45) shows that the PVP/Ir nanoparticles impregnate the glass, similarly to the color change that occurs when PVP/Pt nanoparticles are impregnated in the PVG.

The threshold energy for the PVP/Ir nanoparticles before and after impregnation in the glass, equal to 11214.0 ± 0.3 eV, are obtained from the first maximum of the first derivative spectra (Figure 47), in comparison with Ir foil. Choy and co-workers[132] applied XANES spectroscopy to examine the effect that the absorption L_3-edge energy has on the +4, +5 and +6 oxidation states of iridium oxide in the perovskites, A_2BIrO_6, where A= Ba, Sr, and La; and B = Zn, Mg, Y Ca, Li and Sr. The absorption edge in the normalized XANES spectra for these oxidation states shifted to higher energies and the Ir-O bond distance decreases as the oxidation state increased. Therefore, the absence of a threshold energy shift to higher energies for iridium in XANES, confirms that adsorbing the PVP/Ir nanoparticles into porous Vycor glasses does not change zero oxidation state

nanoparticles even though the water molecules present in the PVG has the capability to oxidize the particles.

After the phase shift correction, the Ir-Ir bond length extracted from the Fourier transform of the EXAFS data of the PVP/Ir nanoparticles before and after impregnation into polished PVG (Figures 49 and 50) were calculated to be 2.41 ± 0.01 Å, which is 0.3 Å slightly shorter than the Ir-Ir bond distance of 2.71 ± 0.01 Å in Ir foil.[131] Miller and co-workers[133] studied the Au-Au bond length of gold particles supported on silica and alumina. They found that as the size of the nanoparticles decreased to less than 30 Å, the contraction in the metal-metal bond length was due to their larger surface area. The authors also noted that the contraction of the Au-Au bond length is independent of the type of support. Therefore, the shorter Ir-Ir bond length is not an error in measurement or calculation but is due to the larger surface area of the PVP/Ir nanoparticles.

This *bottom-up* approach of the solution adsorption technique for introducing the PVP/Ir nanoparticles into porous Vycor proves to be very effective for studying the particles in a substrate without changing the particles themselves. Not only does this method not change the Ir-Ir bond distance but the zero oxidation state of the nanoparticles remains unaffected within a face-centered cubic crystal system.

4.6. Adsorption of PVP/Pt-Ir Nanoparticles into PVG

The subtraction of the spectrum of the PVG background after adsorption of the PVP/Pt-Ir nanoparticles shows a broad shoulder at *ca.* 280 nm (Figure 51b), similar to the shoulder observed at *ca.* 280 nm after subtraction of the spectra of the PVG impregnated with the PVP/Pt and PVP/Ir nanoparticles. Because the TEM images of the PVG

impregnated with the PVP/Pt-Ir nanoparticles did not show any evidence of the presence of nanoparticles, the absence of a shift of the 280-nm band to longer wavelengths establishes that the PVP/Pt-Ir nanoparticles adsorb without additional aggregation.

As shown in Figure 52, the EXAFS spectra of the Pt-Ir foil (80:20 wt%) resembles the spectra of the PVP/Pt-Ir nanoparticles before impregnation into the PVG and also resembles the spectrum of the PVP/Pt-Ir nanoparticles after impregnation into the polished PVG. The threshold energy of the Pt portion from PVP/Pt-Ir nanoparticles impregnated in the glass is 11563.0 ± 0.3 eV and the Pt portion from the Pt foil is also 11563.0 ± 0.3 eV, as obtained from the first maximum of the first derivative spectra (Figure 54). The absence of a threshold energy shift to higher energies in the XANES spectra (Figure 53), suggest that there is no change to the zero oxidation state of the Pt portion from the adsorbed PVP/Pt-Ir nanoparticles in PVG as compared to that from the Pt-Ir foil.

The Fourier transform of the EXAFS data of the Pt portion from the Pt-Ir foil (80:20 wt%), yields a Pt-Pt bond distance of 2.06 ± 0.01 Å (Figure 55). The Pt-Pt bond distance extracted from the EXAFS fitting for the PVP/Pt-Ir nanoparticles before and after adsorption into PVG, without the phase shift correction is 2.04 ± 0.01 Å (Figures 56 and 57), and after the phase shift correction is 2.76 ± 0.01 Å, which is equal to the Pt-Pt bond distance of the individual PVP/Pt nanoparticles previously described (Section 4.4). Given that the Pt-Pt bond distances for the Pt portion of PVP/Pt-Ir nanoparticles before and after impregnation into the polished PVG is identical to the individual Pt-Pt bond distance in the PVP/Pt nanoparticles previously described (Section 4.4), it may be

inferred that the Pt nanoparticles are not bonded to the iridium nanoparticles but are only attached to platinum.

The edge energy of the Ir portion from the PVP/Pt-Ir nanoparticles before impregnation into the glass is 11214.0 ± 0.3 eV and the Ir portion from the adsorbed nanoparticles in the glass is 11214.0 ± 0.3 eV. Both exhibit energies equal to that of the Ir portion from the Pt-Ir foil. The absence of a threshold energy shift to higher energy in the normalized XANES spectrum (Figure 58) illustrates that there is no change in the oxidation state of zero in the iridium nanoparticles from a mixture composed of PVP/Pt-Ir nanoparticles.

The Fourier transform of the EXAFS data of the Ir portion from the Pt-Ir foil is depicted in Figure 60, and yields an Ir-Ir bond distance of 2.04 ± 0.01 Å. The Ir-Ir bond distance obtained from the EXAFS fitting (Figures 61 and 62) for the PVP/Pt-Ir nanoparticles before and after adsorption into the PVG, without the phase shift correction is 1.74 ± 0.01 Å, and after the phase shift correction is 2.41 ± 0.01 Å, which is also equal to the Ir-Ir bond distance of the individual PVP/Ir nanoparticles previously described (Section 4.5). Since the Ir-Ir bond distance for the Ir portion from PVP/Pt-Ir nanoparticles is identical to the individual Ir-Ir bond distance in the PVP/Ir nanoparticles aforementioned, it suggests that the Ir nanoparticles are not attached to the platinum nanoparticles but are only bonded to iridium.

PVP/Pt-Ir nanoparticles prepared by an alcohol reduction method were analyzed by XANES and EXAFS to determine if the mixture is composed of a core-shell nanoparticle, an alloy or a mixture composed of individual platinum and individual

iridium nanoparticles. The similarities in the Pt-Pt and Ir-Ir bond distances obtained for the Pt and Ir portion from the PVP/Pt-Ir nanoparticles in comparison to the bond lengths obtained from the individual Pt and Ir nanoparticles, suggest that a core shell material or an alloy was not produced and that the PVP/Pt-Ir nanoparticles sample contains a mixture of individual platinum and individual iridium nanoparticles.

4.7. PVP removal from adsorbed PVP/Pt nanoparticles into PVG

Since silica can act as an oxidizing matrix because of the water molecules present, the absence of a threshold energy shift (11563.0 ± 0.3 eV) to higher energies in the XANES data, confirms that adsorbing the PVP/Pt nanoparticles into Corning's code 7930 porous Vycor glass and removal of the PVP surfactant shows no change in the oxidation state of zero of the Pt nanoparticles as compared to the Pt foil.

As previously explained in Section 4.4, the Fourier transform magnitude *vs.* the radial distance (Å) of the PVP/Pt nanoparticles impregnated into the PVG yield a Pt-Pt bond length of 2.76 ± 0.01 Å (Figures 42 and 43) and is 0.02 Å shorter than the Pt-Pt bond length, from Pt foil, of 2.78 ± 0.01 Å. However, the EXAFS fitting of the PVP/Pt nanoparticles impregnated into the PVG after PVP removal yield a Pt-Pt bond length of 2.74 ± 0.01 Å after phase shift correction (Figure 65), and so is within experimental error of the Pt-Pt bond length of the Pt foil. If there is an increase in the Pt nanoparticle size after PVP extraction, the peak at *ca.* 280 nm in the absorption spectrum of the impregnated PVG after PVP removal (Figure 66) would be shifted to longer wavelengths. The absence of a shift at 280-nm band to longer wavelengths of the impregnated PVG after PVP removal suggests that there is minimal Pt nanoparticle aggregation.

The FTIR spectra of the extracted PVP versus the pure PVP are depicted in Figure 67. The shift of the carbonyl absorption of the extracted PVP is due to hydrogen bonding,[119] either from the water molecules used in the extraction technique or from the water molecules absorbed from the atmosphere. Three other peaks in the FTIR spectra can also be easily identified for both extracted PVP and pure PVP. The peak at 1490 cm^{-1} corresponds to C-N region. The CH_2 scissor region has an intense peak at 1460 cm^{-1} and the 1376 cm^{-1} peak is assigned to the CH bend region which is similar to those of previous studies.[105] Since the carbonyl vibration at 1668 cm^{-1} for pure PVP is shifted to 1632 cm^{-1} in the extracted PVP, and this 36 cm^{-1} shift is not due to a change in the structure but of hydrogen bonding, we can conclude that there is no change in the PVP structure after extraction.

Five pieces of rolled porous Vycor glasses were impregnated with the PVP/Pt nanoparticles and it took as long as 60 days to extract 0.0046 ± 0.0004 g of the PVP from the glasses. The results from the Soxhlet extraction technique for the amount of PVP extracted from the PVP/Pt nanoparticles adsorbed in the glass and heating at varying temperatures were tabulated (Tables II-V). Experimental data collected suggest that the water has completely evaporated because the amount of the extracted PVP, 46 ± 4%, remained constant after the final heating of 13 days (Table V). Even though the extraction time was long, and perhaps more PVP would have been extracted if the impregnated glasses were left in Soxhlet extractor for a longer period of time, the Soxhlet extraction method was safe, easy to use and was effective in removing the PVP.

4.8. $[Ru(bpy)_2(dpp)]^{2+}$ and $[Ru(bpy)_2(ppz)]^{2+}$ in PVG with PVP/Pt Nanoparticles

The chemistry of 1 x 10^{-5} M $[Ru(bpy)_2(dpp)]^{2+}$ and 6.8 x 10^{-6} M $[Ru(bpy)_2(ppz)]^{2+}$ in acetonitrile impregnated in the PVG with the Pt nanoparticles that were stripped of PVP, was investigated. The amount of $[Ru(bpy)_2(dpp)]^{2+}$ and $[Ru(bpy)_2(ppz)]^{2+}$ impregnated into the glasses were 8.4 x 10^{-8} mol/g and 7.1 x 10^{-8} mol/g, respectively. The number of moles of compound adsorbed, N_{ads}, was calculated from the change in the absorbance of the impregnating solution, as given by,

$$N_{ads} = ((A_i - A_f)/A_i) * n_i \quad (12)$$

where A_i is the absorbance at 420 nm of the $[Ru(bpy)_2(L)]^{2+}$ (L = dpp or ppz) solution before impregnation, A_f is the absorbance at 420 nm of the $[Ru(bpy)_2(L)]^{2+}$ solution after impregnation, and n_i is the number of moles of $[Ru(bpy)_2(L)]^{2+}$ in solution before impregnation. Therefore, the number of moles of $[Ru(bpy)_2(L)]^{2+}$ adsorbed per gram of PVG is equal to the number of moles of compound adsorbed, N_{ads}, divided by the weight of the PVG before impregnation.

The absorption spectrum of 1 x 10^{-5} M $[Ru(bpy)_2(dpp)]^{2+}$ complex impregnated in the PVG with the stripped Pt nanoparticle after subtracting the spectrum of the glass exhibits a peak at 420 nm and another at 470 nm (Figure 68a). These peaks correspond to the MLCT transition to bpy and dpp, respectively.[85] Similarly, the absorption spectrum of 6.8 x 10^{-6} M $[Ru(bpy)_2(ppz)]^{2+}$ impregnated in the PVG with the stripped Pt nanoparticles after subtracting the spectrum of the PVG (Figure 70a), exhibits two localized MLCT bands, one at 420 nm corresponding to bpy and the other at 480 nm corresponding to ppz.[73] The absence of new bands in the vicinity of the MLCT transitions in the resolved

absorption spectra (Figures 68b and 70b), suggests that there is no association of the Pt nanoparticles to the dpp and the ppz ligands of the Ru complexes. The lack of association of the $[Ru(bpy)_2(dpp)]^{2+}$ and $[Ru(bpy)_2(ppz)]^{2+}$ complexes with the stripped Pt nanoparticles also implies that the Ru(II) complexes and the PVP/Pt nanoparticles are not in molecular contact with each other or both are in different parts of the glass, thus prohibiting any interactions.

The absorption spectrum of 1 x 10^{-5} M $[Ru(bpy)_2(dpp)]^{2+}$ impregnated in the glass in the presence of the unstripped PVP/Pt nanoparticles after subtracting the spectrum of the glass is shown in Figure 69a. The amount of $[Ru(bpy)_2(dpp)]^{2+}$ impregnated in the glass is 5.7 x 10^{-8} mol/g. The absence of an additional band beyond the wavelength region of the dpp ligand of the Ru complex upon resolution of the absorption spectrum (Figure 69b), suggests that there is no association between the Pt nanoparticle and the Ru(II) complex. Since, there was no evidence to suggest that the Ru(II) diimines interacted with the stripped or unstripped Pt nanoparticles in PVG, it was deemed necessary to perform the experiments in fluid solutions.

4.9. Association of $[Ru(bpy)_2(ppz)]^{2+}$ with PVP/Pt Nanoparticles

Self-assembly refers to the spontaneous aggregation of smaller molecules into larger ordered aggregates.[134-136] In the absence of a template, self-assembly is thought to occur via intermolecular hydrogen bonding, hydrophobic or hydrophilic interactions, and/or dipole-dipole interactions between the assembling reagents.[137] The absence of any indication of nanoparticle aggregation in the absence of the Ru(II) diimine (Figure 16a) precludes aggregation of the PVP/Pt nanoparticles and subsequent incorporation of the

Ru(II) diimine.

After subtracting the spectrum of the $[Ru(bpy)_2(ppz)^{2+}$-PVP/Pt] from the spectrum of the PVP/Pt nanoparticles, relative to the 420 nm bpy localized transition, the intensity of the 476 nm ppz localized MLCT absorption is reduced, and leads to appearance of a shoulder on the low energy side of the transition (circled in red) (Figure 71b). Resolution of the spectral changes (Figure 72) reveals a new absorption band at 540 nm when the PVP/Pt nanoparticles is added to the $[Ru(bpy)_2(ppz)]^{2+}$ complex. The spectral data suggests that the 540 nm band (Figure 72) does not arise from the surface plasmon of the Pt clusters or from the PVP surfactant. Because the extinction coefficient at 540 nm for the PVP/Pt nanoparticles in the absence of the $[Ru(bpy)_2(ppz)]^{2+}$ complex is 1 x 10^6 $M^{-1}cm^{-1}$ in both 80% water-ethanol solution and in 95% ethanol. Whereas, the extinction coefficient at 540 nm for the PVP/Pt nanoparticles in the presence of the $[Ru(bpy)_2(ppz)]^{2+}$ complex is 4.5 x 10^5 $M^{-1}cm^{-1}$ in 80% water-ethanol solution. Addition of the PVP polymer to the $[Ru(bpy)_2(ppz)]^{2+}$ complex does not produce a growth at 540 nm and only the MLCT bands of bpy and ppz are observed (Figure 73).

Adding aliquots of an aqueous solution of the PVP/Pt nanoparticles to the 1.1 x 10^{-5} M $[Ru(bpy)_2(ppz)]^{2+}$ complex in 80% water-ethanol solution and to the 1.7 x 10^{-5} M $[Ru(bpy)_2(ppz)]^{2+}$ complex in 95% ethanol solution, changes the intensity of the 540-nm band (Figures 74 and 78). Concurrent with the changes in the absorption spectra, the $[Ru(bpy)_2(ppz)]^{2+}$ emission intensity declines in proportion to the amount of nanoparticles added. Since PVP by itself has no effect on either the absorption or

emission spectra of $[Ru(bpy)_2(ppz)]^{2+}$, the decline in the 690 nm and 673 nm emission of $[Ru(bpy)_2(ppz)]^{2+}$ reflects quenching by the Pt nanoparticles.

The peak maximum for the emission quenching of (1.4 ± 0.3) x 10^{-5} M $[Ru(bpy)_2(ppz)]^{2+}$ by the PVP/Pt nanoparticles is sensitive to the solvent environment which shifted the peak from 690-nm in 80% water-ethanol (Figure 76) to 673-nm in 95% ethanol (Figure 79). The fraction of $[Ru(bpy)_2(ppz)]^{2+}$ quenched by the molecular interaction of the PVP/Pt nanoparticles at 690-nm in 80% water-ethanol solution is 64% and in 95% ethanol, the fraction of the $[Ru(bpy)_2(ppz)]^{2+}$ quenched by PVP/Pt nanoparticles is 29%.

Because of the non-linear dependence on the emission quenching of $[Ru(bpy)_2(ppz)^{2+}$-PVP/Pt] *vs.* the PVP/Pt nanoparticles concentration in 80% water-ethanol solution (Figure 77), and a Stern-Volmer quenching constant, K_{sv}, of 6 x 10^6 M^{-1}, suggests a pre-equilibrium association. However, trivial effects were an immediate concern since the nanoparticles absorb and/or scatter light at the excitation, 476 nm, and emission, 690 nm, wavelengths, and one or both could contribute to a decline in the observed emission intensity, and perhaps the shape of the Stern-Volmer plots. Using the measured absorbance at these wavelengths corresponding to the highest concentration of nanoparticles, however, shows that trivial effects account for ≤ 1% of the observed decline in emission intensity.

To confirm whether static or dynamic quenching is taking place in the $[Ru(bpy)_2(ppz)^{2+}$-PVP/Pt] system, time-resolved lifetime measurements were conducted. Stern-Volmer plots of intensity and lifetime quenching (Figure 81) by the PVP/Pt

nanoparticles reveals that ≥ 80% of the quenching in 95% ethanol occurs by a static mechanism. In fact, this may be a low estimate of the static quenching, since lifetime quenching yields a Stern-Volmer constant, K_{sv}, of 9.2 x 10^5 M^{-1}, and the relationship $K_{sv} = k_b\tau$, where τ is the emission lifetime of *$[Ru(bpy)_2(ppz)]^{2+}$ in 95% ethanol, 727 ± 8 ns, yields a bimolecular quenching rate constant, k_b, of (1.3 ± 0.1) x 10^{12} $M^{-1}s^{-1}$. The bimolecular rate constant is exceptional large considering the mass of the nanoparticles and the hydrodynamic drag created by PVP hydrogen bonding to the solvent.[25,26] In fact, it exceeds the rate of proton transfer in aqueous solution, *ca.* 1 x 10^{10} $M^{-1}s^{-1}$.[120] Perhaps the bimolecular rate constant extracted from the lifetime quenching is not a diffusion limited process in the conventional sense of one molecule diffusing up to another.

Figure 82 shows a stepwise increase in the absorbance at 540 nm as a function of the concentration of the PVP/Pt nanoparticles added, in which the concentration were calculated by using the moles of Pt in solution and dividing by the number of atoms per Pt nanoparticle multiplied by Avogadro's number.[108] The two concentrations corresponding to 5.26 x 10^{-8} M and 2.63 x 10^{-8} M of the PVP/Pt nanoparticles, indicated by the arrow, were chosen to determine the stoichiometry from a Job's law plot of the $[Ru(bpy)_2(ppz)^{2+}$-PVP/Pt] interaction. The Job's plot of the absorbance at 540 nm *vs.* the mole fraction of the PVP/Pt nanoparticles, yield PVP/Pt/$[Ru(bpy)_2(ppz)]^{2+}$ ratios < 1. TEM image of 5.26 x 10^{-11} mol PVP/Pt nanoparticles in the presence of 1.92 x 10^{-7} mol $[Ru(bpy)_2(ppz)]^{2+}$, leads to aggregates of 3 or 4 nanoparticles (Figure 84). At 2.10 x 10^{-10} mol PVP/Pt in the presence of 4.8 x 10^{-8} mol $[Ru(bpy)_2(ppz)]^{2+}$, larger aggregates containing as many as 45 PVP/Pt nanoparticles are detected, ranging from close to

circular, to triangular and crescent-like (Figure 85a). Rather, in view of the relatively open structures of the aggregates interlaced with the solvent (Figure 85a), lifetime quenching may reflect the structural changes within the aggregate necessary for quenching to occur. In which case, the bimolecular quenching rate constant, $(1.3 \pm 0.1) \times 10^{12}$ $M^{-1}s^{-1}$ reflects diffusion within the aggregate, and/or structural changes within the aggregates necessary for quenching to occur.

The calculated oxidation and reduction potentials of $*[Ru(bpy)_2(ppz)]^{2+}$, 0.43eV and 0.73 eV, respectively,[73] indicate the excited complex is capable of both oxidative and reductive quenching. Since XANES spectra give no indication of the presence of oxidized Pt in the nanoparticles, reductive quenching,

$$*[Ru(bpy)_2(ppz)]^{2+} + PVP/Pt^{+} \rightarrow *[Ru(bpy)_2(ppz)]^{3+} + PVP/Pt \qquad (13)$$

by an oxidized Pt ion within the nanoparticle is discounted. The one electron oxidation potentials of zero valent Pt is not known, but assuming they are less than or equal to the two electron oxidation of Pt, $E^o = 1.188$ V,[138] oxidative quenching is endergonic and also discounted. The PVP/Pt nanoparticles exhibit absorptions extending into the region of the $*[Ru(bpy)_2(ppz)]^{2+}$ emission in 95% ethanol, 673 nm, and 80% water-ethanol, 690 nm. The absorbance is a linear function of [PVP/Pt] and based on the calculated concentrations of PVP/Pt yields a molar extinction coefficient at the $[Ru(bpy)_2(ppz)]^{2+}$ emission wavelength, 673 nm, of 6.7×10^5 $M^{-1}cm^{-1}$. The origin of these transitions are not known, although recent studies of Pt capped Au nanoparticles reveal the appearance of a broad absorption, tentatively assigned to a plasmon absorption, in the 500-700 nm region as the thickness of the Pt shell increases from 21 to 40 nm.[139] These are

significantly larger than the 3.1 ± 0.4 nm diameter PVP capped Pt nanoparticles examined in these experiments. Nonetheless, nanoparticle absorptions in the energy range of the 673 nm emission from $*[Ru(bpy)_2(ppz)]^{2+}$ raise the possibility of energy transfer quenching. Considering the high spin-obit coupling of Pt and Ru(II) that minimize spin restrictions, however, energy transfer quenching within these preassembled $[Ru(bpy)_2(ppz)^{2+}$-PVP/Pt] aggregates would be expected to occur rapidly and therefore not exhibit lifetime quenching.

On the other hand, lifetime quenching of $*Ru(bpy)_2(ppz)]^{2+}$ by proton transfer is possible. Since hydrogen bonding to PVP is expected to occur at either the C=O or nitrogen of the PVP pyrrolidone ring,[25,26] this implies a more random arrangement of PVP's about the nanoparticles with some fraction of the capping PVP's arranged such that the pyrrolidone ring is exposed to the solvent.

Alternatively, the PVP layers surrounding the nanoparticles may alternate from hydrophobic to polar on further additions of PVP. Since the FTIR indicate the initial interaction occurs between the growing Pt nanoparticles and the pyrrolidone ring of PVP, the initial metal-PVP aggregates create a hydrophobic outer layer. If a second layer of PVP grows on this first layer, the favorable hydrophobic-hydrophobic interaction of the hydrocarbon portions of PVP forces the pyrrolidone to the outside, thereby creating a polar outer layer. The result is an "onion-like" layered structure composed of alternating hydrophobic-polar-hydrophobic-polar layers. In either case, since the hydrogen bonding sites in both PVP and the heteroleptic ligands are Bronsted bases, hydrogen bonding between the two has to be mediated by an intervening water molecule. This model of

hydrogen bonding is structurally more complex than the more diffuse hydrophobic-hydrophobic interaction proposed above. Yet, it implies a more random arrangement of the capping PVP about the Pt nanoparticles with some fraction of the pyrrolidone rings adjacent to the nanoparticles and another fraction exposed to the solvent. This is entropically favored, while the "onion-like" structure is more in line with aggregates with considerable spacing between the individual PVP/Pt nanoparticles (Figure 16a). Both structural models suggest the formation of aggregates interlaced with the solvent.

In the presence of $[Ru(bpy)_3]^{2+}$, however, TEM analyses fail to give any indication of aggregation even at the highest nanoparticle concentration used in the experiments with $Ru(bpy)_2ppz^{2+}$. The ppz ligand differ from bpy in two ways; the availability of slightly basic nitrogens on the ligand periphery, and size and aromaticity, which influences their hydrophobicity and, in turn, their solvation. The occurrence of aggregation in the presence of $[Ru(bpy)_2(ppz)]^{2+}$ points to the complex as the initiation point of nanoparticle aggregation, while the more pronounced changes in the ppz localized MLCT absorption with minimal change in the bpy localized MLCT absorption of the complex more specifically point to the heteroleptic ppz ligand.

However, two fundamental uncertainties exist regarding the formation of the larger aggregates. First, it is not known whether continued aggregation occurs about the complex, *i.e.,* continued aggregation of the nanoparticles occurs about a single $[Ru(bpy)_2(ppz)]^{2+}$ and the initiating complex remains within the interior of the growing aggregate, or the complex is on the outer periphery of the growing aggregate. Regardless of the location of the complex ion, each larger aggregate contains a single complex ion.

Or second, since the concentrations of $[Ru(bpy)_2(ppz)]^{2+}$ exceed the calculated concentrations of the PVP/Pt nanoparticles used in the aggregation experiment, the larger aggregates could be made up of smaller $[Ru(bpy)_2(ppz)^{2+}$-PVP/Pt] aggregates, in which case, the larger aggregates contain more than one complex ion. In the first case, as the number of Pt nanoparticles about the complex increases, the role of the heteroleptic ligand is diluted, and aggregation occurs through an interaction between the PVP cap of Pt nanoparticles on the periphery of the aggregate, and the PVP cap of the adding PVP/Pt nanoparticle. Assuming the PVP caps are spherical, any structural directionality or constraint imposed by the heteroleptic ligand is replaced by random additions of Pt nanoparticles and, as observed, the formation of larger aggregates of differing shapes (Figure 85a). In addition to a loss of structural constraints imposed by the initiating heteroleptic ppz ligand, the increasing size of the aggregate may increase the hydrophobicity of the aggregate as a whole thereby changing the driving force for aggregation from the proposed initial solvent mediated hydrogen bonding to a hydrophobic-hydrophobic interaction.[140,141] The structural implications of the second possibility depend on the ratio of the complex ion to the PVP/Pt nanoparticles within the aggregate. A small ratio approaches the structural implication of the first possibility, whereas a larger ratio increases the influence of the heteroleptic ligand and the structural consequences imposed by the ligand. With more than one complex ion per aggregate, the directionality and/or constraints imposed by the heteroleptic ppz ligand may account for the circular, triangular and crescent shapes of the larger aggregates. The data do not distinguish these structural possibilities, but both possibilities are expected to influence

the absorption and emission spectra of the complex on or within the aggregate, and the quenching of it MLCT emission.

Since protonation of the peripheral pyrazinyl nitrogens in the $[Ru(bpy)_2(ppz)]^{2+}$ complex leads to emission and lifetime quenching,[121,142] and the inversion of the relative basicities that occurs on population of the ppz localized MLCT state, quenching is attributed to proton transfer, and the rate constant extracted from the lifetime quenching, $(1.3 \pm 0.1) \times 10^{12}\ M^{-1}s^{-1}$ is attributed to the rate of solvent rearrangement necessary to accommodate the inversion of basicity accompanying population of the ppz localized MLCT state, and the transfer to the proton to the pyrizinyl nitrogen to quench the excited complex. The coordination of the Ru complex with PVP/Ir nanoparticles was also investigated to study their electronic behavior and the degree of aggregation in the presence of $[Ru(bpy)_2(ppz)]^{2+}$ complex.

4.10. Association of $[Ru(bpy)_2(ppz)]^{2+}$ with PVP/Ir Nanoparticles

Figure 86a shows the absorption spectrum of 1.0×10^{-5} M $[Ru(bpy)_2(ppz)]^{2+}$ with 5.6×10^{-7} M PVP/Ir nanoparticles in 80% water-ethanol solution and has the same spectral fit in comparison to $[Ru(bpy)_2(ppz)^{2+}$-PVP/Pt] aggregates. Resolution of the spectrum reveals a band at 539 nm (Figure 87). Adding aliquots of the PVP/Ir nanoparticles to the $[Ru(bpy)_2(ppz)]^{2+}$ complex in 80% water-ethanol solution, increases the absorbance at 539 nm on the lower energy side of the ppz ligand (Figure 88).

The fraction of $[Ru(bpy)_2(ppz)]^{2+}$ complex quenched by the PVP/Ir nanoparticles at 690 nm in 80% water-ethanol solution is 50%. The Stern-Volmer (S-V) plot of $[Ru(bpy)_2(ppz)]^{2+}$ with PVP/Ir nanoparticles (Figure 90) has a similar non-linear

dependence to the S-V plot of the PVP/Pt nanoparticles in the presence of the $[Ru(bpy)_2(ppz)]^{2+}$ complex previously described in Section 4.9. A trendline added to the non-linear point in the S-V plot (Figure 90), for the reaction of $[Ru(bpy)_2(ppz)]^{2+}$ by the PVP/Ir nanoparticles, gave a Stern-Volmer constant, K_{sv}, of 7.4 x 10^5 M^{-1} and suggests a pre-equilibrium association (Figure 82). XANES data also confirms there is no oxidation of the Ir nanoparticles and the standard redox potential of the half reaction of Ir^0

$$Ir^0 \rightarrow Ir^{3+} + 3e^- \quad (14)$$

is -1.156 V,[138] therefore oxidative $*[Ru(bpy)_2(ppz)]^{2+}$ electron transfer quenching by Ir^0 is endergonic and unlikely.

A plot of absorbance at 539 nm for the interaction of $[Ru(bpy)_2(ppz)]^{2+}$ by the PVP/Ir nanoparticles added, shows a non-linear dependence (Figure 91) and not a "step-like curve to that observed for the PVP/Pt nanoparticles in the presence of $[Ru(bpy)_2(ppz)]^{2+}$ at 540-nm. After the addition of the PVP/Ir nanoparticles to the $[Ru(bpy)_2(ppz)]^{2+}$ in 80% water-ethanol, the solution became cloudy. Because PVP is soluble in water,[23] the absence of a "step-like" curve may be due to changes in the refractive index of the solvent caused by the interaction of the PVP polymer with water.

TEM image show aggregates of the PVP/Ir nanoparticles (Figure 92a) ranging from close to circular with sizes of 60 nm in diameter (circled in red). The particle size of the individual PVP/Ir nanoparticles within the aggregates obtained from the TEM histogram are 1.8 ± 0.3 nm in diameter (Figure 92b), and are identical to the diameters of the individual PVP/Ir nanoparticles in the absence of the $[Ru(bpy)_2(ppz)]^{2+}$ complex. Expanding the images of the $[Ru(bpy)_2(ppz)^{2+}$-PVP/Ir] aggregates (Figure 92a) yields

100 PVP/Ir nanoparticles in the aggregate. Assuming the aggregates, which are close to circular in the two dimensional TEM images, are actually spherical, the radii of the circled PVP/Ir aggregate, 30 nm, yield total aggregate volume of 1.13×10^5 nm^3. Assuming the number of nanoparticles visible in the TEM images is only those in the upper half of the spherical aggregates, the PVP/Ir nanoparticles occupy < 1% of the total aggregate volume. The assumptions that the aggregates are spherical, and the number of nanoparticles present is twice the number evident in the TEM images are, of course, questionable. Nonetheless, the small fraction of the total volume attributable to the PVP/Ir nanoparticles is consistent with the space between the individual nanoparticles evident in the TEM images (Figure 92a) and suggestive of an open structure interlaced by a considerable amount of solvent. As such, this structural model is more consistent with solvent-mediated hydrogen bonding, than an aggregate held together by hydrophobic-hydrophobic interactions while, at the same time, interlaced with polar aqueous-alcohol solvents. The more extensive aggregation in the presence of $[Ru(bpy)_2(ppz)]^{2+}$, which possesses the more basic peripheral nitrogens and the large amount of these polar solvents apparently incorporated into the aggregates (Figure 92a) lead us to propose that the initial interaction between the complex and the PVP/Ir nanoparticles arises from solvent mediated hydrogen bonding between the PVP cap of the nanoparticles and the peripheral nitrogens of the heteroleptic ligand.

The PVP/Ir nanoparticles self-assembled in the presence of the Ru(II) complex through hydrogen bonding interaction without a change in the individual particle size of the PVP/Ir nanoparticles in the aggregate.

4.11. Association of $[Ru(bpy)_2(ppz)]^{2+}$ with Pt^{2+}

The appearance of the 540 nm band in the absorption spectrum for the interaction of the $[Ru(bpy)_2(ppz)]^{2+}$ by PVP/Pt nanoparticles is not due to a change in the zero oxidation state of the Pt nanoparticles. This was confirmed by a room temperature experiment carried out in sulfuric acid solution adjusted to pH=5 using 2 x 10^{-5} M $[Ru(bpy)_2(ppz)]^{2+}$ with the K_2PtCl_4 salt. The addition of the Pt^{2+} salt to the $[Ru(bpy)_2(ppz)]^{2+}$ complex exhibit a lower energy shoulder at 555 nm (Figure 93) and not at the 540-nm band for $[Ru(bpy)_2(ppz)^{2+}$-PVP/Pt] aggregates.

The emission maximum at 690-nm of $[Ru(bpy)_2(ppz)]^{2+}$ complex was quenched by 95% with Pt^{2+} salt added (Figure 94). The Stern-Volmer constant, K_{sv}, of 235.4 M^{-1} was obtained from the plot in Figure 95 and an equilibrium constant, K_{eq}, of 90 was obtained from a least-squares equation modeled for one equilibrium.[121] Changes in the absorption and emission spectra of the interaction of $[Ru(bpy)_2(ppz)]^{2+}$ by the Pt^{2+} salt, suggest that the Pt^{2+} coordinates to the peripheral nitrogen atoms forming the bimetallic $[Ru(bpy)_2(ppz)Pt]^{4+}$. Recall, $*[Ru(bpy)_2(ppz)]^{2+}$ is capable of acting as either an oxidant or reductant.[73] The standard redox potential of the half reaction of Pt^{2+}

$$Pt^{2+} + 2e^- \rightarrow Pt^0 \qquad (15)$$

is 1.188 V,[138] therefore oxidative $*[Ru(bpy)_2(ppz)]^{2+}$ electron transfer quenching by Pt^{2+} is favorable.

As a result, the differences in the Stern-Volmer plot with a K_{sv}, of 235.4 M^{-1} and K_{eq}, of 90 of $[Ru(bpy)_2(ppz)Pt]^{4+}$ in comparison to the $[Ru(bpy)_2(ppz)^{2+}$-PVP/Pt] aggregates, suggests the shoulder in the absorption spectrum at 540 nm for the interaction

of $[Ru(bpy)_2(ppz)]^{2+}$ by PVP/Pt nanoparticles is not due to oxidized Pt, but is due to the zero valent state of the PVP/Pt nanoparticles.

4.12. Association of $[Ru(bpy)_2(dpp)]^{2+}$ with PVP/Pt Nanoparticles

By utilizing a different ligand, dpp, a similar absorption band was observed on the lower energy side of the dpp ligand for the interaction of the 1.00 x 10^{-4} M $[Ru(bpy)_2(dpp)]^{2+}$ by 7.88 x 10^{-7} M PVP/Pt nanoparticles (Figure 97b) in distilled water at room temperature. Resolution of the spectral changes, leads to the appearance of a low intensity growth at 528 nm (Figure 98). To establish that the 528 nm band is not from the interaction with the PVP polymer, a room temperature experiment of 1.0 x 10^{-4} M $[Ru(bpy)_2(dpp)]^{2+}$ with 1.0 x 10^{-5} M PVP in distilled water was conducted. Resolution of the bands indicates that no additional growth exists on the low energy side of the dpp MLCT transition (Figure 99).

A 5 μL sample containing the $[Ru(bpy)_2(dpp)^{2+}$-PVP/Pt] were deposited onto a copper grid and analyzed by TEM to examine if the PVP/Pt nanoparticles self-assembled in the presence of the Ru complex. TEM image of the $[Ru(bpy)_2(dpp)^{2+}$-PVP/Pt] shows randomly scattered particles and a close to circular shape aggregate of 40 nm in diameter, circled in red (Figure 100a). The individual PVP/Pt nanoparticles within the 40 nm aggregate are 2.7 ± 0.3 nm in diameter, similar to the particle size obtained from the TEM histogram of the PVP/Pt nanoparticles (Figure 17b) in the absence of the $[Ru(bpy)_2(dpp)]^{2+}$ complex. The radii of the circled PVP/Pt aggregate, 20 nm, which contains 53 PVP/Pt nanoparticles, yield total aggregate volume of 3.35 x 10^4 nm^3. Because, the larger extent of aggregation with $[Ru(bpy)_2(ppz)]^{2+}$, and the hydrogen

bonding capability of PVP,[25,26] suggests that the initial interaction between the PVP/Pt and PVP/Ir nanoparticles and these heteroleptic complexes is due to hydrogen bonding. The first protonation of $[Ru(bpy)_2(dpp)]^{2+}$ occurs at the dpp peripheral pyridyl nitrogen and titration yields a pK_a of 1.52 ± 0.03.[121] Similarly, NMR spectra show that the first protonation of $[Ru(bpy)_2(ppz)]^{2+}$ occurs at the peripheral nitrogen of the 5,6 pyridine of ppz, and titration of this site yields a pK_a of 2.4 ± 0.1.[142]

In the ground state, the peripheral dpp pyridine in $[Ru(bpy)_2(dpp)]^{2+}$, and the peripheral ppz 5,6 pyridyl nitrogen in $[Ru(bpy)_2(ppz)]^{2+}$ are the strongest bases. In fact, the inductive effect of the Ru(II) reduces the basicities of the peripheral pyrazinyl nitrogens so much that high acidities, $H_o > 5$, are needed to protonate the pyrizinyl nitrogens of both complexes in the ground state.[121,142] Assuming aggregate formation initiates by solvent mediated hydrogen bonding between the PVP caps of the Pt nanoparticles and the heteroleptic ligand of the complex, the relative basicities implies it occurs at the more basic peripheral pyridyl nitrogen of dpp and the 5,6 pyridyl nitrogen of ppz. Population of the dpp or ppz localized MLCT states, however, inverts the relative basicities of the peripheral nitrogens. In $[Ru(bpy)_2(dpp)]^{2+}$, for example, population of the dpp localized MLCT state transfers electron density principally to the peripheral dpp pyrazinyl nitrogen thereby increasing its Bronsted basicity by $> 10^6$ relative to that in the ground state, and by $> 10^2$ relative to the ground state basicity of the peripheral pyridyl nitrogen.[121] Similarly, population of the ppz localized MLCT state in $[Ru(bpy)_2(ppz)]^{2+}$ produces an equivalent inversion of the relative basicities of the peripheral ppz nitrogens. In the ground state, the basicity of the peripheral 5,6 pyridyl nitrogen exceeds that of the

pyrazinyl nitrogen, whereas population of the ppz localized MLCT state increases the Bronsted basicity of the peripheral ppz pyrazinyl nitrogen by close to 10^8 thus making it a much stronger base in the excited state than the peripheral 5,6 pyridyl nitrogen.[142] Nonetheless, $[Ru(bpy)_2(ppz)]^{2+}$ possess the more basic peripheral nitrogens, and with similar concentrations of complex and nanoparticles, TEM images indicate more extensive aggregation in the presence of the ppz complex.

Chapter 5

5. CONCLUSION

5.1. Impregnation into PVG

PVP/Pt, PVP/Ir and PVP/Pt-Ir nanoparticles were synthesized by an alcoholic reduction method. The sizes and crystallinity of the nanoparticles were measured with TEM and XRD. The PVP/Pt and PVP/Ir nanoparticles do appear to be crystalline and there is no evidence of Pt^{4+} or Ir^{4+} remaining in the sample. The shoulder at *ca.* 280 nm in the absorption spectra for the PVP/Pt, PVP/Ir and PVP/Pt-Ir nanoparticles is not due to unreacted Pt(IV) or Ir(IV) salt, but is due to nanoparticle clusters from the excitation of interband transitions (sp-d bands). The oxidation state of zero of the Pt and Ir nanoparticles and the metal-metal bond distance were analyzed by XANES and EXAFS. The XANES studies show that there was no change to the zero oxidation state of the Pt and Ir nanoparticles. If there was a change to the oxidation states, then the threshold energy of 11563.0 ± 0.3 eV for Pt and 11214.0 ± 0.3 eV for Ir will be shifted to higher energies.[117,132] The Fourier transform of the EXAFS data of the PVP/Pt-Ir nanoparticles shows that a mixture of individual Pt and individual Ir nanoparticles are present in the sample as opposed to a core shell material or an alloy. The chemical and structural environment of PVP/Pt, PVP/Ir and PVP/Pt-Ir nanoparticles adsorbed into Corning's code 7930 porous Vycor glasses were discussed. XANES spectroscopic measurements on the PVP/Pt, PVP/Ir and PVP/Pt-Ir showed no change in size or oxidation state before and after impregnation into porous Vycor glasses. EXAFS of the metal-metal bond length of the nanoparticles were slightly shorter in comparison to the respective Pt, Ir, and Pt-Ir

(80:20 wt%) foils but was due to the small size of the nanoparticles and larger surfacing area.[133]

5.2. PVP Removal

The water extraction of PVP-protected Pt nanoparticles adsorbed in Corning's code 7930 porous Vycor glasses was studied by EXAFS and FTIR spectroscopy. These spectroscopic analyses have been shown to be effective in determining the oxidation state and bond length of the Pt nanoparticles adsorbed into porous Vycor glass before and after PVP removal. The results show that there is no change in the oxidation state of the Pt nanoparticles after removal of the PVP. The Pt-Pt bond length of the Pt nanoparticles impregnated into PVG after PVP removal was 2.74 ± 0.01 Å, which is within experimental error of the Pt-Pt bond length before impregnation and the bond length between atoms in the Pt foil. FTIR spectra show that the structure of the PVP before and after extraction did not change into a new compound, but did show hydrogen bonding, arising either from the absorption of water molecules from the extraction technique or from the environment. Experimental data suggest that all the water was removed after heating the extracted PVP at 50 ^{o}C and 70 ^{o}C in a vacuum oven. The amount of PVP extracted, 46 ± 4%, remained constant after heating several times over a period of time. There is the possibility that even more PVP would have been extracted if the impregnated PVG's were left in the Soxhlet extractor for a longer time, but the extraction procedure was time consuming and the extraction was stopped after a total of 60 days.

5.3. Association of Ru(II) Diimines with PVP/Pt and PVP/Ir Nanoparticles

PVP/Pt and PVP/Ir nanoparticles spontaneously aggregate about

$[Ru(bpy)_2(ppz)]^{2+}$ and $[Ru(bpy)_2(dpp)]^{2+}$ in room temperature in aqueous-ethanol solutions. Aggregation initiates at the heteroleptic ligands, and the dependence of the extent of aggregation on the relative basicities of the peripheral ppz and dpp nitrogen atoms suggests that the initial interaction arises from solvent mediated hydrogen bonding. Formation of the aggregate shifts the ppz localized MLCT absorptions to lower energy, and the stepwise change in this absorption with increasing concentration of the PVP/Pt nanoparticles indicates a stepwise formation of larger aggregates. Increasing aggregation dilutes the effect of the heteroleptic ligand suggesting an increasing contribution of less directional hydrophobic interactions, and the formation of aggregates of differing shape. Formation of the aggregates leads to predominantly static quenching of the ppz localized MLCT emission of $[Ru(bpy)_2(ppz)]^{2+}$. The spectral properties of the nanoparticles and photoinduced changes in the acid-base properties of the peripheral ppz nitrogen atoms suggest that quenching occurs either by energy transfer to a lower energy plasmon state of the nanoparticle, or by solvent mediated proton transfer from the PVP cap of the aggregated nanoparticle and the peripheral pyrazinyl nitrogen of the ppz ligand.

Since there was no spectroscopic evidence for an interaction between the Ru(II) diimines with the stripped and unstripped Pt nanoparticles in the porous Vycor glass, our next step would be to use the bimetallic species, $[Ru(bpy)_2(ppz)^{2+}$-PVP/Pt], prepared in room temperature ethanol solution previously described and impregnate it into the porous silica matrix by solution adsorption techniques.

BIBLIOGRAPHY

1. Simon, R. C.; Mendoza, E. A.; Gafney, H. D., Photochemistry of Group 6B Hexacarbonyls Adsorbed onto Porous Vycor Glass. Evidence for the Formation of Methane from Carbon Species in the Glass. *Inorg. Chem.* **1988,** *27* (15), 2733-2742.

2. Xu, S.-P.; Gafney, H. D., Photocatalyzed Conversion of CO_2 to CH_4. *Proc. Electrochem. Soc.* **1993***, 38,* 93.

3. Auvinen, S.; Alatalo, M.; Haario, H.; Jalava, J.-P.; Lamminmäki, R.-J., Size and Shape Dependence of the Electronic and Spectral Properties in TiO_2 Nanoparticles. *J. Phys. Chem. C* **2011,** *115* (17), 8484-8493.

4. Kim, C. W.; Cha, H. G.; Kim, Y. H.; Jadhav, A. P.; Ji, E. S.; Kang, D. I.; Kang, Y. S., Surface Investigation and Magnetic Behavior of Co Nanoparticles Prepared via a Surfactant-Mediated Polyol Process. *J. Phys. Chem. C* **2009,** *113* (13), 5081-5086.

5. Zhou, X.; Xu, W.; Liu, G.; Panda, D.; Chen, P., Size-Dependent Catalytic Activity and Dynamics of Gold Nanoparticles at the Single-Molecule Level. *J. Am. Chem. Soc.* **2010,** *132* (1), 138-146.

6. Cheon, J.; Lee, J.-H., Synergistically Integrated Nanoparticles as Multimodal Probes for Nanobiotechnology. *Acc. Chem. Res.* **2008** *41* (12), 1630-1640.

7. Shapiro, M. G.; Szablowski, J. O.; Langer, R.; Jasanoff, A., Protein Nanoparticles Engineered to Sense Kinase Activity in MRI. *J. Am. Chem. Soc.* **2009,** *131* (7), 2484-2486.

8. Gerion, D.; Herberg, J.; Bok, R.; Gjersing, E.; Ramon, E.; Maxwell, R.; Kurhanewicz, J.; Budinger, T. F.; Gray, J. W.; Shuman, M. A.; Chen, F. F., Paramagnetic Silica-Coated Nanocrystals as an Advanced MRI Contrast Agent. *J. Phys. Chem. C* **2007,** *111* (34), 12542-12551.

9. Liong, M.; Lu, J.; Kovochich, M.; Xia, T.; Ruehm, S. G.; Nel, A. E.; Tamanoi, F.; Zink, J. I., Multifunctional Inorganic Nanoparticles for Imaging, Targeting, and Drug Delivery. *J. Am. Chem. Soc. Nano* **2008,** *2* (5), 889-896.

10. Griset, A. P.; Walpole, J.; Liu, R.; Gaffey, A.; Colson, Y. L.; Grinstaff, M. W., Expansile Nanoparticles: Synthesis, Characterization, and in Vivo Efficacy of an Acid-Responsive Polymeric Drug Delivery System. *J. Am. Chem. Soc.* **2009,** *131* (7), 2469-2471.

11. Nasongkla, N.; Bey, E.; Ren, J.; Ai, H.; Khemtong, C.; Guthi, J. S.; Chin, S.-F.; Sherry, A. D.; Boothman, D. A.; Gao, J., Multifunctional Polymeric Micelles as Cancer-

Targeted, MRI-Ultrasensitive Drug Delivery Systems. *Nano Lett.* **2006,** *6* (11), 2427-2430.

12. Cheng, Y.; Stakenborg, T.; Van Dorpe, P.; Lagae, L.; Wang, M.; Chen, H.; Borghs, G., Fluorescence Near Gold Nanoparticles for DNA Sensing. *Anal. Chem.* **2011,** *83* (4), 1307-1314.

13. Lucena, P.; Vadillo, J. M.; Laserna, J. J., Mapping of Platinum Group Metals in Automotive Exhaust Three-Way Catalysts Using Laser-Induced Breakdown Spectrometry. *Anal. Chem.* **1999,** *71* (19), 4385-4391.

14. Chen, A.; Holt-Hindle, P., Platinum-Based Nanostructured Materials: Synthesis, Properties, and Applications. *Chem. Rev.* **2010** *110* (6), 3767-3804.

15. Barbante, C.; Veysseyre, A.; Ferrari, C.; Velde, K. V. D.; Morel, C.; Capodaglio, G.; Cescon, P.; Scarponi, G.; Boutron, C., Greenland Snow Evidence of Large Scale Atmospheric Contamination for Platinum, Palladium, and Rhodium. *Environ. Sci. Technol.* **2001,** *35* (5), 835-839.

16. Wang, L.; Yamauchi, Y., Facile Synthesis of Three-Dimensional Dendritic Platinum Nanoelectrocatalyst. *Chem. Mater.* **2009,** *21* (15), 3562-3569.

17. Wang, H.; Song, Y.; Medforth, C. J.; Shelnutt, J. A., Interfacial Synthesis of Dendritic Platinum Nanoshells Templated on Benzene Nanodroplets Stabilized in Water by a Photocatalytic Lipoporphyrin. *J. Am. Chem. Soc.* **2006,** *128* (29), 9284-9285.

18. Rioux, R. M.; Song, H.; Hoefelmeyer, J. D.; Yang, P.; Somorjai, G. A., High-Surface-Area Catalyst Design: Synthesis, Characterization, and Reaction Studies of Platinum Nanoparticles in Mesoporous SBA-15 Silica. *J. Phys. Chem. B.* **2005,** *109* (6), 2192-2202.

19. Szczerba, M.; Srodon, J.; Skiba, M.; Derkowski, A. One-dimensional structure of exfoliated polymer-layered silicate nanocomposites: A polyvinylpyrrolidone (PVP) case study. *Appl. Clay Sci.* **2010,** *47,* 235-241.

20. Lihong, L.; Zhongfang, L.; Shaopu, L.; Xiaoli, Hu.; Linfeng, L. Fading Spectrophotometric Method for the Determination of Polyvinylpyrrolidone with Eosin Y. *Chin. J. Chem.* **2009,** *27,* 1505-1509.

21. Bharali, D. J.; Sahoo, S. K.; Mozumdar S.; Maitra, A. Cross-linked polyvinylpyrrolidone nanoparticles: a potential carrier for hydrophilic drugs. *J. Colloid Interface Sci.* **2003,** *258,* 415-423.

22. Peniche, C.; Zaldivar, D.; Pazos, M.; Paz, S.; Bulay, A.; Roman, J. S. Study of the Thermal Degradation of Poly(N-vinyl-2-pyrrolidone) by Thermogravimetry-FTIR. *J. Appl. Polym. Sci.* **1993,** *50,* 485-493.

23. Haaf, F.; Sanner, A.; Straub, F. Polymers of *N*-Vinylpyrrolidone: Synthesis, Characterization and Uses. *Polym. J.* **1985,** *17,* 143-152.

24. Luo, Y.; Sun, X. One-step preparation of poly(vinyl alcohol)-protected Pt nanoparticles through a heat-treatment method. *Mater. Lett.* **2007,** *61,* 2015-2017.

25. Malynych, S.; Luzinov, I.; Chumanov, G. Poly(Vinyl Pyridine) as a Universal Surface Modifier for Immobilization of Nanoparticles. *J. Phys. Chem. B.* **2002,** *106,* 1280-1285.

26. Ping, Z. H.; Nguyen, Q. T.; Chen, S. M.; Zhou, J. Q.; Ding, Y. D. States of water in different hydrophilic polymers – DSC and FTIR studies. *Polymer*, **2001,** *42,* 8461-8467.

27. Kumar, S.; Aswal, V. K., Tuning of nanoparticle–surfactant interactions in aqueous system. *J. Phys.: Condens. Matter* **2011,** *23* (3), 035101.

28. Zhang, L.; Niu, H.; Chen, Y.; Liu, H.; Gao, M., Preparation of platinum nanoparticles using star-block copolymer with a carboxylic core. *J. Colloid Interface Sci.* **2006,** *298* (1), 177-182.

29. Li, D.; Kaner, R. B., Shape and Aggregation Control of Nanoparticles: Not Shaken, Not Stirred. *J. Am. Chem. Soc.* **2006,** *128,* 968-975.

30. Shiraishi, Y.; Nakayama, M.; Takagi, E.; Tominaga, T.; Toshima, N., Effect of quantity of polymer on catalysis and superstructure size of polymer-protected Pt nanoclusters. *Inorg. Chim. Acta.* **2000,** *300-302,* 964-969.

31. Zheng, M.; Gu, M.; Jin. Y.; Jin, G. Optical properties of silver-dispersed PVP thin film. *Mater. Res. Bull.* **2001,** *36,* 853-859.

32. Nguyen, V. L.; Nguyen, D. C.; H.; Ohtaki, M.; Hayakawa, T.; Nogami. M. Chemical synthesis and characterization of palladium nanoparticles. *Adv. Nat. Sci.: Nanosci. Nanotechnol.* **2010,** *1,* 035012 (5 pages).

33. Kemal, L.; Jiang, X. C.; Wong, K.; Yu, A. B. Experimental and Theoretical Study of Poly(vinyl pyrrolidone)-controlled Gold Nanoparticles. *J. Phys. Chem. C.* **2008,** *112,* 15656-15664.

34. Borodko, Y.; Humphrey, S. M.; Tilley, T. D.; Frei, H.; Somorjai, G. A. Charge-Transfer Interaction of Poly(vinylpyrrolidone) with Platinum and Rhodium Nanoparticles. *J. Phys. Chem. C.* **2007,** *111,* 6288-6295.

35. Zhou, M.; Chen, S.; Ren, H.; Wu, L.; Zhao, S. Electrochemical formation of platinum nanoparticles by a novel rotating cathode method. *Physica E.* **2005,** *27,* 341-350.

36. Prabhuram, J.; Wang, X.; Hui, C. L.; Hsing, I-M., Synthesis and Characterization of Surfactant-Stabilized Pt/C Nanocrystals for Fuel Cell Applications. *J. Phys. Chem. B.* **2003,** *107* (40), 11057-11064.

37. Wang, C.; Daimon, H.; Lee, Y.; Kim, J.; Sun, S., Synthesis of Monodisperse Pt Nanocubes and Their Enhanced Catalysis for Oxygen Reduction. *J. Am. Chem. Soc. Commun.* **2007,** *129* (22), 6974-6975.

38. Qin, G. W.; Pei, W.; Ma, X.; Xu, X.; Ren, Y.; Sun, W.; Zuo, L., Enhanced Catalytic Activity of Pt Nanomaterials: From Monodisperse Nanoparticles to Self-Organized Nanoparticle-Linked Nanowires. *J. Phys. Chem. C.* **2010,** *114* (15), 6909-6913.

39. Chen, C-W.; Akashi, M., Synthesis, Characterization, and Catalytic Properties of Colloidal Platinum Nanoparticles protected by Poly(*N*-isopropylacrylamide). *Langmuir* **1997,** *13* (24), 6465-6472.

40. Wang, Z. L.; Petroski, J. M.; Green, T. C.; El-Sayed, M. A., Shape Transformation and Surface Melting of Cubic and Tetrahedral Platinum Nanocrystals. *J. Phys. Chem. B* **1998,** *102* (32), 6145-6151.

41. Du, Y. K.; Yang, P.; Mou, Z. G.; Hua, N. P.; Jiang, L. Thermal Decomposition Behaviors of PVP Coated on Platinum Nanoparticles. *J. Appl. Polym. Sci.* **2006,** *99,* 23-26.

42. Vandenburg, H. J.; Clifford, A. A.; Bartle, K. D.; Carroll, J.; Newton, I.; Garden, L. M.; Dean, J. R.; Costley, C. T., Critical Review Analytical Extraction of Additives From Polymers. *The Analyst* **1997,** *122* (9), 101R-116R.

43. Schnitzler, M. D.; Mangrich, A. S.; Macedo, W. A. A.; Ardisson, J. D.; Zarbin, A. J. G., Incorporation, Oxidation and Pyrolysis of Ferrocene into Porous Silica Glass: a Route to Different Silica/Carbon and Silica/Iron Oxide Nanocomposites. *Inorg. Chem.* **2006,** *45* (26), 10642-10650.

44. Simon, R.; Gafney, H. D.; Morse, D. L., Room-Temperature Isolation and Characterization of Group 6 Pentacarbonyls in Porous Vycor Glass. *Inorg. Chem.* **1983,** *22* (3), 573-574.

45. Kennelly, T.; Gafney, H. D.; Braun, M., Photoinduced Disproportionation of $Ru(bpy)_3^{2+}$ on Porous Vycor Glass. *J. Am. Chem. Soc.* **1985,** *107* (15), 4431-4440.

46. Darsillo, M. S.; Gafney, H. D.; Paquette, M. S., Photochemistry of $Fe(CO)_5$ Adsorbed o3to Porous Vycor Glass. *J. Am. Chem. Soc.* **1987,** *109* (11), 3275-3286.

47. Shi, W.; Gafney, H. D., Spectroscopic Evidence of a Net Formation of MV^+ via Photolysis of $Ru(bpy)_3^{2+}$ and MV^{2+} Adsorbed on Porous Vycor Glass. *J. Am. Chem. Soc.* **1987,** *109*, 1582-1583.

48. Dieter, T.; Gafney, H. D., Thermal and Photochemical Reactions of $Ru_3(CO)_{12}$ Adsorbed onto Porous Vycor Glass. *Inorg. Chem.* **1988** *27* (10), 1730-1736.

49. Darsillo, M. S.; Gafney, H. D.; Paquette, M. S., Photoassisted Catalysis of the 1-Pentene Isomerization by $Fe(CO)_5$ Physisorbed onto Porous Vycor Glass. *Inorg. Chem.* **1988,** *27* (16), 2815-2819.

50. Mendoza, E. A.; Eugene Wolkow; Suni1, D.; Wong, P.; Sokolov, J.; Rafailovich, M. H.; Boer, M. d.; Gafney, H. D., A Comparison of Iron Oxides Photodeposited in Porous Vycor Glass and Tetramethoxysilane/Methanol/Water Xerogels. *Langmuir* **1991,** *7* (12), 3046-3051.

51. Sunil, D.; Sokolov, J.; Rafailovich, M. H.; Duan, X.; Gafney, H. D., Evidence for the Photodeposition of Elemental Iron in Porous Vycor Glass. *Inorg. Chem.* **1993** *32* (21), 4489-4490.

52. Wiltzius, P.; Bates, F. S.; Dierker, S. B., Structure of porous Vycor glass. *Phys. Rev. A* **1987,** *36* (6), 2991-2994.

53. Sunil, D.; Dong, J.; Gafney, H. D., Influence of Amorphous Silica Matrices on the Formation, Structure, and Chemistry of Iron and Iron Oxide Nanoparticles. *J. Am. Chem. Soc.* **2009,** *131* (41), 14768-14777.

54. Krawiec, P.; Kockrick, E.; Simon, P. Auffermann, G.; Kaskel, S., Platinum-Catalyzed Template Removal for the in Situ Synthesis of MCM-41 Supported Catalysts. *Chem. Mater.* **2006,** *18* (11), 2663-2669.

55. Song, H.; Rioux, R. M.; Hoefelmeyer, J. D.; Komor, R.; Niesz, K.; Grass, M.; Yang, P.; Somorjai, G. A., Hydrothermal Growth of Mesoporous SBA-15 Silica in the Presence of PVP-Stabilized Pt Nanoparticles: Synthesis, Characterization, and Catalytic Properties. *J. Am. Chem. Soc.* **2006,** *128* (9), 3027-3037.

56. Zeng, J.; Francia, C.; Dumitrescu, M. A.; Monteverde Videla, A. H. A.; Ijeri, V. S.; Specchia, S.; Spinelli. P., Electrochemical Performance of Pt-Based Catalysts Supported

on Different Ordered Mesoporous Carbons (Pt/OMCs) for Oxygen Reduction Reaction. *Ind. Eng. Chem. Res.* **2011,** (ASAP).

57. Su, F.; Poh, C. K.; Tian, Z.; Xu, G.; Koh, G.; Wang, Z.; Liu, Z.; Lin, J., Electrochemical Behavior of Pt nanoparticles Supported on Meso-and Microporous Carbons for Fuel Cells. *Energ. Fuels* **2010,** *24,* 3727-3732.

58. Lyons, O. D.; Musselwhite, N. E.; Carl, L. M.; Manbeck, K. A.; Marsh, A. L., Synthesis, Characterization, and Reaction Studies of a PVP-Capped Platinum Nanocatalyst Immobilized on Silica. *Langmuir* **2010,** *26* (21), 16481-16485.

59. Kwon, S. J.; Fan, F.-R. F.; Bard, A. J., Observing Iridium Oxide (IrO_x) Single Nanoparticle Collisions at Ultramicroelectrodes. *J. Am. Chem. Soc.* **2010,** *132* (38), 13165-13167.

60. Nakagawa, T.; Bjorge, N. S.; Murray, R. W., Electrogenerated IrO_x Nanoparticles as Dissolved Redox Catalysts for Water Oxidation. *J. Am. Chem. Soc.* **2009,** *131* (43), 15578–15579.

61. Youngblood, W. J.; Lee, S.-H. A.; Kobayashi, Y.; Hernandez-Pagan, E. A.; Hoertz, P. G.; Moore, T. A.; Moore, A. L.; Gust, D.; Mallouk, T. E., Photoassisted Overall Water Splitting in a Visible Light-Absorbing Dye-Sensitized Photoelectrochemical Cell. *J. Am. Chem. Soc.* **2009,** *131* (3), 926-927.

62. Morris, N. D.; Suzuki, M.; Mallouk, T. E., Kinetics of Electron Transfer and Oxygen Evolution in the Reaction of $[Ru(bpy)_3]^{3+}$ with Colloidal Iridium Oxide. *J. Phys. Chem. A* **2004,** *108* (42), 9115-9119.

63. Blakemore, J. D.; Schley, N. D.; Balcells, D.; Hull, J. F.; Olack, G. W.; Incarvito, C. D.; Eisenstein, O.; Brudvig, G. W.; Crabtree, R. H., Half-Sandwich Iridium Complexes for Homogeneous Water-Oxidation Catalysis. *J. Am. Chem. Soc.* **2010,** *132* (45), 16017-16029.

64. Huo, S.; Deaton, J. C.; Rajeswaran, M.; Lenhart, W. C., Highly Efficient, Selective, and General Method for the Preparation of Meridional Homo- and Heteroleptic Tris-cyclometalated Iridium Complexes. *Inorg. Chem.* **2006,** *45* (8), 3155-3157.

65. Dupont, J.; Fonseca, G. S.; Umpierre, A. P.; Fichtner, P. F. P.; Teixeira, S. R., Transition-Metal Nanoparticles in Imidazolium Ionic Liquids: Recyclable Catalysts for Biphasic Hydrogenation Reactions. *J. Am. Chem. Soc.* **2002,** *124* (16), 4228-4229.

66. Marzouk, S. A. M., Improved Electrodeposited Iridium Oxide pH Sensor Fabricated on Etched Titanium Substrates. *Anal. Chem.* **2003,** *75* (6), 1258-1266.

67. Rueping, M.; Koenigs, R. M.; Borrmann, R.; Zoller, J.; Weirich, T. E.; Mayer, J., Size-Selective, Stabilizer-Free, Hydrogenolytic Synthesis of Iridium Nanoparticles Supported on Carbon Nanotubes. *Chem. Mater.* **2011,** *23* (8), 2008-2010.

68. Lu, L.; Eychmuller, A., Ordered Macroporous Bimetallic Nanostructures: Design, Characterization, and Applications. *Acc. Chem. Res.* **2008,** *41* (2), 244-253.

69. Sakai, T.; Alexandridis, P., Ag and Au Monometallic and Bimetallic Colloids: Morphogenesis in Amphiphilic Block Copolymer Solutions. *Chem. Mater.* **2006,** *18* (10), 2577-2583.

70. Shan, C.-C.; Tsai, D.-S.; Huang, Y.-S.; Jian, S.-H.; Cheng, C.-L., Pt-Ir-IrO_2NT Thin-Wall Electrocatalysts Derived from IrO_2 Nanotubes and Their Catalytic Activities in Methanol Oxidation. *Chem. Mater.* **2007,** *19* (3), 424-431.

71. Chen, A.; Russa, D. J. L.; Miller, B., Effect of the Iridium Oxide Thin Film on the Electrochemical Activity of Platinum Nanoparticles. *Langmuir* **2004,** *20* (22), 9695-9702.

72. Yen, C. H.; Shimizu, K.; Lin, Y.-Y.; Bailey, F.; Cheng, I. F.; Wai, C. M., Chemical Fluid Deposition of Pt-Based Bimetallic Nanoparticles on Multiwalled Carbon Nanotubes for Direct Methanol Fuel Cell Application. *Energ. Fuels* **2007,** *21* (4), 2268-2271.

73. Fuchs, Y.; Lofters, S.; Dieter, T.; Shi, W.; Morgan, R.; Strekas, T. C.; Gafney, H. D.; Baker, A. D., Spectroscopic and Electrochemical Properties of Dimeric Ruthenium(II) Diimine Complexes and Determination of Their Excited State Redox Properties. *J. Am. Chem. Soc.* **1987,** *109* (9), 2691-2697.

74. Meyer, T. J., Chemical Approaches to Artificial Photosynthesis. *Acc. Chem. Res.* **1989,** *22* (5), 163-170.

75. Gratzel, M., Artificial Photosynthesis: Water Cleavage into Hydrogen and Oxygen by Visible Light. *Acc. Chem. Res.* **1981,** *14*, 376-384.

76. Gust, D.; Moore, T. A.; Moore, A. L., Solar Fuels via Artificial Photosynthesis. *Acc. Chem. Res.* **2009,** *42* (12), 1890-1898

77. Sutin, N.; Creutz, C., Properties and Reactivities of the Luminescent Excited States of Polypyridine Complexes of Ruthenium(II) and Osmium(II). *Inorganic and Organometallic Photochemistry, Chapter 1,* **1978,** *168*, 1-27.

78. Hicks, C.; Fan, J.; Rutenberg, I.; Gafney, H. D., Excited state acid-base chemistry A new quenching mechanism. *Coord. Chem. Rev.* **1998,** *171*, 71-84.

79. Granger, R. M. I.; Granger, J. N.; Campo, K. d.; Becherer, M. B.; Fanwick, P. E., Synthesis and Crystal Structure of Tetrachloro(1,10-phenanthroline)platinum(IV). *Va. J. Sci.* **1999,** *50* (1), 51-56.

80. Sartori, D. A.; Hurst, S. K.; Wood, N.; Larsen, R. D.; Abbott, E. H., Crystal structure, physical properties and Pt-195 NMR characterization of Pt(bipy)Br. *J. Chem. Crystallogr.* **2005,** *35* (12), 995-998.

81. Hill, H. D.; Macfarlane, R. J.; Senesi, A. J.; Lee, B.; Park, S. Y.; Mirkin, C. A., Controlling the Lattice Parameters of Gold Nanoparticle FCC Crystals with Duplex DNA Linkers. *Nano Lett.* **2008,** *8* (8), 2341-2344.

82. Schmid, G.; Morun, B.; Malm, J.-O., $Pt_{309}Phen_{36}O_{30+/-10}$, a Four-Shell Platinum Cluster. *Angew. Chem. Int. Ed. Engl.* **1989,** *28* (6), 778-780.

83. Toshima, N.; Nakata, K.; Kitoh, H., Giant platinum clusters with organic ligands: preparation and catalysis. *Inorg. Chim. Acta* **1997,** *265*, 149-153.

84. "VYCOR Brand Porous Glass 7930". Corning.com http://www.corning.com/docs/specialtymaterials/pisheets/Vycor%207930.pdf (accessed February 2, 2012).

85. Braunstein, C. H.; Baker, A. D.; Strekas, T. C.; Gafney, H. D., Spectroscopic and Electrochemical Properties of the Dimer Tetrakis (2,2'- bipyridine) (p- 2,3- bis (2-pyridyl) pyrazine) diruthenium (II) and Its Monomeric Analogue. *Inorg. Chem.* **1984,** *23* (7), 857-864.

86. "Microscopes-TEM".Nobelprize.org. http://www.nobelprize.org/educational /physics /microscopes/tem/index.html (accessed October 29, 2011).

87. "Bragg's Law". Panalytical.com. http://www.panalytical.com/index.cfm?pid=314 (accessed October 29, 2011).

88. Levine, I. N. *Physical Chemistry*, 5th ed.; McGraw-Hill: New York, 2002; p 773.

89. Hall, M. D.; Foran, G. J.; Zhang, M.; Beale, P. J.; Hambley, T. W., XANES Determination of the Platinum Oxidation State Distribution in Cancer Cells Treated with Platinum(IV) Anticancer Agents. *J. Am. Chem. Soc.* **2003,** *125* (25), 7524-7525.

90. Lin, C.; Du, C.; Chen, G.; Louh, R.; Lee, P.; Lin, H., Structural investigation of iron sulfides synthesized by mechanochemical reaction. *Mater. Sci. Eng., A* **2004,** *375-377*, 834-838.

91. Alexeev, O. S.; Li, F.; Amiridis, M. D.; Gates, B. C., Effects of Adsorbates on Supported Platinum and Iridium Clusters: Characterization in Reactive Atmospheres and

during Alkene Hydrogenation Catalysis by X-ray Absorption Spectroscopy. *J. Phys. Chem. B*, **2005**, *109* (6), 2338–2349.

92. Lytle, F. W.; Wei, P. S. P.; Greegor, R. B. Via, G. H. and Sinfelt, J. H., Effect of chemical environment on magnitude of x-ray absorption resonance at L_{III} edges. Studies on metallic elements, compounds, and catalysts. *J. Chem. Phys.* **1979,** *70* (11), 4849-4855.

93. Balcha, T.; Strobl, J. R.; Fowler, C.; Dash, P.; Scott, R. W. J., Selective Aerobic Oxidation of Crotyl Alcohol Using AuPd Core-Shell Nanoparticles. *ACS Catal.* **2011**, *1,* 425-436.

94. Izumi, Y.; Nagamori, H.; Kiyotaki, F.; Masih, D.; Minato, T.; Roisin, E.; Candy, J.-P.; Tanida, H.; Uruga, T., X-ray Absorption Fine Structure Combined with X-ray Fluorescence Spectrometry. Improvement of Spectral Resolution at the Absorption Edges of 9-29 keV. *Anal. Chem.* **2005,** *77* (21), 6969-6975.

95. Peak, D.; Sims, J. T.; Sparks, D. L., Solid-State Speciation of Natural and Alum-Amended Poultry Litter Using XANES Spectroscopy. *Environ. Sci. Technol.* **2002,** *36* (20), 4253-4261.

96. "Beamline". BNL.gov. http://beamlines.ps.bnl.gov/beamline.aspx?blid=X10C (accessed October 30, 2011).

97. Dent, A. J., Development of time-resolved XAFS instrumentation for quick EXAFS and energy-dispersive EXAFS measurements on catalyst systems. *Top. Catal.* **2002,** *18* (1-2), 27-35.

98. Zhang, Y.; Toebes, M. L.; Eerden, A. v. d.; O'Grady, W. E.; Jong, K. P. d.; Koningsberger, D. C., Metal Particle Size and Structure of the Metal-Support Interface of Carbon-Supported Platinum Catalysts as Determined with EXAFS Spectroscopy. *J. Phys. Chem. B* **2004,** *108* (48), 18509-18519.

99. Alexeev, O. S.; Siani, A.; Lafaye, G.; Williams, C. T.; Ploehn, H. J.; Amiridis, M. D., EXAFS Characterization of Dendrimer-Pt Nanocomposites Used for the Preparation of Pt/γ-Al_2O_3 Catalysts. *J. Phys. Chem. B* **2006,** *110* (49), 24903-24914.

100. Chao, K. j.; Chang, Y. p.; Chen, Y. c.; Lo, A. S.; Phan, T. h., Morphology of Nanostructured Platinum in Mesoporous Materials-Effect of Solvent and Intrachannel Surface. *J. Phys. Chem. B* **2006,** *110* (4), 1638-1646.

101. Melke, J.; Schoekel, A.; Dixon, D.; Cremers, C.; Ramaker, D. E.; Roth, C., Ethanol Oxidation on Carbon-Supported Pt, PtRu, and PtSn Catalysts Studied by Operando X-ray Absorption Spectroscopy. *J. Phys. Chem. C* **2010,** *114* (13), 5914-5925.

102. Jesus, Y. M. L.-D.; Vicente, A.; Lafaye, G.; Marecot, P.; Williams, C. T., Synthesis and Characterization of Dendrimer-Derived Supported Iridium Catalysts. *J. Phys. Chem. C* **2008,** *112* (36), 13837-13845.

103. Small, M. W.; Sanchez, S. I.; Menard, L. D.; Kang, J. H.; Frenkel, A. I.; Nuzzo, R. G., The Atomic Structural Dynamics of γ-Al_2O_3 Supported Ir-Pt Nanocluster Catalysts Prepared from a Bimetallic Molecular Precursor: A Study Using Aberration-Corrected Electron Microscopy and X-ray Absorption Spectroscopy. *J. Am. Chem. Soc.* **2011,** *133* (10), 3582-3591.

104. Patterson, A. L. The Scherrer Formula for X-Ray Particle Size Determination. *Phys. Rev.* **1939,** *56,* 978-982.

105. Borodko, Y.; Habas, S. E.; Koebel, M.; Yang, P.; Frei, H.; Somorjai, G. A., Probing the Interaction of Poly(vinylpyrrolidone) with Platinum Nanocrystals by UV-Raman and FTIR. *J. Phys. Chem B* **2006,** *110* (46), 23052-23059.

106. "Handbook of Analytical Methods for Materials". Materials Evaluation and Engineering, Inc. http://mee-inc/eds.html (accessed June 5, 2012).

107. Bauccio, M. *ASM Metals Reference Book,* 3rd ed.; ASM International: Materials Park, Ohio, 1993.

108. Liu, X.; Atwater, M.; Wang, J.; Huo, Q., Extinction coefficient of gold nanoparticles with different sizes and different capping ligands. *Colloids Surf. B. Biointerfaces* **2007,** *58* (1), 3-7.

109. Arblaster, J. W., Densities of Osmium and Iridium. Recalculations based upon a review of the latest crystallographic data. *Platinum Met. Rev.* **1989,** *33* (l), 14-16.

110. Koningsberger, D. C.; Mojet, B. L.; van Dorssen, G. E.; Ramaker, D. E., XAFS spectroscopy; fundamentals principles and data analysis. *Top. Catal.* **2000,** *10* (3-4), 143-155.

111. Via, G. H.; Sinfelt, J. H.; Lytle, F. W., Extended x-ray absorption fine structure (EXAFS) of dispersed metal catalysts. *J. Chem. Phys.* **1979,** *71* (2), 690-699.

112. Teo, B.-K.; Lee, P. A., Ab Initio Calculations of Amplitude and Phase Functions for Extended X-ray Absorption Fine Structure Spectroscopy. *J. Am. Chem. Soc.* **1979,** *101* (11), 2815-2832.

113. Teo, B. K. *EXAFS: Basic principles and Data Analysis;* Springer-Verlag: Germany, 1986.

114. Creighton, J. A.; Eadon, D. G., Ultraviolet-Visible Absorption Spectra of the Colloidal Metallic Elements. *J. Chem. Soc. Faraday Trans.* **1991,** *87* (24), 3881-3891.

115. Chytil, S.; Glomm, W. R.; Vollebekk, E.; Bergem, H.; Walmsley, J.; Sjöblom, J.; Blekkan, E. A., Platinum nanoparticles encapsulated in mesoporous silica: Preparation, characterization and catalytic activity in toluene hydrogenation. *Microporous Mesoporous Mater.* **2005,** *86* (1-3), 198-206.

116. Menard, L. D.; Wang, Q.; Kang, J. H.; Sealey, A. J.; Girolami, G. S.; Teng, X.; Frenkel, A. I.; Nuzzo, R. G. Structural characterization of bimetallic nanomaterials with overlapping x-ray absorption edges. *Phys. Rev. B.* **2009,** *80,* 064111 (11 pages).

117. Bera, P.; Priolkar, K. R.; Gayen, A.; Sarode, P. R.; Hedge, M. S.; Emura, S.; Kumashiro, R.; Jayaram, V.; Subbanna, G. N., Ionic Dispersion of Pt over CeO_2 by the Combustion Method: Structural Investigation by XRD, TEM, XPS, and EXAFS. *Chem. Mater.* **2003,** *15* (10), 2049-2060.

118. Teo, B. K.; Joy, D. C. *EXAFS Spectroscopy: Techniques and Applications;* Plenum Press: New York, 1981.

119. Taylor, L. S.; Langkilde, F. W.; Zografi, G. Fourier Transform Raman Spectroscopic Study of the Interaction of Water Vapor with Amorphous Polymers. *J. Pharm. Sci.* **2001,** *90,* 888-901.

120. Lakowicz, J. R. *Principles of Fluorescence Spectroscopy,* 3rd ed.; Springer: New York, 2006.

121. Zambrana, J. L. J.; Elena X. Ferloni; Gafney, H. D., Excited-State Coordination Chemistry: Excited-State Basicity of Bis(2,2′-bipyridyl)(2,3-dipyridylpyrazine) ruthenium(II). *J. Phys. Chem. A* **2009,** *113* (48), 13457-13468.

122. Teranishi, T.; Hosoe, M.; Tanaka, T.; Miyake, M., Size Control Monodispersed Pt Nanoparticles and Their 2D Organization by Electrophoretic Deposition. *J. Phys. Chem. B.* **1999,** *103,* 3818-3827.

123. Xu, T.; Lin, C.; Wang, C.; Brewe, D. L.; Ito, Y.; Lu, J., Synthesis of Supported Platinum Nanoparticles from Li-Pt Solid Solution. *J Am. Chem. Soc. Commun.* **2010,** *132* (7), 2151-2153.

124. Owen, E. A.; Yates, E. L., Precision measurements of crystal parameters. *Philos. Mag.* **1933,** *15* (98), 472-488.

125. Chrisanti, S. A pH electrode based on melt-oxidized iridium complex. M.A. Thesis [Online], Graduate School of the Ohio State University, Columbus, OH, 2003. http://www.matsceng.ohio-state.edu/ims/Thesis_SCh.pdf (accessed Feb 19, 2012).

126. Loukrakpam, R.; Wanjala, B. N.; Yin, J.; Fang, B.; Luo, J.; Shao, M.; Protsailo, L.; Kawamura, T.; Chen, Y.; Petkov, V.; Zhong, C-J., Structural and Electrocatalytic Properties of PtIrCo/C Catalysts for Oxygen Reduction Reaction. *ACS Catal.* **2011,** *1*, 562-572.

127. Barth, T.; Lunde, G. *Z. Phys. Chem. Neue Folge. (Wiesbaden)*, **1926,** *121*, 78.

128. Holt-Hindle, P.; Nigro, S.; Asmussen, M.; Chen, A., Amperometric glucose sensor based on platinum–iridium nanomaterials. *Electrochem. Commun.* **2008,** *10* (10), 1438-1441.

129. Ito, Y.; Winkler, D.; Jain, H.; Williams, D. B., Application of extended energy loss fine structure in determining the structure of amorphous SiO_2. *J. Non-Cryst. Solids* **1997,** *222*, 83-93.

130. Amarasinghe, D. A. S. Micro Structural Environments and Redox States of Iron in Random and Ordered Porous Silica Matrices. Ph.D. Dissertation, The Graduate Center, City University of New York, NY, 2009.

131. Sinfelt, J. H.; Via, G. H.; Lytle, F. W., Structure of bimetallic clusters. Extended x-ray absorption fine structure (EXAFS) studies of Pt-Ir clusters. *J. Chem. Phys.* **1982,** *76* (6), 2779-2789.

132. Choy, J.-H.; Kim, D.-K.; Demazeau, G.; Jug, D.-Y., L_{III}-Edge XANES Study on Unusually High Valent Iridium in a Perovskite Lattice. *J. Phys. Chem.* **1994,** *98* (25), 6258-6262.

133. Miller, J. T.; Kropf, A. J.; Zha, Y.; Regalbuto, J. R.; Delannoy, L.; Louis, C.; Bus, E.; van Bokhoven, J. A., The effect of gold particle size on Au-Au bond length and reactivity toward oxygen in supported catalysts. *J. Catal.* **2006,** *240* (2), 222-234.

134. Northrop, B. H.; Zheng, Y-R.; Chi, K-W.; Stang, P. J., Self-Organization in Coordination-Driven Self-Assembly. *Acc. Chem. Res.* **2009,** *42* (10), 1554-1563.

135. Palmer, L. C.; Stupp, S. I., Molecular Self-Assembly into One-Dimensional Nanostructures. *Acc. Chem. Res.* **2008,** *41* (12), 1674-1684.

136. Ercolani, G., A model of Self-Assembly in Solution. *J. Phys. Chem. B.* **2003,** *107* (21), 5052-5057.

137. Grzelczak, M.; Vermant, J.; Furst, E. M.; Liz-Marzan, L. M., Directed Self Assembly of Nanoparticles. *J. Am. Chem. Soc. Nano.* **2010,** *4* (7), 3591-3605.

138. Bard, A. J.; Parsons, R.; Jordan, J. *Standard Potentials in Aqueous Solutions*, IUPAC (Marcel Dekker), New York, USA, 1985.

139. Cui, L.; Wang, L.; Wu, D.-Y.; Ren, B.; Tian, Z.-Q., Shaping and Shelling Pt and Pd Nanoparticles for Ultraviolet Laser Excited Surface-Enhanced Raman Scattering. *J. Phys. Chem. C.* **2008,** *112* (45), 17618-17624.

140. Hummer, G.; Garde, S.; Garcia, A. E.; Pratt, L. R., New perspective on hydrophobic effects. *Chem. Phys.* **2000,** *258* (2-3), 349-370.

141. Matulis, D.; Bloomfield, V. A., Thermodynamics of the hydrophobic effect. I. Coupling of aggregation and pK(a) shifts in solutions of aliphatic amines. *Biophysical Chem.* **2001,** *93* (1), 37-51.

142. Perri, A.; Gafney, H. D.; Jagassar, P.; Ibarrola, G. Complexes as ligands: Coordination of Ru(II) diimines to bivalent metal ions. Presented at the 242nd National Meeting of the American Chemical Society, Denver, CO, Aug 28-Sep 1, 2011; INOR 561.